A systems biology approach to axis formation during early zebrafish embryogenesis: from biophysical measurements to model inference

Dissertation

der Mathematisch-Naturwissenschaftlichen Fakultät

der Eberhard Karls Universität Tübingen

zur Erlangung des Grades eines

Doktors der Naturwissenschaften

(Dr. rer. nat.)

vorgelegt von

Alexander Blässle

aus Ulm

Tübingen

2017

Gedruckt mit Genehmigung der Mathematisch-Naturwissenschaftlichen Fakultät der Eberhard Karls Universität Tübingen.

Tag der mündlichen Qualifikation: 18. Januar 2018

Dekan:	Prof. Dr. Wolfgang Rosenstiel
1. Berichterstatter:	Dr. Patrick Müller
2. Berichterstatter:	Prof. Dr. Rolf Reuter

Acknowledgements

A PhD is a long journey across valleys and hills and I am glad and thankful for having so many people accompanying me.

First of all, I have to thank Dr. Patrick Müller for his supervision during my PhD. Without his explanations and comments, this dissertation would have been impossible.

I would like to express my deep gratitude to Maria and Luciano for their constant help, encouragement, suggestions for this dissertation, and of course deep friendship. I could have not wished for two better mentors and friends. Collaborating with you has been an utmost rewarding experience. Moreover, I would like to thank the rest of the Systems biology of development group, especially Jelena, David, Hannes, Sarah and Maria, for fruitful discussions and help.

What made the FML and the MPI a truly beautiful place was the people that I am happy to call friends by now. Friends are an essential ingredient for a successful PhD, providing support in bad times and joy in good times. Putting my appreciation into words probably would fill books, but I hope that this little paragraph at least partially does justice.

I also would like to thank Lisa for being a continuous source of tranquility and comfort.

Finally, I would like to thank my family. As always, they have been my backbone, a constant stabilizer throughout this journey. Without their ongoing support and encouragement, this would have been impossible. I need to especially thank my mum for teaching me that hard work and dedication are key to success.

Contents

List of Figures

List of abbreviations

AP ..... Anterior-posterior

AIC ..... Akaike Information Criterion

ADMP ..... Antidorsalizing Morphogenetic Protein

API ..... Application Programming Interface

Bcd ..... Bicoid

BMP ..... Bone Morphogenetic Protein

Cyc ..... Cyclops

Dpp ..... Decapentaplegic

DV ..... Dorsal-ventral

EVF ..... Extracellular Volume Fraction

FCS ..... Fluorescence Correlation Spectroscopy

FDAP ..... Fluorescence Decay After Photoconversion

FGF ..... Fibroblast Growth Factor

FRAP ..... Fluorescence Recovery After Photobleaching

GFP ..... Green Fluorescent Protein

GUI ..... Graphical User Interface

hpf ..... Hours post fertilization

HSPG ..... Heparan Sulfate Proteoglycan

iFRAP ..... Inverse Fluorescence Recovery After Photobleaching

LALI ..... Local Activation Lateral Inhibition

MAD ..... Mothers Against Decapentaplegic

mRNA ..... Messenger RNA

oep ..... One-eyed pinhead

PDE ..... Partial Differential Equation

Pent ..... Pentagone

pSmad ..... Phosphorylated Smad

SDC ..... Synthesis-Diffusion-Clearance

SDI ..... Size-Dependent Inhibition

Shh ..... Sonic Hedgehog

Sqt ..... Squint

TGF ..... Transforming Growth Factor

Tkv ..... Thickveins

WT ..... Wild Type

YSL ..... Yolk Syncytial Layer

1. Summary

During early embryogenesis, secreted proteins dictate the body plan of developing individuals. The resulting patterns are thought to be imposed by a graded distribution of molecular signals. To this day, it is not fully understood how signaling gradients are formed, maintained and adjusted to body sizes of differently sized individuals. This dissertation aims to provide new insights into the biophysical underpinnings of signal molecule gradients of early embryonic patterning and propose novel mechanisms that allow for scale-invariant patterning.

Two of the most important parameters controlling the range and shape of signaling gradients are the rate at which signaling molecules decay and diffuse. Despite their importance, such biophysical parameters have not been measured or have only been assessed under simplified assumptions or contexts for most developmental systems. In this dissertation I present two assays and specialized software packages that allow the assessment of these parameters in living zebrafish embryos.

I then demonstrate how these tools can be used to answer long-standing questions in early embryogenesis, such as how the dorsal-ventral axis is formed. This thesis provides evidence suggesting, in contrast to current hypotheses, that the dorsal-ventral axis is formed by a simple source-sink mechanism.

Moreover, I show how to use mathematical modeling equipped with parameters estimated from the biophysical measurements to describe scale-invariant patterning during germ layer patterning in zebrafish development. My model, together with a rigorous multidimensional parameter screen fitted in normal and artificially size-reduced embryos, was able to identify a new mechanism that allows for scaling of the germ layers in differently-sized embryos with realistic parameter configurations.

In summary, this dissertation outlines how a systems biology approach can play a crucial role to advance the understanding of classical open questions in developmental biology.

2. Zusammenfassung

Der Bauplan von Organismen während der frühen embryonalen Entwicklung wird von sezenierten Molekülen bestimmt. Es wird vermutet, dass die dafür nötigen Muster durch eine gradierte Verteilung von molekularen Signalen festgelegt werden. Es ist jedoch noch unklar, wie sogenannte Signalgradienten gebildet und reguliert werden und sich der Größe des Organismus anpassen. Diese Dissertation gewährt einen tieferen Einblick in die biophysikalischen Grundlagen von Signalmolekülgradienten und stellt neue Mechanismen für skaleninvariante Musterbildung vor.

Die Stabilität und Diffusionsrate der Signalmoleküle sind zwei Parameter, die das Profil und die Reichweite von Signalgradienten stark beeinflussen. Trotz ihrer zentralen Rolle wurde die Messung dieser beiden Parameter bisher vernachlässigt oder nur unter vereinfachenden Annahmen durchgeführt. In dieser Dissertation stelle ich zwei Verfahren inklusive spezialisierten Softwarepaketen vor, die es erlauben, die Stabilität und Diffusionsrate der Signalmoleküle in lebenden Zebrafischembryonen zu bestimmen.

Mit Hilfe dieser Verfahren können Fragen der Embryonalentwicklung, wie beispielsweise die Bildung der dorsoventralen Achse, beantwortet werden, wie ich in meiner Arbeit zeigen werde. Im Gegensatz zu gegenwärtigen Hypothesen sprechen meine Ergebnisse dafür, dass die dorsoventrale Achse mit einem einfachen “Quelle-Senke”-Mechanismus erklärt werden kann.

Aus diesen Methoden erhaltene Parameter können zusammen mit mathematischer Modellierung benutzt werden, um die Keimblattbildung während der embryonalen Entwicklung von Zebrafischen zu beschreiben. Das von mir entwickelte Modell wurde mit einer rigorosen mehrdimensionalen Parametersuche an verschiedene experimentelle Beobachtungen von künstlich verkleinerten Embryos angepasst. Die so identifizierten Parameterkonfigurationen können die Skalierung der Keimblätter biologisch plausibel erklären.

Kurz gefasst beschreibt diese Dissertation, wie klassische Fragen der Entwicklungsbiologie mit Hilfe von systembiologischen Ansätzen beantwortet werden können.

3. List of publications

PyFDAP: Automated analysis of Fluorescence Decay After Photoconversion (FDAP) experiments, **Bläßle, A.**, Müller, P. (2015). *Bioinformatics*, (6):972–974

Measuring protein stability in living zebrafish embryos using Fluorescence Decay After Photoconversion (FDAP), Rogers, K. W., **Bläßle, A.**, Schier, A. F., Müller, P. (2015). *J. Vis. Exp.*, (95):e52266

Dynamics of BMP signaling and distribution during zebrafish dorsal-ventral patterning, Pomreinke, A. P., Soh, G. H., Rogers, K. W., Bergmann, J. K., **Bläßle, A.**, Müller, P., (2017). *eLife*, (6):e25861

Quantitative diffusion measurements using the open-source software PyFRAP, **Bläßle, A.**, Soh, G., Braun, T., Mörsdorf, D., Preiß, H., Jordan, B., Müller, P., *in review at Nature Communications*

Scale-invariant patterning by size-dependent inhibition of Nodal signaling, Almuedo-Castillo, M., **Bläßle, A.** , Mörsdorf, D. , Marcon, L. , Rogers, K. W., Schier, A. F., Müller, P., (2017), *in review at Nature Cell Biology*

4. Introduction

Since the early days of developmental biology, biologists have admired the surprising consistency of the body plan during development, both intraspecific and interspecific. Exactly 100 years ago, D'Arcy Thompson published "On growth and form" (Thompson, 1917), describing how geometric transformations and mathematical relationships can explain embryonic development and interspecific differences. In this groundbreaking book, he was the first to advocate the use of mathematics, physics and mechanics in the young field of developmental biology. He believed that "*in the study of things, number, order and position are the threefold clue to exact knowledge; that these three, in the mathematicians hands furnish the 'first outlines for a sketch of the universe'* ", making him the first systems biologist in developmental biology. Without the knowledge of molecular biology, most of his findings and explanations in "On growth and form" remain mainly descriptive. His ideas, however, have inspired systems biologists until today. Recent advances in computer science, microscopy, biophysics and molecular biology together with increasing collaborations across fields, allow us today to address classical questions in developmental biology in a comprehensive manner. How do cellular tissues and later organs form? How does cellular movement, division and death together with intercellular forces control tissue shapes? How are cell fates specified? And how are proportions between tissues sustained in differently sized embryos?

4.1 Morphogens and signaling gradients

During early embryogenesis, tissue patterning is mainly controlled by signaling molecules. In the 1950s Alan Turing coined the term *morphogens* to describe substances that diffuse between cells and instruct different cell fates depending on the substances' concentration or abundance (Turing, 1952). Turing supported his hypothesis by deriving a mathematical model that allows periodic patterns to emerge from a noise-perturbed uniform distribution of two interacting diffusing species, providing the first explanation for self-organization, that is, the spontaneous

creation of patterns in an originally disorded system, during embryonic development.

The idea that morphogen concentrations direct development was later formalized into the *positional information* framework by Lewis Wolpert (Wolpert, 1969). In this framework, often also referred to as the "French-flag model", morphogens are produced in localized sources from which they spread in the tissue and induce downstream target genes at varying morphogen concentrations (Figure 4.1). Wolpert (1969) also noticed that cell fate determination takes multiple hours and that most specified tissues did not exceeded $\sim$ 100 cells. Following these observations, Crick (1970) showed, using rough calculations, that diffusion of signaling molecules that are absorbed by a distant sink could explain signal gradient formation. In general, diffusion alone is not sufficient to generate stable morphogen gradients that provide equal read-outs at a given distance over time, since continuous diffusion would lead to temporally changing gradients that ultimately converge to a homogeneous morphogen distribution. However, when diffusion is coupled with molecular decay or clearance stable morphogen gradients can be formed (Kicheva *et al.*, 2007, Lander, 2007, Wartlick *et al.*, 2009, Rogers and Schier, 2011, Drocco *et al.*, 2011). Molecules can be cleared, that is, removed from the pool of signaling molecules, through various mechanisms, such as endocytosis, immobilization, or degradation (Lander, 2007). The model that signaling gradients are formed by diffusing molecules that are constantly produced by a source and cleared by a linear degradation term is referred to as the *synthesis-diffusion-clearance* (SDC) model.

4.2 Understanding the biophysical underpinnings of signaling gradients is key to model selection

Even though the idea of morphogen gradients formed by the SDC model is now a well-established framework for embryonic patterning, the biophysical underpinnings of this model in various developmental systems are still unclear. In the past decades, several studies have provided information about the biophysical parameters of different signaling molecules. These measurements however, provided different parameter estimates for the same molecules, leading to the propo-

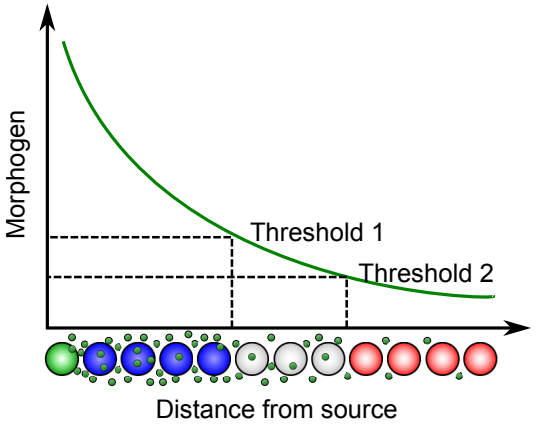

Figure 4.1: Principle of the positional information model. A source cell (green) produces morphogens that spread through the tissue. Cells along the morphogen's path then interpret the morphogen's concentration and differentiate (blue, white, red) dependent on various morphogen concentration thresholds (adapted from (Rogers and Schier, 2011)).

sition of various alternative models and controversy in the field about the correct underlying mechanism. Selecting between models that fit experimental observations based on biophysical measurements has thus been of great interest in the field of developmental biology. Two intensively discussed patterning systems are the formation of the anterior-posterior (AP) axis by Bicoid (Bcd) and patterning of the wing imaginal disc by Decapentaplegic (Dpp) in the fruit fly (*Drosophila melanogaster*) embryo.

4.2.1 Differing diffusion rate estimates complicate Bicoid gradient model inference

Probably the most prominent and well-studied example of a morphogen gradient is the Bcd gradient in *Drosophila* (Driever and Nüsslein-Volhard, 1988a,b, Struhl *et al.*, 1989, Gregor *et al.*, 2007b). The *bcd* messenger RNA (mRNA) is maternally provided on the anterior side of the fly embryo from which the transcription factor Bcd establishes a signaling gradient and ultimately determines cell fates along the anterior-posterior axis. Bcd gradient formation occurs in a highly dynamic environment. During the three hours of Bcd gradient formation in the *Drosophila* syncytium, the nuclei sharing a common cytoplasm in the embryo undergo 13 rounds of division until final cellularization, providing a continuously changing target field for Bcd. Despite extensive research, the exact mechanism by which the Bcd gradient is formed, maintained and

read-out in this dynamic environment is still unknown (Grimm *et al.*, 2010). Possible mechanisms include the SDC model at steady-state (Figure 4.2A) (Driever and Nüsslein-Volhard, 1988a,b, Houchmandzadeh *et al.*, 2002), the SDC model with pre-steady state read-out (Figure 4.2A) (Bergmann *et al.*, 2007), nuclear trapping (Figure 4.2B) (Coppey *et al.*, 2008), a fixed mRNA gradient (Figure 4.2C) (Spirov *et al.*, 2009), and mRNA diffusion (Figure 4.2D) (Lipshitz, 2009). All four proposed models make different predictions on the biophysical properties of Bcd and the interpretation of the Bcd concentration.

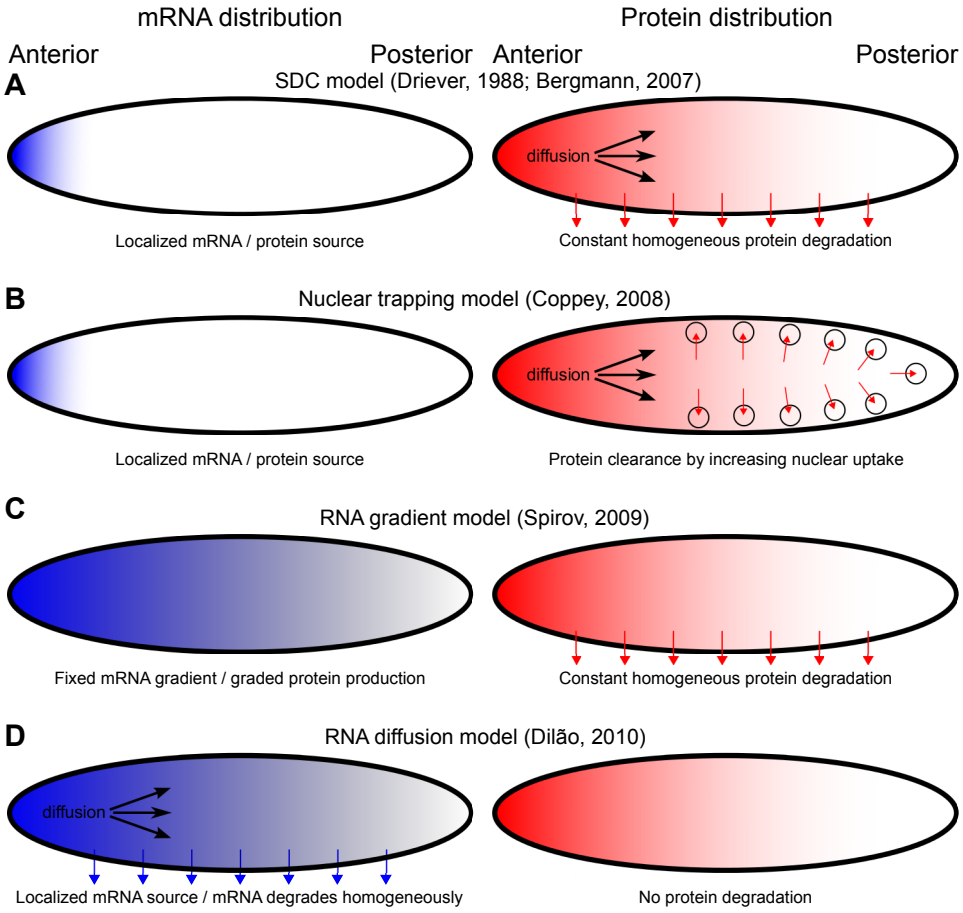

Figure 4.2: Current models for the formation of the Bcd gradient. **A** The SDC model predicts that Bcd is produced locally on the anterior side and forms a signaling gradient by diffusing through the embryo while being degraded homogeneously. **B** In the nuclear trapping model, Bcd is produced locally on the anterior side from where it spreads by diffusion throughout the embryo. Bicoid then agglomerates in the increasing number of nuclei, effectively stabilizing the gradient. **C** The fixed mRNA gradient model postulates that a predetermined graded distribution of *bcd* mRNA produces a graded distribution of Bcd protein, predicting almost identical profiles between mRNA and protein. **D** In the mRNA diffusion model, the Bcd signaling gradient is established by the initially anteriorly localized mRNA diffusing and degrading throughout the embryo, effectively forming a gradient. This graded mRNA distribution then produces a Bcd protein gradient through graded Bcd production.

With the emergence of fluorescence imaging techniques and fluorescent fusion proteins, biophysical measurements of the Bcd gradient determinants became available. For instance, the Bcd diffusion coefficient has been assessed multiple times: Gregor *et al.* (2007b) measured a Bcd diffusion coefficient of $\sim 0.3\,\mu m^2\,s^{-1}$, Abu-Arish *et al.* (2010) obtained $\sim 7\,\mu m^2\,s^{-1}$. Castle *et al.* (2011) reassessed the data of Gregor *et al.* (2007b) with improved analysis methods and found a Bcd diffusivity of $\sim 0.89\,\mu m^2\,s^{-1}$. While the estimate by Gregor *et al.* (2007b) is incompatible with the hypothesis that the Bcd gradient is formed by the SDC model or by nuclear trapping, since the slow Bcd diffusivity would not allow the gradient to be established at the proper time scale (Grimm *et al.*, 2010), Castle *et al.* (2011) argue that their reassessed diffusvity and thus the diffusivity estimated by Abu-Arish *et al.* (2010) are sufficient to explain Bcd gradient formation by both models. Sigaut *et al.* (2014) reassessed both original studies by Gregor *et al.* (2007b) and Abu-Arish *et al.* (2010), and found that both diffusion coefficients are in agreement considering their different measurement techniques and different underlying fitting model assumptions. Temporarily stable gradients and precise diffusion measurements become especially important considering the immense precision at which the Bcd gradient is read-out within less than three hours of syncytial specification during fly development. Gregor *et al.* (2007a) argue that the Bcd gradient is interpreted correctly by nuclei within 1%-2% of total embryo length, that is, roughly within 8 µm. Such precision would require the nuclei's read-out accuracy to be $\sim 10\%$. Considering the diffusion coefficients measured by Gregor *et al.* (2007b) and Castle *et al.* (2011), this would require the cells to perform temporal signal averaging over $\sim 7000\,s$, that is, almost the whole time available for Bcd gradient formation. Gregor *et al.* (2007a) propose that the necessary read-out time is inversely proportional to the morphogen's diffusivity. Thus, the much higher diffusion coefficient determined by Abu-Arish *et al.* (2010) reduces the time frame that is necessary to achieve an accurate Bcd read-out within 8 µm down to ~ 1000 s. More complex spatiotemporal averaging read-out mechanisms might further decrease the necessary time of Bcd interpretation and increase precision (Gregor *et al.*, 2007a). The question about the driving factors of Bcd gradient formation, that is, if diffusion of Bcd protein (Driever and Nüsslein-Volhard, 1988a,b, Bergmann *et al.*, 2007, Houchmandzadeh *et al.*, 2002) or the distribution of Bcd mRNA

(Spirov *et al.*, 2009, Dilão and Muraro, 2010) as well as the role of nuclear uptake (Coppey *et al.*, 2008), are key to a proper formation of the Bcd gradient, has recently been resolved by a more accurate spatiotemporal model including all known parameters and observations (Little *et al.*, 2011). The extended SDC model presented by Little *et al.* (2011) shows that through early nuclear division cycles in the Drosophila embryo, Bcd is diffusing quickly along the AP axis and Bcd mRNA forms a short gradient. With increasing nuclear density, effective Bcd diffusion decreases and Bcd maintains a stable gradient in nuclear division cycle 10–14.

In summary, precise knowledge of the biophysical properties of Bcd combined with accurate modeling were key to selecting between proposed models for Bcd gradient formation and interpretation. Further accurancy of biophysical measurements may foster our understanding of AP axis formation.

4.2.2 Varying diffusion estimates make model selection for the Decapentaplegic gradient in the wing imaginal disc difficult

Another classical example of a morphogen gradient is the Transforming Growth Factor (TGF) superfamily ligand Dpp. During *Drosophila* development, Dpp is produced on the anterior-posterior boundary of the wing imaginal disc, a precursor of the fly wing. Dpp then moves through the wing disc tissue both in the anterior and posterior compartment, forming a long-range signaling gradient of the transcription factor phosphorylated Mothers Against Decapentaplegic (MAD) by binding to its receptor Thickveins (tkv) (Lecuit *et al.*, 1996, Nellen *et al.*, 1996, Podos and Ferguson, 1999, Kicheva *et al.*, 2007). It is currently controversial how the Dpp gradient is formed. The planar transcytosis model by Kicheva *et al.* (2007) postulates that Dpp is mainly located intracellularly and moves by repeated transcytosis through the cells (Figure 4.3A) . Kicheva *et al.* (2007) support this assumption with quantifications of Dpp gradients *in vivo* combined with measurements of a low Dpp diffusion coefficient. A second model for Dpp gradient formation is free extracellular diffusion (Figure 4.3B) (Zhou *et al.*, 2012). The authors revisited diffusion measurements performed by Kicheva *et al.* (2007) and additionally performed multiple other assays for diffusion measurements. Through the combination of these assays with

an improved analysis, Zhou *et al.* (2012) consistently arrive at a two orders of magnitude higher diffusion rate for Dpp compared to the value estimated by (Kicheva *et al.*, 2007). The estimated diffusion rate by Zhou *et al.* (2012) is more than 4-fold slower than free GFP diffusion (Kicheva *et al.*, 2007). This decrease in effective diffusion rate is unlikely to be solely due to the larger molecule size of the fluoresecent fusion protein used for the measurement: the Einstein-Stokes relationship predicts that the volume of the fusion protein would need to be 64 times larger than the one of GFP, however, the fusion protein volume should maximally be around 16 times larger. The diffusion of Dpp is likely to be hindered by additional factors, such as obstacles, and molecules in the extracellular space. The restricted diffusion model postulates that reversible binding with the receptor Tkv and interaction with Heparan Sulfate Proteoglycans (HSPGs) such as Dally and Dally-like protein (Dlp) hinder Dpp diffusion, effectively creating a gradient (Figure 4.3C) (Crickmore, 2006, Akiyama *et al.*, 2008, Schwank *et al.*, 2011, Müller *et al.*, 2013). Each of the three proposed models require effective diffusion rates, that is, the net rate of diffusion, to be in different orders of magnitude and thus assign different roles and importance to biophysical processes. Additionally, each model generates different implications on the precision of the Dpp gradient (Bollenbach *et al.*, 2008). In conclusion, it is necessary to measure parameters dictating Dpp gradient formation and interpretation in the appropriate context using realistic analysis assumptions, allowing for correct morphogen gradient model selection.

4.3 Measuring biophysical properties of morphogens

The examples of the Bcd and Dpp gradient illustrate that a precise quantification of the biophysical properties of a morphogen system is crucial for the correct selection of morphogen gradient models. Despite their importance for the formation and maintenance of morphogen signaling gradients, we still have only a vague knowledge of biophysical parameters of morphogens and other molecules involved in pattern formation. Two biophysical parameters are the main instructors of gradient formation: diffusion and clearance of molecules (Crick, 1970, Lander, 2007). Even though both parameters have already been estimated for different morphogen systems (Gregor

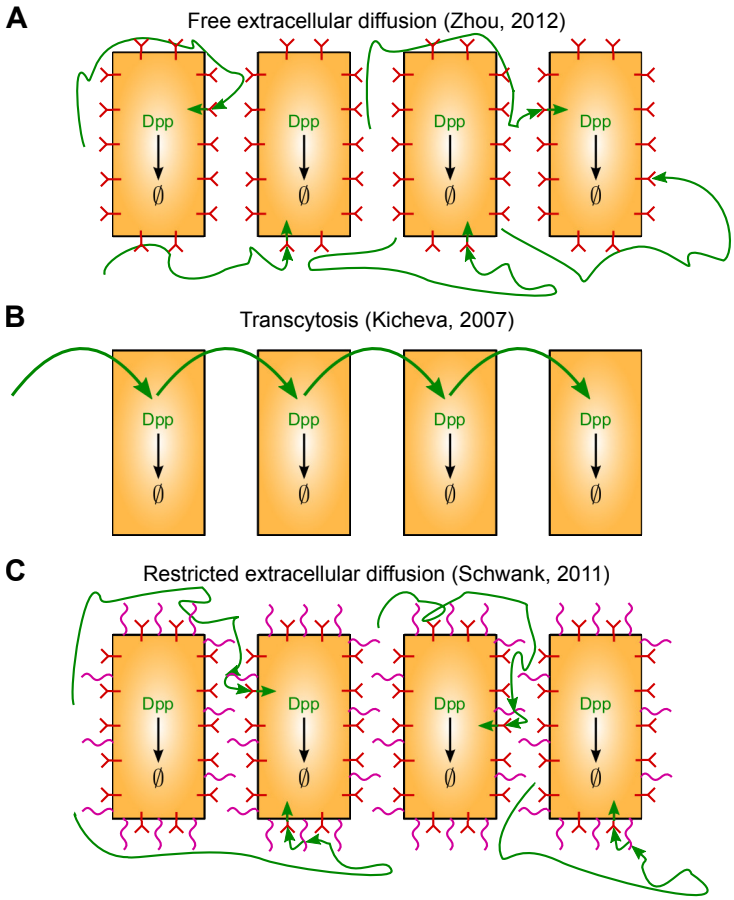

Figure 4.3: Distribution models of Dpp in the wing imaginal disc. **A** Dpp (green) diffuses freely between cells, binds to its receptor Tkv and gets internalized into the cell, where it is degraded. **B** Dpp (green) mostly relocates by uptake and secretion from cell to cell. **C** Dpp (green) diffusion is hindered by reversible binding to HSPGs (magenta) which might function as a co-receptor-like complex, bringing Dpp into the vicinity of Tkv (adapted from (Zhou *et al.*, 2012)).

et al., 2007b, Abu-Arish *et al.*, 2010, Kicheva *et al.*, 2007, Drocco *et al.*, 2011, Castle *et al.*, 2011, Wartlick *et al.*, 2009, Müller *et al.*, 2012), there is still lack of exact quantitative measurements that allow for precise parameterization of and selection of morphogen gradient models. One limitation is that it proves difficult to measure the relevant parameters *in vivo*.

4.3.1 Measuring protein stability and clearance

Protein stability, for instance, has mostly been assessed by radioactive pulse-labeling or cycloheximide chase experiments in cell cultures (Zhou, 2004) or computed indirectly using theoretical models (Kicheva *et al.*, 2007). However, protein half-lives are strongly context-dependent and

could thus differ *in vivo* and *in vitro*. The recently developed assay Fluorescence Decay After Photoconversion (FDAP) provides an alternative to traditional assays for measuring protein stability and clearance (Zhang *et al.*, 2007, Pantazis and Supatto, 2014). In FDAP experiments, a fusion of the protein of interest with a photoconvertible protein is homogeneously distributed inside the organism. A UV light pulse then converts the fluorescence of the fusion protein from the original state (i.e. green) to the photoconverted state (i.e. red). Using a confocal microscope, one then monitors the decay of the photoconverted fluorescent signal and uses model fitting to numerically extract protein half-lives and clearance rates (Figure 4.4A). One advantage of FDAP is that the use of photoconvertible proteins in FDAP allows us to ignore the production of new proteins during the time-lapse experiment since newly produced proteins will be unconverted and thus not contribute to the photoconverted signal. FDAP experiments have been successively applied to assess protein half-lives in zebrafish (*Danio rerio*) Müller *et al.* (2012).

4.3.2 Measuring protein diffusion

As previously discussed, different diffusion rates of morphogens can lead to different implications about the underlying mechanics of gradient formation and patterning. There are currently two popular techniques that allow for *in vivo* assessment of molecular diffusion: Fluorescence Correlation Spectroscopy (FCS) measures the changes in fluorescence in small (i.e. femtoliter) volumes (Magde *et al.*, 1972, 1974, Schwille and Haustein, 2009) and then fits theoretical correlation functions to compute free diffusion coefficients. A second popular assay that measures protein diffusion is Fluorescence Recovery After Photobleaching (FRAP) (Poo and Cone, 1973, Liebman and Entine, 1974, Axelrod *et al.*, 1976, Sprague and McNally, 2005). In FRAP, the fluorescent signal of a molecule is bleached in a region of interest. After bleaching, fluorescent molecules from outside of the bleached region diffuse into the bleached region until the fluorescent signal reaches a steady state throughout the whole sample again. The curve describing the fluorescence recovery in the bleached region can then be used to compute either effective molecular diffusion, or free molecular diffusion with binding kinetics depending on the theoretical model

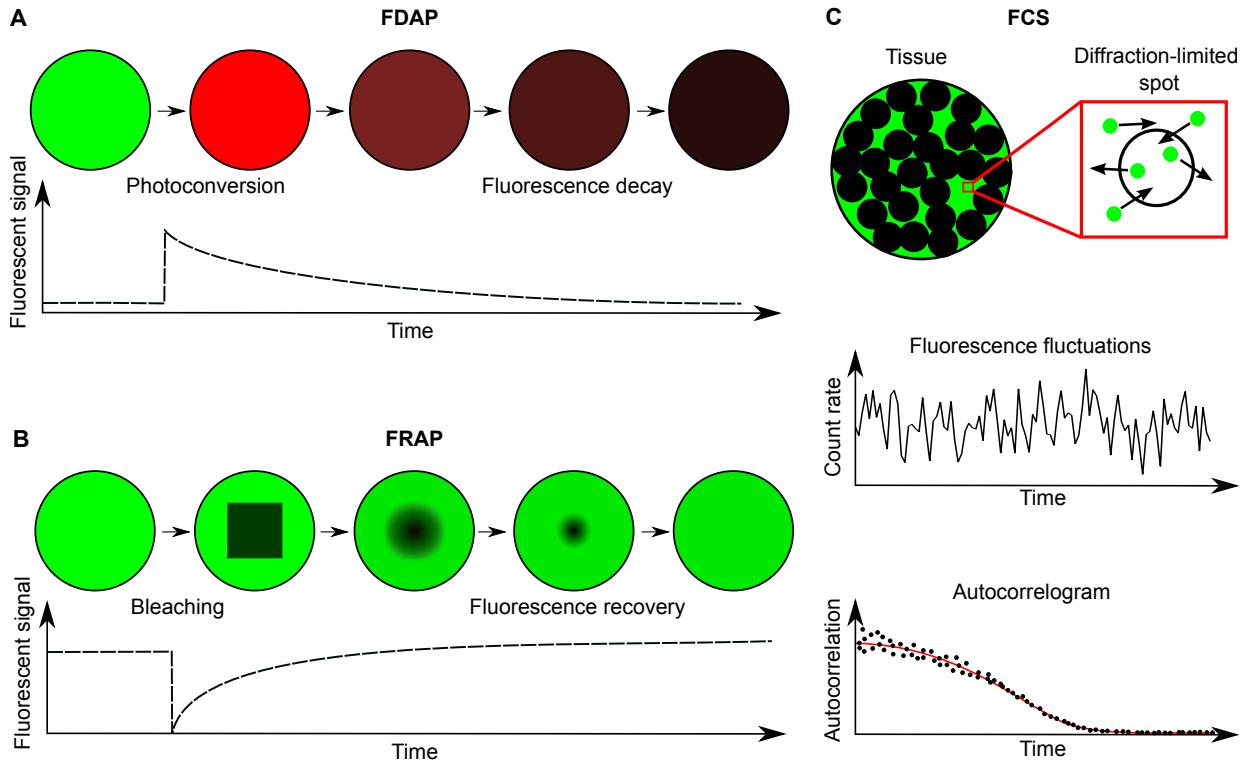

Figure 4.4: Assays for assessing biophysical parameters of molecules. **A** In Fluorescence Decay After Photoconversion (FDAP) a homogeneously distributed fusion protein is photoconverted, and subsequently the photoconverted signal decays over time. Fitting a decay model to the resulting decay curve of photoconverted signal is then used to compute protein clearance rates. **B** Schematic of Fluorescence Recovery After Photobleaching (FRAP). A small region is bleached into a homogeneous fluorophore signal. The curve created from the mobility-driven recovery in the bleached area can then be used to extract the molecule's diffusion rate. **C** Fluorescence Correlation Spectroscopy (FCS) monitors the fluctuations of molecules inside a femtoliter volume in the tissue of interest over time. Fitting the resulting autocorrelation curves can then provide local molecular diffusion rates (adapted from (Müller *et al.*, 2013)).

used (Axelrod *et al.*, 1976, Soumpasis, 1983, Sprague and McNally, 2005). Both assays can be used *in vivo*, however provide different diffusion values. The results provided by FCS directly corresponds to the local diffusion, binding and concentration of the molecule in a femtoliter volume, while FRAP can measure the net diffusion rate on a tissue scale. Such net diffusion rates incorporate hindrance of molecular movement by for instance tortuosity, that is, hindrance by obstacles, or binding processes. Thus, depending on the assay or analysis method chosen, different diffusion measurements may lead to differing morphogen gradient models (Castle *et al.*, 2011, Sigaut *et al.*, 2014).

4.4 Scale-invariant patterning

At the beginning of the 20th century, Hans Spemann performed a classic experiment that demonstrated an extreme example of the consistency of the body plan of organisms (Spemann, 1938, Cooke, 1981). Using a hair, Spemann divided the first two cells of a salamander embryo into two halves, and remarkably one of the two halves healed and formed a half-sized embryo with proper proportions. Allometric scaling, that is, proportional scaling of tissues (Figure 4.5A), is common across taxa and developmental stages, for example in insects (Gregor *et al.*, 2005, Shingleton *et al.*, 2007), amphibians (Spemann, 1938, Ben-Zvi *et al.*, 2008, Inomata *et al.*, 2013), birds (Uygur *et al.*, 2016) or mammals (Lauschke *et al.*, 2013). The experiments by Spemann (1938) showed that in development allometric scaling of tissues is probably kept during the complete developmental process, that is, tissues keep their relative size throughout development. For instance, one could imagine that in differently sized zebrafish embryos, the proportions between dorsal and ventral tissue scale from early development on (Figure 4.5B). However, even today we still do not completely understand the mechanisms underlying scale-invariant patterning, despite extensive work both theoretically (Gierer and Meinhardt, 1972, Othmer and Pate, 1980, Umulis and Othmer, 2013, Rasolonjanahary and Vasiev, 2016, Barkai and Ben-Zvi, 2009, Ben-Zvi and Barkai, 2010, Ben-Zvi *et al.*, 2011b) and experimentally (Ben-Zvi *et al.*, 2008, Inomata *et al.*, 2013).

4.4.1 Mechanisms and models of scale-invariant patterning

Wolpert (1969) already argued that simple signaling gradients as established by the SDC model are not able to scale with body size and that for successful scaling the read-out performed by the cells needs to adjust if body size is altered. Later, Othmer and Pate (1980) found that a relatively simple modification of Turing's model, a simple reaction-diffusion system with a negative feedback loop, can allow for scaling if the diffusion coefficient is spatially dependent. They proposed that this can be achieved by introducing a homogeneously produced auxiliary molecule that modifies the morphogen's diffusivity. In fact, the idea of either active (Gierer

and Meinhardt, 1972, Eldar *et al.*, 2002, Umulis and Othmer, 2013, Ben-Zvi *et al.*, 2008, 2011b, Haskel-Ittah *et al.*, 2012, Averbukh *et al.*, 2014, Rasolonjanahary and Vasiev, 2016) or passive modulators (Umulis, 2009, Coppey *et al.*, 2008) has been followed up by various experimental and theoretical studies. We say a system is regulated by a passive modulator if the morphogen has no influence on the modulator (Figure 4.6A), in contrast to active modulators that are under the control of the morphogen itself (Figure 4.6B) (Umulis and Othmer, 2013).

Passive modulators have been proposed in different systems. Umulis (2009) argued that when a locally secreted morphogen undergoes reversible binding to some kind of static receptor-like molecule (the modulator), its steady-state gradient can scale if the sum of these molecules is constant independent of embryo size, and if the production of the morphogen is constant. Similar to this theoretical model, Coppey *et al.* (2008) proposed that during terminal patterning of the AP axis in *Drosophila* embryos, the gradient of pERK scales due to an increasing nucleus density (the modulator), effectively counteracting the increasing number of produced morphogens by keeping the ratio between the number of morphogens and nuclear morphogen uptake constant. The most prominent example of a passive modulator is the shuttling model (Eldar *et al.*, 2002, Ben-Zvi *et al.*, 2008, Haskel-Ittah *et al.*, 2012). In this model, a morphogen gradient is opposed by a second gradient of a modulator molecule. The modulator molecule reversibly binds to the free morphogen, increasing its effective diffusivity and shuttling it towards the side of its original expression, see Figure 4.6C.

While such passive models can explain scaling for experiments in differently sized embryos, they would fail to explain experiments in which the modulator source is eradicated since they lack the ability to self-regulate, that is, producing a new modulator source. A popular mechanism that allows to self-regulate is the expander. The expander is a modulator under control of the morphogen, that is either produced or repressed by the morphogen (Ben-Zvi *et al.*, 2008, Ben-Zvi and Barkai, 2010, Ben-Zvi *et al.*, 2011b, Umulis and Othmer, 2013, Averbukh *et al.*, 2014). A possible expander mechanism is the expansion-repression model (Ben-Zvi and Barkai, 2010, Ben-Zvi *et al.*, 2011b, Umulis and Othmer, 2013, Averbukh *et al.*, 2014). In this model, the locally produced morphogen represses the expression of the expander molecule while the

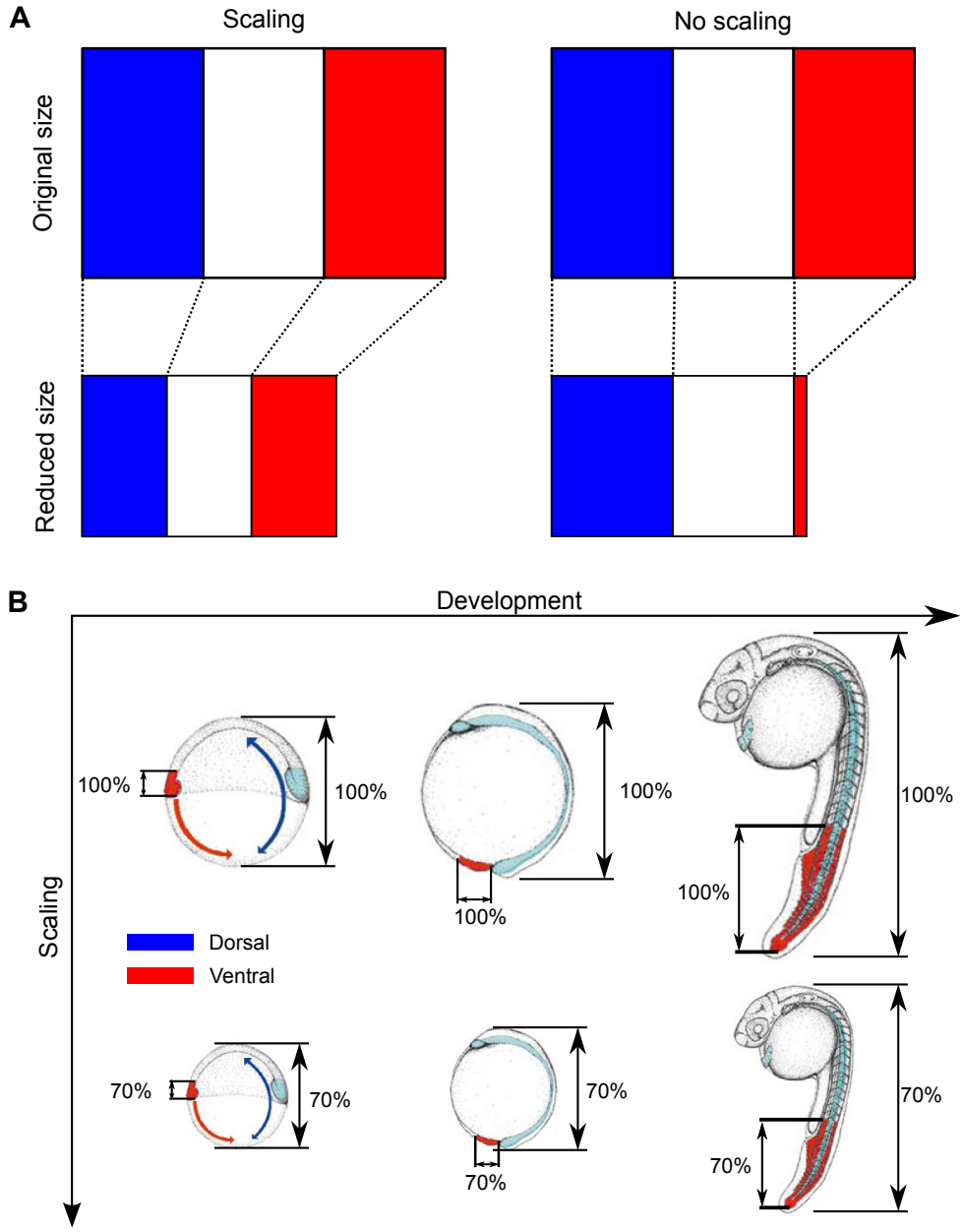

Figure 4.5: Scale invariance during development. **A** Scaling of the French-flag model. In allometric scaling, the proportions between cell fates within a tissue stay constant in differently sized embryos. **B** Maintainance of dorsal-ventral proportions during zebrafish development. Smaller embryos form initially smaller dorsal and ventral progenitors. Throughout development, the successor cells of these progenitors develop into proportionally smaller tissues compared to a normal sized zebrafish embryo (zebrafish illustrations taken from (Agathon *et al.*, 2003)).

expander modulates diffusion or degradation, either increasing or decreasing the range of the morphogen in regions of low morphogen concentrations (Figure 4.6D). Recently it has been proposed that Pentagone (Pent) regulates Dpp signaling during *Drosophila* wing disc development (Ben-Zvi *et al.*, 2011a, Hamaratoglu *et al.*, 2011, Norman *et al.*, 2016). Pent is produced lat-

erally and forms an opposed gradient to Dpp, regulating the range of Dpp signaling gradient while actively being repressed by Dpp signaling, making it an ideal candidate as a modulator in the expansion-repression model (Ben-Zvi *et al.*, 2011a, Hamaratoglu *et al.*, 2011). A more complicated version of an expander model has been presented by Inomata *et al.* (2013). In this "Long-range accumulation and feedback" model, the morphogen enhances production of its long-range modulator. This modulator then stabilizes the inhibitor of the morphogen that is expressed on the opposite side of the embryo, thus increasing the inhibitor's range and effectively reducing the morphogens signaling range.

4.5 Early patterning in the zebrafish embryo

Although multiple mechanisms for signaling gradients and scaling have been proposed, there is a lack of experimental and numerical verification.

In this thesis, I will focus on two problems in developmental axis formation in zebrafish that are similar to the formation of AP identities via Bcd and DV fates by the Dpp gradient in *Drosophila*. In vertebrates, two of the earliest patterns that form during development are the dorsal-ventral axis, which divides the embryo into dorsal and ventral territories, and the three germ layers, ectoderm, mesoderm and endoderm. These two orthogonal developmental axes divide the embryo into multiple regions that later give rise to different tissues such as brain, epidermis, heart, blood, somites or notochord (Figure (4.7A) (Schier and Talbot, 2005). It is generally believed that in the zebrafish embryo, these territories are specified between high-stage roughly 3.5 hours post fertilization (hpf) and 50% epiboly 5.3 hpf (Kimmel *et al.*, 1995, Schier and Talbot, 2005), however it is currently controversial when final cell fate decisions are made and how these are affected by morphogenetic movements (Tuazon and Mullins, 2015). During this time, the number of cells in the zebrafish embryo increases from 1000 cells to 5000 cells (Kimmel *et al.*, 1995). Thus, assigned cell fate territories only span a small number of cells in a given direction. For instance, the precursor of mesendoderm, that is, both endoderm and mesoderm, only spans a range of roughly 12 cells (van Boxtel *et al.*, 2015). One could imagine

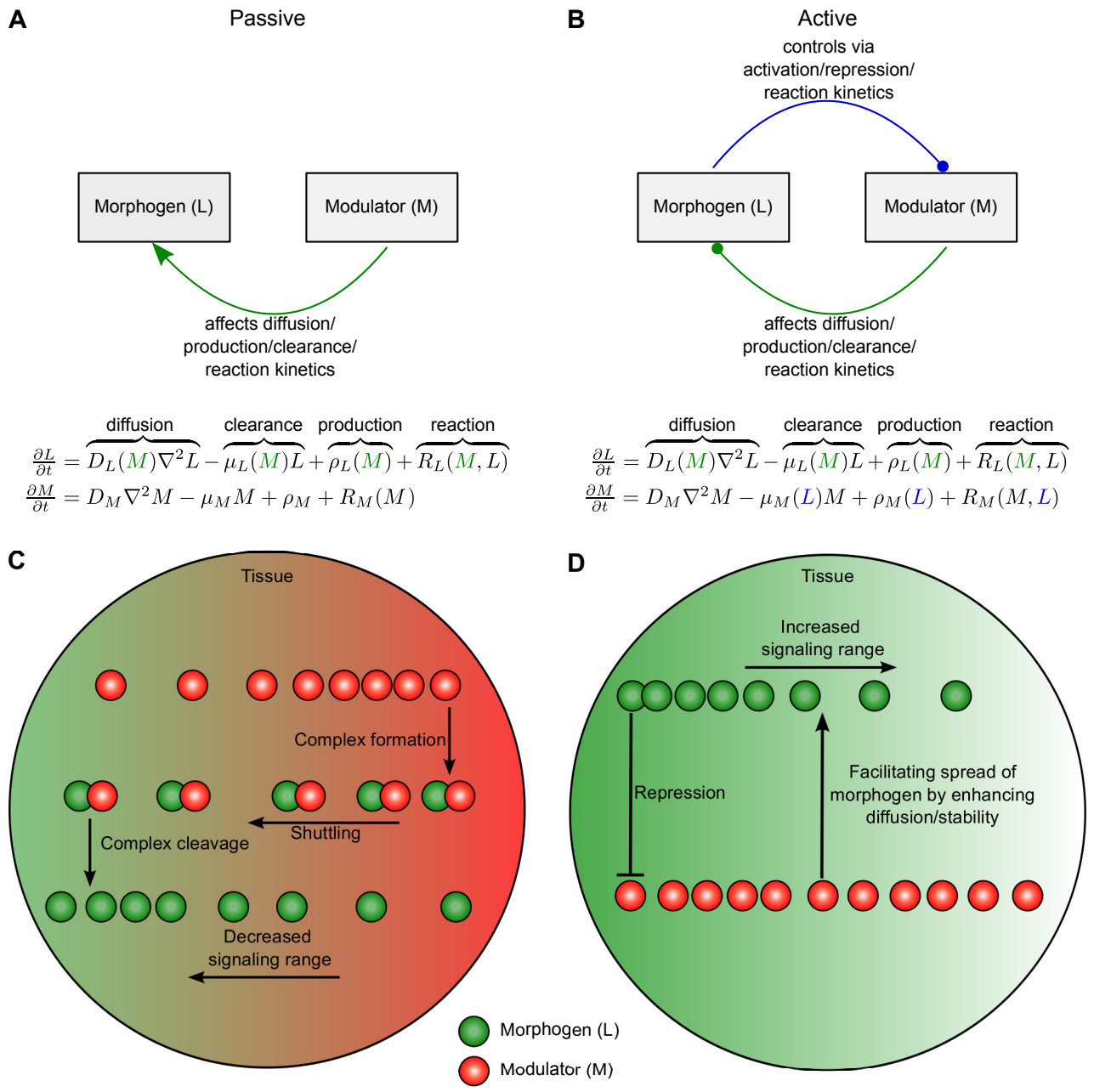

Figure 4.6: Mechanisms for scale-invariant patterning by modulators. A,B Schematics and general reaction-diffusion models of a passive or active modulator-mediated scaling mechanism, respectively. **C** Scale-invariant patterning through shuttling. The oppositely produced modulator binds to the morphogen, increasing its effective diffusivity and ultimately shuttles the morphogen to the region of its production, thus restricting its signaling range. **D** Schematic of the expansion-repression model. The modulator facilitates the redistribution of the morphogen by effectively increasing its stability or diffusion. The facilitated spread of the morphogen then leads to a wider signaling range.

that a single cell difference in the progenitors would alter the size of a tissue by 8%, and, if not compensated, might lead to severe developmental defects. Hence, tissue specification needs to be tightly controlled.

The formation of both germ layers and DV axis is controlled by signaling molecules: the germ layers are defined by the read-out of the TGFβ-superfamily member Nodal (Schier, 2009) while ventral regions are defined by high levels of Bone Morphogenic Protein (BMP), the vertebrate homolog of Dpp and another TGFβ-superfamily member (Langdon and Mullins, 2011).

4.5.1 Germ layer specification by the Nodal/Lefty patterning system

During the blastula stages in zebrafish development, the germ layer specifying morphogen Nodal is secreted at the marginal zone close to the yolk sack (Figure 4.8A) and is thought to diffuse extracellularly towards the animal pole (Schier, 2009, Müller *et al.*, 2012). When one of the two Nodal proteins Squint (Sqt) or Cyclops (Cyc) bind to the type I and II Activin receptors Acvr1/Acvr2 as well as to the EGF-CFC co-receptor one-eyed pinhead (oep), the intracellularly located transcription factors Smad2/3 become phosphorylated and move into the nucleus where they activate the expression of multiple Nodal transcriptional targets, as well as the expression of Nodal itself and the two Nodal inhibitors Lefty1 and Lefty2 (Figures 4.7B and 4.8C) (Schier, 2009, Müller *et al.*, 2012). As a consequence of its localized expression and extracellular diffusion, Nodal could form a classical morphogen gradient (Schier, 2009, Müller *et al.*, 2012, Wang *et al.*, 2016). Indeed, Nodal has been hypothesized to be read-out at two different concentration thresholds activating different transcription factors. For instance, high levels of Nodal lead to the activation of *sox32*, instructing later endodermal tissue, while activation of *ntl* happens at lower Nodal concentrations and leads to mesendodermal specification (Schulte-Merker *et al.*, 1994, Schier, 2009). The hypothesis that Nodal alone induces all three germ layers however has recently been challenged by the fact that Nodal-induced pSmad signaling does not have the necessary range along the animal-vegetal axis (van Boxtel *et al.*, 2015). van Boxtel *et al.* (2015) instead propose that Nodal itself starts a signaling cascade through the activation of Fibroblast Growth Factor (FGF), which extends Nodal signaling. Subsequently, Nodal and FGF are interpreted by a complex gene regulatory network that instructs germ layers. Recently, Müller *et al.* (2012) showed that Lefty diffuses approximately 5-6 times faster than Nodal while decaying at the

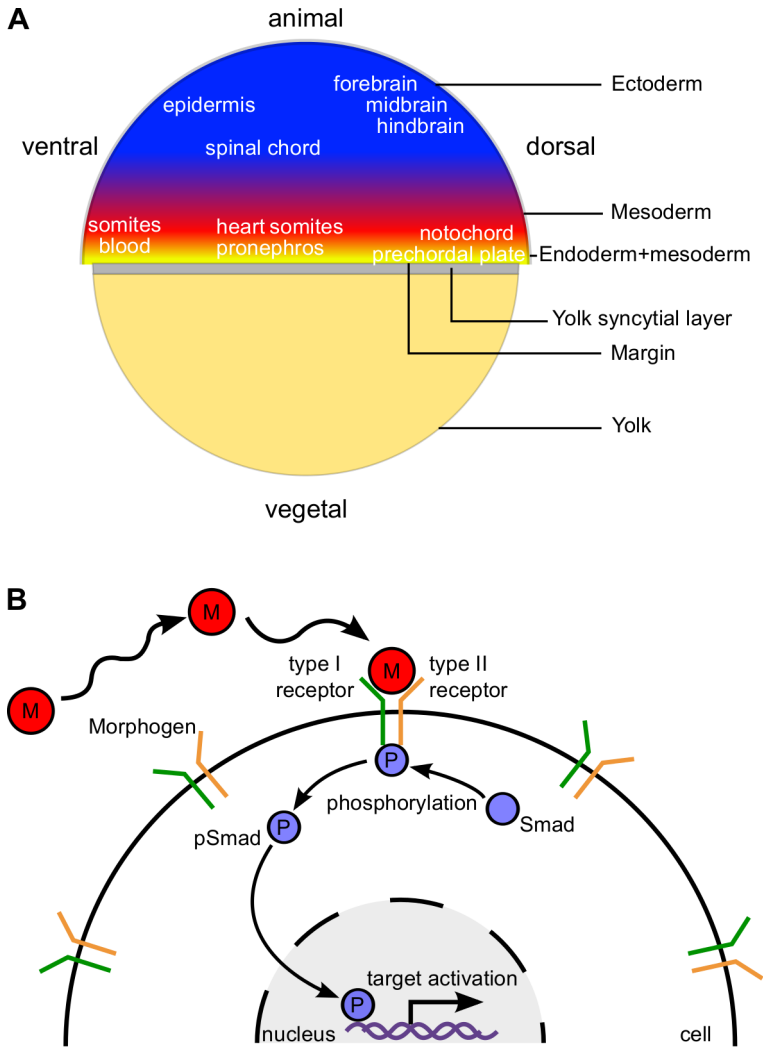

Figure 4.7: The Nodal/Lefty and BMP/Chordin system define the developmental coordinate system during zebrafish embryogenesis. A During the blastula stages, a cross-talk between the Nodal/Lefty system along the animal-vegetal axis and the BMP/Chordin system along the dorsal-ventral axis specifies a blue print of precursors that dictate later cell types (adapted from (Schier and Talbot, 2005)). **B** Basic outline of the signaling cascade of both patterning systems. The morphogen (M) spreads extracellularly by diffusion and binds to a receptor complex of type I and II receptors. Upon binding, intracellular Smad becomes phosphorylated and moves into the nucleus, where it activates downstream targets of either Nodal or BMP.

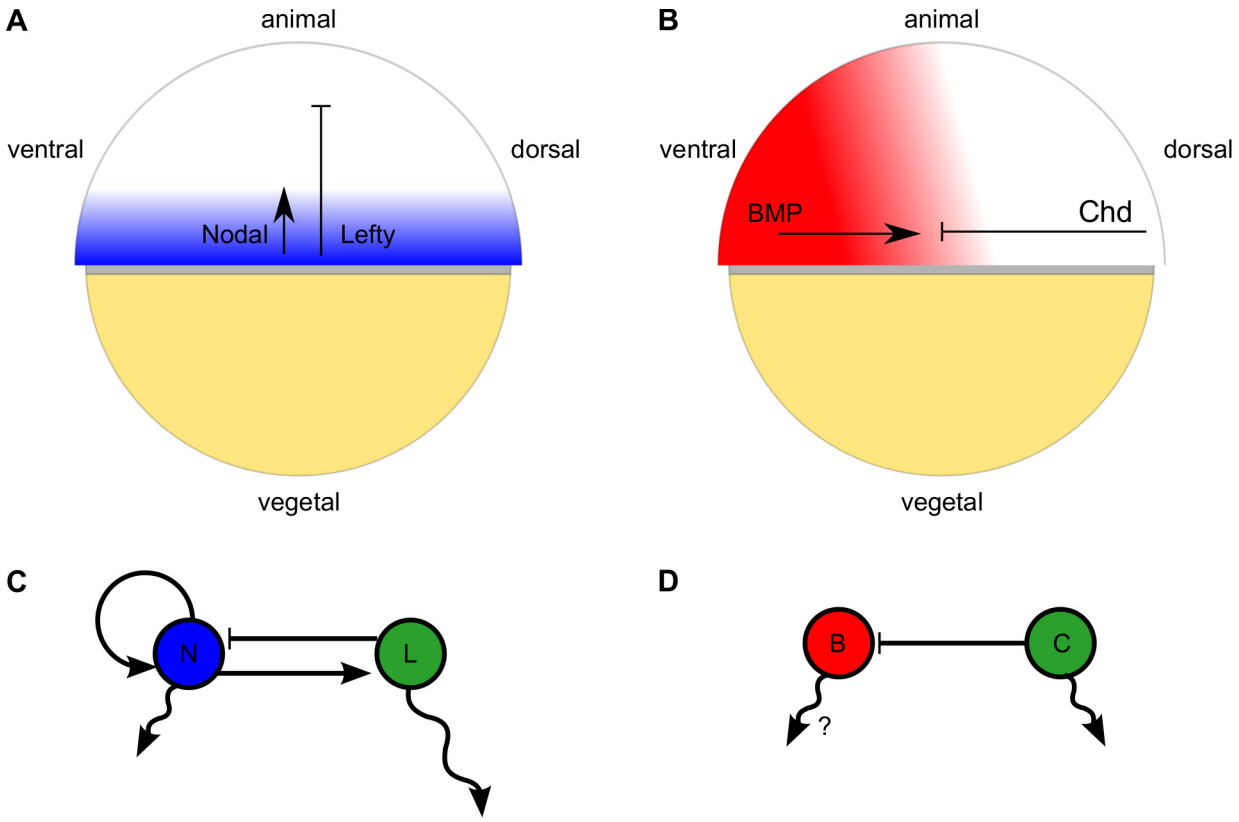

Figure 4.8: Schematics of the Nodal/Lefty and BMP/Chordin system during early zebrafish development. A The short-range activator Nodal is secreted at the marginal zone and forms a signaling gradient towards the animal pole. Nodal's long-range inhibitor Lefty is a direct target of Nodal and is thus predominantly expressed at the marginal zone. **B** BMP is expressed on the ventral side of the embryo and antagonized oppositely by its long-range inhibitor Chordin on the dorsal side. **C** Diagram of the Nodal-Lefty reaction-diffusion network. Nodal (N) activates its own inhibitor Lefty (L) as well as expression of itself. Lefty has been shown to diffuse 5-6 times faster than Nodal. **D** Diagram of the BMP-Chordin reaction-diffusion network. BMP (B) is inhibited by Chordin (C). It is currently unclear if BMP diffusion is relevant for DV patterning.

same rate. Together with the negative feedback of Nodal through Lefty activation, this makes the Nodal-Lefty patterning system a candidate for an activator-inhibitor system as proposed by Gierer and Meinhardt (1972) (Figure 4.8C).

4.5.2 Dorsal-ventral patterning is dictated by the BMP/Chordin system

The dorsal-ventral axis is formed by another pair of antagonists similar to the Nodal-Lefty system, namely BMP and Chordin. Three members of the BMP family BMP2, BMP4 and BMP7 are thought to be short-range activators expressed on the ventral side of the embryo antagonized

by the dorsally secreted long-range inhibitor Chordin (Figure 4.8B) (Langdon and Mullins, 2011). Similar to Nodal, BMP binds extracellularly to its type I and type II receptors Bmpr1/Bmpr2 which leads to phosphorylation of Smad1/5/8 and subsequent activation of downstream target genes (Figure 4.7B). The inhibitor Chordin, in contrast to the Nodal/Lefty system, is not secreted in the same region as BMP. Thus, it is currently controversial if BMP diffusion is required to establish a BMP signaling gradient, since a gradual inhibition by Chordin could also explain a ventral-to-dorsal gradient (Figure 4.8D) (Ramel and Hill, 2013). A second mechanism that would not require BMP to diffuse at a relevant rate is the "Shuttling model" proposed by Ben-Zvi *et al.* (2008). In this model, BMP is "picked up" by the rapidly diffusing Chordin along the DV axis and shuttled towards the ventral side, effectively forming a sharp BMP gradient. Moreover, BMP does not directly activate its inhibitor Chordin, but it is known to activate Sizzled, which effectively stabilizes Chordin by binding to the metalloprotease Tolloid and thus prevents Tolloid-mediated Chordin degradation (Lee *et al.*, 2006, Mullins, 2006). However, the dorsally produced BMP-like ligand Antidorsalizing Morphogenetic Protein (ADMP) has been shown to repress *chordin* on the dorsal side (Reversade and De Robertis, 2005, Plouhinec *et al.*, 2013). Both Francois *et al.* (2009) and Inomata *et al.* (2013) formulated this auto-regulatory network into reaction-diffusion models that are able to explain DV patterning, however make different assumptions about the biophysical properties of BMP and Chordin. While the model proposed by Francois *et al.* (2009) requires low and approximately equal BMP and Chordin diffusion, Inomata *et al.* (2013) attempt to explain DV pattern formation by a high BMP and Chordin diffusivity and a strong difference in BMP and Chordin stability. In summary, there are currently multiple hypotheses that try to explain the formation of a BMP gradient along the DV axis, each making different assumptions about the biophysical properties of BMP and Chordin. However, these assumptions have been left untested so far.

4.6 Aims of research

In this dissertation, I aim at providing a more mechanistic understanding of morphogen signal gradient formation and scale-invariant adjustments of such. There is plenty known about the molecular biology of both dorsal-ventral patterning and germ layer specification during early zebrafish embryogenesis; however, the mechanisms underlying the gradient formation in both systems are still controversial. Thus, both axes serve as ideal templates to test basic principles of signal gradient establishment and maintenance. For a clear biophysical description of signal gradient formation, it is imperative to measure key parameters such as protein diffusion and stability *in vivo*. Thus, the first step of this research project was to develop assays and software tools that provide and improve analysis for these parameters. Having established the necessary tools to measure key biological parameters of morphogens, my collaborators and I were then able to improve our understanding of dorsal-ventral patterning. By measuring diffusion rates and half-lives of the key players in DV axis instruction, we were able to rule out different currently controversial mechanistic models and show that a simple source-sink mechanism is most likely to explain BMP signal gradient formation during zebrafish embryogenesis. I was also interested how germ layer patterning scales with embryo size. For this, my colleagues developed a way to manipulate embryo size and show that germ layers scaled to size if the inhibitor Lefty was available in sufficient amounts, among other factors. Using this information, I developed a mathematical model that uses the accumulation of the fast inhibitor Lefty as a read-out of embryo size. Incorporating already known biophysical parameters of the Nodal/Lefty system, together with a screening of the model over a comprehensive parameter space, returned parameter configurations that not only provided the correct amount of scaling, but also were able to reproduce all experimental observations and show the correct spatiotemporal dynamics of germ layer specification.

5. Results

5.1 PyFDAP: Automated analysis of Fluorescence Decay After Photoconversion (FDAP) experiments

Bläßle, A., Müller, P. (2015). *Bioinformatics*, (6):972–974

5.1.1 Synopsis

The stability of proteins is crucial for the control of protein signaling range. Fluorescence Decay After Photoconversion (FDAP) experiments assess protein stability both *in vitro* and *in vivo*. Following an initial homogeneous photoconversion, the decay of the photoconverted signal of a fluorescently-labeled protein is monitored. Assuming a proportional relationship between fluorescent signal and the amount of present labeled protein, one can then fit decay models to calculate the clearance rate and half-lives of the labeled protein.

In this publication, we present the open-source Python package PyFDAP. PyFDAP can analyze microscopy data from FDAP experiments, fit both linear and non-linear decay models to data and provide statistical analysis of obtained clearance rates and half-lives. Since protein decay is thought to be context-dependent, we equipped PyFDAP with the ability to use a second imaging channel that counter-labels different territories in the sample to separate protein decay by region, for instance extra- and intracellular regions. Additionally, PyFDAP can use background data sets recorded without photoconverted signal to compute the lower bound of protein decay and thus prevents the fitting procedure from underestimating basal fluorescence levels in samples. To provide FDAP analysis to a wide range of users, we equipped PyFDAP with an intuitive Graphical User Interface (GUI). PyFDAP projects and settings are saved in serialized objects and can be opened and reanalyzed , enhancing collaborative work and reproducibility.

5.1.2 Author contribution

Patrick Müller and I conceived the study, designed the software and wrote the manuscript. I implemented and tested the software.

5.2 Measuring protein stability in living zebrafish embryos using Fluorescence Decay After Photoconversion (FDAP)

Rogers, K. W. **Bläßle, A.**, Schier, A. F., Müller, P. (2015). *J. Vis. Exp.*, (95):e52266

5.2.1 Synopsis

Despite the crucial role that protein clearance plays in establishment and maintenance of signaling gradients, little is known about protein half-lives and clearance rates inside living organisms. The recent advancements in the development of photoconvertible proteins however, offer new possibilities to measure protein clearance *in vivo* using time-lapse imaging. Here we present a variant of Fluorescence Decay After Photoconversion (FDAP), that assesses protein half-lives and clearance rates in living zebrafish embryos.

For FDAP, the protein of interest is tagged with a photoconvertible protein such as Dendra2. A mix of mRNA encoding the fusion protein of interest together with an Alexa488-dextran is injected at the 1-cell stage into the zebrafish embryo. When the zebrafish embryo reaches dome stage it is mounted onto a glass-bottom dish in a drop of low-melting agarose animal pole down. To keep the embryo from drying out, it is covered with Danieu's medium. The embryos are then imaged at approximately 80 µm depth in both the photoconverted (i.e. red) and counter-label (i.e. green) channel using an inverted confocal microscope; first, a pre-conversion image is acquired. Subsequently, a UV lamp at maximum intensity is used to photoconvert the proteins of interest. Directly after photoconversion, an image in both channels is taken every ten minutes over five hours.

The open-source package PyFDAP can then be used to import the acquired time-lapse datasets. PyFDAP directly imports the microscope data and fits different linear and non-linear decay models to the data, using the strictly intracellular Alexa488-dextran as a counter-label to provide half-lives and clearance rates for both intra- and extracellular regions.

5.2.2 Author contribution

Katherine Rogers, Alexander Schier and Patrick Müller developed the assay. Katherine Rogers and Patrick Müller wrote the manuscript. Katherine Rogers and I performed the data analysis.

5.3 Quantitative diffusion measurements using the open-source software PyFRAP

Bläßle, A., Soh, G., Braun, T., Mörsdorf, D., Preiß, H., Jordan, B., Müller, P., *in review at Nature Communications*

5.3.1 Synopsis

Tightly regulated movement of macromolecules such as proteins through biological tissue is essential to prevent defects in development and homeostasis (Harmansa *et al.*, 2015, Ornitz and Itoh, 2015). A common assay that measures macromolecule movement is Fluorescence Recovery After Photobleaching (FRAP). A FRAP experiment consists of two steps: First, the fluorescent signal of the molecule of interest is bleached in a region in the biological sample by exposure to a strong laser beam. When the region is sufficiently bleached, the movement-driven recovery of the fluorescent signal in the bleached region is monitored. Inverse FRAP (iFRAP) is the mirror image of a FRAP experiment. In an iFRAP experiment the dissipation of an initially photoactivated or photoconverted molecule out of a region of interest is recorded. The dissipation of the fluorophore leads to a decay curve inverse to the recovery curve of a FRAP experiment. Such recovery or decay curves can then be used to compute molecular movement parameters such as diffusion under the assumption of certain movement models. Currently, such movement models and the involved analysis make simplified assumptions about experimental geometry, bleaching conditions and underlying reaction-kinetics, precluding correct estimation of diffusion rates.

To overcome such current analysis shortcomings, we developed the Python package PyFRAP. PyFRAP allows the user to define exact three-dimensional geometries resembling the sample that serve as a base for simulations of FRAP experiments, numerically matching its initial conditions with the first acquired post-bleach image. These numerical simulations combined with various reaction kinetics can then be fitted to the experimental data. PyFRAP integrates a complete FRAP analysis work flow from microscopy images to statistical analysis and publication-ready figures. The combination of an easy-to-use GUI with a fully documented Application Program-

ming Interface (API) makes PyFRAP suitable for a wide range of researchers, independent of their computational background.

Knowing the correct underlying reaction kinetics of a FRAP experiment is often difficult. PyFRAP's implementation of the Akaike Information Criterion (AIC) allows users to select the most likely model between different reaction-diffusion models based on statistical inference. In a comprehensive *in silico* study we found that PyFRAP not only provides correct diffusion coefficients based on simulated data, but also identifies the correct underlying reaction kinetics when possible using the AIC. Additionally, we performed a second series of *in silico* benchmarking experiments testing PyFRAP's performance against four current FRAP analysis software packages. Our results showed that PyFRAP overall outperforms all tested software solutions.

Moreover, we tested PyFRAP's analysis capabilities with a collection of *in vitro* experiments undergoing purely diffusive processes using both FRAP and inverse FRAP (iFRAP). The FRAP experiments indicate that PyFRAP can reproduce theoretical predictions and literature values of diffusion rates of fluorophore-dextrans with sizes varying over two orders of magnitude as well as recombinant Green Fluorescent Protein (GFP). Additionally, we performed the iFRAP experiments in parallel with FRAP experiments of the photoconvertible protein Dendra2. Strikingly, these tandem FRAP/iFRAP experiments provided nearly equal diffusion coefficients, suggesting that PyFRAP is able to analyze both types of experiments.

In biological samples, macromolecules often need to traverse complex environments such as a field of cells to reach their targets. This leads to tortuous movement, effectively slowing down molecules if they move extracellularly. Using PyFRAP, we show *in silico* that for cell packings with different densities and arrangements, this can lead to a reduction of effective diffusion up to 66% in two-dimensional and 40% in three-dimensional geometries. Analysis of *in vitro* experiments of recombinant GFP mixed with polyacrylamide beads suggested a reduction in the diffusion rate by 18%, agreeing with simulations with an Extracellular Volume Fraction (EVF) of $\sim 50\%$. Similar experiments with a 70 kDa fluorophore-dextran provided a stronger reduction of 39%, indicating a possible interaction between beads and molecules given the experimental setup.

FRAP experiments with recombinant GFP in living zebrafish embryos analyzed by PyFRAP resulted in a 43% stronger reduction of effective diffusivity compared to a mix of GFP with beads *in vitro*, indicating that the approximation of the extracellular matrix as a field of radial cells is limited. Instead, we postulate that the extracellular environment in tissues might be more complex, consisting of narrow spaces between cells, filopodia and a dense extracellular matrix. Equal diffusion coefficients from FRAP experiments with recombinant GFP and secreted GFP produced from injected mRNA *in vivo* showed that PyFRAP is able to account for uniform protein production.

The effective diffusion of macromolecules such as morphogens in tissues is thought to be further reduced by interaction with extracellular and membrane-bound molecules. We tested this prediction by performing FRAP experiments in living zebrafish embryos with the Nodal protein Squint, and indeed, effective Squint diffusion was 95% slower than the theoretically predicted value.

5.3.2 Author contribution

I conceived the study together with Ben Jordan and Patrick Müller. Together with Patrick Müller, I designed the software. Implementation of the software was done by myself. Patrick Müller provided benchmarking simulations to test PyFRAP's Partial Differential Equation (PDE) solver. I performed all remaining data analyses and simulations. Gary Soh, Theresa Braun, David Mörsdorf, and Hannes Preiß conducted the experiments with guidance from Patrick Müller. Patrick Müller and I wrote the manuscript.

5.4 Dynamics of BMP signaling and distribution during zebrafish dorsal-ventral patterning

Pomreinke, A. P., Soh, G. H., Rogers, K. W., Bergmann, J. K., **Bläßle, A.**, Müller, P., (2017). *eLife*, (6):e25861

5.4.1 Synopsis

The dorsal-ventral axis is dictated by a BMP signaling gradient peaking on the ventral side. Currently it is controversial in which way this gradient is established and maintained. There are several postulated models that could explain BMP gradient formation that have however, remained untested directly.

In the source-sink model, BMP initially forms a shallow gradient from the ventral to dorsal side, where it is antagonized by a localized source of its inhibitor Chordin. Chordin diffuses from the dorsal side, effectively creating a "sink" for BMP on the dorsal side and thus sharpening the BMP signaling gradient. It is controversial as to whether BMP diffusion is crucial for BMP gradient formation. The "Long-range accumulation and feedback model" proposes that BMP induces the fast diffusing Chordin protease inhibitor Sizzled that effectively extends the range of Chordin to the ventral side. Ongoing inhibition of BMP then leads to a decrease of Sizzled levels and consequently an increase of Chordin degradation, effectively rendering Chordin less stable than BMP. The "Self-regulating reaction-diffusion model" assumes BMP and Chordin being equally diffusive and stable and adds additional control of both BMP and Chordin via interactions with Sizzled and ADMP, respectively. In the "Shuttling model", highly diffusive Chordin acts as a passive modulator of BMP diffusivity, effectively shuttling BMPs from the dorsal to the ventral side. Each of the five postulated models relies on assumptions about the biophysical properties of the molecules involved in the patterning system and thus could be successively excluded if these requirements are not met.

We rigorously tested these assumptions by assessing protein clearance and diffusion rates using FDAP and FRAP. Our FRAP measurements suggested that BMP, Chordin and Sizzled diffuse with approximately 2.5 $\mu m^2 s^{-1}$, 6.5 $\mu m^2 s^{-1}$and 10 $\mu m^2 s^{-1}$, respectively. Thus, the bio-

physical requirements for the "Source-sink model with immobile BMP", the "Shuttling model" and the "Self-regulating reaction-diffusion model" were not met. FDAP experiments suggested that BMP and Chordin have approximately similar half-lives, excluding the "Long-range feedback and accumulation model". Moreover, overexpression of Chordin had no effect on BMP diffusion in FRAP experiments Also, the distribution of BMP was not altered if two Chordin and BMP expressing clone were juxtaposed in the animal pole of an embryo. These results reject the idea that Chordin shuttles BMP. This rigorous series of tests led us to the conclusion that the BMP signaling gradient is generated by a simple source-sink mechanism; however involving BMP diffusion. Strikingly, in contrast to the other four models, the "Source-sink model with BMP diffusion", equipped with the parameters acquired from FRAP and FDAP experiments, also qualitatively fitted phosphorylated Smad (pSmad) gradient profiles measured by immunostainings before and during epiboly.

5.4.2 Author contribution

Patrick Müller conceived the study, performed the modeling, and wrote the manuscript with input from all authors. I designed and cloned the Chordin-Dendra2 fusion construct necessary for FDAP experiments with help from Katherine Rogers. Together with Katherine Rogers, I performed the FDAP experiments and analyzed the experiments. Katherine Rogers conducted all transplantation experiments. Gary Soh performed all FRAP and FCS experiments. Jennifer Bergmann generated all remaining fusion constructs together with Gary Soh, Katherine Rogers, Autumn Pomreinke and Patrick Müller. Autumn Pomreinke, Gary Soh and Jennifer Bergmann tested the constructs. Autumn Pomreinke performed the immunostaining experiments with help from Gary Soh.

5.5 Scale-invariant patterning by size-dependent inhibition of Nodal signaling

Almuedo-Castillo, M., **Bläßle, A.** , Mörsdorf, D. , Marcon, L. , Rogers, K. W., Schier, A. F., Müller, P., (2017), *in review at Nature Cell Biology*

5.5.1 Synopsis

While body size significantly varies between individuals of a single species, the proportions of the body plan are strikingly consistent. In early development, such body plans are mainly dictated by signaling gradients established by secreted molecules; however, it is currently unclear how such signaling gradients adjust with body size. In this study, we used germ layer patterning as a template to investigate scale-invariance between differently sized zebrafish embryos. We obtained differently sized zebrafish embryos by extirpating 30% of tissue from the animal pole of embryos at blastula stages. Remarkably, smaller embryos developed properly, maintaining correct proportions between germ layers. In particular, regions of gene expression of germ layer markers adjusted to the new body size in extirpated embryos within two hours after extirpation. These genes are targets of the morphogen Nodal. However, it is unlikely that Nodal itself provides feedback information about embryo size since Nodal is expressed at the marginal zone and its low diffusivity is not high enough to reach the animal pole in the relevant time frame. We thus postulated that the highly diffusive Nodal inhibitor Lefty acts as a size sensor and formalized the Nodal/Lefty system into a set of reaction-diffusion equations. Subsequent simulations of this reaction-diffusion model describing the Nodal-Lefty system showed that Lefty adjusts Nodal signaling range by accumulating in smaller embryos effectively reducing the range of Nodal signaling gradients.

We tested the predictions of our simulations by performing extirpation experiments with differing numbers of functional copies of *lefty1* and *lefty2*, measuring the range of the mesendodermal marker *fascin* in both untreated and extirpated embryos. Experiments with *lefty1*$^{-/-}$;*lefty2*$^{-/-}$ double mutants showed that scaling fails in the absence of Lefty since the extent of *fascin* is remarkably expanded in these untreated *lefty* mutants compared to Wild Type (WT) embryos.

Extirpated embryos with one functional copy of each paralog (*lefty1*$^{+/-}$;*lefty2*$^{+/-}$) experienced proper scaling and normal *fascin* regions, indicating that Lefty levels could be regulated through dosage adjustments. Moreover, similar experiments in *lefty1*$^{-/-}$ and *lefty2*$^{-/-}$ mutants showed that both paralogs are necessary for proper germ layer patterning and scaling.

It is known that *lefty* expression is under the control of Nodal; however, it is unclear whether Nodal actively restricting its own range through an indirect negative feedback is crucial for germ layer patterning or if simply the presence of Lefty is needed to control Nodal range passively. We tested this hypothesis by injecting *lefty1-GFP* mRNA into the Yolk Syncytical Layer (YSL) of *lefty1*$^{-/-}$;*lefty2*$^{-/-}$ mutants, effectively creating a constant Lefty1 source that is independent of Nodal activation at the marginal zone. Strikingly, these YSL injections of specific amounts of *lefty1-GFP* mRNA were able to rescue double mutants and produce normally patterned fish, and extirpated embryos injected with *lefty1* mRNA showed proper mesendoderm scaling. This shows that Nodal-mediated activation of Lefty expression is not required for germ layer patterning and scaling, although it might stabilize the system.

In our theoretical model, high Lefty diffusivity is crucial for Lefty reaching the animal pole and thus providing information about embryo size. To test whether Lefty diffusion actually plays a central role in mesendoderm scaling, we co-injected a so-called "morphotrap" together with Lefty1-GFP encoding mRNA into the YSL of *lefty1*$^{-/-}$;*lefty2*$^{-/-}$ double mutants. The morphotrap is a mCherry-labeled nanobody localized on cell membranes that binds GFP. Using the morphotrap, we reduced effective Lefty1-GFP diffusion from $7.7 \pm 3.2\,\mu m^2\,s^{-1}$ to $0.2 \pm 0.2\,\mu m^2\,s^{-1}$. As expected, extirpated embryos injected with the morphotrap did not scale, showing that high Lefty diffusion is essential for mesendoderm scaling.

We performed a computational screen over 400000 parameter configurations and tested whether our reaction-diffusion model can reproduce all experimental observations, that is, (1) failure of scaling and expansion of the *fascin* domain if no Lefty is present, (2) failure of scaling in the absence of Lefty1, (3) proper mesendoderm scaling if Lefty expression is not mediated by Nodal, and (4) failure of scaling if Lefty diffusion is reduced. In contrast to previous studies, we redefined scaling in a biologically more relevant manner for our study: Instead of requiring

Nodal signaling gradients to overlap throughout the embryo, we only needed them to overlap at the distance at which the *fascin* domain is defined within measurement error. We also restricted this requirement to 2 hours post extirpation, taking into account possible temporal dynamics. Remarkably, our screen found multiple parameter configurations that are able to reproduce all experimental findings. Even more strikingly, our model not only fits all experimental findings, but also shows the correct temporal dynamics by shutting down Nodal signaling shortly after mesendoderm range specification.

In conclusion, we propose that size-dependent inhibition due to inhibitor accumulation can explain scaling of germ layer specification in zebrafish and might be a universal mechanism also found in other organisms or patterning systems.

5.5.2 Author contribution

The study was conceived by Maria Almuedo-Castillo, Alexander Schier and Patrick Müller. David Mörsdorf performed all FRAP experiments and contributed to the generation and testing of the morphotrap as well as to the phenotypic analysis of YSL injections. Maria Almuedo-Castillo performed all other experiments. Maria Almuedo-Castillo, I, David Mörsdorf and Patrick Müller analyzed the data. I developed and implemented the mathematical models, screening criteria and pipeline, and carried out the parameter screen with assistance from Luciano Marcon and Patrick Müller. Katherine Rogers and Alexander Schier provided the *lefty* mutants before publication. Katherine Rogers analyzed the activity of Lefty. Alexander Schier and Patrick Müller conceptualized the scaling model. Patrick Müller developed the extirpation assay and supervised the project. The manuscript was written by Maria Almuedo-Castillo and Patrick Müller with input from all authors.

6. Discussion

One of the most fascinating questions in modern biology is how a body of identical cells starts differentiating during embryonic development, forms different tissues and organs, and ultimately becomes a properly developed organism. Groundbreaking research in the past 100 years has shown that many early patterning events are controlled by extracellular signaling molecules that specify tissues by graded signaling. Despite this extensive line of research both experimentally and theoretically, it is still unclear how such signaling gradients are established, maintained and scaled with body size. Different theoretical models describing the spatiotemporal dynamics of signaling gradients have been proposed; however, the lack of measured biophysical parameters has precluded model selection so far. Two important determinants of the range at which morphogens can signal is the speed at which morphogens move, i.e. their diffusion rate, and their stability (Rogers and Schier, 2011, Lander, 2007, Drocco *et al.*, 2011).

6.1 Improved assays and analysis for clearance and diffusion can help unravel the biophysical underpinnings of morphogen gradients

Fluorescence Decay After Photoconversion (FDAP) is a time-lapse imaging assay that monitors the decay of a photoconvertible protein over time (Zhang *et al.*, 2007). In this thesis, I present a variant of FDAP in living zebrafish embryos together with a software package that allows context-dependent extraction of protein half-lives. Müller *et al.* (2012) used FDAP to assess the clearance of the two photoconvertible Nodal fusions Squint-Dendra2 and Cyclops-Dendra2 in zebrafish embryos and found nearly equal protein half-lives of 116 min and 95 min, respectively. Their findings stand in contrast with results by Jing *et al.* (2006) who used pulse-chase experiments *in vitro* to determine the half-lives of 2 h for Cyclops and 8 h for Squint, leading them to the conclusion that the difference in signaling range of Cyclops (short) and Squint (long) is attributed to the difference in protein half-lives. The equal clearance rate coefficients measured by Müller

et al. (2012) *in vivo* however, indicate that the differing signaling ranges must be due to varying diffusion rates.

Molecular diffusion measurements have a long tradition in systems biology and are mostly executed by either Fluorescence Correlation Spectroscopy (FCS) or Fluorescence Recovery After Photobleaching (FRAP). While FCS provides information about the local diffusion of molecules, FRAP measures, depending on the mathematical model applied during analysis, either free or effective diffusion across tissues. Since morphogens are subject to tortuous movement, hindered by the extracellular environment, measuring effective diffusion of morphogens yields the rate at which a morphogen effectively transports information through the embryo. FRAP has been widely used to assess the diffusivity of morphogens (Gregor *et al.*, 2007a, Kicheva *et al.*, 2007, Castle *et al.*, 2011, Müller *et al.*, 2012, Sigaut *et al.*, 2014), however often returned varying diffusion coefficients for the same morphogen, which favored different signaling gradient models. For instance, Bicoid (Bcd) diffusivity has been assessed by FRAP multiple times. Gregor *et al.* (2007b) found a relatively low Bcd diffusion coefficient of $0.27\,\mu m^2\,s^{-1}$. This finding, in combination with control experiments in unfertilized embryos, led Gregor *et al.* (2007b) to the conclusion that the Bcd gradient is mainly shaped by clearance through nuclear uptake, ultimately excluding the long-standing synthesis-diffusion-clearance (SDC) model. However, reassessment by Abu-Arish *et al.* (2010), Castle *et al.* (2011) and Sigaut *et al.* (2014) showed that accounting for diffusing Bcd molecules during the bleaching process and correct diffusion models can provide at least a three- to fourfold higher diffusion coefficient, favoring the SDC model and at the same time allowing the Bcd gradient to be precisely read-out in the proper time-scale (Gregor *et al.*, 2007a). Similarly, Kicheva *et al.* (2007) measured Dpp diffusion in the wing disc of *Drosophila melanogaster* embryos of $\sim 0.1\,\mu m^2\,s^{-1}$ leading the authors to favor a model of Dpp gradient establishment by a process involving extracellular Dpp diffusion and endocytosis. A different series of FRAP, nested FRAP, iFRAP and FCS measurements with improved data analysis by Zhou *et al.* (2012) however provided evidence that a fraction of extracellular Dpp molecules move with a much larger diffusion rate of $\sim 20\,\mu m^2\,s^{-1}$, indicating that free extracellular diffusion might shape the Dpp gradient.

The FRAP analysis tool PyFRAP that I developed as part of my research project overcomes the shortcomings of previous analysis methods (Axelrod *et al.*, 1976, Soumpasis, 1983, Sprague and McNally, 2005, Schaff *et al.*, 2009, Rapsomaniki *et al.*, 2012, Blumenthal *et al.*, 2015). This is achieved by simulating FRAP experiments as a reaction-diffusion process in realistic three-dimensional geometries, taking the initial post-bleach image as the initial condition. This simulation-based approach makes it suitable not only for traditional FRAP experiments, but also iFRAP and nested FRAP experiments as conducted by Zhou *et al.* (2012). PyFRAP's combination of open-source code and a GUI makes it adjustable to researchers' needs while providing an easy-to-use standardized front-end and could thus develop into a new standard in FRAP analysis.

In biological tissues, molecules often have to circumvent obstacles such as cells to reach their target. It has been previously argued that this tortuous movement effectively slows down molecules up to two-fold (Müller *et al.*, 2013, Wang *et al.*, 2016). Using PyFRAP's simulation toolbox, we tested this prediction by simulating FRAP experiments at different cell densities and arrived at a similar conclusion: In two-dimensional geometries, effective diffusion decreased by 66% if 75% of geometry area was covered with cells. This effect was much weaker in 3D: When 38% of geometry volume was extracellular space, we only saw a reduction of effective diffusion of 40%. Both of these estimates however resemble extreme cases in which the obstacles are almost maximally jammed packed (Clusel *et al.*, 2009, Baranau *et al.*, 2016). Such packings are unlikely to happen for radial objects in biological systems, however denser packings of obstacles may be achieved if the obstacles are flexible, such as cells. We performed FRAP experiments similar to our simulations both with and without radial polyacrylamide beads *in vitro*, comparing pure diffusion with tortuosity-mediated effective diffusion for different molecules, showing that beads can reduce GFP diffusion by 18%. Not only were our theoretical simulations and experiments in line with previous analytical and numerical studies (Hrabe *et al.*, 2004, Tao and Nicholson, 2004, Novak *et al.*, 2009, Donovan *et al.*, 2016), but also confirm previously estimated experimental values (Müller *et al.*, 2013). It is worthwhile noting that tortuosity might still have stronger effects if cells are not modelled as rigid radial spheres that only allow small surface areas of

contact, but as geometries with more flexible shapes and consistency (Hrabe *et al.*, 2004, Tao and Nicholson, 2004, Novak *et al.*, 2009, Donovan *et al.*, 2016). This would also allow for the generation of narrow dead-end pores, additionally increasing tortuosity (Hrabe *et al.*, 2004). Such effects might underlie our observation that GFP diffusivity is reduced by 60% in living zebrafish embryos.

When molecules traverse tissues, tortuosity is not the only effector of diffusion (Müller and Schier, 2011). Membrane-bound receptors and Heparan Sulfate Proteoglycans (HSPGs) bind molecules either permanently or reversibly, effectively slowing down the recovery in the bleached region of FRAP experiments and the resulting effective diffusion. Our FRAP experiments with Squint-GFP suggest that Squint-GFP diffuses approximately with 1.7 $\mu m^2 s^{-1}$. Given that Squint-GFP is only 1.4 times larger than GFP itself, one would expect a much faster effective diffusion coefficient of Squint-GFP of 31 $\mu m^2 s^{-1}$. This strong reduction of effective diffusion indicates that hindrance through the extracellular matrix and receptors might be the main effector of Squint-GFP diffusion (Müller and Schier, 2011, Müller *et al.*, 2013). Similarly, Dpp has been suggested to undergo restricted extracellular diffusion mediated by HSPGs and its receptor Tkv (Crickmore, 2006, Akiyama *et al.*, 2008, Schwank *et al.*, 2011, Müller *et al.*, 2013), but it is still controversial (Zhou *et al.*, 2012, Müller *et al.*, 2013). FRAP experiments in embryos that lack diffusion regulators, such as receptors, might further reveal the role of hindrance in diffusion measurements. My work shows that a combination between *in vitro* and *in vivo* FRAP, and iFRAP experiments combined with PyFRAP's analysis and simulation capabilities can shed light on the contributions of different biophysical processes that lead to effective diffusion rates of signaling molecules.

Both FDAP and FRAP experiments presented in this study currently rely on overexpression of the fusion protein of interest *in vivo*. However, overexpression experiments can potentially alter the protein's clearance or diffusivity in living organisms. For instance, if protein clearance is non-linear (Eldar *et al.*, 2002), different injection amounts of mRNA might lead to different clearance rate estimates. Also, protein clearance from the extracellular space can include receptor interactions. Thus, one could imagine that overexpression of signaling proteins might saturate

receptor capacities and might thus lead to non-linear effects. A similar argument can be made for FRAP experiments *in vivo*: in this dissertation I show that effective diffusion estimates of the signaling molecule Sqt are much smaller than theoretically predicted diffusion rates, possibly due to interactions with components in the extracellular matrix, such as HSPGs and receptors. Overexpression of the protein of interest might saturate these binding sites and thus might render the unbound molecules faster than they would be if binding sites would be available. In this thesis, we performed a set of control experiments to minimize such side effects: we made sure to inject the minimal amount of mRNA necessary to obtain a sufficient level of fluorescence whilst avoiding mutant phenotypes. While this approach makes side effects induced by overexpression unlikely, it can not complete them rule out. The ideal way to conduct *in vivo* biophysical measurements would be if the fusion protein of interest would be expressed endogenously. The transgenic organisms required for such experiments could be generated with the recently introduced CRISPR-Cas9 system (Doudna and Charpentier, 2014).

In principle, both FRAP and FDAP are easily adaptable for different model organisms. However, a crucial drawback of the variants of FDAP and FRAP in zebrafish embryos is their dependence on fluorescence microscopy and thus their requirement for isolated transparent samples. Model organisms such as zebrafish, *Caenorhabditis elegans*, *Xenopus laevis* and *Drosophila* embryos provide the necessary levels of transparency and develop outside the mother, and are thus suitable for time-lapse fluorescence microscopy.

6.2 The BMP signaling gradient is formed by a source-sink mechanism through BMP diffusion

In this dissertation, we used both FDAP and FRAP to assess the biophysical underpinnings of dorsal-ventral axis formation by the BMP/Chordin system during zebrafish embryogenesis. Extensive research in *Xenopus laevis* and zebrafish has resulted in the postulation of five alternative models for BMP gradient formation. These models range from simple source-sink models to complex reaction-diffusion systems including shuttling and self-organization. All suggested

models mainly rely on different assumptions about the biophysical properties of the molecules included in the patterning system and thus assign different roles to BMP and Chordin. We found that BMP diffuses at a significant rate with respect to the patterning time window, excluding models that predicted non-significant BMP diffusion (Ben-Zvi *et al.*, 2008, Ramel and Hill, 2013). Moreover, the "Long-range accumulation and feedback model" developed by Inomata *et al.* (2013) predicts BMP stability strongly exceeding Chordin stability. Our FDAP experiments however showed that BMP and Chordin have similar stability, thus excluded this model. The prominent "Shuttling model" proposes that Chordin reversibly binds to BMP and shuttles BMP from the dorsal to the ventral side, effectively sharpening the BMP gradient (Ben-Zvi *et al.*, 2008). However, we were not able to observe a higher BMP mobility in FRAP experiments with *chordin* overexpression or an altered BMP distribution of BMP gradients in transplantation experiments with juxtaposed BMP and Chordin sources, leading us to exclude the "Shuttling model". Furthermore, FRAP measurements of Sizzled suggested that Sizzled diffuses in the same timescale as BMP and Chordin, contradicting the assumptions of the "Self-regulated reaction-diffusion model" (Francois *et al.*, 2009). In contrast to the four previously mentioned models, all biophysical assumptions underlying the source-sink model generated by mobile BMP could be confirmed. Strikingly, the source-sink model was also able to reproduce the experimentally observed pSmad gradients build-up and maintenance in the correct time window both in wild type and Chordin-deficient embryos. Our findings are in line with results by Zinski *et al.* (2017). The authors combined immunostainings of pSmad gradients, FRAP measurements of BMP diffusivity and a comprehensive computational screen to single out a source-sink mechanism as the most likely currently proposed model of dorsal-ventral patterning.

While the "Shuttling model", the "Self-regulating reaction-diffusion model" and the "Long-range accumulation and feedback model" could all explain scale-invariant dorsal-ventral patterning (Ben-Zvi *et al.*, 2008, Francois *et al.*, 2009, Inomata *et al.*, 2013, Umulis and Othmer, 2013), a simple source-sink mechanism generally cannot (Wolpert, 1969, Umulis, 2009, Umulis and Othmer, 2013). However, Wolpert (1969) and later McHale *et al.* (2006) already proposed that opposing gradients might be able to scale to embryo size, indicating that the opposite

setup of BMP and Chordin distribution actually might be key for scaling. In addition, we only tested the effect of Chordin on BMP2 diffusion, however other BMPs (BMP4/7, ADMP) might be experiencing facilitated movement through Chordin. Especially ADMP has been shown to play an important role in the self-regulation of the BMP/Chordin system and is colocalized with Chordin on the dorsal side (Reversade and De Robertis, 2005, Plouhinec *et al.*, 2013). Moreover, we still have only little knowledge about the exact role and biophysical parameters of Sizzled, the two additional BMP inhibitors Noggin and Follistatin or the metalloprotease Tolloid. Interestingly, zebrafish *chordin* mutant embryos can be rescued by homogeneous production of Chordin through mRNA injection and grow up to adulthood without defects (Schulte-Merker *et al.*, 1997), indicating that *chordin* mRNA does not have to be initially located on the dorsal side. While it has been shown that endogenous Chordin gradients are able to self-organize (Plouhinec *et al.*, 2013), it is unclear if in rescue experiments with homogeneous Chordin expression, Chordin becomes quickly localized on the dorsal side via self-organizing properties of the system or if Chordin acting homogeneously as an inhibitor is sufficient for proper BMP gradient formation. It is clear however, that a simple source-sink mechanism is a crude simplification of the genetic network instructing the DV axis and cannot completely describe the dorsal-ventral patterning systems. Further biophysical characterization of all members of the BMP family as well as inhibitors and modulators together with extensions of current models will be necessary to gain a more comprehensive understanding of vertebrate DV patterning.

6.3 Size-dependent inhibition by Lefty can explain scaling of the germ layers during zebrafish embryogenesis

The findings presented in this thesis suggest that the Nodal/Lefty network that controls germ layer formation is a scale-invariant patterning system. We created smaller zebrafish embryos by removing 30% of cells from the animal pole approximately 4 hpf that developed perfectly into smaller and proportional larvae. Our fluorescent *in situ* experiments of the *fascin* domains suggested that mesendodermal tissue adjusts to the embryo size within 2 hours post extirpation.

Scaling however failed in the absence of the Nodal inhibitor Lefty. Moreover, similar experiments with extirpated embryos lacking one of the two *lefty* genes also abrogated scaling. Together, both experiments indicate that Lefty plays a crucial role in scaling and that a sufficient amount of Lefty is needed to guarantee that the Nodal signaling properly scales. We thus postulated that fast diffusing Lefty might act as a size sensor quickly reaching the animal pole and subsequently accumulating throughout the embryo. In smaller embryos, Lefty levels increase and Nodal signaling levels thus become globally reduced, resulting in a shorter Nodal signaling range.

We first tested if Nodal-mediated Lefty induction is crucial for scaling by injecting Lefty-GFP into embryos lacking both Lefty1 and Lefty2. Remarkably, untreated embryos patterned normally and extirpated embryos scaled nearly perfectly, suggesting that Nodal actively controlling Lefty expression is not necessary. Similar experiments but with an additional co-injection of a membrane-bound morphotrap against GFP, tethered Lefty-GFP to cell membranes and thus blocked them from reaching the animal pole. As predicted by our model, the inhibition of Lefty-GFP diffusion prevented scaling in extirpated embryos, clearly showing that fast Lefty diffusion is essential for germ layer scaling. We modeled this Size-dependent Inhibition (SDI) mechanism into a reaction-diffusion system consisting of two species. Restricting diffusion and clearance rates to already assessed values (Müller *et al.*, 2012), we performed a comprehensive computational screen for parameter configurations that resemble all experimental observations whilst returning biological plausible signaling gradients and levels. The screen returned multiple parameter configurations that were in similar orders of magnitude as previously measured values for comparable patterning systems (Kicheva *et al.*, 2007), producing Lefty distributions and pSmad2/3 signaling gradients analogous to the ones observed in experiments with Lefty-GFP injections and immunostainings, respectively.

This study provides novel insights into the concepts of scale-invariant patterning in multiple ways: (1) In contrast to previous studies, we focused on scaling of differently-sized embryos at the same developmental stage beyond natural variation, showing scaling for extreme differences in size. Other studies have focused on interspecific differences (Gregor *et al.*, 2005, 2008, Uygur *et al.*, 2016), scaling between different developmental stages (Hamaratoglu *et al.*, 2011, Ben-Zvi

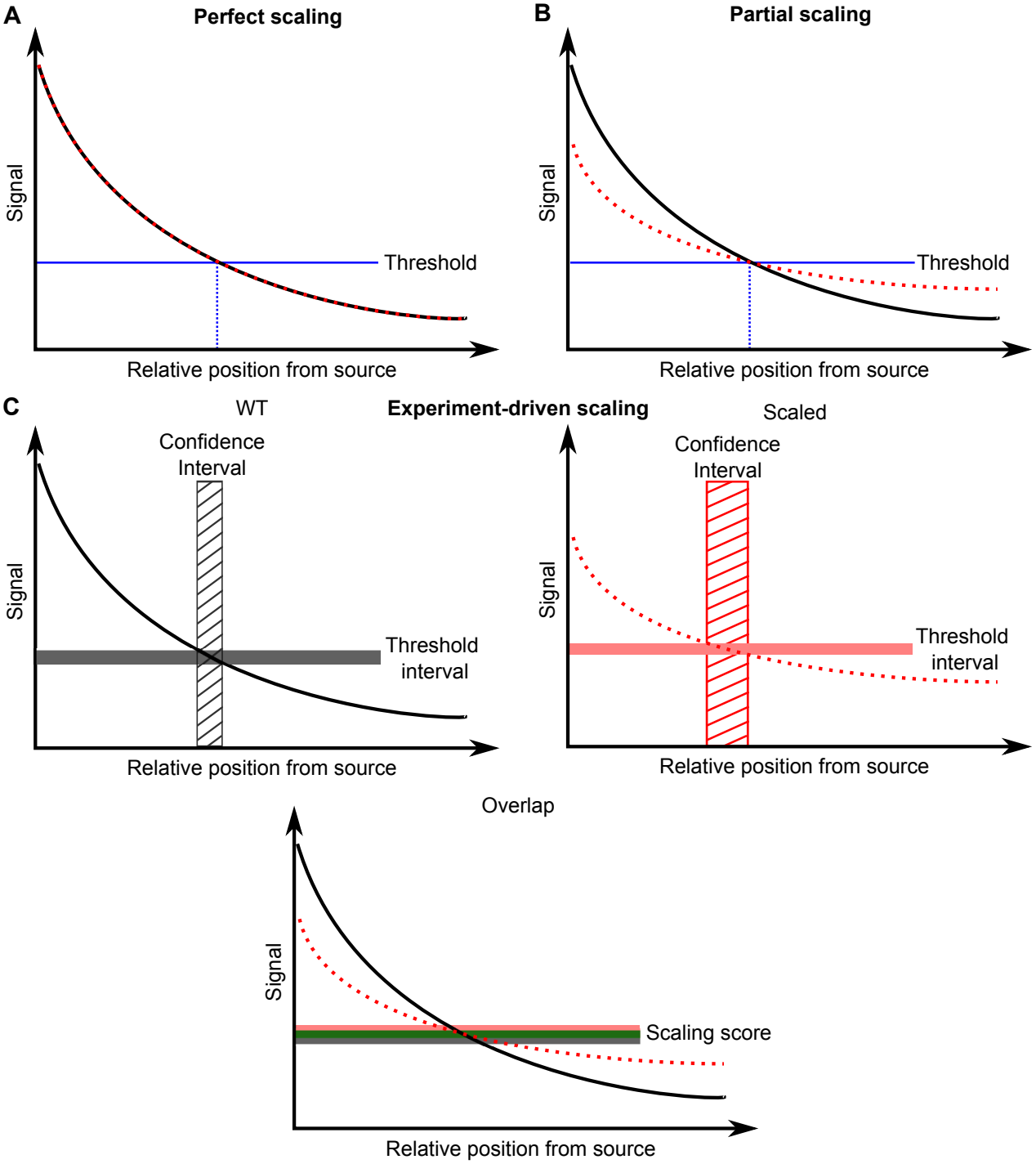

Figure 6.1: Different definitions for scaling. Black lines display the original signaling gradient, red dashed lines the scaled gradient. **A** In perfect scaling, the profile of the scaled and original gradient need to coincide over the complete embryo length. If the gradients scale perfectly, any arbitrary threshold (blue line) would lead to proportional tissues (blue dashed line). **B** The same proportions as in panel A can be achieved if the original and scaled gradient intersect at the relative position of read-out defined by a threshold (blue line). **C** Experiment-driven definition of scaling. Using the 95% confidence intervals of measured tissue sizes, one computes the interval of possible read-out thresholds for both the original (left) and scaled gradient (right). The size of the overlap of the estimated threshold intervals (green, bottom) is then used as a measure of gradient scaling.

et al., 2011a), and natural variation (Coppey *et al.*, 2008, Cheung *et al.*, 2011). Our assay offers a unique way to control external influences and the amount of scaling artificially. (2) Most previous studies focus on perfect or nearly perfect scaling, that is, scaled gradients overlap at any relative position, as illustrated in Figure 6.1A (Othmer and Pate, 1980, McHale *et al.*, 2006, Ben-Zvi *et al.*, 2008, Umulis, 2009, Hamaratoglu *et al.*, 2011, Ben-Zvi *et al.*, 2011a, Averbukh *et al.*, 2014). However, assuming that genes are expressed based on a signaling threshold, to obtain properly scaled tissues, it is sufficient if signaling gradients only intersect at the relative position of the tissue boundary (Figure 6.1B). Such partial scaling is sufficient to allow the organism to form properly scaled patterns (Umulis and Othmer, 2013, Rasolonjanahary and Vasiev, 2016). We thus redefined scaling to be more experiment-driven. We considered that our model scaled if the signaling threshold intervals associated with the 95% confidence intervals of the measured mesendodermal regions in untreated and extirpated embryos completely overlapped, effectively quantifying partial scaling within measurement error and biological variance (Figure 6.1C). (3) It has been shown that signaling gradients undergo a build-up phase and show dynamic range and shape over time (Kicheva *et al.*, 2007, Hamaratoglu *et al.*, 2011, Müller *et al.*, 2012) and are not necessarily interpreted at steady-state (Bergmann *et al.*, 2007, Lander, 2007, Nahmad and Lander, 2011). We thus did not focus on the prominent paradigm of a morphogen at steady-state and instead simulated the SDI model both in time and space, checking for scaling only in the time window of mesendodermal patterning. Strikingly, the SDI model does not only provide scaling of the Nodal signaling gradient at the right time, but also shuts down Nodal signaling afterwards, reproducing the spatiotemporal dynamics of germ layer patterning observed in zebrafish. (4) Most models for scale-invariant patterning rely on complex feedback-loop dependent reaction-diffusion networks where so-called modulators adjust the signaling range of a morphogen by modulating diffusivity (Othmer and Pate, 1980, Ben-Zvi *et al.*, 2008, Barkai and Ben-Zvi, 2009, Ben-Zvi *et al.*, 2011b,a, Haskel-Ittah *et al.*, 2012, Umulis and Othmer, 2013, Norman *et al.*, 2016) or stability (Coppey *et al.*, 2008, Umulis, 2009, Umulis and Othmer, 2013, Inomata *et al.*, 2013). We showed that scaling of embryonic tissue can be achieved by a much simpler passive mechanism without requiring feedbacks. However, it has been shown that active control through

positive feedback might increase gradient precision and robustness (Munteanu *et al.*, 2015). An important aspect of our model is that, in contrast to most modulator models, our model does not impose that the modulator affects biophysical properties of the morphogen, such as the rate of diffusion, ad-hoc.

6.4 Towards more exact morphogen gradient models

The wide-spread paradigm of morphogen gradients has motivated decades of research and still proves as a good approximation for embryonic patterning (Wolpert, 1969, Wartlick *et al.*, 2009, Rogers and Schier, 2011). However, morphogen gradient research is based on a set of assumptions that recently have been questioned: (1) Most studies assume that morphogen gradients are established quickly and then are maintained at steady state for the time window of read-out (Wolpert, 1969, Wartlick *et al.*, 2009, Rogers and Schier, 2011, Briscoe and Small, 2015). However, effective diffusion and reaction rates of morphogens are often not fast enough to quickly form stable gradients (Bergmann *et al.*, 2007, Lander, 2007, Nahmad and Lander, 2011). For instance, using the measured values for BMP and Chordin as parameters for a source-sink model of dorsal-ventral patterning, BMP signaling does not reach steady state in the required time window. Similarly, the Nodal signaling gradient is only shortly stabilized after two hours in the SDI model and then actually shuts down. (2) It is unlikely that simple signaling gradient models are robust with respect to morphological changes such as cell movement and cell division. It has been suggested that signaling molecules are involved in orchestrating morphological changes (Kicheva and Briscoe, 2015), potentially changing the size of their own target field. For instance, Dpp has been found to control proliferation in the developing wing disc (Wartlick *et al.*, 2009) and Nodal signaling has been shown to instruct cell migration during germ layer patterning (Carmany-Rampey and Schier, 2001, Keller *et al.*, 2008). Thus, combined models of morphogenesis that take into account cellular movements, intercellular forces and reaction-diffusion networks are necessary to fully understand gradient formation (Delile *et al.*, 2017). Such models can then be tested by modulating biophysical parameters of morphogens (Alexandre *et al.*, 2014, Harmansa

et al., 2015). (3) Classical models assume a one-to-one relationship between morphogen concentration and interpreted signal (Lander, 2007, Rogers and Schier, 2011, Briscoe and Small, 2015), leading to an all-or-nothing threshold read-out mechanism (Figure 6.2B). While such read-out mechanisms are simple to interpret, they lack robustness with respect to noisy morphogen levels and have recently been challenged (Ochoa-Espinosa *et al.*, 2009, Nahmad and Lander, 2011, Chen *et al.*, 2012, Briscoe and Small, 2015, Kicheva and Briscoe, 2015, Cohen *et al.*, 2015, Sagner and Briscoe, 2017). There are several other ways how morphogen levels could potentially be interpreted: In the slope model, cells "remember" the morphogen's concentration over different times and compute the slope between them (Figure 6.2C) (Romanova-Michaelides *et al.*, 2015). For instance, Sorre *et al.* (2014) show using cell cultures that cells only respond to TGFβ signaling if they are exposed to the signal sufficiently fast. Furthermore, if the morphogen levels follow a build-up with a successive decay phase as illustrated in Figure 6.2A, one could also imagine cells using the transition time, that is, the time at which the slope of the morphogen signal is zero, as a toggle switch turning signaling on or off. A second mechanism that has recently been proposed as a new signal read-out paradigm is signal integration over time (Figure 6.2D). Similar to the slope model, cells accumulate information about the received signal over a time frame, however this time base their decisions on the integral of the signal over time. The duration of such time frame of integration could potentially be controlled by the half-life of activated transcription factors. Experiments in the neural tube by Dessaud *et al.* (2010) suggest that the duration of Sonic Hedgehog (Shh) signaling in neural progenitors is critical for the positional assignment. Similarly, Sako *et al.* (2016) showed that differing Nodal concentrations are not sufficient to induce the prechordal plate and instead the duration of received Nodal signal determines progenitor cell fates. This indicates that morphogen gradients may be interpreted by integrating signals over time (Nahmad and Lander, 2011, Briscoe and Small, 2015, Sagner and Briscoe, 2017). The slope model as well as the integration over time use cumulative information gathered over a longer time frame and are thus robust with respect to temporal fluctuations of morphogen signal. While any of these three read-out mechanisms could work on it's own, it is possible that patterning systems integrate a combination of these mechanisms. Interestingly,

our SDI model produces peak Nodal signaling levels at the time of read-out, followed by a quick decay of signaling, similar to the dynamics illustrated in Figure 6.2A. This timing allows for multiple read-out mechanisms to work: the classical threshold interpretation (Figure 6.2B) as well as the integration over time mechanism (Figure 6.2D). Moreover, the spatiotemporal behavior of the SDI model also would favor the idea of a toggle switch (Figure 6.2C). (4) Experiments flattening the Bcd gradient showed that positional information is not completely abolished and that some downstream target genes of Bcd do not respond by a classical threshold mechanism (Ochoa-Espinosa *et al.*, 2009, Chen *et al.*, 2012). Instead, the authors suggest a complicated downstream gene-regulatory network that incorporates both signals by Bicoid and its repressor Torso to define positional information of gap-genes. Lohr *et al.* (2009) found that this network includes repression of Bicoid in medial-to-posterior compartments by Capicua, which itself is under the control of Torso, and that Capicua is required for proper head formation during Drosophila development. Similarly, the Shh gradient defining dorsal-ventral fates in the vertebrate neural tube has been suggested to activate a mutually repressive gene-regulatory network that redefines and scales tissue sizes after initial specification by morphogen gradients (Kicheva *et al.*, 2014, Kicheva and Briscoe, 2015, Zagorski *et al.*, 2017). Such two phase patterning systems might be more robust to noisy morphogen gradients. Noisy long-range morphogens first define a rough initial sketch of the tissue and tissues are then refined by short-range signals and cell-to-cell interactions and cell sorting (Xiong *et al.*, 2013, Kicheva *et al.*, 2014, Kicheva and Briscoe, 2015, Zagorski *et al.*, 2017). In the case of early zebrafish embryogenesis, it has been shown that two clones of cells injected with either BMP or Nodal transplanted into the animal pole of a zebrafish embryo are able to generate a secondary body axis (Xu *et al.*, 2014). These results suggest that Nodal and BMP are not only sufficient to induce early zebrafish patterning events but that there is an intense cross-talk between both morphogens. The source-sink model for BMP gradient formation and the SDI model do not incorporate this cross-talk, however could be extended in this direction. In general, these results show that patterning events are highly entangled and can not be regarded as independent processes, suggesting that we need more holistic approaches to fully understand embryogenesis.

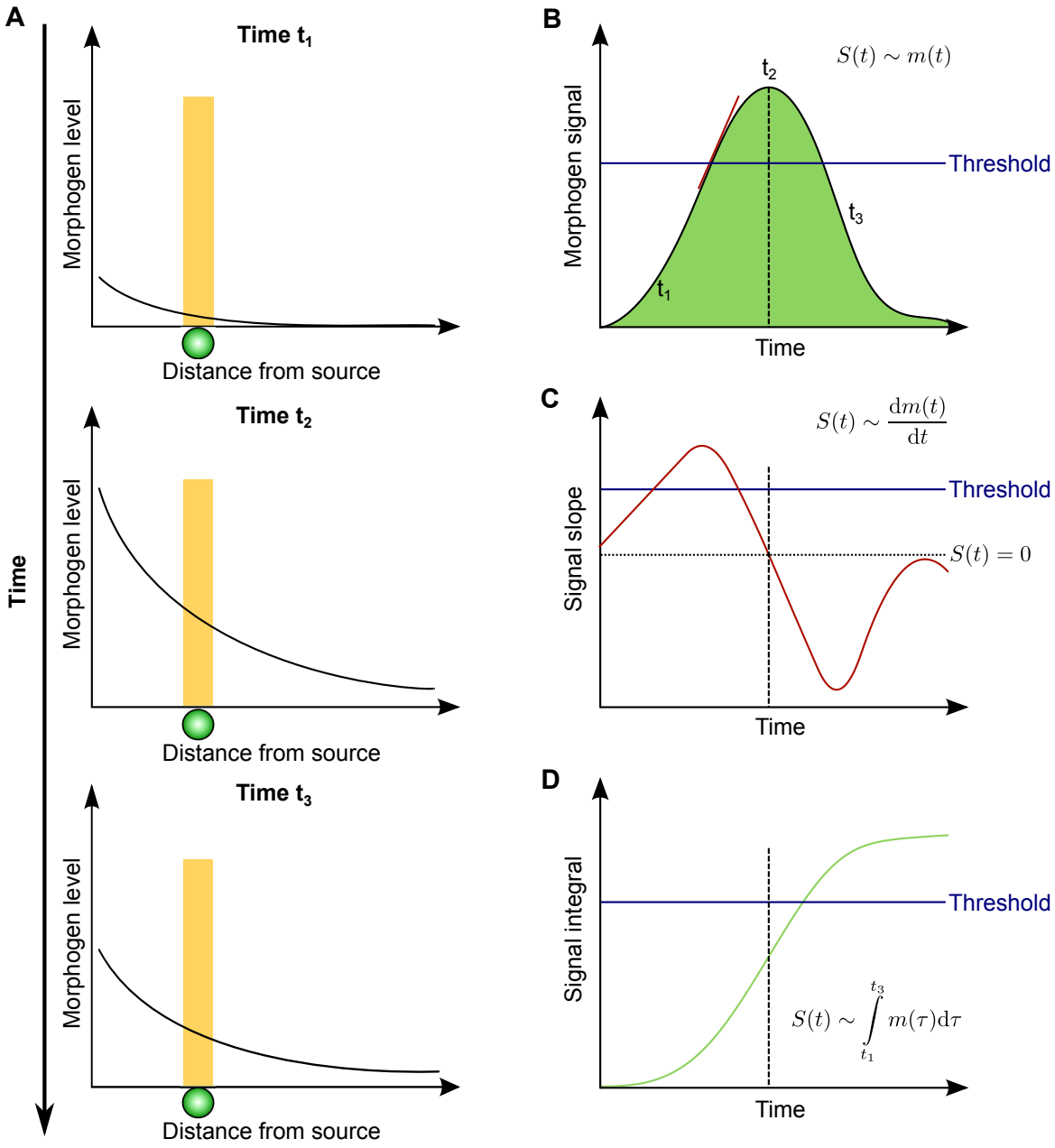

Figure 6.2: Possible spatiotemporal dynamics of a morphogen gradient and read-out mechanisms for morphogen signaling. A Illustration of possible spatiotemporal dynamics of a morphogen gradient. The build up of the gradient (t_1) leads to a period of maximum morphogen levels (t_2) and is followed by the gradient's decay (t_3). The cell (green) receives varying levels of the morphogen signal in the orange area over time. **B** A one-to-one read-out mechanism based on the spatiotemporal dynamics shown in Panel A. The potential morphogen concentration $m(t)$ that a single cell is receiving is directly translated into signal. The cell then decides based on read-out threshold (blue) between different cell fates. The red line indicates the slope of the signal, the green area the integral of signal over time. The vertical dashed line indicates the time of maximum signaling. **C** The slope model. Cells react to the rate at which they are exposed to a morphogen signal. The vertical dashed line indicates the root of the time derivative. **D** Signal transduction by integration over time. The cell accumulates morphogen signal over time and bases fate decisions on the collected information. The vertical dashed line indicates the inflection point of the time integral.

6.5 Systems biology and model complexity

An intrinsic aspect of mathematical modeling in systems biology is to describe biological systems with a low degree of complexity, simplifying the underlying dynamics into more general terms that require less parameters to describe a certain behavior. Such parameters are generally chosen to be the most critical parameters, that is, the parameters that are key to produce the desired outcome of a system. For instance, a graded distribution of a morphogen signal can simply be explained by a single simple reaction-diffusion equation including uniform degradation and a localized source, namely the SDC model. This simple model can describe signaling gradients with only three intuitive parameters: the diffusion coefficient, the degradation and production rate. While these three parameters seem intuitive at the start, they are actually quite abstract: The diffusion rate is not necessarily the diffusion rate of the morphogen, but more the diffusion rate of the signal's information derived from a combination of the morphogen's diffusion rate and the signal transduction rate. Similarly, the degradation rate is not simply the rate at which the morphogen decays, but again a combination of morphogen and transcription factor half-life together with transduction dynamics.

For instance, a simple way to explain Nodal gradient formation is by using the SDC model. However, the biological meaning of the three parameters would not be completely clear and thus the predictive power of the model would be limited. Moreover, a simple implementation of the SDC model cannot explain the scaling of germ layers. By adding the inhibitor Lefty as a second reactant and using experimentally verified reaction kinetics such as Nodal auto-activation, both Müller *et al.* (2012) and Rasolonjanahary and Vasiev (2016) provide more detailed reaction-diffusion systems with seven parameters that also allow for signaling gradient formation. These models however only scale for extreme parameter choices. Extending the model with additional reaction dynamics as done in the present study in the SDI model, increases the model's complexity to eleven parameters. This allows us to explain scale-invariant Nodal signaling for germ layer patterning, however, still suffers from a strong abstraction layer: While Lefty in the SDI model represents actual Lefty protein, the reactant Nodal is a composite

variable that incorporates Nodal signaling as well as Nodal protein dynamics. If we would be solely interested in a simple model that could explain germ layer scaling, the SDI model would fulfill all requirements. However, if we are interested in the role of signaling dynamics in the system, we would have to split Nodal into a stationary signaling and diffusing protein variable, extending the SDI model by another three parameters.

This example illustrates that reducing abstraction layers gives model parameters more biological relevance and makes them more addressable. Consequently, excessively simplifying models can lead to problems. For instance, one of the most common paradigms in embryonic patterning research, Local Activation and Lateral Inhibition (LALI), postulates that the inhibitor of a Turing system needs to diffuse much faster than the activator (Gierer and Meinhardt, 1972). This has recently been challenged by Marcon *et al.* (2016). The authors show that adding a third non-diffusive species, such as signaling, renders the requirement of differential diffusivity unnecessary. Instead, there are multiple network topologies of three or four reactants that could reproduce the same behavior as the LALI mechanism, none of them requiring a difference in diffusion rates.

In summary, while it is easy to study the effects of parameters in simple models, their biological role is often ambiguous and the model itself becomes less explanatory. Indeed, models are strongly context-dependent, that is, the model is designed such that it simplifies identifying key parameters. Or in other words, models are developed such that they help answering a specific question. Therefore, defining and interpreting models in biology bears great predictive power if the limitations of each model are handled appropriately.

7. Conclusion

In this dissertation, I presented how a systems biology approach can provide further insights into two classical questions in developmental biology. Diffusion and clearance have been proposed to be key parameters shaping morphogen gradients that dictate tissue patterning. Due to the lack of suitable assays and analysis tools to measure these parameters in the right context we developed FDAP in living zebrafish embryos together with PyFDAP and PyFRAP. By combining FRAP and FDAP measurements, we assessed the biophysical underpinnings of dorsal-ventral axis formation and showed that, in contrast to most current hypothesis, the BMP signaling gradient is most likely formed by a source-sink mechanism. Moreover, using both size-manipulations experiments of zebrafish embryos and computational modeling, we demonstrate that scale-invariant patterning of the germ layers during zebrafish embryogenesis can be explained by a size-dependent inhibition mechanism.

The project presented in this thesis pictures the typical life-cycle of systems biology: (1) Identifying key biophysical parameters of a biological process. (2) Development of assays and analysis tools to quantify these biological parameters. (3) Quantification of biophysical parameters. (4) Development or updating current models describing the biological process of interest using the newly acquired parameters. (5) Using manipulations of the experimental system together with mathematical modeling to assess the question of interest and infer new questions and key parameters of the biological process.

In summary, the field of developmental biology is currently experiencing a paradigm shift from reductionism to holism under the umbrella of systems biology. Recent advances in computer science, biophysics and molecular biology allow us today to measure, test and computationally verify hypotheses with unprecedented detail: (1) The development of genomic editing tools such as CRISPR (Doudna and Charpentier, 2014) facilitate the generation of mutations and promise novel transgenic organisms, (2) two-photon excitation and light sheet microscopy allow for visualization of *in vivo* protein and tissue dynamics (Höckendorf *et al.*, 2012), and (3) the ever-increasing computational capabilities of modern day computers together with advancements

in artificial intelligence provide the basis of powerful analysis and simulation tools. I am confident that a combination of these techniques and tools built upon the strong foundation of decades of research in developmental biology will soon provide a more complete understanding of the marvelous process that is embryogenesis.

References

Abu-Arish, A., Porcher, A., Czerwonka, A., Dostatni, N., and Fradint, C. (2010). High mobility of Bicoid captured by fluorescence correlation spectroscopy: implication for the rapid establishment of its gradient. *Biophys J*, **99**(4), 33–35.

Agathon, A., Thisse, C., and Thisse, B. (2003). The molecular nature of the zebrafish tail organizer. *Nature*, **424**(6947), 448–452.

Akiyama, T., Kamimura, K., Firkus, C., Takeo, S., Shimmi, O., and Nakato, H. (2008). Dally regulates Dpp morphogen gradient formation by stabilizing Dpp on the cell surface. *Dev Biol*, **313**(1), 408–419.

Alexandre, C., Baena-Lopez, A., and Vincent, J.-P. (2014). Patterning and growth control by membrane-tethered Wingless. *Nature*, **505**(7482), 180–185.

Averbukh, I., Ben-Zvi, D., Mishra, S., and Barkai, N. (2014). Scaling morphogen gradients during tissue growth by a cell division rule. *Development*, **141**(10), 2150–2156.

Axelrod, D., Koppel, D. E., Schlessinger, J., Elson, E., and Webb, W. W. (1976). Mobility measurement by analysis of fluorescence photobleaching recovery kinetics. *Biophys J*, **16**(9), 1055–1069.

Baranau, V., Zhao, S.-C., Scheel, M., Tallarek, U., and Schröter, M. (2016). Upper bound on the Edwards entropy in frictional monodisperse hard-sphere packings. *Soft Matter*, **12**(17), 3991–4006.

Barkai, N. and Ben-Zvi, D. (2009). 'Big frog, small frog'–maintaining proportions in embryonic development. *The FEBS journal*, **276**(5), 1196–1207.

Ben-Zvi, D. and Barkai, N. (2010). Scaling of morphogen gradients by an expansion-repression integral feedback control. *Proc Natl Acad Sci U S A*, **107**(15), 6924–6929.

Ben-Zvi, D., Shilo, B.-Z., Fainsod, A., and Barkai, N. (2008). Scaling of the BMP activation gradient in Xenopus embryos. *Nature*, **453**(7199), 1205–1211.

Ben-Zvi, D., Pyrowolakis, G., Barkai, N., and Shilo, B. Z. (2011a). Expansion-repression mechanism for scaling the Dpp activation gradient in drosophila wing imaginal discs. *Curr Biol*, **21**(16), 1391–1396.

Ben-Zvi, D., Shilo, B.-Z., and Barkai, N. (2011b). Scaling of morphogen gradients. *Current Opin Genet Dev*, **21**(6), 704–710.

Bergmann, S., Sandler, O., Sberro, H., Shnider, S., Schejter, E., Shilo, B. Z., and Barkai, N. (2007). Pre-steady-state decoding of the Bicoid morphogen gradient. *PLoS Biol*, **5**(2), e46.

Blumenthal, D., Goldstien, L., Edidin, M., and Gheber, L. A. (2015). Universal approach to FRAP analysis of arbitrary bleaching patterns. *Sci Rep*, **5**, 11655.

Bollenbach, T., Pantazis, P., Kicheva, A., Bokel, C., Gonzalez-Gaitan, M., and Jülicher, F. (2008). Precision of the Dpp gradient. *Development*, **135**(6), 1137–1146.

Briscoe, J. and Small, S. (2015). Morphogen rules: design principles of gradient-mediated embryo patterning. *Development*, **142**(23), 3996–4009.

Carmany-Rampey, A. and Schier, A. F. (2001). Single-cell internalization during zebrafish gastrulation. *Curr Biol*, **11**(16), 1261–1265.

Castle, B. T., Howard, S. A., and Odde, D. J. (2011). Assessment of transport mechanisms underlying the Bicoid morphogen gradient. *Cell Molecular Bioeng*, **4**(1), 116–121.

Chen, H., Xu, Z., Mei, C., Yu, D., and Small, S. (2012). A system of repressor gradients spatially organizes the boundaries of Bicoid-dependent target genes. *Cell*, **149**(3), 618–629.

Cheung, D., Miles, C., Kreitman, M., and Ma, J. (2011). Scaling of the Bicoid morphogen gradient by a volume-dependent production rate. *Development*, **138**(13), 2741–2749.

Clusel, M., Corwin, E. I., Siemens, A. O. N., and Brujić, J. (2009). A 'granocentric' model for random packing of jammed emulsions. *Nature*, **460**(7255), 611–615.

Cohen, M., Kicheva, A., Ribeiro, A., Blassberg, R., Page, K. M., Barnes, C. P., and Briscoe, J. (2015). Ptch1 and Gli regulate Shh signalling dynamics via multiple mechanisms. *Nat Commun*, **6**, 6709.

Cooke, J. (1981). Scale of body pattern adjusts to available cell number in amphibian embryos. *Nature*, **290**(5809), 775–778.

Coppey, M., Boettiger, A. N., Berezhkovskii, A. M., and Shvartsman, S. Y. (2008). Nuclear trapping shapes the terminal gradient in the Drosophila embryo. *Curr Biol*, **18**(12), 915–919.

Crick, F. (1970). Diffusion in embryogenesis. *Nature*, **225**(5231), 420–422.

Crickmore, M. A. (2006). Hox control of organ size by regulation of morphogen production and mobility. *Science*, **313**(5783), 63–68.

Delile, J., Herrmann, M., Peyriéras, N., and Doursat, R. (2017). A cell-based computational model of early embryogenesis coupling mechanical behaviour and gene regulation. *Nat Commun*, **8**, 13929.

Dessaud, E., Ribes, V., Balaskas, N., Yang, L. L., Pierani, A., Kicheva, A., Novitch, B. G., Briscoe, J., and Sasai, N. (2010). Dynamic assignment and maintenance of positional identity in the ventral neural tube by the morphogen sonic hedgehog. *PLoS Biol*, **8**(6), e1000382.

Dilão, R. and Muraro, D. (2010). MRNA diffusion explains protein gradients in Drosophila early development. *Journal of Theoretical Biology*, **264**(3), 847–853.

Donovan, P., Chehreghanianzabi, Y., Rathinam, M., and Zustiak, S. P. (2016). Homogenization theory for the prediction of obstructed solute diffusivity in macromolecular solutions. *PLoS ONE*, **11**(1), e0146093.

Doudna, J. A. and Charpentier, E. (2014). The new frontier of genome engineering with CRISPR-Cas9. *Science*, **346**(6213), 1258096.

Driever, W. and Nüsslein-Volhard, C. (1988a). A gradient of bicoid protein in Drosophila embryos. *Cell*, **54**(1), 83–93.

Driever, W. and Nüsslein-Volhard, C. (1988b). The Bicoid protein determines position in the Drosophila embryo in a concentration-dependent manner. *Cell*, **54**(1), 95–104.

Drocco, J. A., Grimm, O., Tank, D. W., and Wieschaus, E. (2011). Measurement and perturbation of morphogen lifetime: effects on gradient shape. *Biophys J*, **101**(8), 1807–1815.

Eldar, A., Dorfman, R., Weiss, D., Ashe, H., Shilo, B.-Z., and Barkai, N. (2002). Robustness of the BMP morphogen gradient in Drosophila embryonic patterning. *Nature*, **419**(6904), 304–308.

Francois, P., Vonica, A., Brivanlou, A. H., and Siggia, E. D. (2009). Scaling of BMP gradients in Xenopus embryos. *Nature*, **461**(7260), E1.

Gierer, A. and Meinhardt, H. (1972). A theory of biological pattern formation. *Kybernetik*, **12**, 30–39.

Gregor, T., Bialek, W., van Steveninck, R. R. d. R., Tank, D. W., and Wieschaus, E. F. (2005). Diffusion and scaling during early embryonic pattern formation. *Proc Natl Acad Sci U S A*, **102**(51), 18403–18407.

Gregor, T., Tank, D. W., Wieschaus, E. F., and Bialek, W. (2007a). Probing the limits to positional information. *Cell*, **130**(1), 153–164.

Gregor, T., Wieschaus, E. F., McGregor, A. P., Bialek, W., and Tank, D. W. (2007b). Stability and nuclear dynamics of the Bicoid morphogen gradient. *Cell*, **130**(1), 141–152.

Gregor, T., McGregor, A. P., and Wieschaus, E. F. (2008). Shape and function of the Bicoid morphogen gradient in dipteran species with different sized embryos. *Dev Biol*, **316**(2), 350–358.

Grimm, O., Coppey, M., and Wieschaus, E. (2010). Modelling the Bicoid gradient. *Development*, **137**(14), 2253–2264.

Hamaratoglu, F., de Lachapelle, A. M., Pyrowolakis, G., Bergmann, S., and Affolter, M. (2011). Dpp signaling activity requires pentagone to scale with tissue size in the growing drosophila wing imaginal disc. *PLoS Biol*, **9**(10), e1001182.

Harmansa, S., Hamaratoglu, F., Affolter, M., and Caussinus, E. (2015). Dpp spreading is required for medial but not for lateral wing disc growth. *Nature*, **527**(7578), 317–322.

Haskel-Ittah, M., Ben-Zvi, D., Branski-Arieli, M., Schejter, E. D., Shilo, B.-Z., and Barkai, N. (2012). Self-organized shuttling: generating sharp dorsoventral polarity in the early Drosophila embryo. *Cell*, **150**(5), 1016–1028.

Höckendorf, B., Thumberger, T., and Wittbrodt, J. (2012). Quantitative analysis of embryogenesis: a perspective for light sheet microscopy. *Dev Cell*, **23**(6), 1111–1120.

Houchmandzadeh, B., Wieschaus, E., and Leibler, S. (2002). Establishment of developmental precision and proportions in the early Drosophila embryo. *Nature*, **415**(6873), 798–802.

Hrabe, J., Hrabetová, S., and Segeth, K. (2004). A model of effective diffusion and tortuosity in the extracellular space of the brain. *Biophys J*, **87**(3), 1606–1617.

Inomata, H., Shibata, T., Haraguchi, T., and Sasai, Y. (2013). Scaling of dorsal-ventral patterning by embryo size-dependent degradation of Spemann's organizer signals. *Cell*, **153**(6), 1296–311.

Jing, X., Zhou, S., Wang, W., and Chen, Y. (2006). Mechanisms underlying long- and short-range nodal signaling in zebrafish. *Mech Dev*, **123**(5), 388–394.

Keller, P. J., Schmidt, A. D., Wittbrodt, J., and Stelzer, E. H. K. (2008). Reconstruction of zebrafish early embryonic development by scanned light sheet microscopy. *Science*, **322**(14), 1065–1069.

Kicheva, A. and Briscoe, J. (2015). Developmental pattern formation in phases. *Trends Cell Biol*, **25**(10), 579–591.

Kicheva, A., Pantazis, P., Bollenbach, T., Kalaidzidis, Y., Bittig, T., Jülicher, F., and Gonzalez-Gaitán, M. (2007). Kinetics of morphogen gradient formation. *Science*, **315**(5811), 521–525.

Kicheva, A., Bollenbach, T., Ribeiro, A., Valle, H. P., Lovell-Badge, R., Episkopou, V., and Briscoe, J. (2014). Coordination of progenitor specification and growth in mouse and chick spinal cord. *Science*, **345**(6204), 1254927.

Kimmel, C. B., Ballard, W. W., Kimmel, S. R., Ullmann, B., and Schilling, T. F. (1995). Stages of embryonic development of the zebrafish. *Dev Dyn*, **203**(3), 253–310.

Lander, A. D. (2007). Morpheus unbound: reimagining the morphogen gradient. *Cell*, **128**(2), 245–256.

Langdon, Y. G. and Mullins, M. C. (2011). Maternal and zygotic control of zebrafish dorsoventral axial patterning. *Annu Rev Genet*, **45**, 357–377.

Lauschke, V. M., Tsiairis, C. D., François, P., and Aulehla, A. (2013). Scaling of embryonic patterning based on phase-gradient encoding. *Nature*, **493**(7430), 101–105.

Lecuit, T., Brook, W. J., Ng, M., Calleja, M., Sun, H., and Cohen, S. M. (1996). Two distinct mechanisms for long-range patterning by Decapentaplegic in the Drosophila wing.

Lee, H. X., Ambrosio, A. L., Reversade, B., and De Robertis, E. M. (2006). Embryonic dorsal-ventral signaling: Secreted Frizzled-related proteins as inhibitors of Tolloid proteinases. *Cell*, **124**(1), 147–159.

Liebman, P. A. and Entine, G. (1974). Lateral diffusion of visual pigment in photorecptor disk membranes. *Science*, **185**(4149), 457–459.

Lipshitz, H. D. (2009). Follow the mRNA: a new model for Bicoid gradient formation. *Nat Rev Mol Cell Biol*, **10**(8), 509–512.

Little, S. C., Tkačik, G., Kneeland, T. B., Wieschaus, E. F., and Gregor, T. (2011). The formation of the bicoid morphogen gradient requires protein movement from anteriorly localized mRNA. *PLoS Biology*, **9**(3).

Lohr, U., Chung, H.-R., Beller, M., and Jackle, H. (2009). Antagonistic action of Bicoid and the repressor Capicua determines the spatial limits of Drosophila head gene expression domains. *Proc Natl Acad Sci U S A*, **106**(51), 21695–21700.

Magde, D., Elson, E., and Webb, W. W. (1972). Thermodynamic fluctuations in a reacting system measurement by fluorescence correlation spectroscopy. *Phy Rev Lett*, **29**(11), 705–708.

Magde, D., Elson, E. L., and Webb, W. W. (1974). Fluorescence correlation spectroscopy. II. An experimental realization. *Biopolymers*, **13**(1), 29–61.

Marcon, L., Diego, X., Sharpe, J., and Müller, P. (2016). High-throughput mathematical analysis identifies Turing networks for patterning with equally diffusing signals. *Elife*, **5**, e14022.

McHale, P., Rappel, W.-J., and Levine, H. (2006). Embryonic pattern scaling achieved by oppositely directed morphogen gradients. *Phys Biol*, **3**(2), 107–120.

Müller, P. and Schier, A. F. (2011). Extracellular movement of signaling molecules. *Dev Cell*, **21**(1), 145–158.

Müller, P., Rogers, K. W., Jordan, B. M., Lee, J. S., Robson, D., Ramanathan, S., and Schier, A. F. (2012). Differential diffusivity of Nodal and Lefty underlies a reaction-diffusion patterning system. *Science*, **336**(6082), 721–724.

Müller, P., Rogers, K. W., Yu, S. R., Brand, M., and Schier, A. F. (2013). Morphogen transport. *Development*, **140**(8), 1621–1638.

Mullins, M. C. (2006). Tolloid gets Sizzled competing with Chordin. *Dev Cell*, **10**(2), 154–156.

Munteanu, A., Cotterell, J., Solé, R. V., and Sharpe, J. (2015). Design principles of stripe-forming motifs: the role of positive feedback. *Sci Rep*, **4**, 5003.

Nahmad, M. and Lander, A. D. (2011). Spatiotemporal mechanisms of morphogen gradient interpretation. *Curr Opin Genet Dev*, **21**(6), 726–731.

Nellen, D., Burke, R., Struhl, G., and Basler, K. (1996). Direct and long-range action of a DPP morphogen gradient. *Cell*, **85**(3), 357–368.

Norman, M., Vuilleumier, R., Springhorn, A., Gawlik, J., and Pyrowolakis, G. (2016). Pentagone internalises glypicans to fine-tune multiple signalling pathways. *Elife*, **5**, e13301.

Novak, I. L., Kraikivski, P., and Slepchenko, B. M. (2009). Diffusion in cytoplasm: effects of excluded volume due to internal membranes and cytoskeletal structures. *Biophys J*, **97**(3), 758–767.

Ochoa-Espinosa, A., Yu, D., Tsirigos, A., Struffi, P., and Small, S. (2009). Anterior-posterior positional information in the absence of a strong Bicoid gradient. *Proc Natl Acad Sci U S A*, **106**(10), 3823–3828.

Ornitz, D. M. and Itoh, N. (2015). The fibroblast growth factor signaling pathway. *Wiley Interdiscip Rev Dev Biol*, **4**(3), 215–266.

Othmer, H. G. and Pate, E. (1980). Scale-invariance in reaction-diffusion models of spatial pattern formation. *Proc Natl Acad Sci U S A*, **77**(7), 4180–4184.

Pantazis, P. and Supatto, W. (2014). Advances in whole-embryo imaging: a quantitative transition is underway. *Nat Rev Mol Cell Biol*, **15**(5), 327–339.

Plouhinec, J.-L., Zakin, L., Moriyama, Y., and De Robertis, E. M. (2013). Chordin forms a self-organizing morphogen gradient in the extracellular space between ectoderm and mesoderm in the Xenopus embryo. *Proc Natl Acad Sci U S A*, **110**(51), 20372–20379.

Podos, S. D. and Ferguson, E. L. (1999). Morphogen gradients: new insights from Dpp. *Trends Genet*, **15**(10), 396–402.

Poo, M. M. and Cone, R. A. (1973). Lateral diffusion of rhodopsin in Necturus rods. *Exp Eye Res*, **17**(6), 503–507.

Ramel, M.-C. and Hill, C. S. (2013). The ventral to dorsal BMP activity gradient in the early zebrafish embryo is determined by graded expression of BMP ligands. *Dev Biol*, **378**(2), 170–182.

Rapsomaniki, M. A., Kotsantis, P., Symeonidou, I. E., Giakoumakis, N. N., Taraviras, S., and Lygerou, Z. (2012). EasyFRAP: an interactive, easy-to-use tool for qualitative and quantitative analysis of FRAP data. *Bioinformatics*, **28**(13), 1800–1801.

Rasolonjanahary, M. and Vasiev, B. (2016). Scaling of morphogenetic patterns in reaction-diffusion systems. *J Theor Biol*, **404**, 109–119.

Reversade, B. and De Robertis, E. M. (2005). Regulation of ADMP and BMP2/4/7 at opposite embryonic poles generates a self-regulating morphogenetic field. *Cell*, **123**(6), 1147–1160.

Rogers, K. W. and Schier, A. F. (2011). Morphogen gradients: from generation to interpretation. *Annu Rev Cell Dev Biol*, **27**(1), 377–407.

Romanova-Michaelides, M., Aguilar-Hidalgo, D., Jülicher, F., and Gonzalez-Gaitń, M. (2015). The wing and the eye: A parsimonious theory for scaling and growth control? *Wiley Interdiscip Rev Dev Biol*, **4**(6), 591–608.

Sagner, A. and Briscoe, J. (2017). Morphogen interpretation: concentration, time, competence, and signaling dynamics. *Wiley Interdiscip Rev Dev Biol*, **6**(4), 1–19.

Sako, K., Pradhan, S. J., Barone, V., Inglés-Prieto, Á., Müller, P., Ruprecht, V., Čapek, D., Galande, S., Janovjak, H., and Heisenberg, C. P. (2016). Optogenetic control of Nodal signaling reveals a temporal pattern of Nodal signaling regulating cell fate specification during gastrulation. *Cell Rep*, **16**(3), 866–877.

Schaff, J. C., Cowan, A. E., Loew, L. M., and Moraru, I. I. (2009). Virtual FRAP - an experiment-oriented simulation tool. *Biophys J*, **96**(3), 30a.

Schier, A. F. (2009). Nodal morphogens. *Cold Spring Harbor Perspectives in Biology*, **1**(5), 1–21.

Schier, A. F. and Talbot, W. S. (2005). Molecular genetics of axis formation in zebrafish. *Annu Rev Genet*, **39**, 561–613.

Schulte-Merker, S., Hammerschmidt, M., Beuchle, D., Cho, K. W., De Robertis, E. M., and Nüsslein-Volhard, C. (1994). Expression of zebrafish goosecoid and no tail gene products in wild-type and mutant no tail embryos. *Development*, **120**(4), 843–852.

Schulte-Merker, S., Lee, K. J., McMahon, a. P., and Hammerschmidt, M. (1997). The zebrafish organizer requires Chordino. *Nature*, **387**(6636), 862–863.

Schwank, G., Dalessi, S., Yang, S. F., Yagi, R., de Lachapelle, A. M., Affolter, M., Bergmann, S., and Basler, K. (2011). Formation of the long range Dpp morphogen gradient. *PLoS Biol*, **9**(7), e1001111.

Schwille, P. and Haustein, E. (2009). Fluorescence correlation spectroscopy. An introduction to its concepts and applications. *Biophys. Textb. Online*, **94**, 1–33.

Shingleton, A. W., Frankino, W. A., Flatt, T., Nijhout, H. F., and Emlen, D. J. (2007). Size and shape: the developmental regulation of static allometry in insects. *Bioessays*, **29**(6), 536–548.

Sigaut, L., Pearson, J. E., Colman-Lerner, A., and Ponce Dawson, S. (2014). Messages do diffuse faster than messengers: reconciling disparate estimates of the morphogen Bicoid diffusion coefficient. *PLoS Comput Biol*, **10**(6), e1003629.

Sorre, B., Warmflash, A., Brivanlou, A. H., and Siggia, E. (2014). Encoding of temporal signals by the TGF-β pathway and implications for embryonic patterning. *Dev Cell*, **30**(3), 334–342.

Soumpasis, D. (1983). Theoretical analysis of fluorescence photobleaching recovery experiments. *Biophys J*, **41**(1), 95–97.

Spemann, H. (1938). *Embryonic development and induction*. Yale University Press, New Haven.

Spirov, A., Fahmy, K., Schneider, M., Frei, E., Noll, M., and Baumgartner, S. (2009). Formation of the Bicoid morphogen gradient: an mRNA gradient dictates the protein gradient. *Development*, **136**(4), 605–614.

Sprague, B. L. and McNally, J. G. (2005). FRAP analysis of binding: proper and fitting. *Trends Cell Biol*, **15**(2), 84–91.

Struhl, G., Struhl, K., and Macdonald, P. M. (1989). The gradient morphogen Bicoid is a concentration-dependent transcriptional activator. *Cell*, **57**(7), 1259–1273.

Tao, L. and Nicholson, C. (2004). Maximum geometrical hindrance to diffusion in brain extracellular space surrounding uniformly spaced convex cells. *J Theor Biol*, **229**(1), 59–68.

Thompson, D. W. (1917). *On Growth and Form*. Cambridge University Press, Cambridge.

Tuazon, F. B. and Mullins, M. C. (2015). Temporally coordinated signals progressively pattern the anteroposterior and dorsoventral body axes. *Semin Cell Dev Biol*, **42**, 118–133.

Turing, A. M. (1952). The chemical basis of morphogenesis. *Philos Trans R Soc Lond B Biol Sci*, **237**(641), 37–72.

Umulis, D. M. (2009). Analysis of dynamic morphogen scale invariance. *J R Soc Interface*, **6**(41), 1179–1191.

Umulis, D. M. and Othmer, H. G. (2013). Mechanisms of scaling in pattern formation. *Development*, **140**(24), 4830–4843.

Uygur, A., Young, J., Huycke, T. R., Koska, M., Briscoe, J., and Tabin, C. J. (2016). Scaling pattern to variations in size during development of the vertebrate neural tube. *Dev Cell*, **37**(2), 127–135.

van Boxtel, A. L., Chesebro, J. E., Heliot, C., Ramel, M. C., Stone, R. K., and Hill, C. S. (2015). A temporal window for signal activation dictates the dimensions of a Nodal signaling domain. *Dev Cell*, **35**(2), 175–185.

Wang, Y., Wang, X., Wohland, T., and Sampath, K. (2016). Extracellular interactions and ligand degradation shape the Nodal morphogen gradient. *Elife*, **5**, e13879.

Wartlick, O., Kicheva, A., and Gonzalez-Gaitan, M. (2009). Morphogen gradient formation. *Cold Spring Harb Perspect Biol*, **1**(3), a001255.

Wolpert, L. (1969). Positional information and the spatial pattern of cellular differentiation. *J Theor Biol*, **25**(1), 1–47.

Xiong, F., Tentner, A. R., Huang, P., Gelas, A., Mosaliganti, K. R., Souhait, L., Rannou, N., Swinburne, I. A., Obholzer, N. D., Cowgill, P. D., Schier, A. F., and Megason, S. G. (2013). Specified neural progenitors sort to form sharp domains after noisy Shh signaling. *Cell*, **153**(3), 550–561.

Xu, P.-F., Houssin, N., Ferri-Lagneau, K. F., Thisse, B., and Thisse, C. (2014). Construction of a vertebrate embryo from two opposing morphogen gradients. *Science*, **344**(6179), 87–89.

Zagorski, M., Tabata, Y., Brandenberg, N., Lutolf, M. P., Tkačik, G., Bollenbach, T., Briscoe, J., and Kicheva, A. (2017). Decoding of position in the developing neural tube from antiparallel morphogen gradients. *Science*, **356**(6345), 1379–1383.

Zhang, L., Gurskaya, N. G., Merzlyak, E. M., Staroverov, D. B., Mudrik, N. N., Samarkina, O. N., Vinokurov, L. M., Lukyanov, S., and Lukyanov, K. A. (2007). Method for real-time monitoring of protein degradation at the single cell level. *BioTechniques*, **42**(4), 446–450.

Zhou, P. (2004). Determining protein half-lives. *Methods Mol Biol*, **284**, 67–77.

Zhou, S., Lo, W. C., Suhalim, J. L., Digman, M. A., Gratton, E., Nie, Q., and Lander, A. D. (2012). Free extracellular diffusion creates the Dpp morphogen gradient of the Drosophila wing disc. *Curr Biol*, **22**(8), 668–675.

Zinski, J., Bu, Y., Wang, X., Dou, W., Umulis, D., and Mullins, M. C. (2017). Systems biology derived source-sink mechanism of BMP gradient formation. *Elife*, **6**, e22199.

Bioinformatics, 31(6), 2015, 972–974
doi: 10.1093/bioinformatics/btu735
Advance Access Publication Date: 6 November 2014
Applications Note

OXFORD

Systems biology

PyFDAP: automated analysis of fluorescence decay after photoconversion (FDAP) experiments

Alexander Bläßle and Patrick Müller*

Systems Biology of Development Group, Friedrich Miescher Laboratory of the Max Planck Society, 72076 Tübingen, Germany

*To whom correspondence should be addressed.

Associate Editor: Jonathan Wren

Received on August 18, 2014; revised on October 16, 2014; accepted on November 2, 2014

Abstract

Summary: We developed the graphical user interface PyFDAP for the fitting of linear and non-linear decay functions to data from fluorescence decay after photoconversion (FDAP) experiments. PyFDAP structures and analyses large FDAP datasets and features multiple fitting and plotting options.
Availability and implementation: PyFDAP was written in Python and runs on Ubuntu Linux, Mac OS X and Microsoft Windows operating systems. The software, a user guide and a test FDAP dataset are freely available for download from http://people.tuebingen.mpg.de/mueller-lab.
Contact: pmueller@tue.mpg.de
Supplementary information: Supplementary data are available at *Bioinformatics* online.

1 Introduction

Fluorescence microscopy techniques have been widely used to measure the properties of fluorescently labeled proteins in embryos, tissues and cells (Pantazis and Supatto, 2014). Over the last decade, the repertoire of fluorescent proteins has been extended with the discovery and engineering of photoconvertible proteins that change their emission properties upon light exposure and that can be used to track sub-populations of pulse-labeled proteins (Adam *et al.*, 2014).

Photoconvertible proteins have recently been adapted to determine protein stability via microscopy-based fluorescence decay after photoconversion (FDAP) assays [reviewed in Rogers *et al.* (2015)]. In FDAP assays, a protein of interest is tagged with a photoconvertible protein and expressed *in vivo*. After photoconversion, the decay in fluorescence intensity of the protein is monitored. The data is then fitted with a decay function that models protein clearance to calculate protein half-lives.

Protein stability is context-dependent. For example, protein stability might be different inside cells and in the extracellular space (Müller *et al.*, 2013; Rogers *et al.*, 2015; Zhou *et al.*, 2012). Both intra- and extracellular protein half-lives can be determined by FDAP using a static intracellular signal to create masks for intra- and extracellular intensities (Rogers *et al.*, 2015).

We have previously described how to execute FDAP experiments in living zebrafish embryos (Müller *et al.*, 2012; Rogers *et al.*, 2015). Here, we provide a standardized computational framework to analyse the resulting datasets. Our software PyFDAP features (i) a comprehensive data format for handling, sorting and annotating large FDAP datasets, (ii) the ability to separate FDAP datasets into their intra- and extracellular components based on counter-labeling, (iii) established fitting algorithms and (iv) a user-friendly environment that allows researchers from a non-computational background to easily evaluate FDAP datasets.

2 Implementation

PyFDAP was developed as an open-source graphical user interface (GUI) in Python with PyQT and SciPy to make it accessible across the most frequently used operating systems: Ubuntu Linux, Mac OS X and Microsoft Windows. Python is a widely used scientific programming language and provides PyFDAP users with enormous resources and easily incorporated software packages (Millman and Aivazis, 2011). The PyFDAP GUI was designed to enable the user to simultaneously view the current project tree, project properties and various tabbed plots.

Users import FDAP datasets as '.tif' files. As intra- and extracellular protein stabilities can be different, PyFDAP offers an option to import a second dataset that counter-labels intra- or extracellular space. The separation of fluorescence intensities into intra- or extracellular masks is performed using the Otsu binarization algorithm (Otsu, 1979). The masks and corresponding datasets can then be investigated inside the PyFDAP GUI. The masks are applied to the images of the photoconverted signal, and the average intensities in the intra- and extracellular domains and in the entire image are calculated. PyFDAP organizes all data into a logical hierarchical object structure to facilitate data navigation (Fig. 1).

PyFDAP offers multiple fitting options to fit an exponential decay function given by

$$c(t) = c_0 e^{-kt} + y_0$$

or an inverse power function given by

$$c(t) = \left(c_0^{1-n} - kt(1-n)\right)^{\frac{1}{1-n}} + y_0$$

to the dataset to model linear (Müller *et al.*, 2012) or non-linear decay (Eldar *et al.*, 2003), respectively. Here, $c(t)$ is the intensity of the decaying fluorescent signal, y_0 the baseline of the decay, $c_0 + y_0$ the fluorescent intensity at $t = 0$ and k the decay rate constant of the fluorescent signal. In the case of non-linear decay, n controls the degree of non-linearity. PyFDAP calculates the protein half-lives τ from k as $\tau = \ln(2)/k$ or $\tau = (2^{n-1} - 1)c_0^{1-n}/(k(n-1))$ for linear and non-linear decay, respectively.

PyFDAP offers several established bounded and unbounded optimization algorithms to fit the decay models to the data. The lower bound of fluorescence measurements is limited by the intrinsic background signal of the microscope and the autofluorescence of the imaged sample, and it is therefore crucial to define biologically reasonable bounds for the fit. PyFDAP offers an option to import background and noise measurements and allows the user to choose a lower bound of the baseline y_0 from four presets: (i) the level of noise N estimated from the noise dataset, (ii) the mean level of the pre-conversion background datasets $\overline{B}_{\text{pre}}$, (iii) the mean background level over all background datasets $\overline{B}$ or (iv) a special weighting function F (Müller *et al.*, 2012) given by

$$F_{i,r} = \frac{1}{b}\sum_{j=1}^{b} \min_t \left(\frac{B_{j,r}(t) - N_i}{B_{\text{pre}_{j,r}} - N_i}\right),$$

where i is the current FDAP measurement, $r \in \{$intracellular, extracellular, entire domain$\}$ is the investigated region and $j \in \{1,\ldots,b\}$ represents the indices of background datasets with intensities $B(t)$ at time t. Using the function F, users can compute the lower bound of the baseline for measurement i and region r, $y_{0_{i,r}}$, by

$$y_{0_{i,r}} \geq F_{i,r} \cdot (I_{\text{pre}_{i,r}} - N_i) + N_i,$$

where $I_{\text{pre}_{i,r}}$ denotes the pre-conversion intensity of the FDAP measurement i in region r. Together, these four presets offer a wide range of possibilities for the estimation of the baseline y_0.

Multiple plotting options help the user to remove or improve corrupt datasets or fits. The user can plot the optimized parameters to find outliers and re-run the fits with different options. Moreover, PyFDAP saves the fitting progress and lets the user 'slide' through it to identify points at which optimization algorithms got arrested in a local minimum and where parameters need to be changed.

PyFDAP allows data and results to be saved in various image and video formats. Individual decay curves and fits can be exported as '.csv' files. Similarly, complete PyFDAP project trees (Fig. 1) including all settings and properties can be exported as '.csv' or JavaScript Object Notation (JSON) object files. Object files can easily be reloaded into PyFDAP, which ensures full reproducibility of data analysis and facilitates collaboration among researchers.

To offer customizability and debugging options, PyFDAP also comes with a full Python terminal that allows users to modify FDAP datasets or to improve FDAP data analysis without the need to edit the main PyFDAP code.

A detailed user guide (Supplementary Material) describes the installation and usage of the PyFDAP software as well as the mathematical background for data analysis.

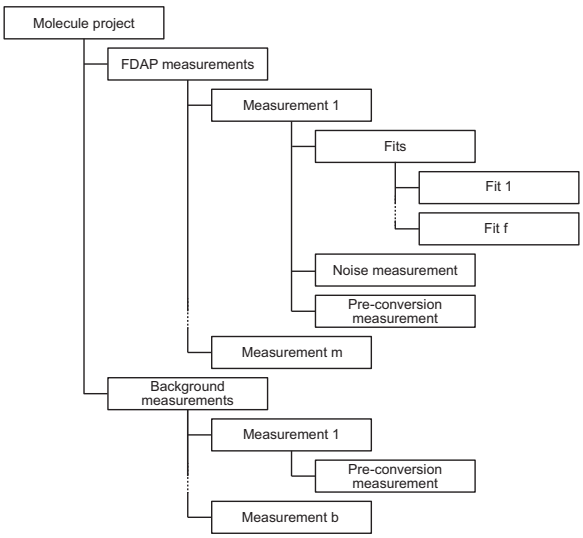

Fig. 1. Hierarchical PyFDAP data structure for FDAP experiments. Experiments are grouped into a main molecule project and divided into FDAP (1 to m) and background (1 to b) pre- and post-conversion measurements. Each FDAP measurement can have multiple fits (1 to f) with different fitting options

3 Conclusion

PyFDAP is an open-source GUI for the analysis and handling of FDAP data. Usage of PyFDAP does not require any programming knowledge. The straightforward GUI provides a quick workflow, and the integrated terminal and open-source nature of PyFDAP enable researchers to extend the software to suit their needs.

Acknowledgements

We thank Katherine Rogers, Luciano Marcon, David Mörsdorf and Gary Soh for useful suggestions and discussions. This work was supported by the Emmy Noether Program of the Deutsche Forschungsgemeinschaft, the Max Planck Society and a Career Development Award from the Human Frontier Science Program.

References

Adam,V. *et al.* (2014) Phototransformable fluorescent proteins: future challenges. *Curr. Opin. Chem. Biol.*, **20C**, 92–102.

Eldar,A. *et al.* (2003) Self-enhanced ligand degradation underlies robustness of morphogen gradients. *Dev. Cell*, **5**, 635–646.

Millman,K.J. and Aivazis,M. (2011) Python for scientists and engineers. *Comput. Sci. Eng.*, **13**, 9–12.

Müller,P. *et al.* (2012) Differential diffusivity of Nodal and Lefty underlies a reaction-diffusion patterning system. *Science*, **336**, 721–724.

Müller,P. *et al.* (2013) Morphogen transport. *Development*, **140**, 1621–1638.
Otsu,N. (1979) A threshold selection method from gray-level histograms. *IEEE Trans. Syst. Man Cybern.*, **9**, 62–66.
Pantazis,P. and Supatto,W. (2014) Advances in whole-embryo imaging: a quantitative transition is underway. *Nat. Rev. Mol. Cell Biol.*, **15**, 327–339.
Rogers,K.W. *et al.* (2015) Measuring protein stability in living zebrafish embryos using Fluorescence Decay After Photoconversion (FDAP). *J. Vis. Exp.*, [Epub ahead of print, doi: 10.3791/52266, January 28, 2015].
Zhou,S. *et al.* (2012) Free extracellular diffusion creates the Dpp morphogen gradient of the Drosophila wing disc. *Curr. Biol.*, **22**, 668–675.

PyFDAP: automated analysis of Fluorescence Decay After Photoconversion (FDAP) experiments

User Guide

Alexander Bläßle and Patrick Müller

Friedrich Miescher Laboratory of the Max Planck Society
Spemannstraße 39
72076 Tübingen
Germany

E-Mail: alexander.blaessle@tuebingen.mpg.de, patrick.mueller@tuebingen.mpg.de
Website: http://people.tuebingen.mpg.de/mueller-lab/

CONTENTS

1 INTRODUCTION

Fluorescence Decay After Photoconversion (FDAP) is a microscopy-based technique for measuring protein half-lives (Rogers *et al.*, 2014). In FDAP experiments, a protein of interest is tagged with a photoconvertible fluorescent protein and expressed *in vivo*. The fluorescent fusion protein is then photoconverted, and the decrease in fluorescence intensity over time is monitored. The resulting intensity data is fitted with a decay function, and half-lives can be calculated from the fits.

Both intracellular and extracellular protein half-lives can be determined using FDAP. A static intracellular signal (e.g. Alexa488-dextran) can be used to create an intracellular mask, such that only intracellular pixels are considered when calculating intracellular intensity. The mask can be inverted to calculate extracellular intensities.

Here, we provide a standardized computational framework to analyze FDAP datasets. Our software PyFDAP features (i) a comprehensive data format for handling, sorting, and annotating large FDAP datasets, (ii) the capability to separate fluorescence intensities in FDAP datasets into intra- and extracellular compartments based on counter-labeling, (iii) established fitting algorithms, and (iv) a user-friendly environment that allows researchers from a non-computational background to easily evaluate FDAP datasets.

2 INSTALLATION

PyFDAP was developed as an open source graphical user interface (GUI) in Python with PyQT and SciPy in order to make it accessible and extendable across the most frequently used operating systems Ubuntu Linux, Mac OS X, and Microsoft Windows. Over the past two decades, Python has become a widely used scientific programming language and provides PyFDAP users with enormous resources and easily addable software packages (Millman and Aivazis, 2011).

All software packages needed to run PyFDAP are freely available. PyFDAP can be installed using stand-alone executables (see Section 2.1). Alternatively, users can run the PyFDAP packages from source (see Section 2.2), which offers the possibility to edit the PyFDAP code and to import new modules.

2.1 Running PyFDAP using stand-alone executables

Download the executable that fits your system from http://people.tuebingen.mpg.de/mueller-lab/. This is suitable for users who want to analyze FDAP experiments and do not need to customize the PyFDAP code. A list of currently available binary files and systems on which the binaries have been tested can be found in Table 1. If there is no executable available for your system, we recommend using the Anaconda installation approach explained in Section 2.2.1.

OS	Version	32-bit	64-bit	Executable	Test System
Linux	3.13.0-36-generic		×	pyfdap_v1.0_Linux_64bit	Thinkpad x230
Mac OS X	10.9.2		×	pyfdap_v1.0_OSX_64bit.app	MacMini6,1
Mac OS X	10.9.2		×	pyfdap_v1.0_OSX_64bit.app	MacBookPro10,2
Mac OS X	10.9.5		×	pyfdap_v1.0_OSX_64bit.app	MacBookPro8,1
Mac OS X	10.9.5		×	pyfdap_v1.0_OSX_64bit.app	MacBookPro8,2
Mac OS X	10.9.5		×	pyfdap_v1.0_OSX_64bit.app	MacBookPro10,2
Windows	7	×		pyfdap_v1.0_Win_32bit.exe	Samsung N150
Windows	8		×	pyfdap_v1.0_Win_64bit.exe	Dell OPTIPLEX 9010

Table 1: List of systems on which the currently available PyFDAP executables have been tested. The executables might also run on systems not listed here.

2.2 Running PyFDAP from source

In order to be able to edit the PyFDAP code and to import new modules, it is necessary to download and install all necessary Python packages and to run PyFDAP from source. There are two ways to do this:

1. Download and install the Anaconda Python distribution (see Section 2.2.1).
2. Download and install all Python packages manually (see Section 2.2.2).

2.2.1 Running PyFDAP using the Anaconda distribution

Anaconda is a bundle of Python packages and includes all packages needed to run PyFDAP. To install Anaconda, follow these steps:

- Go to http://continuum.io/downloads and download the current Python 2.7.x release of Anaconda for your operating system
- Launch the installer by double-clicking (Mac OS X and Windows) or
  - Open a Terminal
  - Go to the directory containing the installer by typing

    ```
    cd path/to/installer
    ```

    and execute the installer with

    ```
    ./installer
    ```

- Follow the instructions of the installer
- Launch PyFDAP by double-clicking `pyfdap_app.py` in the PyFDAP source directory (Windows) or
  - Open a Terminal
  - Go to the directory containing the PyFDAP source files

    ```
    cd path/to/PyFDAP
    ```

  - Launch PyFDAP by typing

    ```
    python pyfdap_app.py
    ```

2.2.2 Running PyFDAP using a manual Python installation

In this section, we explain how to manually install all necessary Python packages on Linux, Mac OS X, and Windows in order to run PyFDAP. The manual installation allows for customizability as well as debugging options. The instructions provided here describe the installation process for computers that currently do not have Python installed. For computers on which Python is already installed, the installation of PyFDAP will differ from the instructions provided below. We recommend running PyFDAP using a Debian-based Linux distribution such as Ubuntu since installing Python packages is more straightforward using such operating systems.

Manual installation under Linux

Here we explain how to manually install and run PyFDAP on Linux operating systems. The following instructions are only suitable for Debian-based Linux distributions and have been tested on Ubuntu Linux 12.04, 13.10, and 14.04 (64-bit). Installation steps may vary between different versions and distributions of Linux (e.g. RedHat-based Linux distributions such as Fedora or Suse).

- Open a Terminal
- In your Terminal, type (you will need sudo rights)

```
sudo apt-get install python-numpy
sudo apt-get install python-scipy
sudo apt-get install python-matplotlib
sudo apt-get install python-qt4
sudo apt-get install python-skimage
```

  Note: On Ubuntu versions older than 12.10, python-skimage needs to be installed from `http://neuro.debian.net/pkgs/python-skimage.html`.

- Download and unpack the current version of PyFDAP from `http://people.tuebingen.mpg.de/mueller-lab`
- Go to your PyFDAP folder by typing

```
cd path/to/PyFDAP/
```

  and launch PyFDAP by typing

```
python pyfdp_app.py
```

  If PyFDAP does not launch, open a Python Terminal and try to import all necessary packages by typing

```
import numpy
import scipy
import matplotlib
import matplotlib.image
import PyQt4
import code
```

  If you receive an error message while importing any of these modules, try to re-install the packages or visit the development website of the problematic package.

Manual installation under Mac OS X

Here we explain how to manually install and run PyFDAP on Mac OS X. The following instructions have only been tested on Mac OS X Snow Leopard 10.6.8 (64-bit) and Mac OS X Maverick 10.9.2, 10.9.4, 10.9.5 (64-bit). Installation steps may vary between different versions of OS X.

- Installing Python packages requires the C++ compiler gcc. gcc can be obtained by downloading XCode from the Apple AppStore.

- Launch a Terminal in Applications → Utilities → Terminal
- Type

```
gcc
```

  You should see a pop-up window asking you to install Command Line Tools. Follow the instructions in the pop-up window.

- Homebrew is a package manager for Mac OS X that facilitates installing packages under OS X. Download Homebrew by typing

```
ruby -e "$(curl -fsSL https://raw.github.com/Homebrew/homebrew/
    go/install)"
```

- Check the Homebrew installation by typing

```
brew update
brew doctor
```

  If the ouput returns any problems, visit the Homebrew website (http://brew.sh/) for further instructions.

- Install Python by typing into the Terminal

```
brew install python
```

  Note that Mac OS X comes with a native Python installation. If you want to use the native Python installation, you can install all packages separately by using the Python Package Index (pip), or you can use Homebrew to install all packages and then link them using the `site` package from https://docs.python.org/2/library/site.html. However, we recommend using the Python installation of Homebrew.

- Link the new Homebrew installation by typing into the Terminal

```
brew link python
brew linkapps
```

- Link the new Python installation into .bash_profile by launching the text editor `nano`

```
nano ~/.bash_profile
```

  and add the following lines

```
PATH="/usr/local/bin:${PATH}"
export PATH
export PYTHONPATH=/usr/local/lib/python2.7/site-packages/:
```

  Press `Ctrl+O` and `Ctrl+X` to save the new .bash_profile and exit. Restart the Terminal and type

```
which python
```

  The output should be

```
/usr/local/bin/python
```

If not, ensure that you have set the Python path properly and use the appropriate Homebrew installation prefix. If everything went correctly, you will now use the Homebrew Python installation when you call `python` in the Terminal.

- Download and install PyQT4 and SIP by typing into the Terminal

```
brew install sip
brew install pyqt
brew linkapps
```

- Download and install Nose and NumPy by typing into the Terminal

```
pip install nose
brew install numpy
brew link numpy
```

Sometimes NumPy can also be found by typing into the Terminal

```
brew install homebrew/python/numpy
brew link numpy
```

- Download and install SciPy by typing into the Terminal

```
pip install scipy
```

or

```
brew install scipy
```

- Download and install scikit-image by typing into the Terminal

```
pip install cython
pip install scikit-image
```

- Download and install Matplotlib by typing into the Terminal

```
pip install python-dateutil
pip install pyparsing
brew install matplotlib
```

- Download and install PIL by typing into the Terminal

```
brew install Homebrew/python/pillow
```

- Download and unpack the current version of PyFDAP from `http://people.tuebingen.mpg.de/mueller-lab/`
- Go to your PyFDAP folder by typing into the Terminal

```
cd path/to/PyFDAP/
```

and launch PyFDAP by typing into the Terminal

```
python pyfdp_app.py
```

If PyFDAP does not launch, open a Python Terminal and try to import all necessary packages by typing into the Terminal

```
import numpy
import scipy
import matplotlib
import matplotlib.image
import PyQt4
import code
```

If you receive an error message while importing any of these modules, try to re-install the packages or visit the development website of the problematic package.

Manual installation under Microsoft Windows

Here we explain how to manually install and start PyFDAP on Microsoft Windows. The following instructions have only been tested for Microsoft Windows 8 (64-bit) and may differ for other versions.

- Download and install the current version of Python 2.7x from `https://www.python.org/download`.
- Download and install the current version of PyQt4 from http://www.riverbankcomputing.co.uk/. The Windows installer will also install the required package SIP and all necessary QT libraries.
- Download and install the current version of SciPy Stack from http://www.lfd.uci.edu/~gohlke/pythonlibs. SciPy Stack includes important Python packages such as Nose, NumPy, SciPy, and Matplotlib. We recommend using SciPy Stack, but if you need to install the packages separately because there is no suitable installation binary of SciPy Stack available, you can use the following links:
  - NumPy: `http://sourceforge.net/projects/numpy/files/NumPy/` if you are running a 32-bit system, on a 64-bit system go to `http://www.kfd.uci.edu/~gohlke/pythonlibs/`
  - SciPy: `http://sourceforge.net/projects/scipy/files/scipy/`
  - Matplotlib: `http://matplotlib.org/downloads.html`
  - Nose: `https://nose.readthedocs.org/en/latest/`
  - IPython: `https://github.com/ipython/ipython/releases`
- Download and install the current version of scikit-image from http://www.lfd.uci.edu/~gohlke/pythonlibs/.
- Download and unpack the current version of PyFDAP from `http://people.tuebingen.mpg.de/mueller-lab`.
- Go to your PyFDAP folder and launch `pyfdp_app.py`. If PyFDAP does not launch, open a Python Terminal and try to import all necessary packages by typing

```
import numpy
import scipy
import matplotlib
import matplotlib.image
import PyQt4
import code
```

If you receive an error message while importing any of these modules, try to re-install the packages or visit the development website of the problematic package.

2.3 Enabling video output for PyFDAP

PyFDAP can convert image series into video files for presentation purposes (see also Section 3.4.1). This requires the installation of MEncoder:

Under Linux, open a Terminal and type

```
sudo apt-get install mencoder
```

If you have followed the manual installation instructions for OS X (see Section 2.2.2), open a Terminal and type

```
brew install mplayer
```

More information about data output in PyFDAP can be found in Section 3.4.

3 WORKING WITH PYFDAP

3.1 The PyFDAP main window

The PyFDAP main window consists of four major compartments: The object list on the left-hand side (red), the property list on the right-hand side (blue), the plot tab in the center (green), and the console at the bottom (magenta).

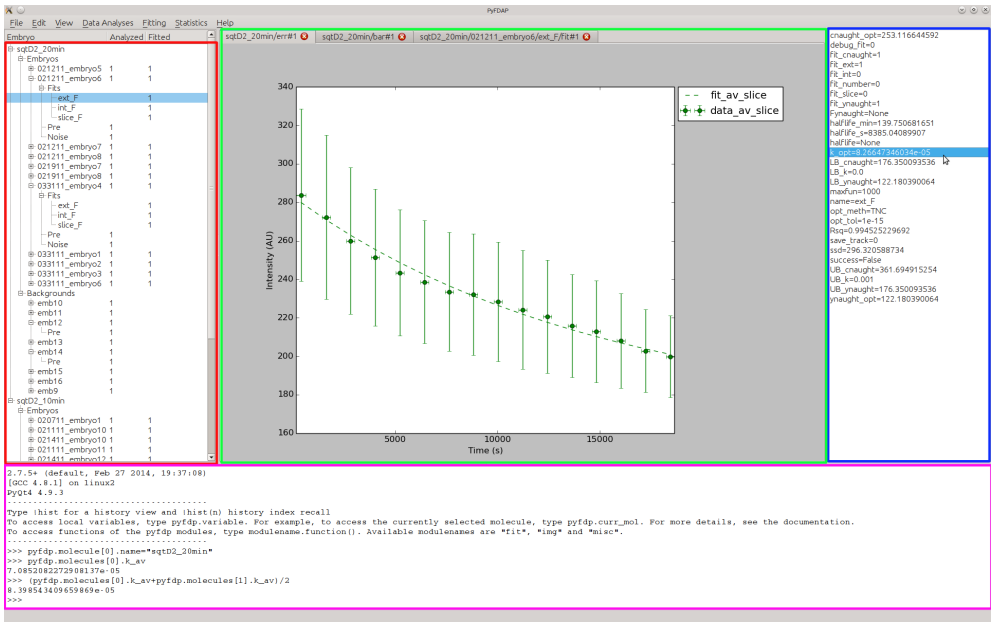

After creating a new molecule, FDAP, background dataset, or fit, the newly created object is shown in the object list according to its hierarchical structure (see Section 4). To inspect the object properties, double-click on the object of choice. The object properties are then listed in the property list on the right-hand side. Many functions in PyFDAP will require you to select the right type of object and will return an error message if not done so.

PyFDAP provides the user with several plotting options. Each plot opens in a new tab with a name according to the currently selected object and the plot type. You can easily switch between plots by clicking on the open tabs.

PyFDAP also comes with an internal Python console. NumPy and the three main PyFDAP modules *img, fit, misc* are automatically imported. You can use the console to manipulate all PyFDAP objects such as molecules and embryos (FDAP datasets), call other Python functions or simply let PyFDAP return molecule or embryo properties such as longer vectors that are not shown in the property list. PyFDAP also uses the console for debugging outputs, so having a look at the console is often useful.

All major PyFDAP functions can be found in the menu bar at the top of the PyFDAP window. The menus are sorted according to the normal workflow of FDAP experiment analysis.

3.2 First steps with PyFDAP

We provide a fully analyzed FDAP dataset on our website. If you wish to try out PyFDAP using this test dataset, go to `http://people.tuebingen.mpg.de/mueller-lab`, download the test dataset *TestDataset.zip*, and unzip it to your PyFDAP folder. If you wish to put it somewhere else, you need to adjust some paths in the molecule file in PyFDAP later. You can now analyze the raw images of the test dataset or your own data (see Section 3.2.1), or you can load a pre-analyzed dataset (see Section 3.2.2).

3.2.1 Analyzing an FDAP dataset

The following section guides you through the major steps of how to use PyFDAP to analyze and fit FDAP datasets if you wish to perform your own FDAP analysis.

1. Create a new molecule project by clicking on *File* → *New Molecule*.

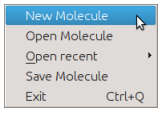

2. Change the name of the molecule project by clicking on *Edit* → *Edit Molecule*.

3. Add a new embryo object (FDAP measurement):

   (a) Go to *Data Analyses* → *Embryo* → *New Embryo*

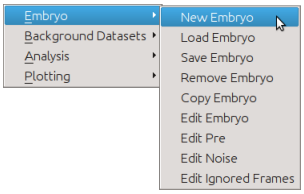

   (b) Choose the photoconverted folder (images of photoconverted proteins) and counter-labeled folder (images of cell-tracing molecules, e.g. Alexa488-Dextran). For the

test dataset, these can be found in the folder *TestDataset/squint-dendra2_20min-interval/embryo6/post*; the photoconverted folder is called *red*, and the counter-labeled folder is called *green*.

(c) Enter the dataset-specific properties such as intervals between images (20 min = 1200 s for the test dataset), post-delay (delay between first and second post-conversion pictures resulting from re-adjustment), and center and radius for each image. You can easily select the center and the radius for each image by clicking on the picture. The first click will define the center, the second the radius, and the third click will delete both selections. If you wish to copy the selected radius and center for all following images, click on *Copy geometry for following images*. When you are done defining the dataset, click on *Done*.

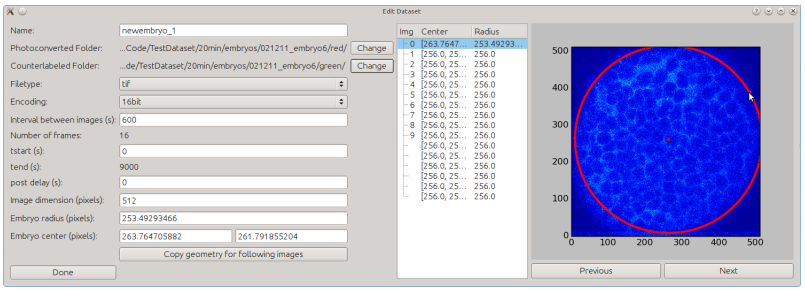

(d) The next pop-up window will allow you to set the "photoconverted" folder, counter-labeled folder, and specific properties of the pre-conversion images similar to the post-conversion dataset in steps (b) and (c). For the test dataset, these can be found in *TestDataset/squint-dendra2_20min-interval/embryo6/pre*; the "photoconverted" folder is called *red*, and the counter-labeled folder is called *green*.

(e) The third pop-up window will allow you to define the method of noise calculation. You can choose between three methods:

- *Outside* will average intensities outside of the selected radius for each image defined in (c) and then average over all of the calculated averages.
- *Predefined* gives you the possibility to enter a value for the noise level yourself.
- *Separate Dataset* lets you analyze a separate dataset taken to calculate noise levels. These images are generally taken before or after the experiments without a sample.

After clicking *Done*, all important settings for the embryo object are entered.

(f) You can add additional embryo objects (FDAP measurements) to the molecule by repeating steps (a) - (e).

4. Add a new background object:

(a) Go to *Data Analyses* → *Background Datasets* → *Add background dataset*.

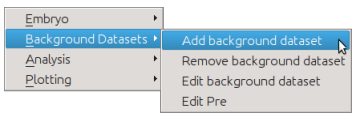

(b) Choose the "photoconverted" folder (images of "photoconverted" proteins) and counter-labeled folder (images of cell-tracing molecules). For the test dataset, these can be found in *TestDataset/squint-background_20min-interval/embryo10/post*; the "photoconverted" folder is called *red*, and the counter-labeled folder is called *green*.

(c) Similar to the embryo object, select parameters specific to the dataset by using the given text fields or by clicking on the image.

(d) The next pop-up window will allow you to set the folders and properties of the pre-conversion images of the background dataset similar to the post-conversion dataset. For the test dataset, these can be found in *TestDataset/squint-background_20min-interval/embryo10/pre*; the "photoconverted" folder is called *red*, and the counter-labeled folder is called *green*.

(e) After clicking *Done*, all important settings for the background object are entered. You can add additional background objects to the molecule by repeating steps (a) - (d).

5. Analyze the molecule project by going to *Data Analyses* → *Analysis* → *Analyze Molecule*. This can take several minutes depending on the amount of datasets added to the molecule project (see Section 5).

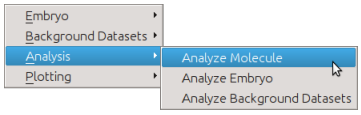

The image analysis progress will be printed into the PyFDAP console.

6. Double-click on the embryo object you want to analyze and add a new fit object:

(a) Go to *Fitting* → *Fits* → *New fit*.

(b) Enter the parameters of the fit. The most important are:

- *opt_meth* is the optimization method (see Table 3 for details) used for finding the minimum of the SSD (sum of squared differences).
- *opt_tol* is the level of tolerance (i.e how good the fit needs to be) given to the optimization algorithm.
- *maxfun* is the maximum number of iterations used by the optimizer.
- *Model* is the underlying decay model used for the fit. See Section 6.1 for more information.
- *x0_k, x0_c0, x0_y0* are the initial guesses for the three parameters k, c_0, and y_0.
- *LB_k, UB_k, LB_c0, UB_c0, LB_y0, UB_y0* are the lower and upper bounds for the three parameters k, c_0, and y_0 given to the optimizer. You can use the checkboxes to set each variable bounded or unbounded from below and above. For the lower bound of y_0, PyFDAP offers several presets:
  - *Custom* allows you to enter a value yourself.
  - *Noise* takes the level of noise as the lower bound for y_0.
  - *Bkgd_pre* takes the level of the background pre-conversion images as the lower bound for y_0.
  - *Bkgd* takes the average background level as the lower bound for y_0.
  - *F* takes the weighting function given in Müller *et al.* (2012) as the lower bound for y_0.

  More details on the estimation of initial guesses and variable bounds can be found in Section 6.2. Note that not all optimization algorithms offer bounded optimization (see Section 6.3 for more details).
- *fit_ext, fit_int, fit_slice* define which regions of the images need to be fitted. You can only select one of the three regions intracelluar, extracelluar, and slice (i.e. total imaged domain) to be fitted during one particular fit.

- *fit_c0, fit_y0* are flags on which parameters are kept fixed and which are free. If a parameter is unchecked, the optimization algorithm will keep this parameter at its initial guess value.

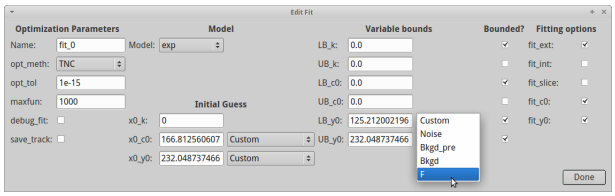

- After clicking *Done*, all important settings for the fit object are entered. The fit is performed instantly, and you will see the fitted data. To inspect the optimal parameters resulting from the fit, double-click on the current fit and look in the property list on the right-hand side for *k_opt* (the decay rate constant) and *halflife_min* (the half-life in minutes).

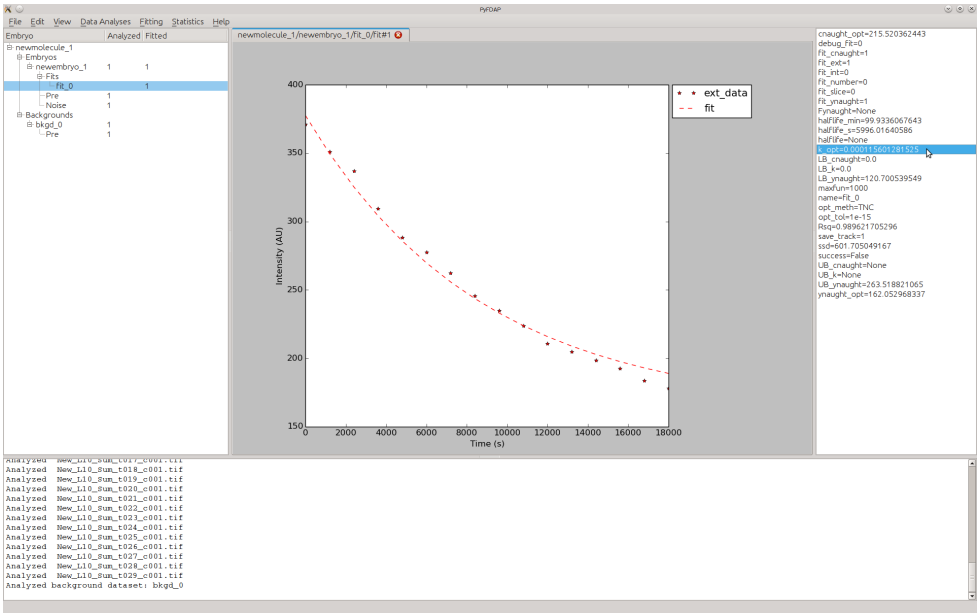

(c) You can add additional fit objects to the molecule project by repeating steps (a) and (b) described above.

7. If you changed any settings of a fit (by selecting *Fitting* → *Fits* → *Edit fit*) and want it to be performed again, select the fit in the left column and go to *Fitting* → *Perform Fits* → *Perform fit*.

8. If you have added and fitted multiple embryo objects (FDAP measurements) and wish to find the average fit over all embryo objects, go to *Statistics* → *Plotting* → *Plot average fit* (see Section 3.3 for details).

3.2.2 Loading a pre-analyzed dataset

Launch PyFDAP, go to *File* → *Open Molecule*, and select the file *TestDataset/results/Test-Dataset_20min.pk*. You have now successfully loaded a molecule project including one embryo

object (FDAP dataset) and one background dataset. You can now try out all features of PyFDAP including all plotting functions.

3.3 Making use of statistical functions in PyFDAP

PyFDAP comes with a few statistical tools for data averaging and analysis. To average the fits from multiple embryo objects (FDAP measurements), go to *Statistics* → *Average Molecule*. A pop-up window will ask you to select fits from different embryo objects:

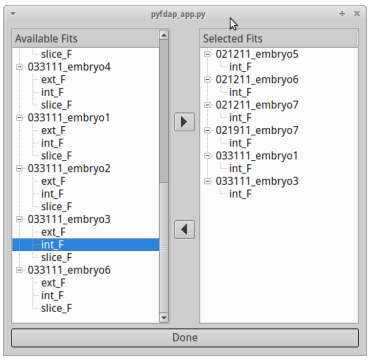

You can add the fits that you want to be considered for averaging to the selection on the right-hand side by double-clicking on the particular fit or by using the arrow buttons on the screen. You can also remove fits from the selection by double-clicking or by using the arrow buttons. Note that for averaging to work, you can only select fits of the same region, e.g. you cannot average a fit for the extracellular region with one for the intracellular region. It is also not possible to let two fits of the same embryo object contribute to the averaged fit.

After selecting the fits that you want to include for averaging, press *Done*. PyFDAP will automatically compute averages of all important fitting parameters and display them in the property list on the right-hand side. Details on how these averages are computed can be found in Section 6.4. After averaging a selection of fits, you can use PyFDAP's bar plot functions to compare fitting results from different embryos. Go to *Statistics* → *Plotting* and choose between *Plot ks by fit*, *Plot y0s by fit*, *Plot c0s by fit* to plot each of the parameters by fit in a bar plot, or choose *Plot all parameters by fit* to plot all three optimal parameters by fit.

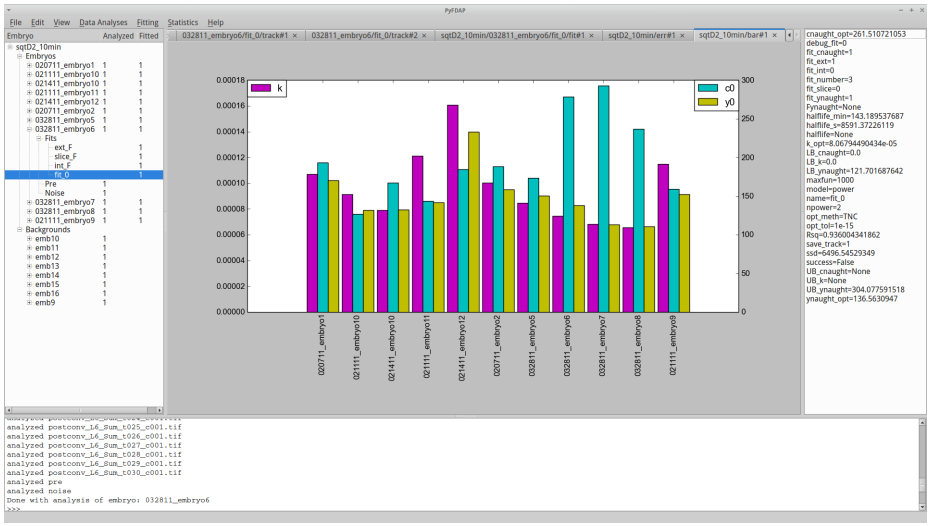

This plot allows you to identify fits that produce parameters strongly deviating from the mean. You can then go back to those fits and adjust the fitting parameters to optimize your final result.

You can also plot the averaged time-dependent fluorescence decay data as error bar plots for unnormalized data or for data normalized between values of 0 and 1. To generate these plots, go to *Statistics* → *Plotting* → *Plot average fit* or *Statistics* → *Plotting* → *Plot normed average fit*.

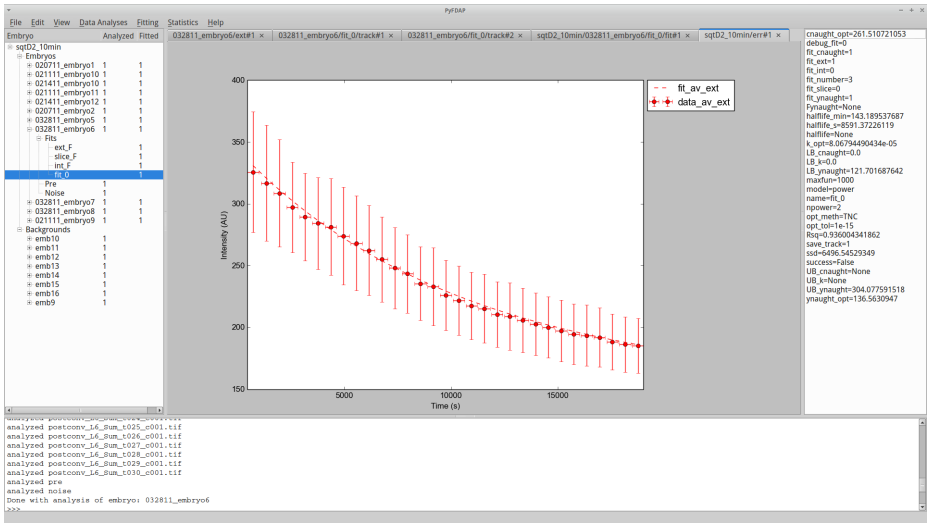

Mathematical details for error bar computation and data normalization can be found in Section 6.4.

Since Version 1.1 PyFDAP also includes statistical tests for comparison between different samples and a normality test. To compare two samples, load two different molecule files, then select the test you want to perform via *Statistics* → *Tests*. Select the two molecules you want to compare and click *Done*. The test statistic will then be displayed in the terminal window. Note: Both molecules need to be averaged before via *Statistics* → *Average molecule*. More details about the implemented statistical tests can be found in Section 6.4.1

3.4 Saving results from PyFDAP

PyFDAP offers multiple ways to save and share FDAP project data and details such as plots, videos, analysis settings, and whole molecule projects.

3.4.1 Saving figures and movies

In *Data Analysis* → *Plotting*, users can find plotting commands for

- Data and background images for the whole region (slice) as well as for extra- and intracellular domains
- Masked images for the whole region (slice) as well as for extra- and intracellular domains
- Masks for the whole region (slice) as well as for extra- and intracellular domains
- Analysis results for all three regions including background values

Moreover, users can plot fitting results and the fitting progress under *Fitting* → *Plotting*. Single plot frames can be saved as *.png, *.pdf, *.eps, *.jpg, *.pgf, *.ps, *.rgba, *.svg, or *.tif. In

order to edit the plots using a vector graphics software, we recommend saving images as *.pdf or *.eps files.

PyFDAP also allows users to export image series (such as the fitting progress) as *.mpg or *.avi movies for presentation purposes. Note that PyFDAP does not automatically provide the necessary package for the conversion of image files to movie files; more information about the installation process to enable video output can be found in Section 2.3.

3.4.2 Saving molecule and embryo files

Users can save their molecule sessions to JavaScript Object Notation (JSON) object files. These object files follow the logical hierarchical structure explained in Section 4 and contain all of the data used for the FDAP analysis as well as the fitting results. The molecule and embryo files can be re-loaded into PyFDAP to enable researchers to continue working on a session and to facilitate collaboration among researchers in different locations.

3.4.3 Saving plots and results as .csv files

Plots as well as molecule and embryo objects can also be saved as comma-separated value files that can then be read into other plotting or analysis software such as Excel or Matlab. The molecule and embryo *.csv files follow the hierarchical system of the JSON files (see above). Note that image data will not be exported to *.csv files.

4 DATA STRUCTURE

PyFDAP provides a hierarchical object structure to organize the datasets obtained from FDAP experiments and to facilitate data navigation (Figure 1).

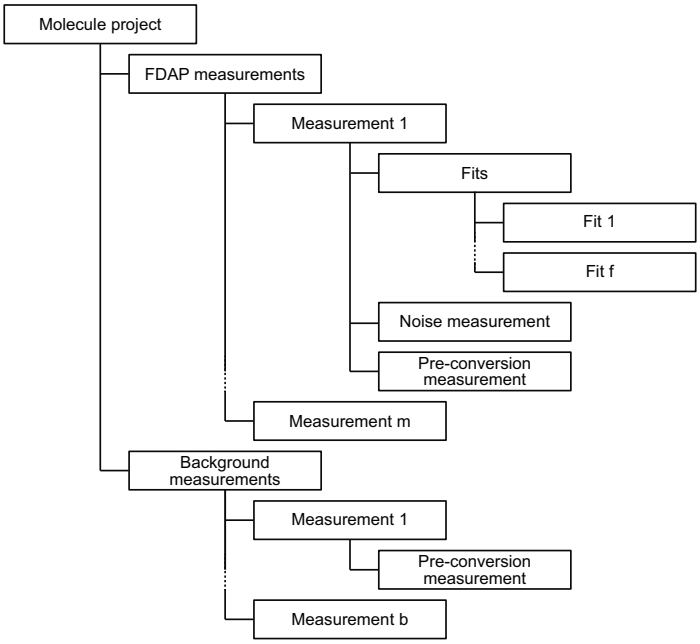

Figure 1: Hierarchical PyFDAP data structure for FDAP experiments. Experiments are grouped into a main molecule project and divided into FDAP (1 to m) and background (1 to b) pre- and post-conversion measurements. Each FDAP measurement can have multiple fits (1 to f) with different fitting options.

Molecule projects: Replicate experiments with the same protein are grouped into a main molecule project. PyFDAP can handle multiple molecule projects in one session.

FDAP measurements: Replicate experiments are divided into FDAP and background pre- and post-conversion measurements. Intra- and extracellular protein stability can be different, and PyFDAP can import a second dataset that counter-labels intra- or extracellular space. The separation of fluorescence intensities into intra- or extracellular masks is performed using the Otsu binarization algorithm (Otsu, 1979). The masks and corresponding datasets can be investigated inside the PyFDAP GUI by clicking on *Data Analysis* → *Plotting* → *Background Dataset*. The masks are applied to the images of the photoconverted signal, and the average intensities in the intra- and extracellular domains and in the entire image are calculated. Each PyFDAP embryo dataset (FDAP measurement) can have multiple fits for various regions, using different fitting parameters and different data points to allow maximum flexibility. The fits are automatically included in the PyFDAP data structure.

Noise measurements: Noise measurements can be imported for each embryo dataset and can be used to calculate estimates for the baseline of the fit (see Section 6.2).

Pre-conversion measurements: Pre-conversion intensity measurements provide information about the levels of autofluorescence and can be used to calculate estimates for the baseline of the fit (see Section 6.2).

Background measurements: Background measurements provide information about the levels of autofluorescence after mock-photoconversion in the presence of unlabeled variants of the protein of interest and can be used to calculate estimates for the baseline of the fit (see Section 6.2).

5 PERFORMANCE

We tested PyFDAP on various system configurations and ran a test script measuring the total operation time. The test script contained the following operations:

1. Open a test molecule file
2. Analyze a single FDAP dataset with all necessary additional data
3. Analyze a background dataset with all necessary additional data
4. Perform three fits for the intra- and extracellular and slice data

The dataset used for this performance test is freely available from `http://people.tuebingen.mpg.de/mueller-lab/`, and the results of our performance tests are listed in Table 2.

System	OS	CPU	Memory	Operational Time
Thinkpad x230	Xubuntu 14.04	Intel(R) Core(TM) i7-3520M, 2.90 GHz	8 GB	55 s
MacBookPro7.1	Mac OS X 10.9.4	Intel(R) Core(TM) 2 Duo-P8600, 2.40 GHz	4 GB	88 s
MacBookPro8.1	Mac OS X 10.9.5	Intel(R) Core(TM) i5-2410M , 2.30 GHz	4 GB	55 s

Table 2: Performance test results of PyFDAP.

6 MATHEMATICAL BACKGROUND

6.1 Decay models

PyFDAP supports two different decay models: Linear- and non-linear decay. Linear decay is given by the ordinary differential equation (ODE)

$$\frac{\mathrm{d}c}{\mathrm{d}t} = -kc$$

where c is the concentration of a molecule and k is the rate constant of the decay. Since we assume that the level of fluorescence is proportional to the molecule concentration, we can substitute the concentration with fluorescence intensity. Solving this ODE results in

$$c(t) = c_0 e^{-kt} + y_0$$

where $c(t)$ is the concentration of a molecule at time t, $c(0) = c_0$ is the concentration at time $t = 0$, and y_0 is the baseline fluorescence intensity to which the population of decaying molecules converges. In terms of fluorescence intensity, y_0 resembles the baseline level of noise and autofluorescence. From k we can then compute the molecule's half-life τ by

$$\tau = \frac{\ln(2)}{k}.$$

Some molecules are proposed to decay non-linearly (Eldar *et al.*, 2003), and we have

$$\frac{\mathrm{d}c}{\mathrm{d}t} = -kc^n$$

where $n > 1$ is the degree of non-linearity and k is the decay rate constant of the molecule. We can solve this ODE and obtain the power-law solution

$$c(t) = \left(c_0^{1-n} - kt(1-n)\right)^{\frac{1}{1-n}} + y_0.$$

For the case of a non-linear decay model, we compute the molecule's half-life by

$$\tau = \frac{(2^{n-1}-1)c_0^{1-n}}{k(n-1)}.$$

6.2 Estimation of initial guesses and bounds for variables

PyFDAP offers multiple options to calculate initial guesses and bounds for variables that are used by the fitting algorithms to obtain biologically reasonable estimates based on noise, pre-conversion, and background measurements (see Section 4).

Initial guess for the estimation of c_0: A good estimate for c_0 is the difference between the pre-conversion and the first post-conversion image, i.e.

$$I_{\mathrm{post}}(t_{\mathrm{start}}) - I_{\mathrm{pre}},$$

where I_{post} and I_{pre} are the fluorescence intensities after and before photoconversion, respectively, and t_{start} is the time at which the first image was taken.

Initial guess for the estimation of the baseline y_0: PyFDAP offers the two presets $I_{\mathrm{post}}(t_{\mathrm{start}})$ and $I_{\mathrm{post}}(t_{\mathrm{end}})$, where t_{end} is the time at which the last image was taken and where protein decay should be almost complete. Our tests showed that the optimization algorithms worked well if $y_{0,\mathrm{opt}}$ is approached from above using $I_{\mathrm{post}}(t_{\mathrm{start}})$ as the initial guess for y_0.

Estimation of the lower bound for the baseline y_0: This estimate is a crucial part of the fitting process. PyFDAP offers several algorithms to perform this estimation based on the amount and quality of the data available.

- The simplest estimate of the lower bound of y_0 is the average background noise of the measurements $\bar{N}$. Due to autofluorescence of the samples, this estimate is generally too low, but it serves as the lower bound of the lower bounds of y_0.
- Alternatively, the lower bound of the baseline y_0 can be estimated from the average level of autofluorescence represented by

$$\bar{B}_{\mathrm{pre}_r} = \frac{\sum_{j=1}^{b} B_{\mathrm{pre}_{j,r}}}{b},$$

  where $r \in \{\text{intracellular, extracellular, entire domain}\}$ is the investigated region, and $j \in \{1, ..., b\}$ are the indices of background pre-conversion datasets with intensities $B_{\mathrm{pre}_{j,r}}$.
- PyFDAP also offers the possibility to use the average background intensity as the lower bound of the baseline y_0:

$$\bar{B}_r = \frac{\sum_{j=1}^{b} \bar{B}_{j,r}}{b},$$

  where $\bar{B}_{j,r}$ is the mean intensity in region r of a background dataset over all data points given by

$$\bar{B}_{j,r} = \frac{\sum_{l=1}^{T} B(t_l)_{j,r} + B_{\mathrm{pre}_{j,r}}}{T+1}.$$

  Here, t_l with $l \in \{1, ..., T\}$ is the time when the l-th image was taken and T is the number of post-conversion images.
- PyFDAP includes a special weighting function F (Müller *et al.*, 2012) given by

$$F_{i,r} = \frac{1}{b} \sum_{j=1}^{b} \min_t \left(\frac{B_{j,r}(t) - N_i}{B_{\mathrm{pre}_{j,r}} - N_i} \right),$$

  where i is the current FDAP measurement, r is the investigated region, and j is the index of background datasets with intensities $B(t)$ at time t. Here, the noise measurement of measurement i is given by N_i. Using the function F, users can compute the lower bound of the baseline $y_{0_{i,r}}$ for measurement i and region r by

$$y_{0_{i,r}} \geq F_{i,r} \cdot (I_{\mathrm{pre}_{i,r}} - N_i) + N_i,$$

  where $I_{\mathrm{pre}_{i,r}}$ denotes the pre-conversion intensity of the FDAP measurement i in region r.

Method	Name in PyFDAP	Type	Reference
Bounded methods			
Limited-memory BFGS	L-BFGS-B	quasi-Newton	Byrd *et al.* (1995)
Truncated Newton Conjugate	TNC	Newton conjugate	Nash (1984)
Sequential Least Squares Programming	SLSQP	sequential quadratic	Kraft (1988)
Brute force	brute	brute force	SciPy Reference Guide
Unbounded methods			
Nelder-Mead	Nelder-Mead	simplex	Nelder and Mead (1965)
Broyden-Fletcher-Goldfarb-Shanno	BFGS	quasi-Newton	Broyden (1970); Goldfarb (1970); Fletcher (1970); Shanno (1970)
Nonlinear Conjugate Gradient	CG	Newton conjugate	Polak and Ribière (1969)

Table 3: List of optimization algorithms in PyFDAP.

6.3 Optimization algorithms

PyFDAP comes with a wide selection of optimization algorithms taken from the SciPy optimize package (http://docs.scipy.org/doc/scipy/reference/optimize.html) (Nelder and Mead (1965); Polak and Ribière (1969); Broyden (1970); Goldfarb (1970); Fletcher (1970); Shanno (1970); Nash (1984); Kraft (1988); Byrd *et al.* (1995); Nocedal and Wright (2006)). A list of all optimization algorithms available in PyFDAP can be found in Table 3.

6.4 Statistics

PyFDAP can average over multiple fits from different embryo objects (FDAP measurements). Details of how to select fits for averaging are described in Section 3.3.

PyFDAP averages the optimal parameters for k, y_0, c_0, and protein half-lives τ through an arithmetic mean. For example, the average decay rate constant $\bar{k}$ is obtained by

$$\bar{k} = \frac{\sum_{i=1}^{\tilde{m}} k_i}{\tilde{m}},$$

where $\tilde{m}$ is the number of fits to be averaged. The average half-life $\bar{\tau}$ can be computed in two ways resulting in different average half-lives. PyFDAP computes the average half-life $\bar{\tau}$ through the arithmetic mean given by

$$\bar{\tau} = \frac{\sum_{i=1}^{\tilde{m}} \tau_i}{\tilde{m}}.$$

For the linear decay model, this yields

$$\bar{\tau} = \frac{1}{\tilde{m}} \sum_{i=1}^{\tilde{m}} \frac{\ln(2)}{k_i}, \tag{1}$$

and in the case of the non-linear decay model we obtain

$$\bar{\tau} = \frac{1}{\tilde{m}} \sum_{i=1}^{\tilde{m}} \frac{(2^{n-1}-1)c_{0,i}^{1-n}}{k_i(n-1)}. \tag{2}$$

However, computing the average half-life $\bar{\tau}$ directly from the average decay rate $\bar{k}$ yields

$$\bar{\tau} = \frac{\ln(2)}{\frac{1}{\tilde{m}} \sum_{i=1}^{\tilde{m}} k_i}, \tag{3}$$

for the linear decay model and

$$\bar{\tau} = \frac{(2^{n-1}-1)\frac{1}{\tilde{m}} \sum_{i=1}^{\tilde{m}} c_{0,i}^{1-n}}{\frac{1}{\tilde{m}} \sum_{i=1}^{\tilde{m}} k_i(n-1)}. \tag{4}$$

in case of the non-linear decay model. It is obvious that equations 1 and 3 as well as equations 2 and 4 do not produce the same half-lives, and the user needs to decide which way of half-life computation is appropriate for the application.

PyFDAP can produce different error bar plots for each averaged region. Clicking on *Statistics → Plotting → Plot average fit* will result in a plot in which each average data point $\bar{c}(t_j)$ is computed as the arithmetic mean

$$\bar{c}(t_j) = \frac{1}{\tilde{m}} \sum_{i=1}^{\tilde{m}} c_i(t_j).$$

Error bars are computed as the standard deviation for each time t_j. Clicking on *Statistics → Plotting → Plot normed average fit* returns a plot in which all data points are normalized between values of 0 and 1. The normalization is performed by subtracting the baseline value $y_{0,i}$ from each data point and dividing the result by $c_{0,i}$, i.e.

$$\tilde{c}_i(t_j) = \frac{c_i(t_j) - y_{0,i}}{c_{0,i}},$$

where $\tilde{c}_i(t_j)$ is the normalized data point at time t_j. This normalization facilitates the comparison of decay curve shapes, but it substantially changes the meaning of the error bars. Since all data series are pinned to a value of 1 at their first time point, the standard deviation vanishes for this data point. The following data points will generally produce increasing error bars since the decay curves generally diverge. The length of the normalized error bars can be interpreted as the extent to which the decay curves diverge throughout the experiments.

6.4.1 Statistical tests

PyFDAP offers multiple statistical tests both to

- test the normality of the distribution of degradation constants,
- and compare two different molecule files and determine of the resulting degradation constants are significantly different.

Method	Requires normality	Reference
Standard t-test	Yes	Student (1908)
Welch's t-test	Yes	Welch (1947)
Mann-Whitney U Test	No	Mann and Whitney (1947)
Wilcoxon	No	Wilcoxon (1945)

Table 4: List of statistical comparison methods in PyFDAP.

A multitude of statistical tests such as the Students t-test (Student, 1908) require normally distributed samples. One way to test this is using the Shapiro-Wilk test (Shapiro and Wilk, 1965), which was recently found to have the best sensibility compared to other common normality tests (Razali and Wah, 2011).

PyFDAP offers four methods to compare the degradation of two molecules. All methods are summarized in table 4.

7 ACKNOWLEDGMENTS

We thank Katherine Rogers and Gary Soh for useful suggestions and for testing PyFDAP. We thank Katherine Rogers and Alex Schier for providing the test dataset.

8 LIST OF FREQUENTLY USED ABBREVIATIONS AND VARIABLES

Name	Description
Abbreviations	
LB	Lower bound
UB	Upper bound
ODE	Ordinary differential equation
SSD	Sum of squared differences
Variables	
b	Number of background measurements
B	Background intensity
c	Molecule concentration
c_0	Initial molecule concentration
$\tilde{c}$	Normalized molecule concentration
f	Number of fits
F	Weighting function for the estimation of the lower bound of y_0
i	Control variable
I	Fluorescence intensity
j	Control variable
k	Molecule decay rate constant
l	Control variable
m	Number of measurements
$\tilde{m}$	Number of selected fits for averaging
n	Degree of non-linearity of molecule decay
N	Noise intensity
r	Region of measurement
t	Time
T	Number of post-conversion frames
τ	Molecule half-life
x_0	Initial parameter guess
y_0	Molecule decay baseline
Variable subscripts	
ext	Extracellular
int	Intracellular
$post$	After photoconversion
pre	Before photoconversion
$slice$	Entire optical slice

9 REFERENCES

Broyden, C. G. (1970). The convergence of a class of double-rank minimization algorithms. 1. General considerations. *IMA Journal of Applied Mathematics*, **6**(1), 76–90.

Byrd, R. H., Lu, P., Nocedal, J., and Zhu, C. (1995). A limited memory algorithm for bound constrained optimization. *SIAM J. Sci. Comput.*, **16**(5), 1190–1208.

Eldar, A., Rosin, D., Shilo, B. Z., and Barkai, N. (2003). Self-enhanced ligand degradation underlies robustness of morphogen gradients. *Dev. Cell*, **5**(4), 635–646.

Fletcher, R. (1970). A new approach to variable metric algorithms. *The Computer Journal*, **13**(3), 317–322.

Goldfarb, D. (1970). A family of variable-metric methods derived by variational means. *Mathematics of Computation*, **24**, 23–26.

Kraft, D. (1988). A software package for sequential quadratic programming. *DFVLR-FB 88-28, Köln, Germany*.

Mann, H. and Whitney, D. (1947). On a test of whether one of two random variables is stochastically larger than the other. *The annals of mathematical statistics*.

Millman, K. J. and Aivazis, M. (2011). Python for scientists and engineers. *Computing in Science & Engineering*, **13**(2), 9–12.

Müller, P., Rogers, K. W., Jordan, B. M., Lee, J. S., Robson, D., Ramanathan, S., and Schier, A. F. (2012). Differential diffusivity of Nodal and Lefty underlies a reaction-diffusion patterning system. *Science*, **336**(6082), 721–724.

Nash, S. G. (1984). Newton-type minimization via the Lanczos method. *SIAM Journal on Numerical Analysis*, **21**(4), 770–788.

Nelder, J. A. and Mead, R. (1965). A simplex method for function minimization. *The Computer Journal*, **7**(4), 308–313.

Nocedal, J. and Wright, S. J. (2006). *Numerical optimization*. Springer series in operations research and financial engineering. Springer, New York, 2. ed. edition.

Otsu, N. (1979). A threshold selection method from gray-level histograms. *IEEE Trans Syst., Man, Cybern.*, **9**(1), 62–66.

Polak, E. and Ribière, G. (1969). Note sur la convergence de méthodes de directions conjuguées. *Revue Française d'Informatique et de Recherche Opérationnelle*, **16**, 35–43.

Razali, N. M. and Wah, Y. B. (2011). Power comparisons of Shapiro-Wilk, Kolmogorov-Smirnov, Lilliefors and Anderson-Darling tests. **2**, 21–33.

Rogers, K. W., Bläßle, A., Schier, A. F., and Müller, P. (2014). Measuring protein stability in living zebrafish embryos using Fluorescence Decay After Photoconversion (FDAP). *Journal of Visualized Experiments, doi:10.3791/52266*.

Shanno, D. F. (1970). Conditioning of quasi-Newton methods for function minimization. *Mathematics of Computation*, **24**(111), 647–656.

Shapiro, S. and Wilk, M. (1965). An analysis of variance test for normality (complete samples). *Biometrika*, **52**, 591–611.

Student (1908). The probable error of a mean. *Biometrika*, **6**, 1–25.

Welch, B. (1947). The generalization ofstudent's' problem when several different population variances are involved. *Biometrika*, (2).

Wilcoxon, F. (1945). Individual comparisons by ranking methods. *Biometrics bulletin*, **1**, 80–83.

Video Article

Measuring Protein Stability in Living Zebrafish Embryos Using Fluorescence Decay After Photoconversion (FDAP)

Katherine W. Rogers[1], Alexander Bläßle[2], Alexander F. Schier[1], Patrick Müller[2]

[1]Department of Molecular and Cellular Biology, Harvard University

[2]Systems Biology of Development Group, Friedrich Miescher Laboratory of the Max Planck Society

Correspondence to: Patrick Müller at patrick.mueller@tuebingen.mpg.de

URL: http://www.jove.com/video/52266
DOI: doi:10.3791/52266

Keywords: Developmental Biology, Issue 95, Fluorescence Decay After Photoconversion (FDAP), protein stability, clearance rate, confocal microscopy, photoconvertible protein, Dendra2, embryo, zebrafish

Date Published: 1/28/2015

Citation: Rogers, K.W., Bläßle, A., Schier, A.F., Müller, P. Measuring Protein Stability in Living Zebrafish Embryos Using Fluorescence Decay After Photoconversion (FDAP). *J. Vis. Exp.* (95), e52266, doi:10.3791/52266 (2015).

Abstract

Protein stability influences many aspects of biology, and measuring the clearance kinetics of proteins can provide important insights into biological systems. In FDAP experiments, the clearance of proteins within living organisms can be measured. A protein of interest is tagged with a photoconvertible fluorescent protein, expressed in vivo and photoconverted, and the decrease in the photoconverted signal over time is monitored. The data is then fitted with an appropriate clearance model to determine the protein half-life. Importantly, the clearance kinetics of protein populations in different compartments of the organism can be examined separately by applying compartmental masks. This approach has been used to determine the intra- and extracellular half-lives of secreted signaling proteins during zebrafish development. Here, we describe a protocol for FDAP experiments in zebrafish embryos. It should be possible to use FDAP to determine the clearance kinetics of any taggable protein in any optically accessible organism.

Video Link

The video component of this article can be found at http://www.jove.com/video/52266/

Introduction

The levels of proteins in cells and organisms are determined by their rates of production and clearance. Protein half-lives can range from minutes to days[1-4]. In many biological systems, the stabilization or clearance of key proteins has important effects on cellular activity. Modulation of intracellular protein stability is required for cell cycle progression[5,6], developmental signaling[7-9], apoptosis[10], and normal function and maintenance of neurons[11,12]. Extracellular protein stability affects the distribution and availability of secreted proteins, such as morphogens[13,14], within a tissue.

Over the last few decades, protein stability has mainly been assessed in cell culture using radioactive pulse-labeling or cycloheximide chase experiments[15]. In such pulse-chase experiments, cells are either transiently exposed to a “pulse” of radioactive amino acid precursors that are incorporated into newly synthesized proteins, or they are exposed to cycloheximide, which inhibits protein synthesis. Cultured cells are then collected at different time points, and either immunoprecipitation followed by autoradiography (in radioactive pulse-chase experiments) or western blotting (in cycloheximide experiments) is used to quantify the clearance of protein over time.

Conventional protein stability assays have several shortcomings. First, proteins in these assays are often not expressed in their endogenous environments, but rather in tissue culture and sometimes in cells from different species. For proteins whose stability is context-dependent, this approach is problematic. Second, it is not possible to follow protein clearance in individual cells or organisms over time, and the data from these assays reflects an average of different populations of cells at different time points. Since individual cells may have started with different amounts of protein, may have taken up the radioactive label or cycloheximide at different times, or may have different clearance kinetics, such aggregate data could be misleading. Finally, in the case of cycloheximide chase experiments, addition of the protein synthesis inhibitor may have unintended physiological effects that could artificially alter protein stability[16-18]. These shortcomings can be avoided by using Fluorescence Decay After Photoconversion (FDAP), a technique that utilizes photoconvertible proteins to measure protein clearance dynamically in living organisms[19-25] (see **Discussion** for limitations of the FDAP technique).

Photoconvertible proteins are fluorescent proteins whose excitation and emission properties change after exposure to specific wavelengths of light[26]. One commonly used variant is Dendra2, a “green-to-red” photoconvertible protein that initially has excitation and emission properties similar to green fluorescent proteins, but after exposure to UV light—“photoconversion”—its excitation/emission properties become similar to those of red fluorescent proteins[23,27]. Importantly, new protein produced after photoconversion will not have the same excitation/emission properties as the photoconverted protein, allowing decoupling of production and clearance upon photoconversion and observation of only a pool

of photoconverted protein. Tagging proteins of interest with photoconvertible proteins thus provides a convenient way to pulse-label proteins in intact, optically accessible living organisms.

In FDAP assays (**Figure 1A**), a protein of interest is tagged with a photoconvertible protein and expressed in a living organism (**Figure 1B**). The fusion protein is photoconverted, and the decrease in photoconverted signal over time is monitored by fluorescence microscopy (**Figure 1C**). The data is then fitted with an appropriate model to determine the half-life of the fusion protein (**Figure 1D**).

The FDAP assay described here was designed to determine the extracellular half-lives of secreted signaling proteins in zebrafish embryos during early embryogenesis[19]. However, this approach can be adapted to any transparent model organism that tolerates live imaging, and could be used to monitor the clearance of any taggable intracellular or extracellular protein. Variations of the technique described here have been performed in cultured cells[20,23] and *Drosophila*[22] and mouse[21] embryos.

Protocol

1. Generating a Photoconvertible Fusion Construct and Injecting Dechorionated Zebrafish Embryos

1. Generate a functional construct containing the protein of interest fused to a green-to-red photoconvertible protein (see **Discussion**), then use *in vitro* transcription to generate capped mRNA encoding the fusion protein as in Müller *et al.,* 2012[19].
2. Use pronase to remove the chorions from about 30 zebrafish embryos at the one-cell stage. Alternatively, manually dechorionate embryos using forceps[28].
   Note: Embryos must be dechorionated for subsequent imaging. If desired, embryos can be injected through the chorion and dechorionated later, just prior to imaging.
   1. Make a 5 mg/ml stock solution of pronase from *Streptomyces griseus* in standard zebrafish embryo medium[19]. Rock the solution gently at RT for 10 min to allow the protease to dissolve. Aliquot 2 ml into microcentrifuge tubes and freeze at -20 °C.
   2. Transfer one-cell stage embryos to a 5 cm diameter glass or agarose-coated plastic Petri dish containing ~8 ml embryo medium. Add 2 ml of thawed pronase stock solution to the dish and incubate at RT for 5 to 10 min.
   3. Avoid exposing embryos to air or plastic, as contact with either will cause dechorionated embryos to rupture. Fill a 200 ml glass beaker with embryo medium. Transfer the embryos to the beaker by tilting the Petri dish while submerging it in the medium.
   4. After the embryos have settled to the bottom of the beaker, pour out most of the embryo medium, then pour fresh embryo medium into the beaker. The mild swirling of the medium pouring into the beaker causes embryos to lose their weakened chorions.
   5. Repeat step 1.2.4.
3. Transfer the dechorionated embryos to an agarose-coated injection dish[29] using a glass Pasteur pipette with a flamed tip. Flaming the pipette tip prevents jagged edges from injuring embryos.
4. Co-inject the mRNA and a 3 kDa Alexa488-dextran conjugate[29,30] (**Figure 1B**; see Discussion for suggested mRNA and Alexa488-dextran amounts). Inject directly into the center of the cell (not the yolk) to ensure even distribution of mRNA and fluorescent dye once cleavage commences.
   Note: The Alexa488 signal will be used during data analysis to generate compartmental masks in order to distinguish between intracellular and extracellular fluorescence.
5. Transfer injected embryos to a 1–2% agarose-coated well of a six-well plastic dish filled with embryo medium. Incubate in the dark at 28 °C until embryos have reached late sphere stage[31] (approximately 5 hr post fertilization). Check embryos every one to 2 hr under a stereomicroscope and remove any debris generated by embryos that have died.

2. Mounting Zebrafish Embryos for Photoconversion and Imaging on an Inverted Confocal Microscope

1. Use a stereomicroscope to identify one to five healthy embryos, and use a glass Pasteur pipette with a flamed tip to remove them from the dish.
2. Gently eject the embryos into a microcentrifuge tube containing ~1 ml of melted 1% low melting point agarose in 1x Danieau's embryo medium (see Materials List) (**Figure 2A**).
   Note: Agarose should have a temperature between 40 and 42 °C; higher temperatures could damage the embryos.
3. Draw the embryos back into the pipette along with some agarose. Gently eject the agarose and embryos onto the cover glass of a glass-bottom dish (**Figure 2B**). Ensure that the thickness of the cover glass is compatible with the objective on the confocal microscope.
   1. Re-use the glass pipette if desired. To clean the residual agarose out of the pipette and prevent clogging, quickly pipette embryo medium up and down. Place a 15 ml tube filled with ~5 ml of embryo medium next to the stereomicroscope for this purpose.
4. Use a metal probe to position the embryos so that the animal pole (blastoderm) faces the cover glass. Work quickly since the agarose will solidify in 20–30 sec. Use the stereomicroscope to monitor the embryos' positions and readjust as necessary until the agarose hardens.
5. Repeat steps 2.1–2.4 until the desired number of embryos has been mounted.
   Note: In a typical experiment, four agarose drops containing four or five embryos each will fit easily on the cover glass. About 16 embryos can be imaged during a single ideal experiment (**Figure 2C**).
6. When the agarose has solidified, fill the glass-bottom dish with 1x Danieau's embryo medium.

3. Photoconverting and Measuring the Decrease of the Photoconverted Signal

A 25X or 40X water objective is appropriate for the size and refractive index of zebrafish embryos. It is best to use immersion oil with the same refractive index as water rather than actual water, since water will evaporate during the course of the five-hour experiment. Ensure that the immersion oil is designed to be used with a water (not oil) objective.

1. Place a large drop of immersion oil on the objective to ensure that the oil film between the objective and cover glass will not break as the stage moves to different embryo positions during imaging. Securely place the glass-bottom dish onto the stage so that the dish will not shift when the stage moves. If possible, use a heated stage at 28 °C, the optimal temperature for zebrafish development.
2. Define each embryo's position in the confocal microscope's software package. Adjust the z-depth for each embryo, and attempt to target roughly the same plane in each embryo.
   Note: About 30 µm from the animal pole is a good depth since at this depth the enveloping layer of the embryo can be avoided, imaging area is maximized, and light scattering is minimal. A single optical slice with a thickness of ~3.3 µm provides sufficient data; there is no need to acquire a z-stack (see Section 5).
3. Collect two signals during the experiment: the "green" signal from the Alexa488-dextran conjugate—which will be used during data analysis to isolate extracellular and intracellular fluorescence—and the "red" signal from the fusion protein after it is photoconverted.
   1. Excite Alexa488 using a 488 nm laser, and collect emitted fluorescence between ~500 and 540 nm. Note: After photoconversion, many green-to-red photoconvertible proteins (*e.g.*, Dendra2) can be excited with a 543 nm laser and emit fluorescence between ~550 and 650 nm. Adjust as necessary based on the photoconvertible protein used.
4. Acquire "pre-photoconversion" images, and configure the confocal microscope's software to image each of the previously defined positions (from step 3.2) with the appropriate imaging conditions every 10 or 20 min for a five-hour time course (see Section 5 and Discussion).
5. To photoconvert the fusion protein, switch to a 10X objective and expose groups of embryos to UV light from a mercury arc lamp with a ~300–400 nm excitation filter at 100% output for 2 min. Shift the focus along the z-axis to promote uniform photoconversion (see Section 5**).** Ensure that the immersion oil does not drip onto the 10x objective during photoconversion.
   Note: The shifting of focus during photoconversion could be automated in order to avoid variability among experimenters.
6. Switch back to the 25X or 40X objective immediately after photoconversion. Ensure that the previously defined positions from step 3.2 are still accurate. If the dish shifted during photoconversion, re-define the positions of the embryos.
   1. Start the program created in step 3.4 and allow imaging to continue for 5 hr. Note the time elapsed between photoconversion and the start of imaging for each embryo.
7. Occasionally check on the experiment. Monitor the level of Danieau's medium and add more if necessary. Restart the software if it has stalled.
8. In order to determine the background fluorescence values that will be used during data analysis to estimate the asymptote of an exponentially decreasing model, include some embryos that have been injected with Alexa488-dextran but not mRNA in the experiment. To determine the instrument noise, which will also be used during subsequent data analysis, acquire an image in the absence of a sample.

4. Analyzing the Data Using PyFDAP

1. Visually inspect the time course data sets from each embryo. Discard data sets from embryos that died during imaging, that shifted significantly, that have very low levels of photoconverted signal, or that contain regions of cells that look unusual and have stopped moving and dividing (typical of injured or sick embryos).
   Note: Occasionally, bubbles in the immersion oil or other artifacts will appear in one or two images in an otherwise usable data set. Note any images that contain artifacts; they will be discarded later, and the remaining time points from such a data set can still be analyzed.
2. Use the Python-based software package PyFDAP to analyze the FDAP data. PyFDAP calculates half-lives by determining the average intracellular and extracellular red fluorescence intensity in each image and fitting the data with an exponentially decreasing function[56] (**Figure 3**).
   1. Download PyFDAP (see Materials List).
   2. Use PyFDAP to separate intracellular and extracellular photoconverted signal (**Figure 3A,B**). Use the Alexa488 signal, which is strictly intracellular, to create an intracellular mask. Apply this mask to the corresponding red channel image to prevent intracellular pixels from being considered when calculating average extracellular intensity. To measure average intracellular intensity, invert the mask.
   3. In PyFDAP, display the masked images generated in step 4.2.2. Visually inspect these images and discard data sets in which masks do not accurately distinguish intracellular from extracellular space (this should be rare; note that cell membranes are included in images in which extracellular space has been masked, but they could be removed by altering the thresholding algorithm or by introducing a membrane mask (*e.g.*, using membrane-CFP)). Also discard any single images containing artifacts (*e.g.*, bubbles in the immersion oil) identified in step 4.1.
   4. Use PyFDAP to calculate average extracellular and intracellular fluorescence intensities for each image. PyFDAP calculates these averages by summing the intensities of pixels that fall outside of the mask and dividing by the total number of pixels summed.
   5. Fit the fluorescence data (**Figure 3C**) with the following exponential function:
      $$c(t) = c_0 e^{-kt} + y_0$$
      where t is time post-photoconversion, $c(t)$ is intensity at a given value of t, c_0 is the intensity at $t = 0$, k is the clearance rate constant, and y_0 is the asymptote that the function approaches as fluorescence decreases (**Figure 1D**). y_0 can be constrained based on the measurements in step 3.8[19].
   6. Use PyFDAP to calculate the extracellular and intracellular protein half-lives (τ) from the clearance rate constants (k) using the following relationship:

$$\text{Half-life } \tau = \frac{\ln(2)}{k}$$

5. Control Experiments to Assess Photobleaching, Inadvertent Photoconversion, and Photoconversion Uniformity

1. Assessing photobleaching
   Note: Photobleaching could cause an artifactual decrease in fluorescence intensity that reflects the bleaching properties of the fluorescent protein in addition to the clearance of the protein of interest.
   1. To assess possible photobleaching, perform one set of FDAP experiments with 10 min intervals between imaging and a second set with 20 min intervals between imaging (**Figure 4**). Analyze the data from both sets of experiments using PyFDAP as described in Section 4.
   2. Compare the half-lives from the 10 and 20 min interval experiments. Longer half-lives from 20 min interval experiments indicate significant photobleaching. If the half-lives from both experiments are identical, photobleaching is not a significant concern.
   3. Alternatively, assess photobleaching by acquiring a series of ~30 images immediately after photoconversion. A significant decrease in fluorescence intensity indicates significant photobleaching.
   4. If photobleaching is detected, use lower laser power, decrease imaging time, or consider using a more photostable photoconvertible protein[32].

2. Assessing inadvertent photoconversion.
   Note: Dendra2 can be photoconverted using 488 nm illumination[27]. When exciting Alexa488 with the 488 nm laser as described in step 3.3.1, inadvertent photoconversion and therefore an artifactual increase in the apparent half-life of the protein of interest is possible. However, we and others[33] have found that 488 nm illumination is an inefficient method of photoconversion in zebrafish embryos.
   1. Use the control experiment described in step 5.1.1 to detect inadvertent photoconversion. Compare the half-lives from the 10 and 20 min interval experiments. Shorter half-lives from 20 min interval experiments indicate significant inadvertent photoconversion. If the half-lives from both experiments are identical, inadvertent photoconversion is not a significant concern.
   2. If inadvertent photoconversion is detected, use a lower 488 nm laser power and shorter imaging times to avoid inadvertently photoconverting Dendra2.

3. Assessing photoconversion uniformity.
   Note: If photoconversion is biased toward the animal pole of the embryo, the decrease in fluorescence will be influenced by protein diffusion or cell movement into deeper planes (**Figure 5A**).
   1. To determine whether photoconversion is uniform, express a secreted photoconvertible protein (for experiments with extracellular fusion proteins) or a cytoplasmic photoconvertible protein (for experiments with intracellular fusion proteins). Photoconvert as usual, then acquire a z-stack encompassing most of the blastoderm every 20 min for 80 min.
   2. If photoconversion is biased toward the animal pole, the fluorescence intensity in deeper planes will increase over time due to diffusion or cell movement (**Figure 5B**). If non-uniform photoconversion is detected, focus deeper into the embryos during photoconversion.

Representative Results

FDAP has been used to determine the half-lives of extracellular signaling proteins in zebrafish embryos[19]. One of these proteins, Squint, induces expression of mesendodermal genes during embryogenesis[34]. Squint-Dendra2 activates expression of mesendodermal genes at levels similar to untagged Squint, as demonstrated by qRT-PCR and *in situ* hybridization assays[19]. Embryos were co-injected with Alexa488-dextran and mRNA encoding Squint-Dendra2 and subjected to the FDAP assay. A decrease in the extracellular photoconverted signal intensity over time is evident (**Figure 4A**). Extracellular intensity profiles from 23 embryos were generated using PyFDAP. The resulting data was fitted in PyFDAP with a first-order clearance kinetics model, and an average clearance rate constant k of 1.00 x 10^{-4}/sec, corresponding to an average half-life τ of 116 min, was determined. Similar intensity profiles and clearance rate constants were obtained when the intervals between imaging were 10 or 20 min, suggesting that photobleaching or inadvertent photoconversion did not contribute significantly to intensity changes (**Figure 4B**).

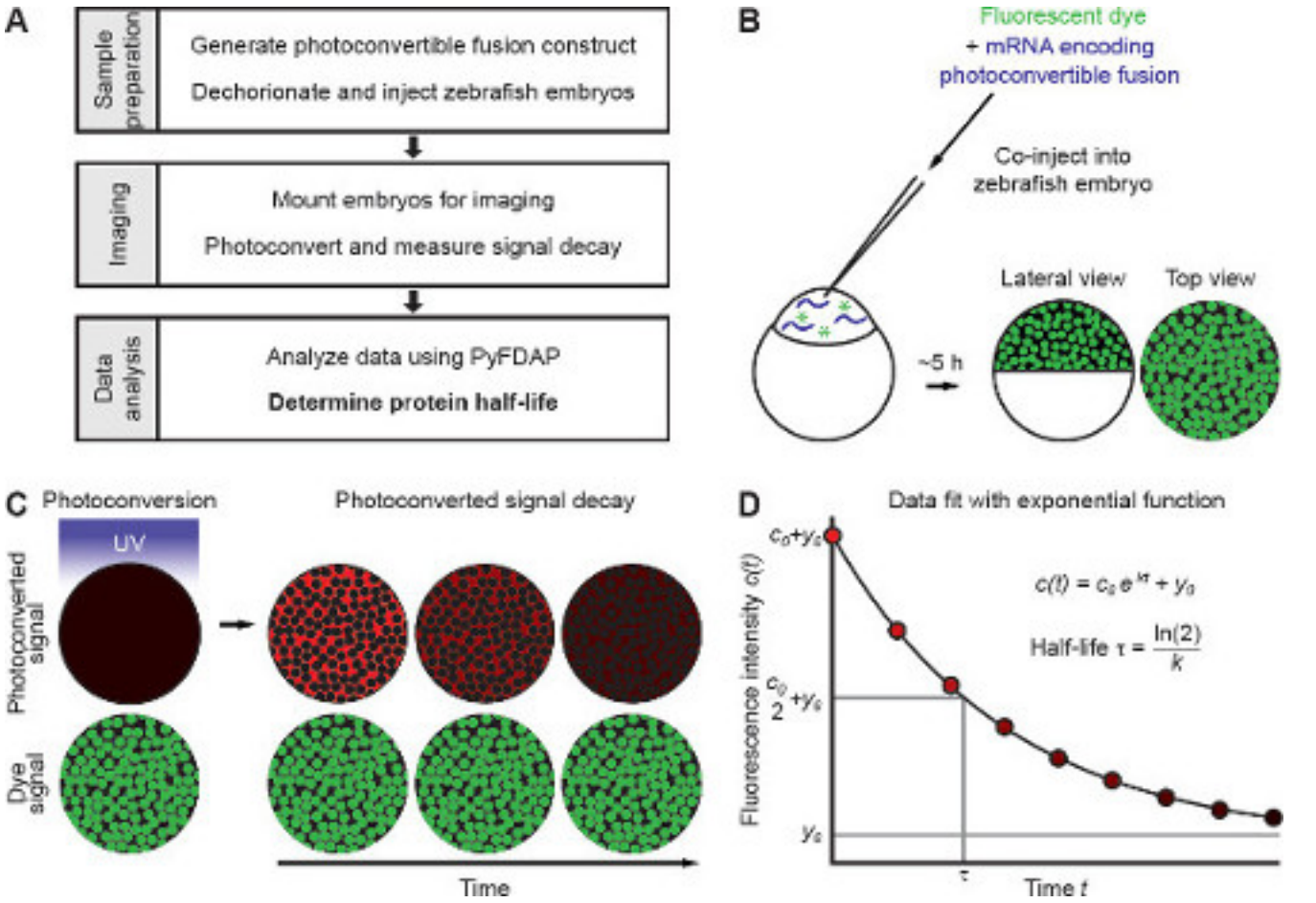

Figure 1. Fluorescence Decay After Photoconversion (FDAP) overview. (**A**) Workflow of an FDAP experiment. (**B**) Injection of mRNA and a fluorescent dye into a zebrafish embryo at the one-cell stage. Protein is produced from the mRNA as the embryo develops over about 5 hr prior to imaging. The dye labels cells (green circles). (**C**) The fusion protein is photoconverted using a UV pulse, and the decrease in the intensity of the photoconverted signal over time is monitored. (**D**) The data are fitted with an exponentially decreasing function to obtain clearance rate constants (*k*) and half-lives (τ). Please click here to view a larger version of this figure.

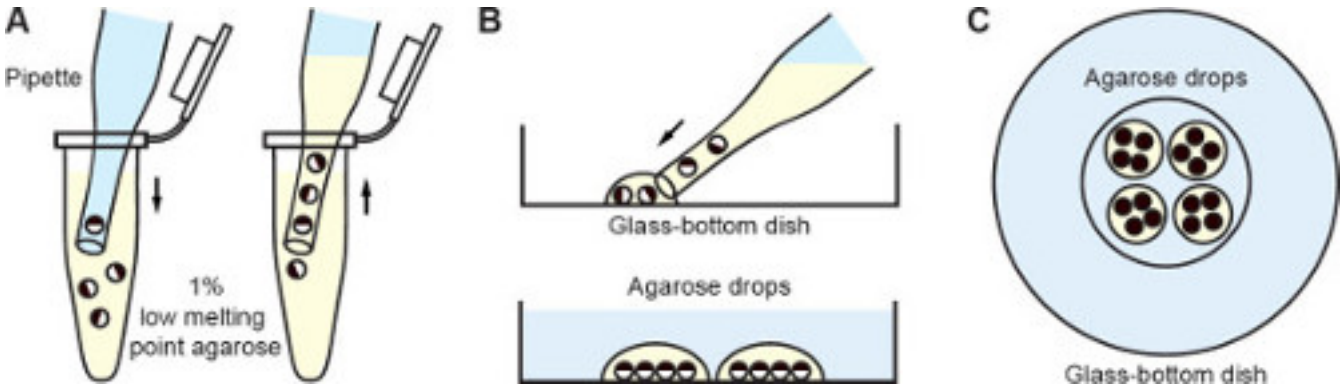

Figure 2. Mounting zebrafish embryos for FDAP experiments. (**A**) Zebrafish embryos (blastoderm = white, yolk = black) are transferred from embryo medium (blue) into melted agarose (yellow). (**B**) Embryos and agarose are placed onto the cover glass of a glass-bottom dish. Embryos are then manually positioned so that the animal pole faces the cover glass. A cross-section of a glass-bottom dish is shown. (**C**) Schematic overview of a glass-bottom dish with several agarose drops containing four embryos each (view looking down into the dish). Please click here to view a larger version of this figure.

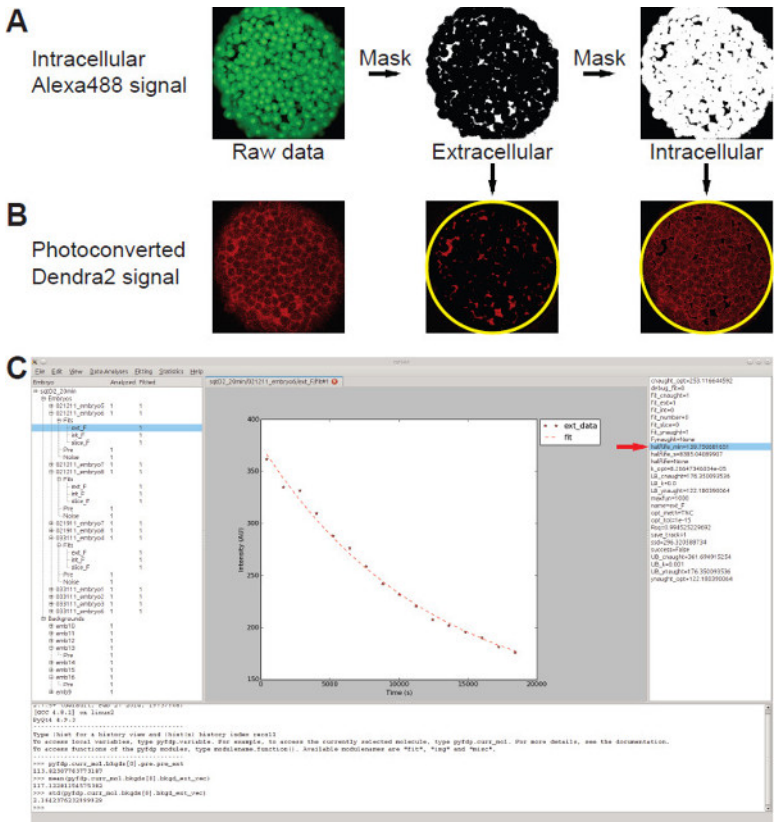

Figure 3. Data analysis using PyFDAP. (**A**) PyFDAP uses the Otsu thresholding algorithm[35] to generate intra- and extracellular masks from the intracellular Alexa488 signal (green). (**B**) Photoconverted signal (red) from an embryo expressing a secreted Dendra2 fusion protein (Squint-Dendra2[19]). Average extra- and intracellular fluorescence intensities were calculated using the masks shown in (A). The space outside of the embryo was excluded from these calculations by discarding pixels outside of the yellow circle. (**C**) PyFDAP screenshot displaying extracellular intensity data from an FDAP experiment (black circles) fitted with an exponentially decreasing function (red dashed line). The extracellular half-life is indicated by the red arrow. Please click here to view a larger version of this figure.

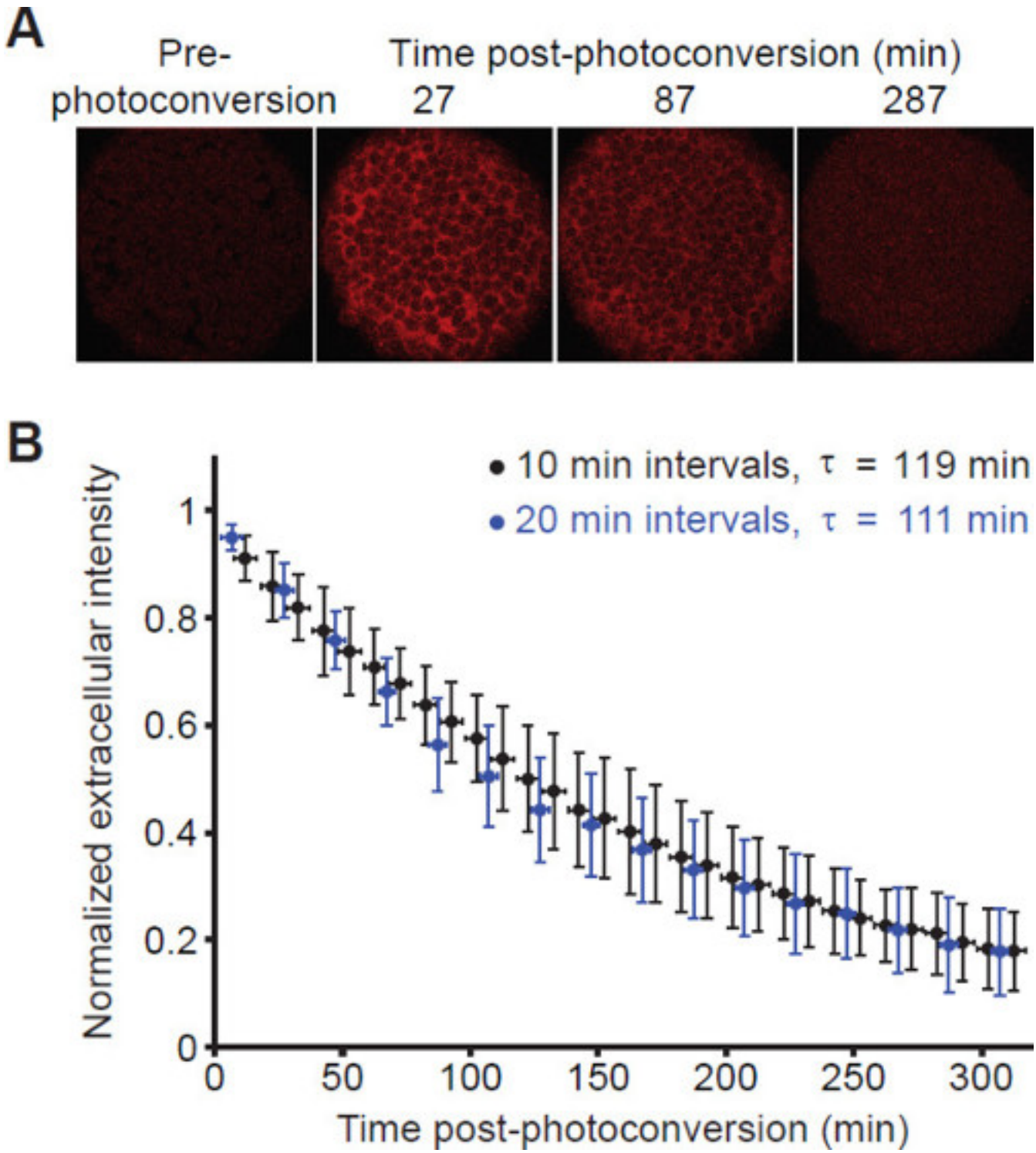

Figure 4. Representative FDAP results. (**A**) A representative embryo expressing secreted Squint-Dendra2 just prior to photoconversion (far left) and 27, 87, and 287 min post-photoconversion. (**B**) To control for photobleaching and inadvertent photoconversion (see Section 5), experiments with 10 or 20 min intervals were performed (data from Müller *et al.,* 2012[19]). In PyFDAP, extracellular intensity profiles were generated, fitted with exponentially decreasing functions, and normalized by subtracting the fitted y_0 value from each data point and dividing by the fitted c_0 value. Data from the 10 min (black, n = 11) and 20 min (blue, n = 12) interval experiments were then averaged, respectively. Error bars indicate standard deviation. Please click here to view a larger version of this figure.

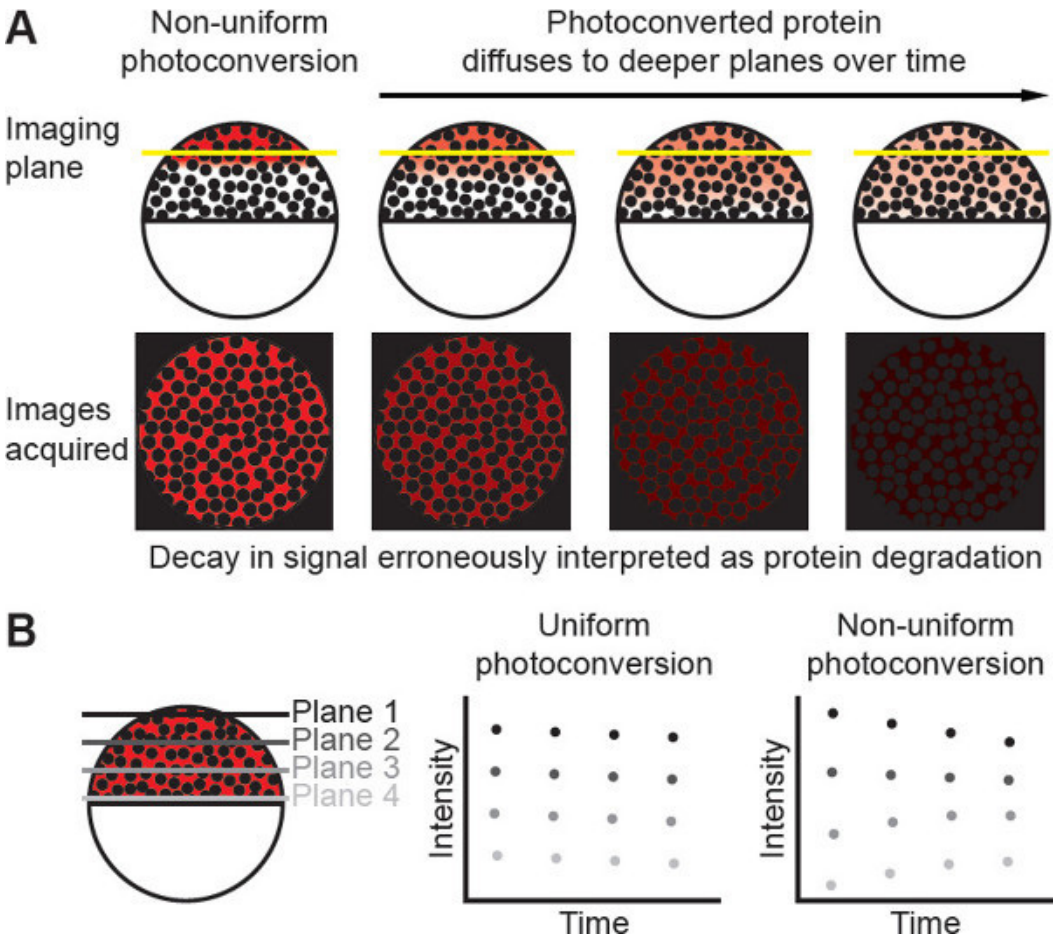

Figure 5. Assessing photoconversion uniformity. (**A**) Non-uniform photoconversion of an extracellular protein can lead to an erroneously short apparent half-life if photoconverted protein diffuses into deeper planes over time. (**B**) To determine whether photoconversion is uniform, a z-stack covering most of the blastoderm is acquired at several time points post-photoconversion. Fluorescence intensity will increase in deeper planes over time if photoconversion was non-uniform (note that light scattering causes deeper planes to appear dimmer than higher planes). Please click here to view a larger version of this figure.

Discussion

The success of an FDAP experiment relies on the generation of a functional photoconvertible fusion protein. Tagging a protein can affect its biological activity and/or biophysical properties, including its localization, solubility, and stability[36-41]. Be prepared to test the activity of several different fusion constructs in order to find one that is active. We have found that changing the position of the photoconvertible protein relative to the protein of interest or using longer linkers (*e.g.*, using the amino acid sequence LGDPPVAT[19]) can enhance the activity of the fusion protein. In the case of signaling proteins, the activity of the fusion protein can be determined by testing its ability to induce expression of target genes[19]. qRT-PCR or *in situ* hybridization provide good readouts of target gene expression[19]. Note that the protocol described here is designed to determine the stability of proteins in the early zebrafish embryo and would require modification to assess protein stability in other contexts.

The green-to-red photoconvertible protein Dendra2[27] has been used successfully in zebrafish FDAP experiments[19] (**Figure 4**), but other options are available[26,42]. To avoid potential artifacts due to aggregation of the fusion protein, choose a monomeric photoconvertible protein. Photoactivatible proteins can also be used in FDAP assays[20-22,26].

Before performing an FDAP experiment, several aspects of the protocol need to be optimized. Inject different amounts of mRNA to determine the lowest amount that provides useable signal after photoconversion; ~50 pg mRNA is a good starting amount. In order to generate meaningful compartmental masks (**Figure 3**), the Alexa488 signal must be bright enough to compete against the signal from the non-photoconverted fusion protein that is constantly produced from the injected mRNA; inject between 0.2 and 4 ng of Alexa488-dextran to find the optimal amount of fluorescent dye. Find the optimal post-conversion imaging conditions and use the same conditions for all experiments with a given construct. Use good quantitative imaging practices[43], and choose an appropriate dynamic range to avoid saturated pixels in the red channel. Determine the appropriate imaging interval for each fusion protein. Proteins with very short half-lives may require more frequent imaging over a shorter total time period. Establish the optimal photoconversion technique based on the organism and photoconvertible protein used. We describe one robust photoconversion method using a mercury arc lamp in step 3.5, but Dendra2 can also be photoconverted with a 405 [33] or 488 nm laser[27].

One limitation of this FDAP protocol is that overexpression of the protein of interest is required. Overexpression could affect protein stability, for instance, through abnormal expression of other genes that modify the protein's clearance kinetics[14,44]. If the protein of interest is a signaling molecule, consider performing experiments in the presence of a signaling inhibitor to determine whether blocking expression of target genes affects protein stability. In the future, it may be possible to generate transgenic embryos expressing photoconvertible fusions under the control of endogenous expression elements[45-50]. If transgenic embryos produce sufficient signal, FDAP experiments in a non-overexpression context are conceivable, perhaps using light-sheet microscopy to observe fluorescence decrease in the entire embryo[51].

Possible further applications of FDAP include investigating the mechanisms that regulate protein stability by examining the effects of different perturbations (*e.g.*, expression of putative proteases) or protein modifications (*e.g.*, phosphorylation) on stability. For example, the factors controlling the extracellular stability of Squint are currently unknown. Many secreted developmental signals are internalized by cells[52-55], which could contribute to the clearance of Squint and other ligands from the extracellular space. FDAP experiments in which internalization is blocked might provide information about mechanisms controlling extracellular protein clearance.

In contrast to conventional assays for measuring protein stability[15], FDAP offers a microscopy-based alternative in which the clearance of proteins can be monitored over time within living organisms. Similar methods have been used to monitor protein clearance in model systems other than zebrafish embryos[20-23]. This FDAP protocol has the potential to be adapted to determine the half-life of any taggable protein in biological systems where live imaging is feasible.

Disclosures

The authors have no conflicts to disclose.

Acknowledgements

The authors would like to thank Jeffrey Farrell, James Gagnon, and Jennifer Bergmann for comments on the manuscript. KWR was supported by the National Science Foundation Graduate Research Fellowship Program during the development of the FDAP assay. This work was supported by grants from the NIH to AFS and by grants from the German Research Foundation (Emmy Noether Program), the Max Planck Society, and the Human Frontier Science Program (Career Development Award) to PM.

References

1. Schwanhäusser, B., *et al.* Global quantification of mammalian gene expression control. *Nature.* **473** (7347), 337—342, doi: 10.1038/nature10098 (2011).
2. Boisvert, F. M., et al. A Quantitative Spatial Proteomics Analysis of Proteome Turnover in Human Cells. *Molecular & Cellular Proteomics.* **11** (3), M111.011429, doi: 10.1074/mcp.M111.011429 (2012).
3. Belle, A., Tanay, A., Bitincka, L., Shamir, R., & O'Shea, E. K. Quantification of protein half-lives in the budding yeast proteome. *Proceedings of the National Academy of Sciences of the United States of America.* **103** (35), 13004—13009, doi: 10.1073/pnas.0605420103 (2006).
4. Eden, E., *et al.* Proteome Half-Life Dynamics in Living Human Cells. *Science.* **331** (6018), 764—768, doi: 10.1126/science.1199784 (2011).
5. Parry, D. H., & O'Farrell, P. H. The schedule of destruction of three mitotic cyclins can dictate the timing of events during exit from mitosis. *Current Biology.* **11** (9), 671—683 (2001).
6. Holloway, S. L., Glotzer, M., King, R. W., & Murray, A. W. Anaphase is initiated by proteolysis rather than by the inactivation of maturation-promoting factor. *Cell.* **73** (7), 1393—1402 (1993).
7. Dharmasiri, N., & Estelle, M. Auxin signaling and regulated protein degradation. *Trends Plant Sci.* **9** (6), 302—308, doi: 10.1016/j.tplants.2004.04.003 (2004).
8. MacDonald, B. T., Tamai, K., & He, X. Wnt/beta-catenin signaling: components, mechanisms, and diseases. *Developmental Cell.* **17** (1), 9—26, doi: 10.1016/j.devcel.2009.06.016 (2009).
9. Chen, X., *et al.* Processing and turnover of the Hedgehog protein in the endoplasmic reticulum. *The Journal of Cell Biology.* **192** (5), 825—838, doi: 10.1083/jcb.201008090 (2011).
10. Elmore, S. Apoptosis: A Review of Programmed Cell Death. *Toxicologic Pathology.* **35** (4), 495—516, doi: 10.1080/01926230701320337 (2007).
11. Yi, J. J., & Ehlers, M. D. Emerging Roles for Ubiquitin and Protein Degradation in Neuronal Function. *Pharmacological Reviews.* **59** (1), 14—39, doi: 10.1124/pr.59.1.4 (2007).
12. Rubinsztein, D. C. The roles of intracellular protein-degradation pathways in neurodegeneration. *Nature.* **443** (7113), 780—786, doi: 10.1038/nature05291 (2006).
13. Müller, P., & Schier, A. F. Extracellular Movement of Signaling Molecules. *Developmental Cell.* **21** (1), 145—158, doi: 10.1016/j.devcel.2011.06.001 (2011).
14. Eldar, A., Rosin, D., Shilo, B.-Z., & Barkai, N. Self-enhanced ligand degradation underlies robustness of morphogen gradients. *Developmental Cell.* **5** (4), 635—646, doi: 10.1016/S1534-5807(03)00292-2 (2003).
15. Zhou, P. Determining protein half-lives. *Methods In Molecular Biology (Clifton, N.J.).* **284**, 67—77, doi: 10.1385/1-59259-816-1:067 (2004).
16. Woodside, K. H. Effects of cycloheximide on protein degradation and gluconeogenesis in the perfused rat liver. *Biochim Biophys Acta.* **421** (1), 70—79, doi: 10.1016/0304-4165(76)90170-7 (1976).
17. Schimke, R. T., & Doyle, D. Control of enzyme levels in animal tissues. *Annual Review of Biochemistry.* **39**, 929—976, doi: 10.1146/annurev.bi.39.070170.004433 (1970).
18. Kenney, F. T. Turnover of rat liver tyrosine transaminase: stabilization after inhibition of protein synthesis. *Science.* **156** (3774), 525—528 (1967).

19. Müller, P., *et al.* Differential Diffusivity of Nodal and Lefty Underlies a Reaction-Diffusion Patterning System. *Science.* **336** (6082), 721—724, doi: 10.1126/science.1221920 (2012).
20. Kiuchi, T., Nagai, T., Ohashi, K., & Mizuno, K. Measurements of spatiotemporal changes in G-actin concentration reveal its effect on stimulus-induced actin assembly and lamellipodium extension. *The Journal of Cell Biology.* **193** (2), 365—380, doi: 10.1083/jcb.201101035.dv (2011).
21. Plachta, N., Bollenbach, T., Pease, S., Fraser, S. E., & Pantazis, P. Oct4 kinetics predict cell lineage patterning in the early mammalian embryo. *Nature Cell Biology.* **13** (2), 117—123, doi: 10.1038/ncb2154 (2011).
22. Drocco, J. A., Grimm, O., Tank, D. W., & Wieschaus, E. Measurement and Perturbation of Morphogen Lifetime: Effects on Gradient Shape. *Biophys J.* **101** (8), 1807—1815, doi: 10.1016/j.bpj.2011.07.025 (2011).
23. Zhang, L., *et al.* Method for real-time monitoring of protein degradation at the single cell level. *BioTechniques.* **42** (4), 446—450, doi: 10.2144/000112453 (2007).
24. Miyawaki, A. Proteins on the move: insights gained from fluorescent protein technologies. *Nat Rev Mol Cell Biol.* **12** (10), 656—668, doi: 10.1038/nrm3199 (2011).
25. Pantazis, P., & Supatto, W. Advances in whole-embryo imaging: a quantitative transition is underway. *Nat Rev Mol Cell Biol.* **15** (5), 327—339, doi: 10.1038/nrm3786 (2014).
26. Lukyanov, K. A., Chudakov, D. M., Lukyanov, S., & Verkhusha, V. V. Innovation: Photoactivatable fluorescent proteins. *Nat Rev Mol Cell Biol.* **6** (11), 885—891, doi: 10.1038/nrm1741 (2005).
27. Gurskaya, N. G., *et al.* Engineering of a monomeric green-to-red photoactivatable fluorescent protein induced by blue light. *Nature Biotechnology.* **24** (4), 461—465, doi: 10.1038/nbt1191 (2006).
28. Zou, J., & Wei, X. Transplantation of GFP-expressing Blastomeres for Live Imaging of Retinal and Brain Development in Chimeric Zebrafish Embryos. *Journal of Visualized Experiments.* **41**, doi: 10.3791/1924 (2010).
29. Yuan, S., & Sun, Z. Microinjection of mRNA and Morpholino Antisense Oligonucleotides in Zebrafish Embryos. *Journal of Visualized Experiments.* **27**, doi: 10.3791/1113 (2009).
30. Rosen, J. N., Sweeney, M. F., & Mably, J. D. Microinjection of Zebrafish Embryos to Analyze Gene Function. *Journal of Visualized Experiments.* **25**, doi: 10.3791/1115 (2009).
31. Kimmel, C. B., Ballard, W. W., Kimmel, S. R., Ullmann, B., & Schilling, T. F. Stages of embryonic development of the zebrafish. *Developmental Dynamics.* **203** (3), 253—310, doi:10.1002/aja.1002030302 (1995).
32. McKinney, S. A., Murphy, C. S., Hazelwood, K. L., Davidson, M. W., & Looger, L. L. A bright and photostable photoconvertible fluorescent protein. *Nature Methods.* **6** (2), 131—133, doi: 10.1038/nmeth.1296 (2009).
33. Dempsey, W. P., Qin, H., & Pantazis, P. *In Vivo* Cell Tracking Using PhOTO Zebrafish. *Methods in Molecular Biology.* **1148** (Chapter 14), 217—228, doi: 10.1007/978-1-4939-0470-9_14 (2014).
34. Schier, A. F. Nodal Morphogens. *Cold Spring Harbor Perspectives in Biology.* **1** (5), a003459—a003459, doi: 10.1101/cshperspect.a003459 (2009).
35. Otsu, N. A threshold selection method from gray-level histograms. *IEEE Trans Syst Man Cybern.* **9** (1), 62-66. doi: 10.1109/TSMC.1979.4310076 (1979).
36. Pédelacq, J.-D., Cabantous, S., Tran, T., Terwilliger, T. C., & Waldo, G. S. Engineering and characterization of a superfolder green fluorescent protein. *Nature Biotechnology.* **24** (1), 79—88, doi: 10.1038/nbt1172 (2005).
37. Swulius, M. T., & Jensen, G. J. The Helical MreB Cytoskeleton in Escherichia coli MC1000/pLE7 Is an Artifact of the N-Terminal Yellow Fluorescent Protein Tag. *Journal of Bacteriology.* **194** (23), 6382—6386, doi: 10.1128/JB.00505-12 (2012).
38. Landgraf, D., Okumus, B., Chien, P., Baker, T. A., & Paulsson, J. Segregation of molecules at cell division reveals native protein localization. *Nature Methods.* **9** (5), 480—482, doi: 10.1038/nmeth.1955 (2012).
39. Stadler, C., *et al.* Immunofluorescence and fluorescent-protein tagging show high correlation for protein localization in mammalian cells. *Nature Methods.* **10** (4), 315—323, doi: 10.1038/nmeth.2377 (2013).
40. Quattrocchio, F. M., Spelt, C., & Koes, R. Transgenes and protein localization: myths and legends. *Trends Plant Sci.* **18** (9), 473—476, doi: 10.1016/j.tplants.2013.07.003 (2013).
41. Morimoto, Y. V., Kojima, S., Namba, K., & Minamino, T. M153R Mutation in a pH-Sensitive Green Fluorescent Protein Stabilizes Its Fusion Proteins. *PLoS ONE.* **6** (5), e19598, doi: 10.1371/journal.pone.0019598.t002 (2011).
42. Shaner, N. C., Steinbach, P. A., & Tsien, R. Y. A guide to choosing fluorescent proteins. *Nature Methods.* **2** (12), 905—909, doi: 10.1038/nmeth819 (2005).
43. Waters, J. C. Accuracy and precision in quantitative fluorescence microscopy. *The Journal of Cell Biology.* **185** (7), 1135—1148, doi: 10.1083/jcb.200903097 (2009).
44. Moll, U. M., & Petrenko, O. The MDM2-p53 interaction. *Mol Cancer Res.* **1** (14), 1001—1008 (2003).
45. Auer, T. O., Duroure, K., De Cian, A., Concordet, J. P., & Del Bene, F. Highly efficient CRISPR/Cas9-mediated knock-in in zebrafish by homology-independent DNA repair. *Genome Research.* **24** (1), 142—153, doi: 10.1101/gr.161638.113 (2014).
46. Bedell, V. M., *et al. In vivo* genome editing using a high-efficiency TALEN system. *Nature.* **491** (7422), 114—118, doi: 10.1038/nature11537 (2012).
47. Hruscha, A., *et al.* Efficient CRISPR/Cas9 genome editing with low off-target effects in zebrafish. *Development.* **140** (24), 4982—4987, doi: 10.1242/dev.099085 (2013).
48. Hwang, W. Y., *et al.* Heritable and Precise Zebrafish Genome Editing Using a CRISPR-Cas System. *PLoS ONE.* **8** (7), e68708, doi: 10.1371/journal.pone.0068708.s005 (2013).
49. Hwang, W. Y., *et al.* Heritable and Precise Zebrafish Genome Editing Using a CRISPR-Cas System. *PLoS ONE.* **8** (7), e68708, doi: 10.1371/journal.pone.0068708 (2013).
50. Zu, Y., *et al.* TALEN-mediated precise genome modification by homologous recombination in zebrafish. *Nature Methods.* **10** (4), 329—331, doi: 10.1038/nmeth.2374 (2013).
51. Keller, P. J., Schmidt, A. D., Wittbrodt, J., & Stelzer, E. H. K. Reconstruction of Zebrafish Early Embryonic Development by Scanned Light Sheet Microscopy. *Science.* **322** (5904), 1065—1069, doi: 10.1126/science.1162493 (2008).
52. Blanchet, M. H., *et al.* Cripto Localizes Nodal at the Limiting Membrane of Early Endosomes. *Science Signaling.* **1** (45), ra13—ra13, doi: 10.1126/scisignal.1165027 (2008).
53. Jullien, J., & Gurdon, J. Morphogen gradient interpretation by a regulated trafficking step during ligand-receptor transduction. *Genes & Development.* **19** (22), 2682—2694, doi: 10.1101/gad.341605 (2005).

54. Incardona, J. P., *et al.* Receptor-mediated endocytosis of soluble and membrane-tethered Sonic hedgehog by Patched-1. *Proceedings of the National Academy of Sciences of the United States of America.* **97** (22), 12044—12049, doi: 10.1073/pnas.220251997 (2000).
55. Scholpp, S., & Brand, M. Endocytosis Controls Spreading and Effective Signaling Range of Fgf8 Protein. *Current Biology.* **14** (20), 1834—1841, doi: 10.1016/j.cub.2004.09.084 (2004).
56. Bläßle, A., & Müller, P. PyFDAP: Automated analysis of Fluorescence Decay After Photoconversion (FDAP) experiments. *Bioinformatics*. In Press, doi: 10.1093/bioinformatics/btu735 (2014).

Quantitative diffusion measurements using the open-source software PyFRAP

Alexander Bläßle[1], Gary Soh[1], Theresa Braun[1,2], David Mörsdorf[1], Hannes Preiß[1], Ben Jordan[3], and Patrick Müller[1,*]

[1]Friedrich Miescher Laboratory of the Max Planck Society, Tübingen, Germany
[2]Present address: University of Konstanz, Konstanz, Germany
[3]Department of Organismic and Evolutionary Biology, Harvard University, Cambridge, USA

[*]Correspondence to: patrick.mueller@tuebingen.mpg.de (P.M.)

Abstract

Nearly all biological processes require the diffusion of macromolecules. Fluorescence Recovery After Photobleaching (FRAP) and inverse FRAP (iFRAP) assays have been extensively used to assess the mobility of fluorescent molecules. These assays measure diffusion by monitoring the return of fluorescence in bleached regions (FRAP), or the dissipation of fluorescence from photoconverted regions (iFRAP). However, current analysis methods for FRAP and iFRAP data suffer from simplified assumptions about sample geometry, bleaching/photoconversion inhomogeneities, and the underlying reaction-diffusion kinetics; furthermore, analysis software is often difficult to implement. To address these shortcomings, we developed the software "PyFRAP" (available at https://mueller-lab.github.io/PyFRAP), which fits numerical simulations on realistic three-dimensional models to FRAP/iFRAP data and accounts for bleaching/photoactivation inhomogeneities. Using PyFRAP we determined the diffusivities of fluorescent dextrans and proteins spanning two orders of magnitude in molecular weight. We measured the tortuous effects that cell-like obstacles exert on effective diffusivity and show that reaction kinetics can be accurately accounted for by model selection. These applications demonstrate the utility of the open-source software PyFRAP, which can be widely adapted as a new extensible standard for FRAP analysis.

Introduction

The diffusion of molecules is important for almost any process across all scales of biological organization, from transcription factors finding their targets on DNA to signaling molecules spreading through tissues during development and homeostasis[1,2]. The biological function of a molecule is affected by its action range and therefore its mobility, but effective diffusion of molecules moving through complex tissues is difficult to measure quantitatively. More than 40 years ago, Poo & Cone[3] and Liebman & Entine[4] developed a method to assess the diffusivities of fluorescent molecules. In these Fluorescence Recovery After Photobleaching (FRAP) experiments, the fluorescence of molecules in a small region of the sample is bleached by exposure to a strong laser pulse. The dynamics of fluorescence recovery in the bleached region can then be used to infer the mobility of the fluorescent molecules (Fig. 1a). Inverted FRAP (iFRAP) assays have recently been developed as an extension of FRAP experiments[5–8], which eliminate the often harsh bleaching conditions used in FRAP experiments. iFRAP assays utilize photoconvertible molecules that can be induced to alter their fluorescence excitation/emission properties after

exposure to "photoconverting" light. In iFRAP experiments, the spread of signal from a small photoconverted domain into the neighboring regions of the sample is monitored over time and thus represents an experimental mirror image of FRAP (Fig. 1b).

Diffusion coefficients are commonly extracted from FRAP experiments by fitting analytical solutions computed from theoretical models to the measured recovery curves[9–16], and a few simulation-based analysis methods have been developed[17–19]. However, these current approaches rely on several assumptions that are not necessarily accurate. First, most current methods reduce the FRAP analysis to one-dimensional or two-dimensional simplifications[9–19], often assuming that the fluorescent pool is infinitely large[9–12,14,15], or ignoring more complex geometries of biological samples that could play important roles in molecule movement (Fig. 1c). Indeed, recent studies have argued that geometry is crucial for dynamic biological processes[20,21], and must be taken into account for accurate analysis of FRAP data (Fig. 1d).

Second, the bleaching process in FRAP experiments is often inaccurately modeled. Bleaching is posited to be homogenous or to follow a Gaussian distribution throughout bleached circular or rectangular regions, while the molecules outside of the bleached region are assumed to remain unbleached[9–11,13–16]. However, molecules diffusing during the bleaching process can create inhomogeneities both inside and outside of the bleached region; moreover, a delay between bleaching and the start of the recovery measurement can lead to further inhomogeneities (Fig. 1c). Incorrect assumptions about the bleaching process can thus lead to a severe misestimation of diffusion coefficients[12,22–25] (Fig. 1e).

Third, *in vivo* FRAP experiments can be strongly influenced by additional reaction kinetics such as production or degradation of fluorescent molecules, which can contribute to the observed recovery curve (Fig. 1c). However, this is mostly neglected in classical FRAP analysis models and can lead to erroneous diffusion estimates (Fig. 1f)[9–15].

To address these shortcomings, we developed the versatile Python-based FRAP analysis software "PyFRAP". To facilitate data analysis, PyFRAP is equipped with an intuitive graphical user interface (GUI, Fig. 2a), which gives users without a computational background access to a sophisticated FRAP data analysis work flow from image analysis to statistical model comparison methods (Fig. 2b). PyFRAP applies the first post-bleach image as initial condition (Fig. 2c), and simulates the FRAP experiment using a finite volume scheme in realistic two- or three-dimensional experiment geometries (Fig. 2d,e); the solution from this numerical simulation is then fitted to the experimental data. Furthermore, PyFRAP can accurately account for both uniform production and degradation during FRAP experiments. PyFRAP saves all analyzed data and settings in a logical data structure that can be shared with collaborators or reused for later analyses (Fig. 2f). The software is freely available at https://mueller-lab.github.io/PyFRAP, and the open-source environment allows for rapid expansion through collaborative work[26] to adjust analysis methods to the users' needs.

To demonstrate the utility of PyFRAP, we conducted several typical *in vitro* and *in vivo* FRAP experiments (Supplementary Fig. 1). We found that PyFRAP accurately determined the diffusion coefficients of fluorescent molecules ranging from 3 to 500 kDa in both artifical and biological contexts. In contrast to currently available software, PyFRAP's flexible initial conditions also allow analysis of iFRAP experiments, producing results comparable to FRAP. We used PyFRAP to measure the influence that obstacles such as cells exert on the movement of diffusing molecules, and found that such interactions decrease diffusivity by about one third. Moreover, PyFRAP provides accurate modeling of reaction kinetics, including production and degradation. Finally, to test the impact of extracellular binding on protein diffusivity, we measured the diffusion of signaling molecules in living zebrafish embryos. We found that the effective diffusivity was reduced to about a tenth of its predicted value, in agreement with hindered diffusion models postulating interactions of embryonic signaling molecules with diffusion regulators[20,27]. Together, our analyses highlight how detailed examination of FRAP data can be used to determine the contribution of individual factors to the movement of molecules in controlled artificial and biological contexts[28].

Results

PyFRAP: A versatile FRAP/iFRAP analysis package

Current FRAP analysis methods often make simplified assumptions about FRAP experimental conditions to aid in the derivation of analytical solutions[9–14,16], and to facilitate numerical simulations[18,19]. Such assumptions include reducing complex sample geometries to lower dimensions, idealizing the initial bleaching profile, or ignoring additional reaction kinetics potentially underlying fluorescence recovery (Fig. 1c), which can lead to erroneous diffusion estimates (Fig. 1d-f). To tackle these shortcomings, we developed "PyFRAP": PyFRAP numerically simulates FRAP experiments in realistic three-dimensional geometries using an interpolation of the first post-bleach image as initial condition. This simulation is then fitted to the experimental data, incorporating reaction kinetics such as uniform production and degradation.

PyFRAP is an open-source Python-based FRAP analysis software that runs on the major operating systems Microsoft Windows, Mac OSX, and Linux. Over the past 20 years, Python has become the standard programming language for scientific research due to the availability of versatile add-on packages and its intuitive and simple syntax[29]. Building on the resourcefulness of Python, PyFRAP is based on commonly used packages such as PyQT, SciPy, and FiPy[30]. PyFRAP comes with an intuitive graphical user interface (GUI, Fig. 2a) and a fully documented application programming interface (API) allowing quick development of scripts or modifications of the PyFRAP code. PyFRAP's functionalities include sophisticated image processing functions useful for FRAP analysis, customizable geometry and analysis region definitions, a finite element PDE solver that simulates FRAP/iFRAP experiments with adjustable options, statistical tools for averaging and model comparison, and multiple plotting and input/output functions (see Materials and Methods, and Supplementary Texts 1-3 for details). To make the software easily accessible, dialog boxes ("software wizards") guide the users step-by-step through data import, image analysis, simulation, and fitting.

Integrated image analysis

We programmed PyFRAP to import image data from most common microscope formats (.tif, .lsm, and .czi) through its built-in Fiji[31] interface. Users can define arbitrary regions of interests (ROIs) that are then used for image analysis, simulation, and fitting (Supplementary Fig. 2a). In some cases, the imaged sample is larger than the field of view; the concentration of molecules in regions outside of the image can be estimated from selected areas in the first image of the recovery image series (Supplementary Fig. 2b). PyFRAP corrects uneven illumination artifacts by normalization using pre-bleach images or using a correction matrix computed from a secondary data set[32–34] (Supplementary Fig. 2c, see Materials and Methods for details). To avoid numerical instabilities, PyFRAP allows the user to smooth or denoise the image data using a Gaussian or median filter (see Materials and Methods for details, Supplementary Table 1, Supplementary Fig. 3).

Numerical simulations in realistic geometries using accurate initial conditions

FRAP and iFRAP experiments have been performed in a variety of contexts, from the cigar-shaped *Drosophila* embryo and the relatively flat *Drosophila* wing disc to the dome-shaped pre-gastrula stage zebrafish embryo[8,27,35]. These structures have distinct geometries that could impact fluorescence recovery. In fact, we found that simplifying the 3D zebrafish embryo to a 2D disc can frequently lead up to a more than 200% error in estimated diffusion coefficients (Fig. 1d).

In PyFRAP, users can define arbitrary two- and three-dimensional geometries using Gmsh[36] or CAD STereoLithography (.stl) files that are then spatially discretized into tetrahedral meshes by Gmsh in combination with TetGen[37]. PyFRAP provides various meshing options, such as local mesh refinements,

boundary layer meshes, and attractor meshes, allowing users to adapt the mesh to experimental details (see Fig. 2 and Supplementary Fig. 4 for example geometries and meshes).

In current FRAP analysis methods, the initial condition of the FRAP experiment is often simplified to a simple rectangular function or a Gaussian profile[9,10,12–16,38–40]. However, light scattering, imperfect bleaching and diffusion during the bleaching process can lead to more complex bleaching profiles and thus need to be considered during FRAP analysis to avoid misestimation of diffusion coefficients[22,23,28,41]. To overcome this issue, PyFRAP's initial conditions are given by a bilinear interpolation between pixels of the first post-bleaching image, closely resembling initial experimental bleaching profiles and concentration distributions (Fig. 2c).

Finally, in contrast to most current FRAP analysis methods[9–16,39,40], PyFRAP does not fit a mathematical expression based on simplified assumptions to the data; instead, PyFRAP uses FiPy[30] to simulate the experiment numerically, resulting in a solution that incorporates the realistic three-dimensional geometry and initial conditions (Supplementary Fig. 4). The numerical simulation is then fitted to the FRAP data by minimizing the sum of squared differences using classical optimization algorithms[42–44] (see Materials and Methods for details).

Accounting for reaction kinetics

In typical FRAP and iFRAP experiments, a protein of interest is tagged with a fluorescent protein and expressed within a tissue. In such an experiment, the fusion protein is often actively produced at the same time that FRAP is carried out; additionally, fusion proteins undergo degradation over time. Depending on how the fusion protein is expressed (promoter-driven expression, mRNA injection, etc.), its degradation kinetics, and the timescale of the FRAP/iFRAP experiment, production and degradation can dramatically influence recovery curves. Ignoring reaction kinetics in FRAP experiments could therefore lead to erroneous diffusion coefficient estimates. Indeed, recovery curves with pure diffusion fitted to a simulated reaction-dominant data set often resulted in more than 200% error in the estimated diffusion coefficients (Fig. 1f).

To ensure that the appropriate reaction kinetics are considered when analyzing FRAP data, PyFRAP is equipped with four models: 1) Pure diffusion, 2) diffusion with production, 3) diffusion with degradation, and 4) diffusion with production and degradation (see Materials and Methods for details). The model can be constrained with previous reaction rate measurements from assays such as Fluorescence Decay After Photoconversion[45,46]; alternatively, production and degradation rates can be directly obtained from fitting the FRAP data. In the "Statistical tools and model comparison" section below, we discuss tools to determine which approaches are most appropriate for a given data set.

Statistical tools and model comparison

An advantage of PyFRAP is its ability to assess FRAP data using multiple models of varying complexity. However, determining which model is appropriate for a given data set can be challenging. Choosing the incorrect model can lead to overfitting and potentially false diffusion coefficients[47]. The Akaike Information Criterion (AIC) is a statistical tool that can aid in model selection[48]. PyFRAP's implementation of the AIC allows users to compare the models mentioned above (see Section "Accounting for reaction kinetics") and determines the most likely model based on a relative weighted measure that includes both the model's log-likelihood and its degrees of freedom (i.e. the number of model parameters).

Moreover, PyFRAP provides several statistical tests (Supplementary Table 2) to assess differences between measurements and obtained fits, such as Student's t-test[49] for normally distributed data or the Mann-Whitney-U-test[50], which does not require normally distributed data. The Shapiro-Wilk-test can be used to assess whether the measured diffusivities follow a normal distribution[51] and whether application of Student's t-test or the Mann-Whitney-U-test is justified.

Data export

PyFRAP's object-oriented data structure (Fig. 2f) can be saved into serialized objects and easily loaded for further analysis or shared with collaborators. Loading a PyFRAP object automatically gives users access to all of PyFRAP's functionalities. Additionally, PyFRAP lets users visualize every aspect of PyFRAP's analysis work flow and save plots and images into publication-ready figures.

Benchmarking PyFRAP

To validate PyFRAP, we first determined whether it can recover true diffusion coefficients and reaction kinetics from simulated data. We used our previous in-house solution[20,27,52] based on the commercial programs MATLAB and Comsol Multiphysics to simulate 24 FRAP experiments with different reaction kinetics and diffusion coefficients. Using PyFRAP, the simulated data sets were fitted with all four possible reaction-diffusion models (see Section "Accounting for diffusion and reaction kinetics"). The maximum error between simulated and estimated diffusion coefficients was 10% (average error: 2%, Supplementary Table 3), demonstrating that PyFRAP recovers correct diffusion coefficients within the error tolerance of the numerical simulations.

Next, we tested whether PyFRAP's implementation of the AIC can correctly predict the model underlying the simulated data (Supplementary Table 3). When the data was simulated with models describing either pure diffusion, diffusion and degradation, or diffusion and production, the AIC predicted the correct underlying model. However, the AIC failed to retrieve the correct model for data sets that included diffusion combined with both production and degradation, and models with a lower degree of freedom were favored. Simulations involving diffusion, production and degradation can generate data effectively indistinguishable from data simulated with only diffusion and production or diffusion and degradation, explaining why the AIC cannot predict the correct model in this case.

To assess PyFRAP's performance in comparison with other available software packages based on analytical[15,39,40,53] or numerical[18,19,54] approaches (Supplementary Table 4), we used easyFRAP[40], Virtual FRAP[18], FrapCalc[39], simFRAP[19], and PyFRAP itself to analyze simulated FRAP experiments (Supplementary Text 2, Fig. 3). We simulated 18 experiments in which geometry, relative bleach window size, and diffusion coefficients differed. Simulations were conducted either in a simple circular two-dimensional domain or a complex three-dimensional zebrafish embryo-like geometry (Fig. 2e). FrapCalc and easyFRAP assume circular bleach windows[10,39,40]; to facilitate comparison, we therefore simulated FRAP experiments with circular bleach windows. Bleach window sizes comprised 5%, 10%, or 50% of the slice diameter, representing different proportions between fluorescent and bleached pools (Fig. 3b); simulations were performed with three biologically relevant diffusion coefficients: 10 μm^2/s, 50 μm^2/s, and 200 μm^2/s.

Simulation-based programs (PyFRAP, virtualFRAP, and simFRAP) generally provided better results than analytical solutions (easyFRAP and FrapCalc): FrapCalc and easyFRAP were either unable to determine diffusion coefficients, or provided diffusivities that were off by at least 20% for most experiments (Fig. 3c). Fast diffusion was challenging for all tested software. One reason for this is that fewer data points were recorded during the actual recovery process of fast diffusing molecules due to a fixed frame rate of 1 frame/s in the simulated test data sets, leading to larger errors; moreover, for fast diffusing processes errors from interpolating simulations onto images are more severe. The analytical software packages provided better results for the two-dimensional compared to three-dimensional geometries, while simulation-based approaches showed no clear trend regarding geometry. In terms of bleach window radius, the analytical solutions performed worst if the window diameter was 50% of the slice diameter. This effect might due to the assumption of an infinite pool of fluorescent molecules outside of the bleached region[10] – when the bleach window is very large, the pool of unbleached fluorescent molecules is small, which conflicts with the assumption of an infinite pool. In contrast, PyFRAP outperformed all current software packages and exhibited the smallest error between predicted and simulated diffusion coefficients (Fig. 3c).

Applications of PyFRAP to measure diffusion hindrance *in vitro* and *in vivo*

In vivo, it is thought that the overall movement of molecules is affected by binding interactions and by the presence of obstacles such as cells, resulting in a reduced effective diffusion coefficient of secreted proteins that move through tissues[20]. However, the effects of these interactions have not been rigorously tested experimentally. We therefore employed PyFRAP to examine the effects of tortuosity and binding partners on the effective diffusivity of dextrans and proteins in experimentally controlled *in vitro* geometries and in living zebrafish embryos.

Measuring pure diffusion

First, we measured diffusion coefficients of a wide range of differently sized molecules (Supplementary Table 5) in a simple *in vitro* context in the absence of binding partners or obstacles. We performed FRAP experiments with fluorophore-coupled dextrans ranging from 3 to 500 kDa (Fig. 4a-d, Supplementary Fig. 5), and compared the results with theoretical predictions and literature values. Fluorescence recovery in these *in vitro* experiments should be purely defined by diffusion, and the theoretical diffusivities D of spherical molecules can be calculated from their radii r based on the relationship $D \sim 1/r$ as postulated by the Einstein-Stokes equation (Supplementary Text 3). The diffusion coefficients determined by PyFRAP were in good agreement with literature values and theoretical predictions (Fig. 5a, Supplementary Table 6, Supplementary Table 7).

A variant of FRAP that allows to exclude reaction kinetics and thus decrease the number of unknown experimental parameters is iFRAP (Fig. 1b). To perform *in vitro* iFRAP experiments, we used the green-to-red photoconvertible protein Dendra2. Since photoconverting Dendra2 from green to red can also be interpreted as bleaching the original green fluorescence, measuring unconverted and converted protein distributions produces both FRAP and iFRAP experiments at the same time. To test whether PyFRAP correctly analyzes iFRAP data, we used the experimental FRAP and iFRAP sets independently and assessed whether the obtained diffusion values are equal (Fig. 4e-h, Fig. 5e). Indeed, in all ten experiments the difference between the two diffusivities per data set was on average 2.6 $\pm$ 1.5 μm^2/s (Fig. 5f). Using FRAP we measured a Dendra2 diffusivity of 52.9 $\pm$ 5.2 μm^2/s, and using iFRAP we obtained a similar value of 53.3 $\pm$ 3.1 μm^2/s (Fig. 5e).

Measuring diffusion hindrance *in vitro*

Next, we examined the effect of tortuosity on diffusion. In biological samples, molecules must move around obstacles such as cells and thus undergo tortuous movement. Here, we define tortuosity[55] as $\theta = D^*/D$, where D and D^* are the diffusion coefficients with and without obstacles, respectively. To assess the expected magnitude of tortuosity on altering effective diffusivity, we first performed numerical simulations of FRAP experiments with and without radial obstacles in two- and three-dimensional geometries. Radial obstacles were either placed regularly, randomly, or following a nearly ideal packing scheme, resulting in an extracellular volume fraction (EVF, i.e. the space available for molecules to diffuse) ranging from 72% down to 25% (Supplementary Fig. 6). These simulations demonstrated that recovery rates are slowed down as the EVF decreases (Fig. 5b, Supplementary Table 8). If the geometry is two-dimensional, an EVF of 25% results in an expected reduction in effective diffusivity of approximately 66%. In three-dimensional simulation experiments, we obtained a reduction of effective diffusion coefficients by 40% when the EVF was decreased to 38% (Supplementary Text 3).

To determine whether the presence of obstacles decreases effective diffusivity as predicted by our simulations, we performed FRAP assays *in vitro* with a fluorescein-coupled 70 kDa dextran (Fig. 4i,j) or recombinant GFP (Supplementary Fig. 7c,d) in the presence of polyacrylamide beads. Consistent with our predictions, recovery was slower in the presence of beads, and the effective diffusivity of fluorescein-dextran dropped from 24.1 $\pm$ 0.4 μm^2/s to 14.8 $\pm$ 0.5 μm^2/s, suggesting an EVF of 39% ($\theta = 61\%$)

(Fig. 5b,c, Supplementary Table 8, Supplementary Table 9). Similarly, for recombinant GFP effective diffusivity dropped by 18% (Fig. 5d, Supplementary Table 10, Supplementary Fig. 7a-d).

Measuring diffusion hindrance *in vivo*

To assess diffusion hindrance *in vivo*, we injected recombinant GFP protein into the extracellular space of living zebrafish embryos. We found that the effective diffusivity *in vivo* was 60% lower than for freely diffusing GFP, and 53% lower than in *in vitro* experiments with beads (Fig. 5d, Supplementary Table 10, Supplementary Fig. 7e,f). This suggests that tortuosity in zebrafish embryos is higher than in the *in vitro* bead assay. Importantly, we found similar diffusion coefficients of 36 μm^2/s *in vivo* for extracellularly injected recombinant GFP and secreted GFP constantly produced from injected mRNA, showing that PyFRAP can properly account for both diffusion and production (Fig. 5d, Supplementary Table 10, Supplementary Fig. 7g,h).

Finally, we examined the effects of binding interactions on effective diffusivity. GFP presumably does not experience significant binding interactions with extracellular molecules in zebrafish embryos, although its movement is affected by obstructions like cells and cellular extensions. In contrast, secreted signaling molecules are expected to interact with extracellular molecules such as receptors and extracellular matrix components[20]. To assess the effect that interactions with extracellular molecules might have on secreted signaling molecules, we injected mRNA encoding the TGFβ-superfamily member Squint fused to GFP into zebrafish embryos[27]. Squint-GFP is $\approx$1.5 times larger than GFP and according to the Einstein-Stokes equation (Supplementary Text 3) would be predicted to have a $\approx$1.14 times smaller diffusion coefficient than GFP (effective diffusivity D(GFP) = 36 μm^2/s, expected effective diffusivity D(Squint-GFP) = 31 μm^2/s). However, we measured an effective diffusion coefficient of $\approx$3 μm^2/s for Squint-GFP in living zebrafish embryos, approximately 90% lower than the predicted diffusion coefficient (Fig. 5d, Supplementary Table 10, Supplementary Fig. 7i,j). These findings are consistent with previous measurements[27] and with the idea that interactions with so far unidentified binding partners slow down the effective diffusion of embryonic signaling molecules like Squint-GFP[20,27].

Discussion

Although FRAP analyses have long been used to measure relative differences in mobilities between macromolecules, analysis tools to accurately and quantitatively determine effective diffusion coefficients from FRAP data are lacking. Current analysis tools impose several problematic simplifications including one- or two-dimensional reductions of complex three-dimensional geometries, idealized bleaching conditions, and the absence of important reaction kinetics, which can yield incorrect diffusion coefficients (Fig. 1). PyFRAP addresses these shortcomings by providing a simulation-based analysis that incorporates realistic geometries, bleaching conditions, and reaction kinetics.

We found that PyFRAP's data analysis pipeline is numerically reliable, recovered the correct diffusion coefficients and reaction kinetics, and additionally predicted the correct underlying reaction-diffusion models for simulated test data sets with known diffusion, production, and degradation parameters. PyFRAP consistently outperformed all other tested software packages, demonstrating its strength as a novel FRAP analysis method. Furthermore, PyFRAP was able to determine diffusion coefficients comparable to both theoretical and previously experimentally measured estimates for macromolecules with molecular weights ranging over two orders of magnitude.

Since PyFRAP can analyze data independently of any assumptions about the initial conditions, it is suitable to analyze both FRAP and iFRAP experiments. iFRAP has recently been developed as an alternative to FRAP due the increasing availability of photoconvertible proteins and allows ignoring reaction kinetics such as production. We performed tandem FRAP/iFRAP experiments to analyze the diffusion of the photoconvertible protein Dendra2 and found equal diffusion coefficients *in vitro* with both methods.

FRAP experiments are typically performed in tissues in which macromolecules need to move around cellular obstacles, resulting in slower fluorescence recovery. We were interested in how this tortuosity might affect diffusion coefficients estimated from FRAP experiments. First, we simulated FRAP experiments in two- and three-dimensional geometries introducing radial beads at different densities to vary the extracellular volume fraction (EVF). Our simulations show a strong correlation between tortuosity and effective diffusivity and agree with previous theoretical work including Monte-Carlo simulations and homogenization theory[55–58]. We then tested the predictions from these simulations with *in vitro* experiments using polyacrylamide beads to mimic cells. Compared to experiments without beads, the effective diffusion coefficient decreased by 39% (tortuosity $\theta = 61\%$) for 70 kDa fluorescein-dextran and 18% (tortuosity $\theta = 82\%$) for recombinant GFP. In living zebrafish embryos, effective diffusivity is much further reduced (Fig. 5d). This is unlikely due to a different viscosity of the extracellular medium *in vivo*, since free GFP diffusion is only marginally reduced in zebrafish embryos[20]. Instead, it is plausible that the complex geometries of real extracelluar environments – which include filopodia, extracellular matrix, and cavities that might act as dead end pores – could further increase tortuosity[55]. Moreover, most *in vivo* FRAP experiments are affected by biochemical reactions such as production and degradation of proteins, which must be taken into account for accurate diffusion coefficient estimates (Fig. 1). PyFRAP includes various models for different reaction kinetics and can accurately estimate diffusion coefficients from data that includes constant production and degradation.

PyFRAP measures effective diffusion, but due to its built-in PDE solver it could be extended in the future to consider spatially inhomogeneous kinetics and advective fluxes. While PyFRAP can simulate three-dimensional FRAP experiments, FRAP data is currently almost exclusively obtained from two-dimensional confocal microscopy. In recent years, the development of light-sheet microscopy made fast three-dimensional imaging with low phototoxicity feasible[59]. In the future, PyFRAP's image analysis tools could be extended to fit light-sheet microscopy data, which might provide deeper insights into the three-dimensional dynamics of molecule movement including convective flows or anomalous diffusion.

Materials and Methods

Data analysis implemented in PyFRAP

ROI selection

PyFRAP's image analysis depends on defining specific regions of interest (ROIs) for the experimental data and simulations. Users can define multiple different geometrical shapes of ROIs in three-dimensional space such as cylinders, prisms, and any kind of addition or subtraction between ROIs. The specified ROIs are then used for image analysis, estimating concentrations outside the field of view, evaluating the simulation, and fitting to the analyzed data. PyFRAP is equipped with an ROI manager and wizards for several standard sets of ROIs.

Image analysis

Let Ω_i, $i \in 1, 2, ...$ be the list of ROIs specified for PyFPAP's analysis. The mean intensity over the ROI Ω_i at time step t_j is then calculated by

$$\bar{I}_{\Omega_i}(t_j) = \frac{1}{A_{\Omega_i}} \sum_{(x_k,y_k)\in\Omega_i} I(x_k, y_k, t_j) \tag{1}$$

where A_{Ω_i} is the area covered by Ω_i, and $I(x_k, y_k, t_j)$ is the intensity at pixel (x_k, y_k).

FRAP image data was analyzed within the ROIs Ω_{bleached} and Ω_{slice}. Ω_{slice} was defined as a circular domain with center C_{slice} and radius r_{slice}. Since the imaging depth varied between experiments, both C_{slice} and r_{slice} were cropped for each data set. The bleached ROI Ω_{bleached} was defined as a square with sidelength $s_{\text{bleached}} = 174.1$ pixels and left lower corner at $O_{\text{bleached}} = C_{\text{slice}} - \frac{1}{2}(s_{\text{bleached}}, s_{\text{bleached}})$. The definition of both ROIs is shown in Supplementary Fig. 2a.

Accounting for uneven illumination

Uneven imaging due to inhomogeneous sample illumination is a common problem in microscopy[32–34]. We implemented two solutions in PyFRAP to address this problem: 1) Normalization by an image acquired before bleaching, and 2) applying a flattening mask derived from imaging a homogeneous fluorescent sample. The pixel-wise mean image over n_{images} images can be defined as

$$M(x_k, y_k) = \frac{1}{n_{\text{images}}} \sum_{m=1}^{n_{\text{images}}} I(x_k, y_k) \tag{2}$$

To avoid noise-induced singularities when normalizing, PyFRAP computes a mean normalization mask M_{pre} over multiple pre-bleach images, and then divides each image of the recovery time series pixel-wise by the computed mask

$$\tilde{I}(x_k, y_k, t_j) = \frac{I(x_k, y_k, t_j) + O_{\text{norm}}}{M_{\text{pre}}(x_k, y_k) + O_{\text{norm}}} \tag{3}$$

where O_{norm} is the optimal data offset computed via

$$O_{\text{norm}} = \max\{\min_{k,j}(I(x_k, y_k, t_j)), \min_{k,j}(M_{\text{pre}}(x_k, y_k, t_j))\} + 1 \tag{4}$$

Similarly, the flattening mask M_{flat} is computed as a mean over multiple images of a fluorophore spread homogeneously across a cover slip:

$$F(x_k, y_k) = \frac{\max_k(M_{\text{flat}}(x_k, y_k)) + O_{\text{flat}}}{M_{\text{flat}}(x_k, y_k) + O_{\text{flat}}} \tag{5}$$

Here, similar to the normalization in equation (4), the optimal data offset O_{flat} is obtained by taking the maximum over all minimum intensities of images in both recovery and flattening data sets. The recovery data set is then evened out by pixel-wise multiplication of the flattening mask obtained in equation (5) with each recovery image:

$$\tilde{I}(x_k, y_k, t_j) = F(x_k, y_k) \cdot I(x_k, y_k, t_j) \tag{6}$$

An outline of both correction methods is shown in Supplementary Fig. 2c.

In the present study, two pre-bleach images were acquired per sample for the normalization mask, and two images of fluorescein conjugated to a 40 kDa dextran or recombinant GFP homogeneously spread on a cover slip were acquired for the flattening approach. The effects of flattening and normalization on data analysis are described in Supplementary Text 1.

Accounting for background fluorescence

Background subtraction is a standard procedure to extract the true signal of microscope images[33,34]. Similar to the flattening and normalization masks, PyFRAP takes the average over multiple pixels to obtain a background mask and then subtracts it pixel-wise[33,34]:

$$\tilde{I}(x_k, y_k, t_j) = I(x_k, y_k, t_j) - M_{\text{bkgd}}(x_k, y_k) \tag{7}$$

The mean of two images without a sample was determined to compute a background mask. The effect of background subtraction is discussed in Supplementary Text 1.

Application of filters for noise reduction

Microscope data sets are often noisy, causing problems for normalization and simulation. PyFRAP smooths noisy pixels by either applying a Gaussian blur with standard deviation σ_{gauss}, or a median filter with filter window radius r_{median}. We found that $\sigma_{\text{gauss}} = 2$ and $r_{\text{median}} = 5$ provided good results for the data in the present study (see Supplementary Text 1).

Accounting for fluorophore concentration outside of the imaging view

In some cases it is not possible to capture the whole sample in one field of view under the microscope, and the concentration in the non-imaged regions needs to be estimated. PyFRAP solves this by letting users define an ROI Ω_{rim} to select an approximation of the average unbleached intensity from the first image of the recovery image series:

$$c_{\text{rim}} = \frac{1}{A_{\text{rim}}} \sum_{(x_k, y_k) \in \Omega \text{rim}} I(x_k, y_k, t_0) \tag{8}$$

where Ω_{rim} is defined by

$$\Omega_{\text{rim}} = \{(x_k, y_k) \in \Omega_{\text{slice}} \mid \rho_{\text{rim}} r_{\text{slice}}) < ||(x_k, y_k) - C_{\text{slice}}||_2\} \tag{9}$$

i.e. all pixels (x_k, y_k) inside Ω_{slice} that are at least $\rho_{\text{rim}} r_{\text{slice}}$ distant from the center C_{slice} (Supplementary Fig. 2b). $\rho_{\text{rim}} = 0.66$ and $\rho_{\text{rim}} = 0.4585$ were found to provide good values for the *in vitro* and *in vivo* experiments, respectively.

Simulations

PyFRAP simulates FRAP experiments numerically. Ignoring reaction kinetics, a FRAP experiment can be described by the diffusion equation

$$\frac{\partial c(\mathbf{x},t)}{\partial t} = D\nabla^2 c(\mathbf{x},t)\ ,\ \mathbf{x} \in \Omega \tag{10}$$

where $c(x,t)$ is the concentration of the measured molecule at position $\mathbf{x} = \langle x, y, z\rangle$ and time t inside the domain Ω, and D is its diffusion coefficient. The diffusion coefficient is assumed to be independent of the position **x**, i.e.

$$D(\mathbf{x}) = D\ ,\ \mathbf{x} \in \Omega \tag{11}$$

Since the sample is a closed system, no-flux Neumann boundary conditions were defined as

$$\frac{\partial c(\mathbf{x},t)}{\partial \mathbf{n}} = 0\ ,\ \mathbf{x} \in \partial\Omega \tag{12}$$

where **n** is the normal vector of the boundary $\partial\Omega$ at position **x**.

Initial conditions

The initial conditions are given by the bilinear interpolation F between pixels of the initial post-bleaching image:

$$\begin{aligned} F(x,y) = &\frac{1}{(x_1-x_2)(y_2-y_1)}\,(x_2-x, x-x_1) \\ &\cdot \begin{pmatrix} I(x_1,y_1) & I(x_1,y_2) \\ I(x_2,y_1) & I(x_2,y_2) \end{pmatrix} \begin{pmatrix} y_2-y \\ y-y_1 \end{pmatrix} \end{aligned} \tag{13}$$

$I(x_i,y_i)\ i \in 1,2$ represent the intensities in the initial image of the four pixels surrounding (x,y). If (x,y) is outside of the visible ROI in the initial image (Ω_{image}), the rim concentration c_{rim} given in equation (8) is applied to it, leading together with equation (13) to the initial condition

$$c(\mathbf{x},0) = \begin{cases} F(x,y) & \text{if } (x,y) \in \Omega_{\text{image}} \forall z \\ c_{\text{rim}} & \text{else} \end{cases} \tag{14}$$

Simulation geometry

PyFRAP comes with its own geometry definition tool that is parsed to Gmsh[36]. PyFRAP can read Gmsh's geometry definition files, use Gmsh's mesh files, or import STereoLithography (.stl) files, allowing users to define arbitrary two- and three-dimensional geometries. This gives users the ability to describe a realistic FRAP experiment geometry with the necessary precision.

The simulation geometry Ω for the *in vitro* experiments was a conical frustum with upper radius $r_{\text{upper}} = 317.65$ pixels, lower radius $r_{\text{lower}} = 224.25$ pixels, and height $h \approx 90.33$ pixels (Supplementary Fig. 4b). For the *in vivo* experiments, the simulation geometry resembled a zebrafish embryo at dome stage, i.e. the intersection of two hemispheres intersecting each other at the equator of the outer hemisphere. Since the geometry depends on the radius of the embryo in the initial image, r_{imaging} was calculated separately for each experiment[27,60]. Assuming that the radius of the inner hemisphere r_{inner} is 10% larger than the one of the outer hemisphere, r_{outer}, the geometry can be computed by

$$\begin{aligned} r_{\text{outer}} &= \frac{r_{\text{imaging}}^2 + h_{\text{imaging}}^2}{-2h_{\text{imaging}}} \\ r_{\text{inner}} &= 1.1 \cdot r_{\text{outer}} \\ d_{\text{center}} &= \sqrt{r_{\text{inner}}^2 - r_{\text{outer}}^2} \end{aligned} \tag{15}$$

where d_{center} is the distance between the two centers of the hemispheres. Supplementary Fig. 4a shows a schematic of the zebrafish dome stage geometry.

Meshing

PyFRAP discretizes simulation geometries using Gmsh[36] in combination with TetGen[37] into tetrahedral meshes. PyFRAP utilizes almost all functionalities of Gmsh – such as boundary layer meshes, attractor meshes, mesh merging and mesh refinement – allowing users to apply fine meshes where they are needed.

The overall default element size in the present study was $v = 25$ pixels^3. To overcome numerical instabilities, such as Gibbs phenomena at the boundary of Ω_{bleached}, the mesh around the bleached area boundary was refined using a boundary layer mesh of thickness $w_{\text{BL}} = 30$ pixels and element size $v_{\text{BL}} = 15$ pixels^3. Since only the simulation inside Ω_{slice} and Ω_{bleached} is used to fit the FRAP experiments, the mesh inside Ω_{slice} was also refined to an element size of $v_{\text{slice}} = 15$ pixels^3. Supplementary Fig. 4c,e shows an example of a tetrahedral mesh with both slice refinement and boundary layer meshes for the zebrafish dome geometry described in the previous section.

PDE solver

All reaction-diffusion systems were simulated using the FiPy toolbox[30]. The LU factorization algorithm or the Preconditioned-Conjugated-Gradient algorithm implemented in PySparse were used to solve the linear system at each time step.

Simulation parameters

All simulations were performed with a reference diffusion coefficient of $D = 50$ pixels^2/s. To ensure that the simulations run long enough to capture the full recovery of the FRAP experiment, the end time point of the simulation was set to $t_{\text{sim,end}} = 1680$ s for experiments conducted with an acquisition interval of $\Delta t = 1$ s. Since the recovery is steepest at the beginning of the simulations, a logarithmic time-stepping scheme was used, making early time steps shorter to achieve greater accuracy. A summary of all simulation parameters used to analyze the FRAP data in the present study is given in Supplementary Table 11.

Fitting

To avoid the need to re-simulate the FRAP experiment for each choice of diffusion coefficient D, PyFRAP uses the self-similarity property of the solution to equation (10). For example, a simulated FRAP experiment with the diffusion coefficient $D = 50$ pixels^2/s results in the same recovery behavior as an experiment with the diffusion coefficient $D = 200$ pixels^2/s, just four times slower. This can be described as

$$c(\mathbf{x}, t, D) = c\left(\mathbf{x}, \frac{D_{\text{ref}}}{D} t, D_{\text{ref}}\right) \tag{16}$$

where D_{ref} is the reference diffusion coefficient, i.e. the diffusion coefficient used for the simulation of equation (10). Supplementary Fig. 3d shows simulated recovery curves for various diffusion coefficients illustrating this self-similarity property.

PyFRAP allows users to fit four different models to FRAP data: 1) Pure diffusion, 2) diffusion and production, 3) diffusion and degradation, 4) diffusion with degradation and production, and each of these models with an additional set of equalization parameters (see below). In case of pure diffusion, the solution for the diffusion coefficient D over a given ROI Ω_i is simply given by the volume integral of the solution in equation (16):

$$\tilde{c}(\Omega_i, t, D) \equiv \int\limits_{\mathbf{x} \in \Omega_i} c(\mathbf{x}, t, D) \mathrm{d}V \tag{17}$$

Accounting for varying fluorophore fractions by equalization

FRAP experiments can vary in intensity during the experiment due to, for example, an increase or decrease in extracellular volume fraction, due to molecules moving in and out of the imaging plane, or due to an immobile fraction of fluorescent molecules. These effects are accounted for by equalization, which normalizes both simulation and data recovery curves to an equivalent scale between 0 and 1. During the fitting process, the simulated recovery curves are slightly lifted or lowered to better resemble overall fluorescence levels. This can be written as

$$\tilde{c}(\Omega_i, t, D) = \frac{1}{c_{\max} E_i} \left(\int\limits_{\mathbf{x}\in\Omega_i} c(\mathbf{x}, t, D)\mathrm{d}V - c_{\min} \right) \tag{18}$$

where E_i is the equalization factor for ROI Ω_i. The background $c_{\min}$ was chosen to be the smallest concentration of the bleached ROI inside the imaging region (Ω_{bleached}), over the whole time series

$$c_{\min} = \min_t \int\limits_{\mathbf{x}\in\Omega_{\text{bleached}}} c(\mathbf{x}, t)\mathrm{d}V \tag{19}$$

and the normalization value $c_{\max}$ to be the maximum concentration inside the whole imaging ROI (Ω_{slice}), over the whole time series

$$c_{\max} = \max_t \int\limits_{\mathbf{x}\in\Omega_{\text{slice}}} c(\mathbf{x}, t)\mathrm{d}V \tag{20}$$

Extending the diffusion model with reaction kinetics

Spatially uniform production was added to the scaled FRAP model defined in equation (16) or in equation (18) by

$$\tilde{c}(\Omega_i, t, D) = c(\Omega_i, t, D) + k_2 t \tag{21}$$

where k_2 is the production rate. To add spatially uniform degradation, the resulting solution is given by

$$\tilde{c}(\Omega_i, t, D) = c(\Omega_i, t, D)e^{-k_1 t} \tag{22}$$

The parameter k_1 represents the degradation rate constant. Adding both degradation and production to the system results in the following superposition of solutions:

$$\tilde{c}(\Omega_i, t, D) = c(\Omega_i, t, D)e^{-k_1 t} + \left(1 + e^{-k_1 t}\right) \frac{k_2}{k_1} \tag{23}$$

Choosing one of the models defined in equations (16) - (23), the sum of squared differences, SSD, was calculated by

$$SSD = \sum_i \sum_{t_j} \left(\tilde{c}(\Omega_i, t_j, D) - I_{\Omega_i}(t_j)\right)^2 \tag{24}$$

where $t_j \in 0, .., T$ are all time points of the FRAP data set, and $\Omega_i \in \Omega_{\text{bleached}}, \Omega_{\text{slice}}$ are the two ROIs of interest yielding a mean optimal fit between all fitted ROIs. The minimization of equation (24) was carried out using a constrained Nelder-Mead algorithm[42]. Since especially for a larger number of degrees of freedom the minimization algorithm tended to stop in local minima, initial guesses for the diffusion coefficient D were tested over two orders of magnitude, and the fit yielding the minimum SSD was considered optimal.

Statistics

PyFRAP offers four statistical tools (Supplementary Table 2) allowing users to test whether the estimated diffusion coefficient for one experimental group is significantly different from another one. The statistical tools include the two most prominent parametric significance tests, the Student's t-test[49] and a modification of this test, Welch's t-test[61], which both assume normally distributed test groups. PyFRAP also provides the Shapiro-Wilk test, allowing PyFRAP users to quickly assess whether the estimated diffusion coefficients follow a normal distribution. The Shapiro-Wilk test was recently found to have the best sensitivity compared to other common normality tests[62]. If normality cannot be guaranteed, PyFRAP offers two non-parametric ranked hypothesis tests: The Wilcoxon signed-rank test[63] and the Mann-Whitney U test[50].

Often, the underlying reaction kinetics of FRAP experiments or the relevance of their contribution might be unknown[47]. However, models with more parameters generally provide better fits than simpler models. The Akaike Information Criterion (AIC)[48] allows users to evaluate which model fits the data the best while keeping model complexity low. For this, let

$$\Theta := (k_1, k_2, D, E_1, E2, ...) \tag{25}$$

be the vector of unknown diffusion coefficient D, reaction rates k_1 and k_2, and $E_1, E_2, ...$ a list of equalization factors. Moreover, let $m = m(\Theta)$ be the model prediction using Θ. Assuming that the data is distributed normally around the model

$$d_i - m_i \sim \mathcal{N}(\mu, \sigma) \tag{26}$$

the log-likelihood function at data point i, L_i becomes

$$L_i(\Theta|d_i - m_i) = (d_i - m_i)^2 \tag{27}$$

and is thus identical with the sum of squared differences used for optimization in equation (24):

$$L(\Theta) = \sum_i L_i(\Theta) = SSD \tag{28}$$

The AIC is then given by

$$AIC = 2k - 2L(\hat{\Theta}) \tag{29}$$

where k is the number of parameters of model m and

$$\hat{\Theta} = \text{argmin}(L(\Theta|d_i - m_i, i = 1..n)) \tag{30}$$

is the parameter configuration Θ minimizing the log-likelihood function (equation (28)), i.e. the parameter configuration returned from fitting the model to data. The best model according to the AIC is then $m(\text{argmin}(AIC_i - AIC_{\text{min}}))$. If the number of sample points is small, the corrected AIC (AICc) provides a more accurate model selection technique:

$$AICc = AIC + \frac{2k(k+1)}{n-k-1}, \tag{31}$$

where n is the number of data points. A rule of thumb for when the AIC (equation (29)) or its corrected version (equation (31)) should be used is

$$\frac{n}{k} > 40 \tag{32}$$

PyFRAP automatically selects which statistical model is more appropriate if not specified differently.

PyFRAP also provides R^2-values for each fit: An R^2-value for each fitted ROI and the product and mean of these values. In general, PyFRAP computes an R^2-value of an ROI Ω_j by

$$R^2(\Omega_j) = 1 - \frac{\sum_i m_i - d_i}{\sum_i d_i - \bar{d}}, \tag{33}$$

where m_i and d_i are model and data at time i, and $\bar{d}$ is the mean over all data points.

FRAP/iFRAP experiments *in vitro*

FRAP experiments to measure pure diffusion and tortuosity effects were conducted in a frustum-like plexiglass hole. Holes around 700 μm in diameter and about 100 μm in depth were drilled into a plexiglass block using a dental drill. Due to the small depth, the resulting shape was frustum-like with an upper base of 510 μm diameter.

Holes were filled with aqueous solutions of FITC-/fluorescein-labeled dextrans of different sizes, recombinant GFP, or Dendra2 protein (Supplementary Table 5) using a micro-pipette. Dendra2 protein was centrifuged at 16,000 g for 30 min at 4°C to remove protein aggregates. Excess liquid was removed by pipetting under observation with a stereo microscope.

To model the effect of tortuosity in the *in vitro* FRAP experiments, polyacrylamide beads were added to the sample solution. The microbeads (Bio-Gel P-2 Gel, < 45 μm wet bead size) were first soaked in distilled water overnight for hydration. The beads were then centrifuged at 300 g, the supernatant removed, and the required quantity of beads transferred to another tube for resuspension in fluorescein-dextran or GFP + BSA solution. This was repeated and followed by removal of the supernatant, leaving a concentrated slurry of beads and fluorescent solution for the experiments. The beads were transferred into the plexiglass template and settled within 1-2 min.

To prevent evaporation, mineral oil (Sigma) was placed around the solution before sealing the hole with a cover slip (No 1.5). Supplementary Fig. 1a outlines the sample preparation process for *in vitro* experiments. The sample was upended carefully and mounted on an inverted confocal microscope. Images were taken using an LSM 780 NLO microscope (ZEISS) with an LD LCI Plan-Apochromat 25x/0.8 Imm Korr DIC objective (ZEISS) and immersion oil (Immersol TM W, $n = 1.334$ at 23°C, Zeiss). First, a plane approximately in the middle of the hole was chosen and the z-position set to zero. Then, the position of the highest and lowest point was determined. Cuboid volumes (141.42 μm $\times$ 141.42 μm $\times$ $\mathrm{depth}_{\mathrm{hole}}$) were bleached by imaging a z-stack at highest laser power (488 nm) or photoconverted at moderate laser power. Time series of 300 images (512×512 pixels with 566.79 μm $\times$ 566.79 μm) were taken with a speed of 1 frame/s (pixel dwell time: 3.15 μs) over a duration of 5 min. The zoom was set to 0.7, and the resulting images had a size of 566.79 μm $\times$ 566.79 μm.

After the FRAP experiment, the template was cleaned using distilled water, soap, and an interdental toothbrush.

FRAP experiments *in vivo*

Zebrafish embryos (*Danio rerio*) were collected 10 min after mating and proteolytically dechorionated[20,27,52]. For the experiments with recombinant GFP, 100 pg of recombinant GFP were injected into the extracelluar space when zebrafish embryos reached high stage[20,27,64] (Supplementary Table 10). For experiments with secreted GFP, 100 pg of the mRNA encoding the fluorescent protein were injected at the one-cell stage. For experiments with Squint-GFP, either 30 pg or 200 pg of mRNA were injected at the one-cell stage. At dome stage, embryos were mounted in drops of 1% low-melting-point agarose animal pole down onto a glass-bottom dish (MatTek Corp. P35G-1.5-20-C), and as soon as the drops solidified covered with Danieau's medium[27,52] to prevent the embryos from drying out. Supplementary Fig. 1b outlines the *in vivo* sample preparation process.

Confocal images were taken roughly at a 40 μm depth into the embryo. For data sets injected with 200 pg of Squint-GFP-encoding mRNA, images were acquired with the same settings as described for

the *in vitro* experiments either with 1 frame/s for 300 s, or 1 frame/10 s for 3000 s. Images of embryos injected with 30 pg of Squint-GFP-encoding mRNA were taken with a spatial resolution of 340.08 μm $\times$ 340.08 μm and 1 frame/10 s for 3000 s. Data sets for recombinant GFP *in vivo* were acquired with the same microscope settings as the experiments conducted *in vitro*.

Data exclusion

We performed a rigorous screen of all data sets, and excluded data sets that showed strong radial inhomogeneities in the first post-bleach image due to inhomogeneous distribution of fluorescent molecules. Moreover, we excluded *in vitro* data sets that showed unstable distributions in the overall fluorescence intensity levels, indicating incomplete bleaching through the depth of the sample.

Acknowledgements

We thank Ekkehard Kröwerath (University Hospital Tübingen, Center for Dentistry, Oral Medicine, and Maxillofacial Surgery) for the preparation of plexiglass holes, Katherine Rogers and Fabian Fröhlich for discussions and suggestions, and Sarah Keim and Katherine Rogers for testing PyFRAP. This work was supported by the Emmy Noether Program of the Deutsche Forschungsgemeinschaft, the Max Planck Society, and an ERC Starting Grant to P.M.

Author contributions

A.B., B.J., and P.M. conceived the study. A.B. and P.M. designed the software and performed data analysis and simulations. A.B. implemented the software. G.S., T.B., D.M., and H.P. conducted experiments with guidance from P.M.. A.B. and P.M. wrote the manuscript.

References

1. Crick, F. Diffusion in embryogenesis. *Nature* **255,** 420–422 (1970).
2. Lander, A. D., Nie, Q. & Wan, F. Y. M. Do morphogen gradients arise by diffusion? *Developmental Cell* **2,** 785–796 (2002).
3. Poo, M. M. & Cone, R. A. Lateral diffusion of rhodopsin in Necturus rods. *Experimental Eye Research* **17,** 503–507 (1973).
4. Liebman, P. A. & Entine, G. Lateral diffusion of visual pigment in photorecptor disk membranes. *Science* **185,** 457–459 (1974).
5. Lippincott-Schwartz, J., Altan-Bonnet, N. & Patterson, G. H. Photobleaching and photoactivation: following protein dynamics in living cells. *Nature Cell Biology* **5,** S7–S14 (2003).
6. Bancaud, A., Huet, S., Rabut, G. & Ellenberg, J. Fluorescence perturbation techniques to study mobility and molecular dynamics of proteins in live cells: FRAP, photoactivation, photoconversion, and FLIP. *Cold Spring Harbor Protocols* **12,** 1303–1325 (2010).
7. Griffin, E. E., Odde, D. J. & Seydoux, G. Regulation of the MEX-5 gradient by a spatially segregated kinase/phosphatase cycle. *Cell* **146,** 955–958 (2011).
8. Zhou, S. *et al.* Free extracellular diffusion creates the Dpp morphogen gradient of the Drosophila wing disc. *Current Biology* **22,** 668–675 (2012).
9. Axelrod, D., Koppel, D. E., Schlessinger, J., Elson, E. & Webb, W. W. Mobility measurement by analysis of fluorescence photobleaching recovery kinetics. *Biophysical Journal* **16,** 1055–1069 (1976).
10. Soumpasis, D. Theoretical analysis of fluorescence photobleaching recovery experiments. *Biophysical Journal* **41,** 95–97 (1983).
11. Sprague, B. L. & McNally, J. G. FRAP analysis of binding: Proper and fitting. *Trends in Cell Biology* **15,** 84–91 (2005).
12. Kang, M., Day, C. A., Drake, K., Kenworthy, A. K. & DiBenedetto, E. A generalization of theory for two-dimensional Fluorescence Recovery After Photobleaching applicable to confocal laser scanning microscopes. *Biophysical Journal* **97,** 1501–1511 (2009).
13. Deschout, H. *et al.* Straightforward FRAP for quantitative diffusion measurements with a laser scanning microscope. *Optics Express* **18,** 22886–22905 (2010).
14. Kang, M., Day, C. A., Kenworthy, A. K. & DiBenedetto, E. Simplified equation to extract diffusion coefficients from confocal FRAP data. *Traffic* **13,** 1589–1600 (2012).
15. Kraft, L. J., Dowler, J. & Kenworthy, A. K. *Frap-Toolbox: Software for the analysis of Fluorescence Recovery After Photobleaching* (accessed: 2016-12-12). `http://www.fraptoolbox.com` (2014).
16. Lin, L. & Othmer, H. G. Improving parameter inference from FRAP data: an analysis motivated by pattern Formation in the drosophila wing disc. *Bulletin of Mathematical Biology* **79,** 448–497 (2017).
17. Beaudouin, J., Mora-Bermúdez, F., Klee, T., Daigle, N. & Ellenberg, J. Dissecting the contribution of diffusion and interactions to the mobility of nuclear proteins. *Biophysical Journal* **90,** 1878–1894 (2006).
18. Schaff, J. C., Cowan, A. E., Loew, L. M. & Moraru, I. I. Virtual FRAP - an experiment-oriented simulation tool. *Biophysical Journal* **96,** 30a (2009).
19. Blumenthal, D., Goldstien, L., Edidin, M. & Gheber, L. A. Universal approach to FRAP analysis of arbitrary bleaching patterns. *Scientific Reports* **5,** 11655 (2015).

20. Müller, P., Rogers, K. W., Yu, S. R., Brand, M. & Schier, A. F. Morphogen transport. *Development* **140,** 1621–1638 (2013).

21. Umulis, D. M. & Othmer, H. G. The importance of geometry in mathematical models of developing systems. *Current Opinion in Genetics and Development* **22,** 547–552 (2012).

22. Weiss, M. Challenges and artifacts in quantitative photobleaching experiments. *Traffic* **5,** 662–671 (2004).

23. Mazza, D., Cella, F., Vicidomini, G., Krol, S. & Diaspro, A. Role of three-dimensional bleach distribution in confocal and two-photon fluorescence recovery after photobleaching experiments. *Applied Optics* **46,** 7401–7411 (2007).

24. Macháň, R., Foo, Y. H. & Wohland, T. On the equivalence of FCS and FRAP: simultaneous lipid membrane measurements. *Biophysical Journal* **111,** 152–161 (2016).

25. Braga, J., Desterro, J. M. & Carmo-Fonseca, M. Intracellular macromolecular mobility measured by Fluorescence Recovery After Photobleaching with confocal laser scanning microscopes. *Molecular Biology of the Cell* **15,** 4749–4760 (2004).

26. Blischak, J. D., Davenport, E. R. & Wilson, G. A quick introduction to version control with Git and GitHub. *PLoS Computational Biology* **12,** e1004668 (2016).

27. Müller, P. *et al.* Differential diffusivity of Nodal and Lefty underlies a reaction-diffusion patterning system. *Science* **336,** 721–724 (2012).

28. Sigaut, L., Ponce, M. L., Colman-Lerner, A. & Dawson, S. P. Optical techniques provide information on various effective diffusion coefficients in the presence of traps. *Physical Review E* **82,** 051912 (2010).

29. Millman, K. J. & Aivazis, M. Python for scientists and engineers. *Computing in Science and Engineering* **13,** 9–12 (2011).

30. Guyer, J. E., Wheeler, D. & Warren, J. A. FiPy: Partial differential equations with Python. *Computing in Science & Engineering* **11,** 6–15 (2009).

31. Schindelin, J. *et al.* Fiji: an open-source platform for biological-image analysis. *Nature Methods* **9,** 676–682 (2012).

32. Lindblad, J. & Bengtsson, E. *A comparison of methods for estimation of intensity non-uniformities in 2D and 3D microscope images of fluorescence stained cells* in *Proceedings of the 12th Scandinavian Conference on Image Analysis (SCIA)* (2001), 264–271.

33. Waters, J. C. Accuracy and precision in quantitative fluorescence microscopy. *The Journal of Cell Biology* **185,** 1135–48 (2009).

34. Schwarzfischer, M. *et al. Efficient fluorescence image normalization for time lapse movies* in *Proceedings of Microscopic Image Analysis with Applications in Biology* (2011).

35. Gregor, T., Bialek, W., de Ruyter van Steveninck, R. R., Tank, D. W. & Wieschaus, E. F. Diffusion and scaling during early embryonic pattern formation. *Proc. Natl. Acad. Sci. U.S.A.* **102,** 18403–18407 (2005).

36. Geuzaine, C. & Remacle, J.-F. Gmsh: A 3-D finite element mesh generator with built-in pre- and post-processing facilities. *International Journal for Numerical Methods in Engineering* **79,** 1309–1331 (2009).

37. Si, H. TetGen, a Delaunay-based quality tetrahedral mesh generator. *ACM Trans. Math. Softw.* **41,** 11:1–11:36 (2015).

38. Sprague, B. L., Pego, R. L., Stavreva, D. A. & McNally, J. G. Analysis of binding reactions by Fluorescence Recovery After Photobleaching. *Biophysical Journal* **86,** 3473–3495 (2004).

39. Miura, K. *FrapCalc* (accessed: 2016-12-12). `http://wiki.cmci.info/downloads/frap_analysis` (2016).

40. Rapsomaniki, M. A. *et al.* EasyFRAP: An interactive, easy-to-use tool for qualitative and quantitative analysis of FRAP data. *Bioinformatics* **28,** 1800–1801 (2012).

41. Castle, B. T., Howard, S. A. & Odde, D. J. Assessment of transport mechanisms underlying the Bicoid morphogen gradient. *Cellular and Molecular Bioengineering* **4,** 116–121 (2011).

42. Nelder, J. A. & Mead, R. A simplex method for function minimization. *The Computer Journal* **7,** 308–313 (1965).

43. Nash, S. G. Newton-type minimization via the Lanczos method. *SIAM Journal on Numerical Analysis* **21,** 770–788 (1984).

44. Nocedal, J. & Wright, S. J. *Numerical optimization* 2. ed. (Springer, New York, 2006).

45. Bläßle, A. & Müller, P. PyFDAP: Automated analysis of Fluorescence Decay After Photoconversion (FDAP) experiments. *Bioinformatics* **6,** 972–974 (2015).

46. Rogers, K. W., Bläßle, A., Schier, A. F. & Müller, P. Measuring protein stability in living zebrafish embryos using Fluorescence Decay After Photoconversion (FDAP). *J. Vis. Exp.* **95** (e52266 2015).

47. Mai, J. *et al.* Are assumptions about the model type necessary in reaction-diffusion modeling? A FRAP application. *Biophysical Journal* **100,** 1178–1188 (2011).

48. Akaike, H. A new look at the statistical model identification. *IEEE Transactions on Automatic Control* **19,** 716–723 (1974).

49. Student. The probable error of a mean. *Biometrika* **6,** 1–25 (1908).

50. Mann, H. B. & Whitney, D. R. On a test of whether one of two random variables is stochastically larger than the other. *The Annals of Mathematical Statistics* **18,** 50–60 (1947).

51. Shapiro, S. S. & Wilk, M. B. An analysis of variance test for normality (complete samples). *Biometrika* **52,** 591–611 (1965).

52. Pomreinke, A. P. *et al.* Dynamics of BMP signaling and distribution during zebrafish dorsal-ventral patterning. *Elife* **6,** e25861 (2017).

53. Aaron, J. *FRAP* (accessed: 2016-12-12). `https://de.mathworks.com/matlabcentral/fileexchange/47327-frap-zip` (2016).

54. Ulrich, M. *et al.* Tropical-parameter estimation and simulation of reaction-diffusion models based on spatio-temporal microscopy images. *Bioinformatics* **22,** 2709–2710 (2006).

55. Hrabe, J., Hrabetová, S. & Segeth, K. A model of effective diffusion and tortuosity in the extracellular space of the brain. *Biophysical Journal* **87,** 1606–1617 (2004).

56. Tao, L. & Nicholson, C. Maximum geometrical hindrance to diffusion in brain extracellular space surrounding uniformly spaced convex cells. *Journal of Theoretical Biology* **229,** 59–68 (2004).

57. Novak, I. L., Kraikivski, P. & Slepchenko, B. M. Diffusion in cytoplasm: Effects of excluded volume due to internal membranes and cytoskeletal structures. *Biophysical Journal* **97,** 758–767 (2009).

58. Donovan, P., Chehreghanianzabi, Y., Rathinam, M. & Zustiak, S. P. Homogenization theory for the prediction of obstructed solute diffusivity in macromolecular solutions. *PLoS ONE* **11,** e0146093 (2016).

59. Höckendorf, B., Thumberger, T. & Wittbrodt, J. Quantitative analysis of embryogenesis: a perspective for light sheet microscopy. *Developmental Cell* **23,** 1111–1120 (2012).

60. Kimmel, C. B., Ballard, W. W., Kimmel, S. R., Ullmann, B. & Schilling, T. F. Stages of embryonic development of the zebrafish. *Developmental Dynamics* **203,** 253–310 (1995).

61. Welch, B. L. The generalisation of Student's problems when several different population variances are involved. *Biometrika* **34,** 28–35 (1947).

62. Razali, N. M. & Wah, Y. B. Power comparisons of Shapiro-Wilk, Kolmogorov-Smirnov, Lilliefors and Anderson-Darling tests. *Journal of Statistical Modeling and Analytics* **2,** 21–33 (2011).

63. Wilcoxon, F. Individual comparisons by ranking methods. *Biometrics Bulletin* **1,** 80–83 (1945).

64. Yu, S. R. *et al.* Fgf8 morphogen gradient forms by a source-sink mechanism with freely diffusing molecules. *Nature* **461,** 533–536 (2009).

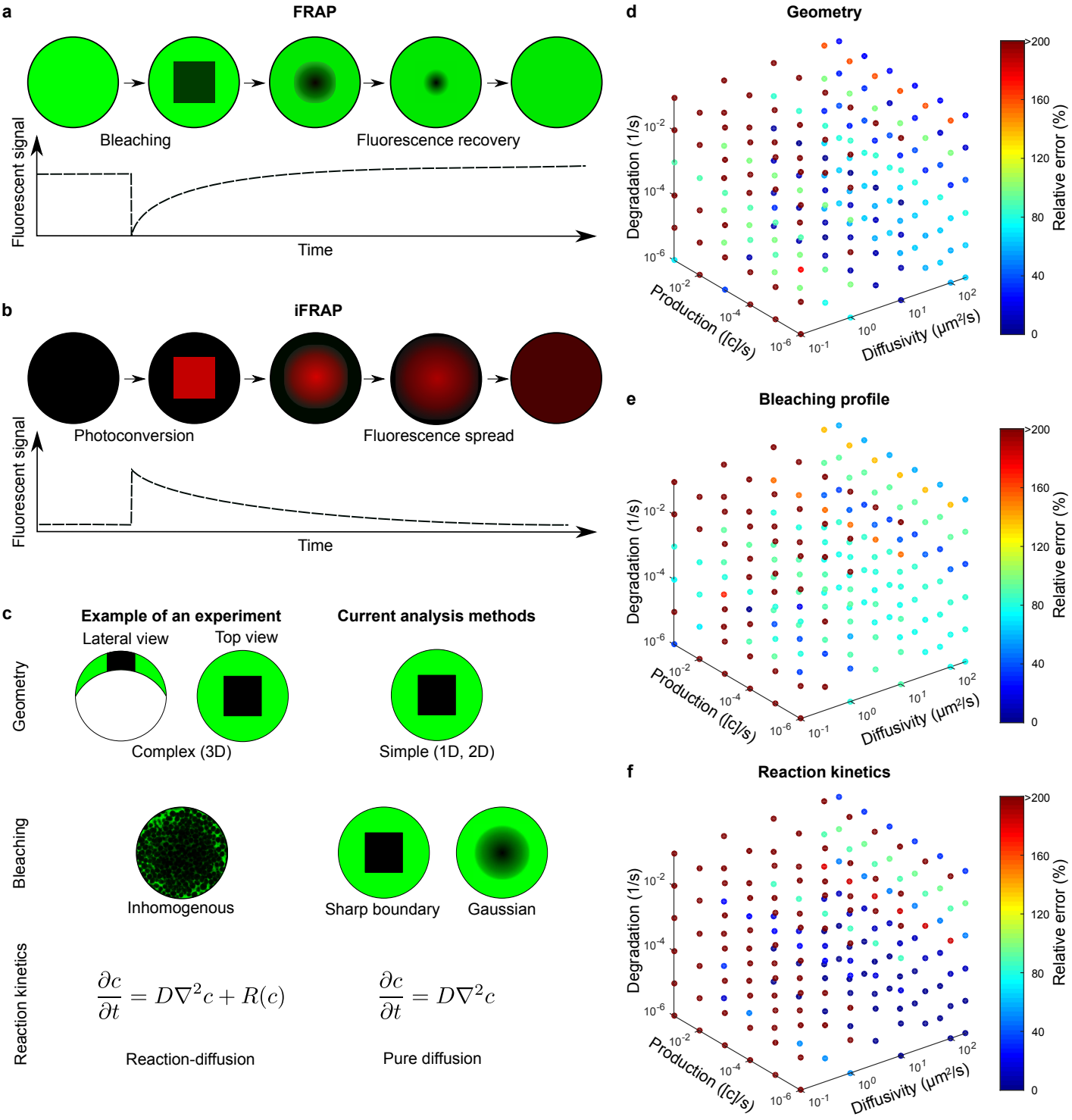

Figure 1 | Fluorescence perturbation techniques used for effective diffusion measurements, and drawbacks of current analysis methods. (a) In Fluorecence Recovery After Photobleaching (FRAP) experiments, a small region in the sample is bleached. After bleaching, the diffusion-driven recovery in the bleached region is monitored. **(b)** Inverse FRAP (iFRAP) is an experimental mirror image of FRAP: Molecules in a given region are photoconverted and then spread throughout the sample, resulting in the loss of fluorescent signal in the region of photoconversion. **(c)** Drawbacks of current analysis methods exemplified with zebrafish development at late blastula stages. Current analysis methods simplify sample geometry, idealize bleaching profiles, or ignore underlying reaction kinetics. **(d-f)** Possible relative error in diffusion coefficient estimates that can occur if false assumptions are made about sample geometry, bleaching conditions, or reaction kinetics, respectively. The maximum displayed error was capped to a value of 200%, but can be up to 1000%.

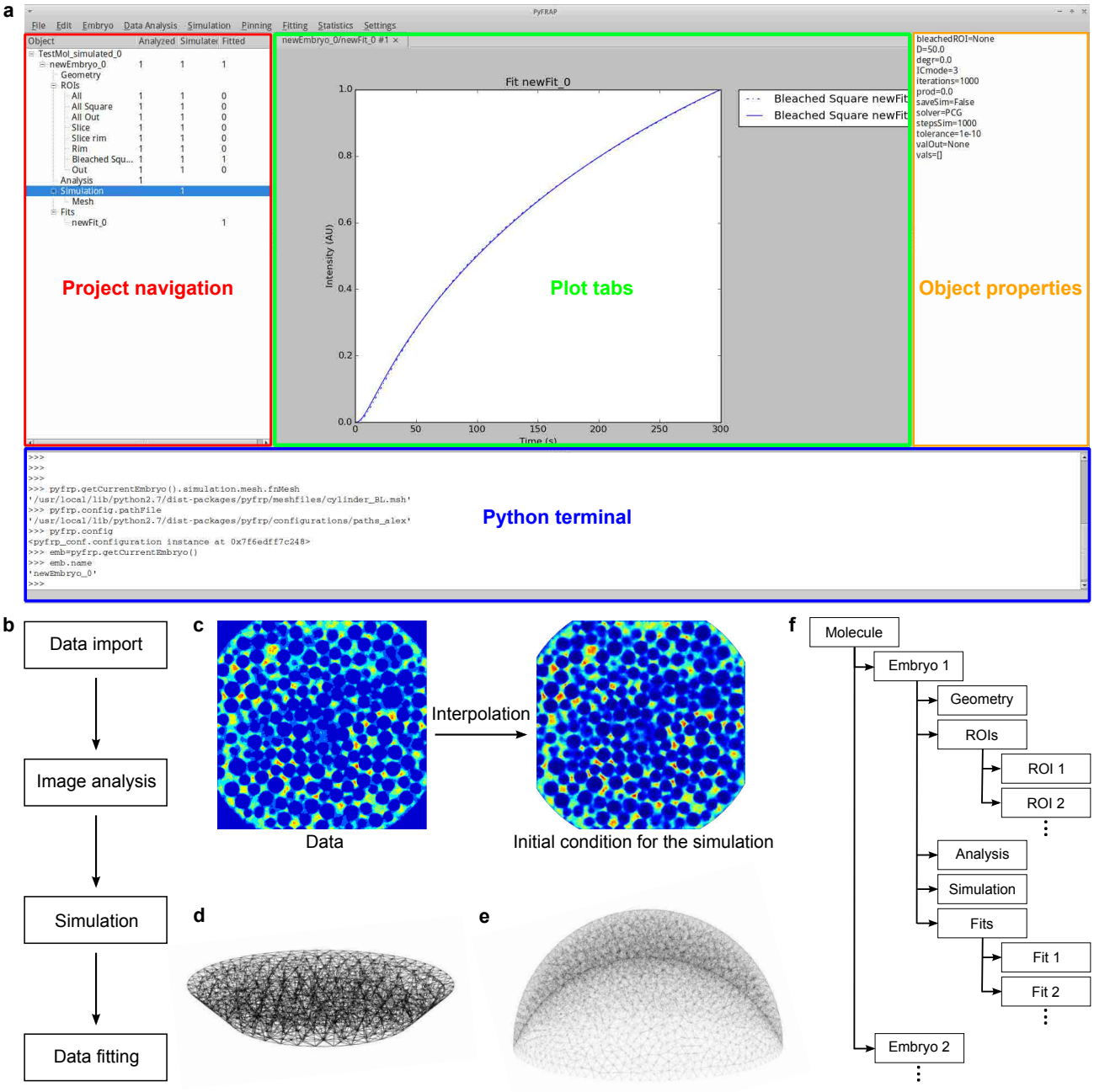

Figure 2 | The PyFRAP software package. (a) Annotated snapshot of the PyFRAP main GUI with project navigation tree (red), plot tabs (green), object property display (orange), and integrated Python terminal (blue). **(b)** PyFRAP work flow. **(c)** PyFRAP's interpolation of the first post-bleach images as initial condition for FRAP simulations. **(d,e)** Spatial discretization of geometries resembling **(d)** a frustum, and **(e)** a zebrafish embryo at late blastula stages (dome stage). **(f)** PyFRAP's data structure.

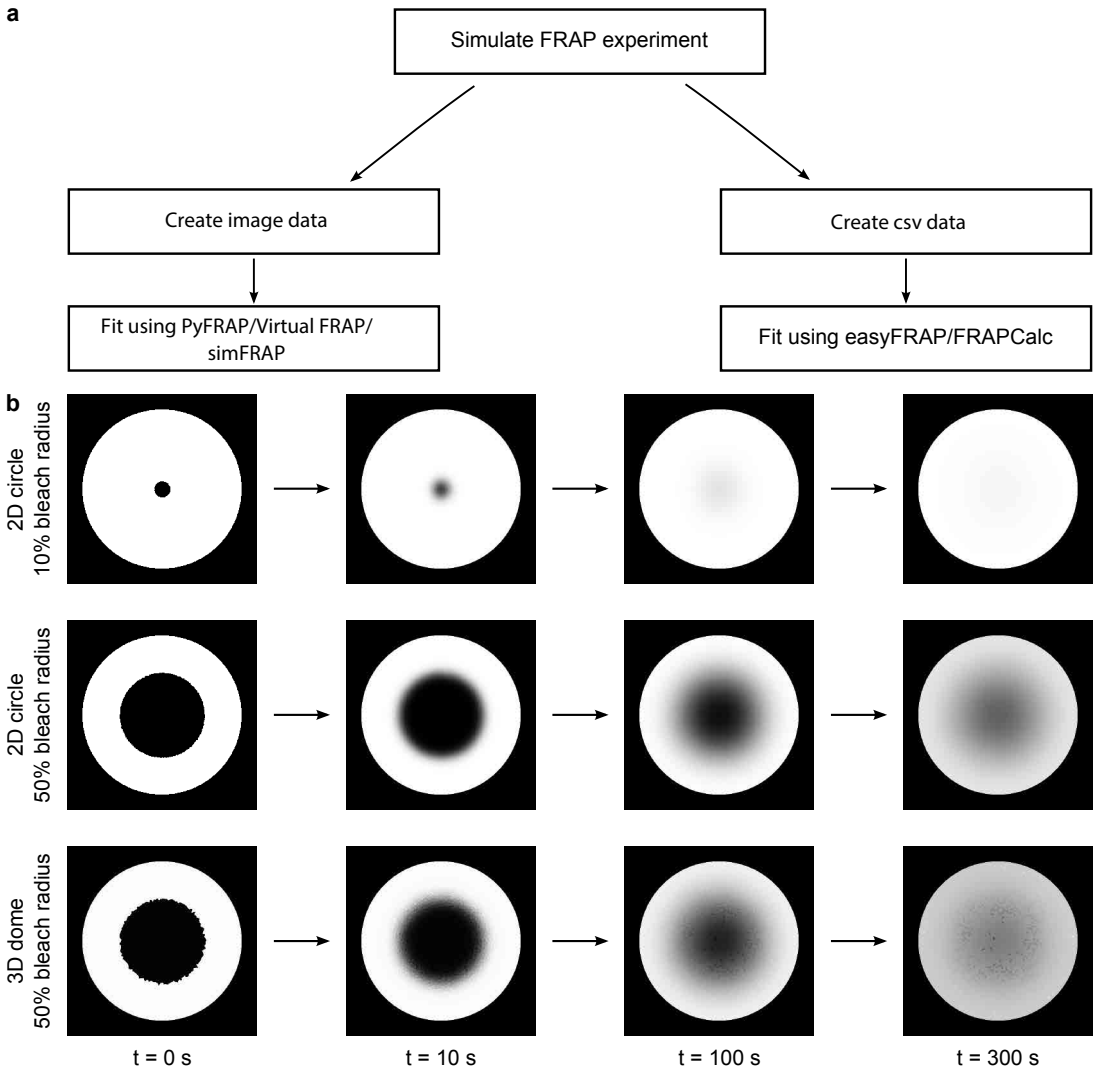

c

Geometry	Bleach domain radius (%)	Simulated D (μm²/s)	PyFRAP D (μm²/s)	FrapCalc D (μm²/s)	easyFRAP* D (μm²/s)	simFRAP D (μm²/s)	virtualFRAP D (μm²/s)
2D circle	5	10	9.8	9.0	14.0	9.3	9.1
2D circle	10	10	9.7	9.7	21.5	9.5	9.1
2D circle	50	10	9.8	10.4	89.1	13.1	10.3
2D circle	5	50	47.5	37.2	38.2	39.8	44.2
2D circle	10	50	49.5	45.2	70.7	47.9	44.3
2D circle	50	50	48.4	63.6	260.5	19.0	42.0
2D circle	5	200	245.0	112.7	67.3	n.a.	39.3
2D circle	10	200	179.0	157.6	161.0	8.7	177.8
2D circle	50	200	197.1	503.1	910.0	n.a.	191.7
3D dome	5	10	11.9	n.a.	17.2	9.7	11.3
3D dome	10	10	9.0	n.a.	23.8	10.1	9.0
3D dome	50	10	10.3	24.0	83.3	12.7	13.3
3D dome	5	50	56.9	n.a.	61.5	47.7	41.8
3D dome	10	50	44.2	n.a.	90.7	49.5	43.4
3D dome	50	50	47.4	n.a.	310.4	48.7	34.1
3D dome	5	200	211.6	n.a.	139.2	185.6	40.5
3D dome	10	200	172.4	n.a.	264.5	192.5	188.0
3D dome	50	200	191.1	n.a.	1021.9	177.3	113.5

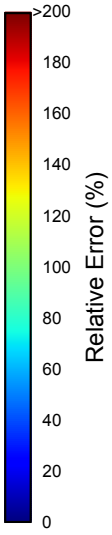

Figure 3 | PyFRAP benchmarking simulation experiment. (a) Work flow of PyFRAP benchmarking. **(b)** Examples of simulated data sets for different bleach spot sizes and geometries. **(c)** Benchmarking results of PyFRAP against currently available software packages using simulated FRAP experiments. Simulation experiments varied in bleached region size, diffusion coefficient, and experiment geometry. All diffusion coefficients and estimates are given in units of μm²/s. n.a. indicates that the software was not able to fit the simulated data. Colors indicate relative estimation error in %. Diffusion coefficients determined by easyFRAP (asterisk) were computed in combination with an equation providing a relationship between recovery rate, bleached domain size, and diffusivity[38].

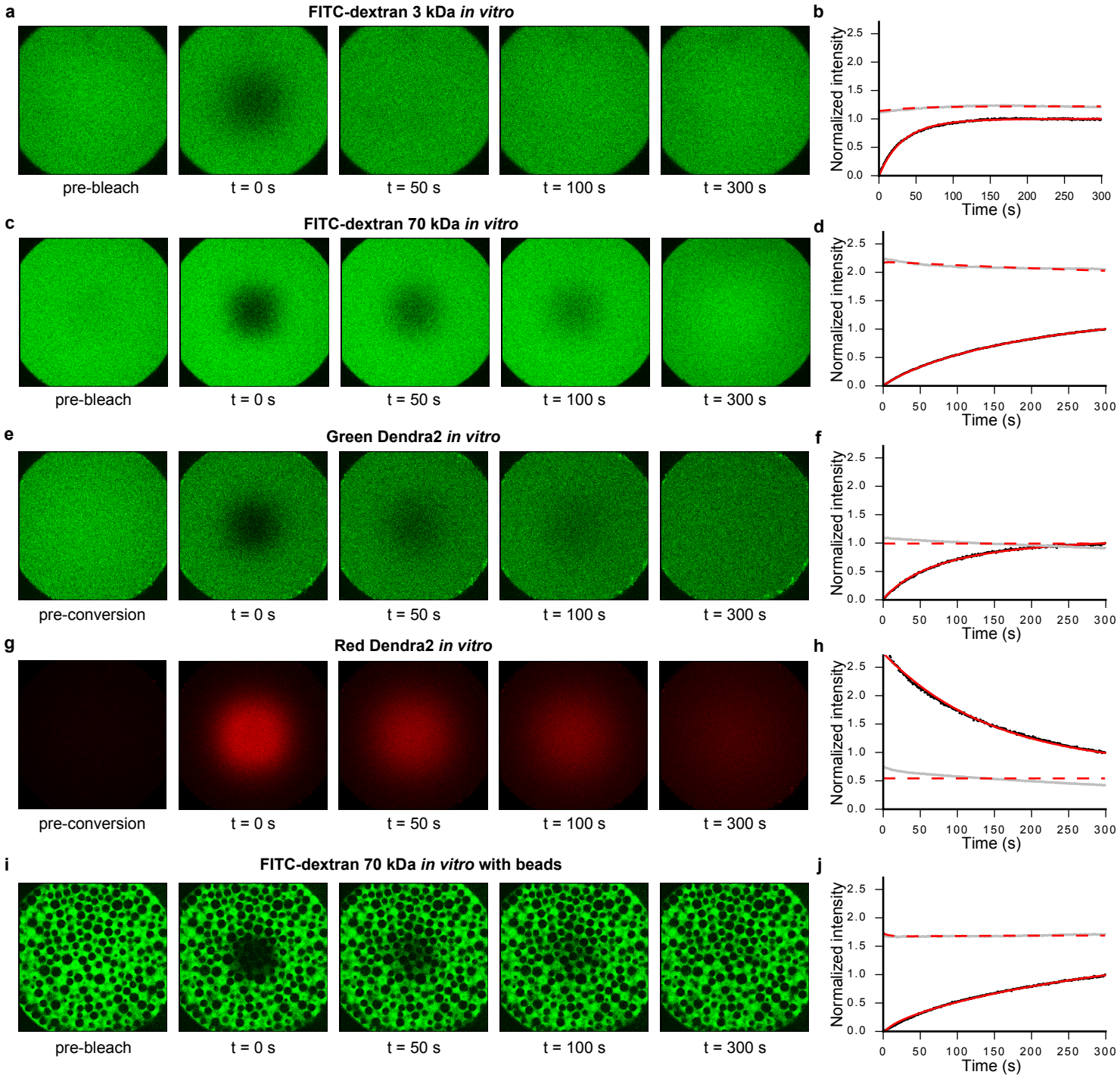

Figure 4 | Examples of *in vitro* FRAP and iFRAP experiments and the resulting fits to measure free diffusion. (a,c,e,g,i) *In vitro* FRAP and iFRAP experiment images and **(b,d,f,h,j)** fits with PyFRAP. Black and gray dots represent data points of bleached and slice ROI, respectively. Red solid and dashed lines show the respective fits. (a,b,c,d) FRAP experiments with 3 kDa and 70 kDa fluorescent dextrans (see Supplementary Fig. 5 for the full data set with fluorescent dextrans between 3 kDa and 500 kDa). (e,f,g,h) iFRAP experiment with photoconverted Dendra2 protein showing data for the green (e,f) and the red (g,h) channel. (i,j) FRAP experiment with 70 kDa fluorescent dextran in the presence of polyacrylamide beads. Recovery curves were normalized between 0 (intensity in the bleached ROI at the first post-bleach time point) and 1 (intensity in the bleached ROI at the last post-bleach time point) to facilitate comparison across data sets.

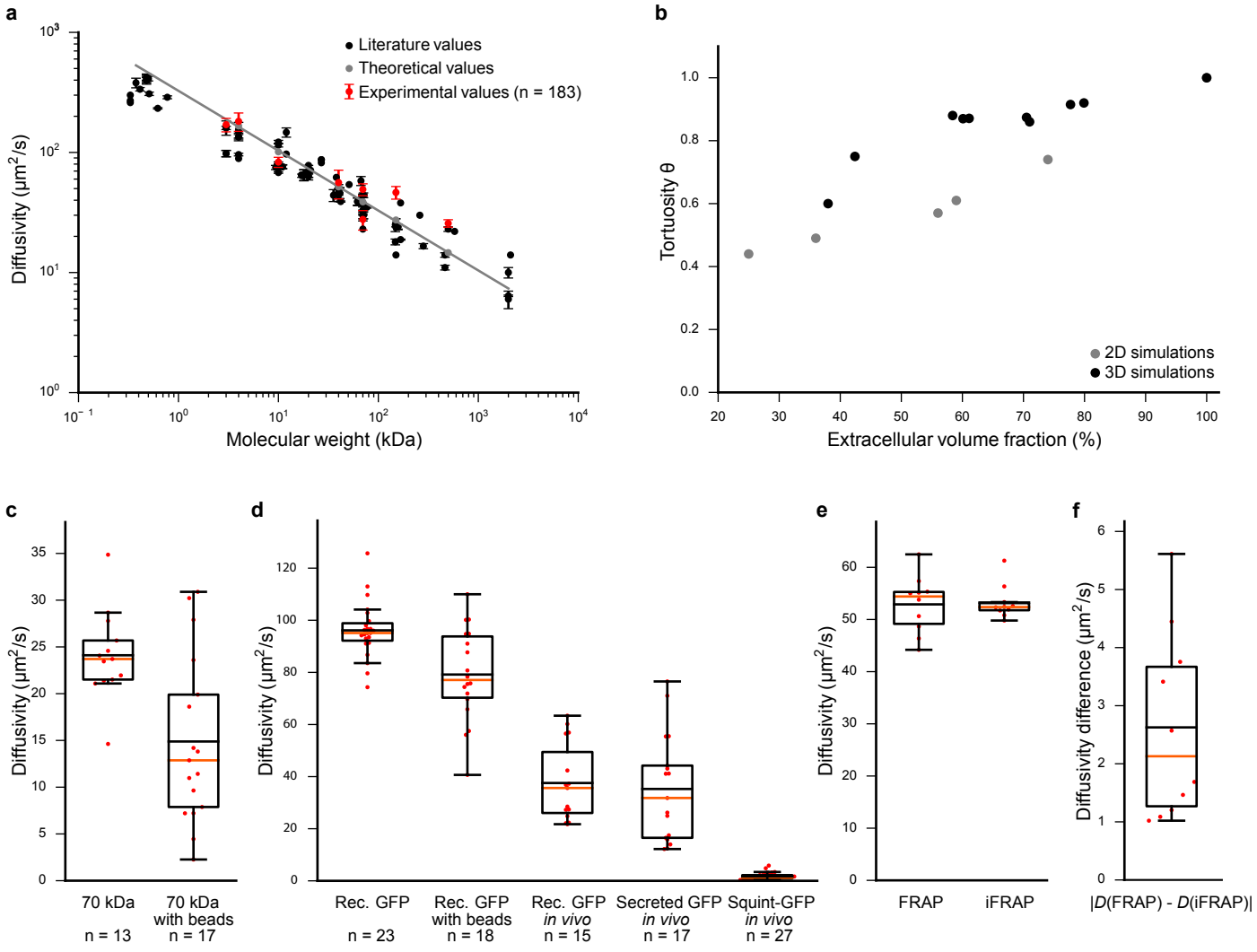

Figure 5 | Effective diffusion coefficients determined by PyFRAP. (a) Results of *in vitro* experiments and PyFRAP analysis for freely diffusing fluorescent dextrans of different molecular weights. Black markers indicate literature values for fluorescent dextrans, red markers the mean effective diffusion estimates obtained by *in vitro* experiments and PyFRAP analysis, and gray markers the theoretical estimates derived from the Einstein-Stokes equation (see Supplementary Text 3). Error bars show the standard deviation of PyFRAP's effective diffusion estimates. The gray line represents a linear regression fit to the theoretical values. **(b)** Results of simulations investigating the influence of tortuosity on effective diffusion for differently packed bead experiments. Gray and black markers indicate 2D and 3D simulation results, respectively. **(c)** Results of fluorescent dextran experiments showing the impact of tortuosity on effective diffusivities. Box plot indicates median (orange line), mean (black line), 25% quantiles (box), and all included data points (red markers). **(d)** Results of GFP experiments showing the impact of tortuosity, extracelluar matrix, protein production, and extracellular binding on the effective diffusion estimates. Box plot indicates median (orange line), mean (black line), 25% quantiles (box), and all included data points (red markers). **(e,f)** Results of FRAP/iFRAP experiments for the photoconvertible protein Dendra2. Box plot indicates median (orange line), mean (black line), 25% quantiles (box), and all included data points (red markers).

Supplementary Information for

Quantitative diffusion measurements using the open-source software PyFRAP

Alexander Bläßle[1], Gary Soh[1], Theresa Braun[1,2], David Mörsdorf[1], Hannes Preiß[1], Ben Jordan[3], and Patrick Müller[1,*]

[1]Friedrich Miescher Laboratory of the Max Planck Society, Tübingen, Germany
[2]Present address: University of Konstanz, Konstanz, Germany
[3]Department of Organismic and Evolutionary Biology, Harvard University, Cambridge, USA

[*]Correspondence to: patrick.mueller@tuebingen.mpg.de (P.M.)

This PDF includes:
Supplementary Texts 1-3
Supplementary References 1-43
Supplementary Tables 1-12
Supplementary Figures 1-8

Supplementary Text 1: Analysis method selection

To assess how image correction by flattening, normalization, background subtraction, Gaussian blur, and median filter affects effective diffusion estimates from FRAP experiments, we tested the 24 analysis combinations listed in Supplementary Table 1. We assessed whether 1) the resulting diffusion estimate D is affected, 2) the standard deviation σ of the estimated diffusion coefficients is affected (i.e. whether correcting and smoothing the images makes the diffusion estimates more exact), and 3) the goodness of the fits (i.e. R^2-values) is affected. We quantified the effect of an analysis option by

$$H(v, \alpha) = \frac{v(\alpha)}{v(\alpha_0)} \tag{1}$$

where $\alpha = \{n, f, b, g, m\}$ represents an analysis option defined by five binary entries indicating whether normalization n, flattening f, background subtraction b, Gaussian blur g, or median filter m was used. If we did not correct images, we denote this by α_0. The variable v describes the quantified result, such as the mean diffusion coefficient. Supplementary Fig. 3 shows a subset of this analysis for three different variables v: The mean diffusion coefficient D, the variance of diffusion coefficients σ, and the fit quality R^2. FRAP experiments performed in the present study (see Materials and Methods) were grouped by condition (*in vitro* experiments with free diffusion, *in vitro* with beads, and *in vivo* experiments) to isolate condition-specific effects. We did not correct for potential illumination inhomogeneities in *in vivo* experiments, since these only covered a small centered area of the total image, and illumination is homogeneous in this region. Moreover, normalization cannot be used for the analysis of *in vitro* experiments containing beads, since normalization would introduce artificially high intensity areas at the locations of the beads.

If only normalization and flattening were applied, we observed an increase of the measured diffusion coefficients and an improvement in fit quality for free diffusion (Supplementary Fig. 3a,c). Both techniques only mildly affected the variance of diffusion coefficients (Supplementary Fig. 3b). Background subtraction had no effect on any measure (Supplementary Fig. 3a-c). Moreover, noise reduction or smoothing via median filter or Gaussian blur tended to decrease variance in all conditions (Supplementary Fig. 3b) and improve fits for free diffusion (Supplementary Fig. 3b).

We also tested whether a combination between an illumination correction technique (n or f) and the remaining three manipulation techniques (b, g and m) can further improve the analysis. Supplementary Fig. 3d shows that this can lead to an increase in mean diffusion estimates similar to those observed in Supplementary Fig. 3a. Moreover, applying a median filter or Gaussian blur in combination with flattening improves fit quality and decreases diffusion estimate variance (Supplementary Fig. 3e,f).

To keep the extent of image manipulation as minimal as possible while obtaining comparable low-variance estimates from high-quality fits, we only applied flattening to correct the images from *in vitro* experiments. Since both Gaussian blur and median filter treatments appeared to stabilize diffusion coefficient estimates (i.e. reducing their variance) to a similar extent, we restricted image smoothing to the application of a median filter for all other analyses.

Supplementary Text 2: Comparison of PyFRAP to other FRAP analysis software

We selected four current FRAP analysis software packages for comparison with PyFRAP: The two analytical programs easyFRAP[1] and FrapCalc[2], and the two numerical packages virtualFRAP[3] and simFRAP[4] (Supplementary Table 4).

To assess the performance of PyFRAP in comparison with other FRAP analysis software solutions, we created simulated FRAP data sets using PyFRAP's simulation toolbox. We found that PyFRAP and our in-house software based on MATLAB and COMSOL Multiphysics[5–7] produced identical simulated data, and chose to use PyFRAP to simulate the experiments due to the ease of PyFRAP's scripting abilities. We simulated two-dimensional or three-dimensional FRAP experiments with circular bleaching spots of various sizes for a 300 s time-course. Two-dimensional simulated experiments were conducted in a circle with radius 215 μm, and three-dimensional experiments resembled a zebrafish at dome stage with $r_{\text{imaging}} = 215$ μm and $h_{\text{imaging}} = 80$ μm (see Materials and Methods for details). Molecules were allowed to move with diffusion coefficients of 10 μm^2/s, 50 μm^2/s, or 200 μm^2/s, covering a range of typical diffusivities in biological samples. Bleached spots were placed in the center of the simulation geometry and comprised 5%, 10%, or 50% of the slice radius. We chose the boundary layer mesh described in the Materials and Methods section to envelope the bleached spot, guaranteeing numerical accuracy of the simulation experiments. PDEs were simulated over 4000 logarithmically-spaced time steps. The simulations were saved in a csv sheet specifically formatted for the use of easyFRAP or FrapCalc, or in 301 images by interpolation of the numerical solution onto a 512 μm$\times$ 512 μm grid. We then either imported and analyzed the csv sheet using FrapCalc (`https://github.com/miura/FrapCalc` using IgorPro7) or easyFRAP, or read in and analyzed the simulated images using simFRAP or virtualFRAP. The benchmarking analysis was performed using Microsoft Windows 8.1.

In contrast to other programs that determine absolute diffusion coefficients, easyFRAP only provides recovery half times ($1/\tau_{\frac{1}{2}}$). Thus, to compute diffusion coefficients from easyFRAP, we used

$$D = \frac{-\omega^2 \ln\left(\frac{1}{2}\right)}{\tau_{\frac{1}{2}}}$$

with various dimensions of the bleached spot ω as described previously[8].

We used PyFRAP's standard pipeline to analyze the saved simulated FRAP images files in an unbiased manner, only knowing imaging depth and radius.

Supplementary Text 3: Data analysis and control experiments

Computation of theoretical diffusion coefficients

We compared our *in vitro* FRAP results for differently sized fluorescein-labeled dextrans to predictions derived from the Einstein-Stokes equation

$$D = \frac{k_B T}{6\pi\eta r} \tag{2}$$

where $k_B = 1.38064852 \times 10^{-23}\mathrm{m}^2/(\mathrm{s}^2\mathrm{K})$ is the Boltzmann constant. The FRAP experiments were conducted in an aqueous solution with viscosity $\eta = 0.9321 \times 10^{-3}\mathrm{kg}/(\mathrm{sm})$ at $T = 296$ K. Stokes radii r were obtained from the manufacturers' websites, and are listed along with the calculated theoretical diffusion coefficients in Supplementary Table 5.

Simulating tortuosity

The movement of molecules during FRAP experiments is affected by obstacles such as cells, nuclei, or filopodia, and such tortuous molecule movements have been suggested to alter recovery rates and diffusion estimates[6].

To obtain a better understanding of how obstacles alter effective diffusion coefficients, we performed a simulation study in two- and three-dimensional geometries. We placed objects with a radius of $r_{\mathrm{Bead}} \approx 20\ \mu\mathrm{m}$ (similar to the dimensions of cells and beads used in the present study) in each geometry in three different ways: 1) Equally sized beads aligned as a regular grid (Supplementary Fig. 6a), 2) randomly placed within the domain with radii drawn from a cut-off normal distribution (Supplementary Fig. 6b,d), and 3) equally sized beads placed according to a hexagonal close-packing (Supplementary Fig. 6c). Beads were placed with different minimal gaps between them, ranging from 0.05 µm up to 10 µm. For 2D simulations, the overall geometry was a circle with radius 300 µm. We chose a cylinder with equal radius and height 100 µm or a cuboid with dimensions 600 µm × 600 µm × 100 µm for all 3D simulations experiments. The combination between various placement methods and gap sizes allowed us to vary the extracellular volume fraction (EVF) – i.e. the space available for the diffusing molecules – from 25% up to 78%.

Confirming previous analyses[9–12], we found that the introduction of beads delayed molecule recovery in the bleached ROI, and the effect of tortuosity increased as the EVF decreased (Fig. 5b, Supplementary Fig. 6e,f, Supplementary Table 8). Moreover, the effect in two-dimensional experiments was more severe. For example, FRAP simulations with EVF = 36% reduced diffusion by 51% compared to only 40% for EVF = 38% in a three-dimensional simulation. Both observations are in line with theoretical predictions and previous results[9–12].

BSA does not affect fluorophore diffusivity

We found a stronger effect of bead-mediated tortuosity on 70 kDa FITC-dextran molecules than on GFP *in vitro*. BSA was added to the aqueous solution with GFP to avoid GFP from interacting with the plexiglass surface of the drilled hole in the *in vitro* experiments. To test whether BSA might also interact with the polyacrylamide beads and thus distort FRAP results, we repeated the experiments with 70 kDa FITC-dextran both for pure diffusion with beads in addition to experiments with 70 kDa FITC-dextran + BSA + beads. We found that BSA had no influence on the recovery rates, yielding equal results within standard error, i.e. $14.9 \pm 2.1\ \mu\mathrm{m}^2/\mathrm{s}$ for bead experiments and $15.1 \pm 2.4\ \mu\mathrm{m}^2/\mathrm{s}$ for experiments with additional BSA (Supplementary Fig. 8a).

Varying the experimental settings for Squint-GFP FRAP experiments does not consistently affect measured diffusion coefficients

For the FRAP experiments with Squint-GFP produced from injected mRNA, we acquired data sets varying the amount of injected mRNA, the frame rate and length of image acquisition, and the zoom factor of the microscope. Results were partitioned into three experimental groups, i.e. images recorded with 1) a frame rate of 1 frames/10 s for 3000 s with 30 pg of injected mRNA and a spatial resolution of 340.08 $\mu\mathrm{m} \times 340.08$ $\mu\mathrm{m}$, 2) a frame rate of 1 frame/10 s for 3000 s with 200 pg of injected mRNA and a spatial resolution of 566.79 $\mu\mathrm{m} \times 566.79$ $\mu\mathrm{m}$, and 3) a frame rate of 1 frame/s for 300 s with 200 pg of injected mRNA and a spatial resolution of 566.79 $\mu\mathrm{m} \times 566.79$ $\mu\mathrm{m}$.

There were no clear trends between different acquisition methods (Supplementary Fig. 8b). However, acquiring images at a higher frame rate for a shorter period of time appeared to make experiments and thus estimated diffusion coefficients more noisy, possibly resulting from the slow transport process underlying Squint-GFP diffusion.

Supplementary References

1. Rapsomaniki, M. A. *et al.* EasyFRAP: An interactive, easy-to-use tool for qualitative and quantitative analysis of FRAP data. *Bioinformatics* **28,** 1800–1801 (2012).
2. Miura, K. *FrapCalc* (accessed: 2016-12-12). `http://wiki.cmci.info/downloads/frap_analysis` (2016).
3. Schaff, J. C., Cowan, A. E., Loew, L. M. & Moraru, I. I. Virtual FRAP - an experiment-oriented simulation tool. *Biophysical Journal* **96,** 30a (2009).
4. Blumenthal, D., Goldstien, L., Edidin, M. & Gheber, L. A. Universal approach to FRAP analysis of arbitrary bleaching patterns. *Scientific Reports* **5,** 11655 (2015).
5. Müller, P. *et al.* Differential diffusivity of Nodal and Lefty underlies a reaction-diffusion patterning system. *Science* **336,** 721–724 (2012).
6. Müller, P., Rogers, K. W., Yu, S. R., Brand, M. & Schier, A. F. Morphogen transport. *Development* **140,** 1621–1638 (2013).
7. Pomreinke, A. P. *et al.* Dynamics of BMP signaling and distribution during zebrafish dorsal-ventral patterning. *Elife* **6,** e25861 (2017).
8. Sprague, B. L., Pego, R. L., Stavreva, D. A. & McNally, J. G. Analysis of binding reactions by Fluorescence Recovery After Photobleaching. *Biophysical Journal* **86,** 3473–3495 (2004).
9. Hrabe, J., Hrabetová, S. & Segeth, K. A model of effective diffusion and tortuosity in the extracellular space of the brain. *Biophysical Journal* **87,** 1606–1617 (2004).
10. Tao, L. & Nicholson, C. Maximum geometrical hindrance to diffusion in brain extracellular space surrounding uniformly spaced convex cells. *Journal of Theoretical Biology* **229,** 59–68 (2004).
11. Novak, I. L., Kraikivski, P. & Slepchenko, B. M. Diffusion in cytoplasm: Effects of excluded volume due to internal membranes and cytoskeletal structures. *Biophysical Journal* **97,** 758–767 (2009).
12. Donovan, P., Chehreghanianzabi, Y., Rathinam, M. & Zustiak, S. P. Homogenization theory for the prediction of obstructed solute diffusivity in macromolecular solutions. *PLoS ONE* **11,** e0146093 (2016).
13. Student. The probable error of a mean. *Biometrika* **6,** 1–25 (1908).
14. Welch, B. L. The generalisation of Student's problems when several different population variances are involved. *Biometrika* **34,** 28–35 (1947).
15. Wilcoxon, F. Individual comparisons by ranking methods. *Biometrics Bulletin* **1,** 80–83 (1945).
16. Mann, H. B. & Whitney, D. R. On a test of whether one of two random variables is stochastically larger than the other. *The Annals of Mathematical Statistics* **18,** 50–60 (1947).
17. Shapiro, S. S. & Wilk, M. B. An analysis of variance test for normality (complete samples). *Biometrika* **52,** 591–611 (1965).
18. Akaike, H. A new look at the statistical model identification. *IEEE Transactions on Automatic Control* **19,** 716–723 (1974).
19. Kraft, L. J., Dowler, J. & Kenworthy, A. K. *Frap-Toolbox: Software for the analysis of Fluorescence Recovery After Photobleaching* (accessed: 2016-12-12). `http://www.fraptoolbox.com` (2014).
20. Aaron, J. *FRAP* (accessed: 2016-12-12). `https://de.mathworks.com/matlabcentral/fileexchange/47327-frap-zip` (2016).

21. Ulrich, M. *et al.* Tropical-parameter estimation and simulation of reaction-diffusion models based on spatio-temporal microscopy images. *Bioinformatics* **22,** 2709–2710 (2006).

22. Zhang, Z., Nadezhina, E. & Wilkinson, K. J. Quantifying diffusion in a biofilm of Streptococcus mutans. *Antimicrobial Agents and Chemotherapy* **3,** 1075–1081 (2011).

23. Pluen, A., Netti, P. A., Jain, R. K. & Berk, D. A. Diffusion of macromolecules in agarose gels: Comparison of linear and globular configurations. *Biophysical Journal* **1,** 542–552 (1999).

24. Guiot, E. *et al.* Molecular dynamics of biological probes by Fluorescence Correlation Microscopy with two-photon excitation. *Journal of Fluorescence* **4,** 413–419 (2000).

25. Braga, J., Desterro, J. M. & Carmo-Fonseca, M. Intracellular macromolecular mobility measured by Fluorescence Recovery After Photobleaching with confocal laser scanning microscopes. *Molecular Biology of the Cell* **15,** 4749–4760 (2004).

26. Periasamy, N. & Verkman, A. Analysis of fluorophore diffusion by continuous distributions of diffusion doefficients: application to photobleaching measurements of multicomponent and anomalous diffusion. *Biophysical Journal* **1,** 557–567 (1998).

27. Schuster, E., Hermansson, A. M., Öhgren, C., Rudemo, M. & Lorén, N. Interactions and diffusion in fine-stranded β-lactoglobulin gels determined via FRAP and binding. *Biophysical Journal* **1,** 253–262 (2014).

28. Gendron, P. O., Avaltroni, F. & Wilkinson, K. J. Diffusion coefficients of several rhodamine derivatives as determined by pulsed field gradient-nuclear magnetic resonance and Fluorescence Correlation Spectroscopy. *Journal of Fluorescence* **6,** 1093–1101 (2008).

29. Visser, N. V., Hink, M. A., Hoek, A. V. & Visser, A. J. Comparison between Fluorescence Correlation Spectroscopy and time-resolved fluorescence anisotropy as illustrated with a fluorescent dextran conjugate. *Journal of Fluorescence* **3,** 251–255 (1999).

30. Kihara, T., Ito, J. & Miyake, J. Measurement of biomolecular diffusion in extracellular matrix condensed by fibroblasts using Fluorescence Correlation Spectroscopy. *PLoS ONE* **11** (2013).

31. Peters, R. Nucleo-cytoplasmic flux and intracellular mobility in single hepatocytes measured by fluorescence microphotolysis. *The EMBO Journal* **8,** 1831–6 (1984).

32. Lang, I., Scholz, M. & Peters, R. Molecular mobility and nucleocytoplasmic flux in hepatoma cells. *Journal of Cell Biology* **4,** 1183–1190 (1986).

33. Gribbon, P. & Hardingham, T. E. Macromolecular diffusion of biological polymers measured by confocal Fluorescence Recovery After Photobleaching. *Biophysical Journal* **2,** 1032–1039 (1998).

34. Gorisch, S. M. Histone acetylation increases chromatin accessibility. *Journal of Cell Science* **24,** 5825–5834 (2005).

35. Keminer, O. & Peters, R. Permeability of single nuclear pores. *Biophysical Journal* **1,** 217–228 (1999).

36. Floury, J., Madec, M. N., Waharte, F., Jeanson, S. & Lortal, S. First assessment of diffusion coefficients in model cheese by Fluorescence Recovery After Photobleaching (FRAP). *Food Chemistry* **2,** 551–556 (2012).

37. Arrio-Dupont, M., Cribier, S., Foucault, G., Devaux, P. & D'Albis, A. Diffusion of fluorescently labeled macromolecules in cultured muscle cells. *Biophysical Journal* **5,** 2327–2332 (1996).

38. Terry, B., Matthews, E. & Haseloff, J. Molecular characterization of recombinant green fluorescent protein by Fluorescence Correlation Microscopy. *Biochemical and Biophysical Research Communications* **1,** 21–27 (1995).

39. Swaminathan, R., Hoang, C. & Verkman, A. Photobleaching recovery and anisotropy decay of green fluorescent protein GFP-S65T in solution and cells: cytoplasmic viscosity probed by green fluorescent protein translational and rotational diffusion. *Biophysical Journal* **4,** 1900–1907 (1997).

40. Gulot, E. *et al.* Heterogeneity of diffusion inside microbial biofilms determined by Fluorescence Correlation Spectroscopy under two-photon excitation. *Photochemistry and Photobiology* **6,** 570–8 (2002).

41. Müller, K. P. *et al.* Multiscale analysis of dynamics and interactions of heterochromatin protein 1 by fluorescence fluctuation microscopy. *Biophysical Journal* **11,** 2876–2885 (2009).

42. Waharte, F., Steenkeste, K., Briandet, R. & Fontaine-Aupart, M. P. Diffusion measurements inside biofilms by image-based Fluorescence Recovery After Photobleaching (FRAP) analysis with a commercial confocal laser scanning microscope. *Applied and Environmental Microbiology* **17,** 5860–5869 (2010).

43. Braeckmans, K., Peeters, L., Sanders, N. N., De Smedt, S. C. & Demeester, J. Three-dimensional Fluorescence Recovery After Photobleaching with the confocal scanning laser microscope. *Biophysical Journal* **4,** 2240–2252 (2003).

Supplementary Table 1. Combinations of image correction and smoothing methods used to analyze FRAP experiments (see Supplementary Fig. 3 for the results of this analysis). Note that flattening and normalization were never applied at the same time since this would have distorted the image data.

Combination	Normalization	Flattening	Background subtraction	Gaussian filter	Median filter
1	Off	Off	Off	Off	Off
2	Off	Off	Off	Off	On
3	Off	Off	Off	On	Off
4	Off	Off	Off	On	On
5	Off	Off	On	Off	Off
6	Off	Off	On	Off	On
7	Off	Off	On	On	Off
8	Off	Off	On	On	On
9	Off	On	Off	Off	Off
10	Off	On	Off	Off	On
11	Off	On	Off	On	Off
12	Off	On	Off	On	On
13	Off	On	On	Off	Off
14	Off	On	On	Off	On
15	Off	On	On	On	Off
16	Off	On	On	On	On
17	On	Off	Off	Off	Off
18	On	Off	Off	Off	On
19	On	Off	Off	On	Off
20	On	Off	Off	On	On
21	On	Off	On	Off	Off
22	On	Off	On	Off	On
23	On	Off	On	On	Off
24	On	Off	On	On	On

Supplementary Table 2. Statistical tools available in PyFRAP.

Method	Purpose	Type	Publication
Student's t-test	Significance testing	Parametric	[13]
Welch's t-test	Significance testing	Parametric	[14]
Wilcoxon signed-rank test	Significance testing	Non-parametric	[15]
Mann-Whitney U test	Significance testing	Non-parametric	[16]
Shapiro-Wilk test	Normality testing	Parametric	[17]
Akaike Information Criterion (AIC)	Model comparison	Parametric	[18]

Supplementary Table 3. Benchmarking PyFRAP against an in-house software combination of MATLAB and Comsol Multiphysics. Data was simulated with MATLAB and Comsol Multiphysics[5–7], and then fitted with PyFRAP for each of the four available reaction-diffusion models.

MATLAB + Comsol Multiphysics			***PyFRAP***			***R^2-value***		***AIC***
D (μm^2/s)	**Degradation (10^{-4}/s)**	**Production (10^{-4} [c]/s)**	**D (μm^2/s)**	**Degradation (10^{-4}/s)**	**Production (10^{-4} [c]/s)**	**Bleached window**	**Slice**	**Correct model prediction**
Pure diffusion								
1	0	0	1.0	0	0	0.998	0.972	yes
5	0	0	4.8	0	0	1.000	0.910	yes
10	0	0	9.5	0	0	1.000	0.932	yes
40	0	0	39.1	0	0	0.999	0.870	yes
110	0	0	109.4	0	0	0.999	0.984	yes
200	0	0	199.1	0	0	0.999	0.990	yes
Diffusion + degradation								
1	5.0	0	1.0	5.8	0	0.998	0.921	yes
5	5.0	0	4.9	5.5	0	1.000	0.959	yes
10	5.0	0	9.7	5.4	0	1.000	0.972	yes
40	5.0	0	39.0	5.0	0	0.999	0.950	yes
110	5.0	0	108.1	4.9	0	0.999	0.943	yes
200	5.0	0	198.0	5.0	0	0.999	0.982	yes
Diffusion + production								
1	0	5.0	1.0	0	4.4	0.999	0.950	yes
5	0	5.0	5.0	0	4.6	1.000	0.972	yes
10	0	5.0	9.8	0	4.7	1.000	0.978	yes
40	0	5.0	38.9	0	5.0	1.000	0.991	yes
110	0	5.0	108.3	0	5.1	1.000	0.998	yes
200	0	5.0	198.4	0	5.0	1.000	0.999	yes
Diffusion + production + degradation								
1	5.0	7.0	1.1	4.8	6.2	0.992	0.845	no
5	5.0	7.0	5.0	4.8	6.4	1.000	0.894	no
10	5.0	7.0	9.5	5.9	7.5	1.000	0.910	no
40	5.0	7.0	39.2	4.1	6.3	1.000	0.979	no
110	5.0	7.0	105.2	9.7	12.0	0.999	0.995	no
200	5.0	7.0	192.6	11.6	13.3	1.000	0.996	no

Supplementary Table 4. Selection of currently available FRAP analysis software packages.

Software	Fit type	Result type	Input data	Publication	Platform	Tested	Comments
easyFRAP	Analytical	Qualitive	CSV	[1]	Windows, Mac OSX	Yes	Requires Matlab Runtime, only produces $\tau_{1/2}$
FrapCalc	Analytical	Qualitive	CSV	[2]	Windows, Mac OSX	Yes	Requires IgorPro
virtualFRAP	Simulation	Quantitive	Image files	[3]	Windows	Yes	
FRAPToolbox	Simulation	Quantitive	Image files	[19]	Cross-platform	No	Unable to read non-OME formats
FRAP	Analytical	Qualitive	Image files	[20]	Cross-platform	No	Requires specialized Matlab toolboxes
Tropical	Simulation	Quantitive	Image files	[21]	Windows, Linux	No	Software unavailable
simFRAP	Simulation	Quantitive	Image files	[4]	Cross-platform	Yes	Fiji Plugin

Supplementary Table 5. Fluorescent samples used for *in vitro* experiments, and their calculated theoretical diffusion coefficients (see Materials and Methods for details). Theoretical values were only computed if an estimate of the molecule's Stokes radius could be found.

Fluorophore	Molecular weight (kDa)	Concentration (µM)	Manufacturer	Stokes radius (nm)	Theoretical D ($\mu m^2/s$)
Fluorescein-dextran	3	1	Thermo Fisher	1.36	171
FITC-dextran	4	1	Sigma-Aldrich	1.4	166
FITC-dextran	4	15	Sigma-Aldrich	1.4	166
FITC-dextran	4	100	Sigma-Aldrich	1.4	166
Fluorescein-dextran	40	1	Thermo Fisher	2.3	101
Fluorescein-dextran	70	1	Sigma-Aldrich	4.5	52
Fluorescein-dextran	70	1	Thermo Fisher	6.0	39
FITC-dextran	150	1	Sigma-Aldrich	8.5	27
Fluorescein-dextran	500	1	Thermo Fisher	15.8	15
GFP	25	4	Biovision	n.a.	n.a.
Dendra2	25	0.5	Hoelzel Diagnostics	n.a	n.a.

Supplementary Table 6. Diffusion coefficients determined by *in vitro* experiments and PyFRAP analysis. Theoretical values were only computed if an estimate of the molecule's Stokes radius could be found. Mean D values determined by PyFRAP as well as literature values are given with standard deviation.

			PyFRAP		***Literature***		
Dextran size (kDa)	**Manufacturer**	**D (µm²/s) theoretical**	**D (µm²/s) experimental**	**n**	**D (µm²/s) experimental**	**Technique**	**Reference**
3	Thermo Fisher	171	170.3 ± 21.9	19	161 ± 22	FCS	[22]
4	Sigma-Aldrich	166	181.1 ± 31.6	31	135 ± 10	FRAP	[23]
10	Thermo Fisher	101	83.1 ± 8.0	12	122 ± 4	FCS	[22]
40	Thermo Fisher	52	56.1 ± 15.1	14	47 ± 2	FCS	[22]
70	Thermo Fisher	39	27.7 ± 4.8	21	37 ± 7	FCS	[22]
70	Sigma-Aldrich	39	49.2 ± 5.6	31	30 ± 2	FRAP	[24]
150	Sigma-Aldrich	27	46.4 ± 5.6	31	26 ± 2	FRAP	[24]
500	Thermo Fisher	15	25.7 ± 1.8	11	23.2 ± 1.1	FRAP	[25]

Supplementary Table 7. Literature values used for Figure 5.

Molecule	MW (kDa)	Temperature during measurement (°C)	Manufacturer	D ($\mu m^2/s$)	Stdev ($\mu m^2/s$)	Technique	Reference
Fluorescein	0.33	22	Sigma-Aldrich	300	n.a.	FCS	[24]
Fluorescein	0.33	23	n.a.	270	n.a.	FRAP	[26]
Fluorescein	0.33	23	n.a.	260	n.a.	FRAP	[26]
Na2-Fluorescein	0.376	25	Fluka	380	35	FRAP	[27]
Oregon Green 488 carboxylic acid	0.41230	23	Thermo Fisher	336	11	FCS	[22]
Rhodamine B	0.47901	23	Fluka	420	20	FCS	[22]
Rhodamine B	0.47901	22.5	Sigma-Aldrich	420	30	FCS	[28]
Rhodamine 6 G	0.47901	22.5	Molecular Probes	400	30	FCS	[28]
Rhodamine 6 G	0.47901	23	Thermo Fisher	400	20	FCS	[22]
TetramethylRhodamine methyl ester	0.50093	23	Thermo Fisher	412	18	FCS	[22]
Oregon Green 488 carboxylic acid succinimidyl ester	0.50938	23	Thermo Fisher	308	10	FCS	[22]
Rhodamine green succinimdyl ester	0.621	20	Molecular Probes	233	3	FCS	[29]
Alexa488 alkyne	0.774	32	Life Technologies	288	8	FCS	[30]
Fluorescent dextran	3	23	Thermo Fisher	161	22	FCS	[22]
Alexa488-dextran	3	32	Life Technologies	160	5	FCS	[30]
FITC-dextran	3	22	Pharmacia	98	6	FRAP	[31]
FITC-dextran	3	n.a.	Pharmacia	98	6	FRAP	[32]
FITC-dextran	4	25	Sigma-Aldrich	149	n.a.	FRAP	[33]
FITC-dextran	4	25	Sigma-Aldrich	135	10	FRAP	[23]
FITC-dextran	4	32	Sigma-Aldrich	135	6	FCS	[30]
FITC-dextran	4	20	Sigma-Aldrich	96	2.4	FCS	[34]
FITC-dextran	4	22	Sigma-Aldrich	89	n.a.	FRAP	[35]
FITC-dextran	4	19	Sigma-Aldrich	155	23	FRAP	[36]
FITC-dextran	9.4	20	Sigma-Aldrich	75	3	FRAP	[37]
Fluorescent dextran	10	23	Thermo Fisher	122	4	FCS	[22]
Rhodamine green dextran	10	20	Molecular Probes	115	4	FCS	[29]
Alexa488-dextran	10	32	Life Technologies	82	1.4	FCS	[30]
FITC-dextran	10	22	Sigma-Aldrich	76	n.a.	FRAP	[31]
FITC-dextran	10	20	Sigma-Aldrich	68	1	FCS	[34]
FITC-dextran	11	n.a.	Sigma-Aldrich	76	2.5	FRAP	[32]
FITC-dextran	11	22	Sigma-Aldrich	76	3	FRAP	[31]
FITC-dextran	12	25	Sigma-Aldrich	97	n.a.	FRAP	[33]
FITC-Insulin	12	25	Sigma-Aldrich	147	13	FRAP	[33]
FITC-dextran	17	22	Sigma-Aldrich	65	n.a.	FRAP	[31]
FITC-dextran	17.2	20	Sigma-Aldrich	64	2	FRAP	[37]
FITC-dextran	18	22	Sigma-Aldrich	65	7	FRAP	[31]
FITC-dextran	18	n.a.	Sigma-Aldrich	65	6.5	FRAP	[32]
FITC-dextran	20	22	Sigma-Aldrich	78	n.a.	FCS	[24]
FITC-dextran	20	22	Sigma-Aldrich	64	2	FRAP	[24]
FITC-dextran	20	29	Sigma-Aldrich	70	8	FRAP	[36]
FITC-dextran	20	22	Sigma-Aldrich	63	4	FRAP	[25]
FITC-dextran	21	25	Sigma-Aldrich	71	n.a.	FRAP	[33]
GFP	26.9	25	custom-made	87	n.a.	FCS	[38]
GFP	26.9	n.a.	custom-made	87	n.a.	FRAP	[39]
GFP	26.9	22	Clontech	82	n.a.	FCS	[24]

FITC-dextran	35.6	20	Sigma-Aldrich	44	5	FRAP	[37]
FITC-dextran	38	25	Sigma-Aldrich	62	n.a.	FRAP	[33]
Fluorescent dextran	40	23	Thermo Fisher	47	2	FCS	[22]
FITC-dextran	40	22	Sigma-Aldrich	45	n.a.	FCS	[40]
FITC-dextran	40	22	Sigma-Aldrich	45	n.a.	FCS	[24]
FITC-dextran	40	32	Sigma-Aldrich	45	1.1	FCS	[30]
FITC-dextran	40	22	Sigma-Aldrich	44	5	FRAP	[24]
FITC-dextran	40	22	Sigma-Aldrich	52	2	FRAP	[25]
FITC-dextran	41	22	Sigma-Aldrich	46	5	FRAP	[31]
FITC-dextran	41	n.a.	Sigma-Aldrich	46	4.6	FRAP	[32]
FITC-dextran	42	20	Sigma-Aldrich	39	0.4	FCS	[34]
FITC-dextran	51	25	Sigma-Aldrich	54	n.a.	FRAP	[33]
FITC-dextran	62	n.a.	Sigma-Aldrich	39	2.6	FRAP	[32]
FITC-dextran	62	22	Sigma-Aldrich	39	3	FRAP	[31]
FITC-BSA	67	25	n.a.	58	5	FRAP	[33]
FITC-dextran	70	22	Sigma-Aldrich	38	n.a.	FCS	[24]
FITC-dextran	70	22	Sigma-Aldrich	38	n.a.	FCS	[40]
Fluorescent dextran	70	23	Thermo Fisher	37	7	FCS	[22]
FITC-dextran	70	n.a.	Fluka	33	2.1	FCS	[41]
FITC-dextran	70	22	Sigma-Aldrich	30	2	FRAP	[24]
FITC-dextran	70	25	Thermo Fisher	30	3.1	FRAP	[27]
FITC-dextran	70	23	n.a.	23	n.a.	FRAP	[26]
FITC-dextran	70	22	Sigma-Aldrich	44	1	FRAP	[25]
FITC-dextran	71	25	Sigma-Aldrich	44	2	FRAP	[23]
FITC-dextran	71.2	20	Sigma-Aldrich	30	2	FRAP	[37]
FITC-dextran	77	20	Sigma-Aldrich	35	0.6	FCS	[34]
FITC-dextran	148	20	Sigma-Aldrich	25	3.1	FCS	[34]
FITC-dextran	148	20	Sigma-Aldrich	18	1	FRAP	[37]
FITC-dextran	150	22	Sigma-Aldrich	26	2	FRAP	[24]
FITC-dextran	150	22	Sigma-Aldrich	24	n.a.	FCS	[40]
FITC-dextran	150	22	Sigma-Aldrich	24	n.a.	FCS	[24]
FITC-dextran	150	20	Sigma-Aldrich	14	n.a.	FRAP	[42]
FITC-dextran	157	n.a.	Sigma-Aldrich	24	1.3	FRAP	[32]
FITC-dextran	157	22	Sigma-Aldrich	24	1	FRAP	[31]
FITC-dextran	167	25	Sigma-Aldrich	38	n.a.	FRAP	[33]
FITC-dextran	167	n.a.	Sigma-Aldrich	18.8	0.2	FRAP	[43]
FITC-dextran	260	25	Sigma-Aldrich	30	n.a.	FRAP	[33]
FITC-dextran	282	20	Sigma-Aldrich	16.6	0.8	FCS	[34]
FITC-dextran	464	20	Sigma-Aldrich	14	0.6	FCS	[34]
FITC-dextran	464	n.a.	Sigma-Aldrich	11	0.5	FRAP	[43]
FITC-dextran	500	22	Sigma-Aldrich	23	1	FRAP	[25]
FITC-dextran	580	25	Sigma-Aldrich	22	n.a.	FRAP	[33]
FITC-dextran	2000	25	Sigma-Aldrich	10	1	FRAP	[23]
Fluorescent dextran	2000	23	Thermo Fisher	6	1	FCS	[22]
FITC-dextran	2000	n.a.	Sigma-Aldrich	6.4	0.09	FRAP	[43]
FITC-dextran	2101	25	Sigma-Aldrich	14	n.a.	FRAP	[33]

Supplementary Table 8. Summary of tortuosity simulations.

Dimension	Geometry	Packing	Extracelluar volume fraction (EVF) (%)	Tortuosity θ
2D	Circle	Regular	74	0.74
2D	Circle	Regular	59	0.61
2D	Circle	Random	56	0.57
2D	Circle	Random	36	0.49
2D	Circle	Ideal	25	0.44
3D	Cylinder	Regular	71	0.86
3D	Cylinder	Random	78	0.92
3D	Cylinder	Random	58	0.88
3D	Cylinder	Ideal	78	0.92
3D	Cylinder	Ideal	71	0.874
3D	Cylinder	Ideal	61	0.871
3D	Cylinder	Ideal	60	0.870
3D	Cylinder	Ideal	42	0.75
3D	Cuboid	Ideal	38	0.60

Supplementary Table 9. Diffusion coefficients determined by *in vitro* experiments and PyFRAP analysis in the presence of polyacrylamide beads. Mean diffusion values are given with standard error.

Dextran size (kDa)	Manufacturer	Condition	D ($\mu m^2/s$)	n
70	Thermo Fisher	Free	24.1 ± 0.4	13
70	Thermo Fisher	Beads	14.9 ± 0.5	17

Supplementary Table 10. Diffusion coefficients determined by *in vitro* and *in vivo* experiments and PyFRAP analysis with GFP and GFP fusion proteins. Mean diffusion values are given with standard error.

Molecule	**Manufacturer**	**Source**	**Condition**	**Context**	**D (µm^2/s) PyFRAP**	**n**
Recombinant GFP	Biovision	Protein	Free	*In vitro*	96.1 ± 2.2	23
Recombinant GFP	Biovision	Protein	Beads	*In vitro*	79.2 ± 4.1	18
Recombinant GFP	Biovision	Injected protein	Extracelluar matrix	*In vivo*	37.6 ± 3.7	15
Secreted GFP	In-house	Injected mRNA	Extracelluar matrix + production	*In vivo*	35.3 ± 4.8	17
Squint-GFP	In-house	Injected mRNA	Extracelluar matrix + production + binding	*In vivo*	1.7 ± 0.25	27

Supplementary Table 11. Parameters used for the simulation of FRAP experiments.

Variable	Definition	Default value
	Simulation	
D	Diffusion coefficient	$D = 50$ pixels^2/s
	Time stepping	
$t_{\mathrm{sim,start}}$	Simulation start time	0 s
$t_{\mathrm{sim,end}}$	Simulation end time	1680 s
n_{sim}	Number of time steps	4000
t_{scale}	Time-stepping scheme	Logarithmic
	Geometry	
r_{upper}	Upper radius of frustum	317.65 pixels
r_{lower}	Lower radius of frustum	224.25 pixels
h	Height of frustum	90.33 pixels
	Meshing	
v	Mesh element size	25 pixels^3
v_{BL}	Boundary layer element size	15 pixels^3
v_{slice}	Slice refinement element size	15 pixels^3
w_{BL}	Boundary layer thickness	30 pixels
	Solver	
ϵ	Solver tolerance	10^{-10}
N_{iter}	Solver iterations	1000

Supplementary Table 12. Fitting and model parameters, initial guesses, and bounded ranges. Note that we tried different initial guesses for the diffusion coefficient D, and then took the fit that yielded the minimum SSD to avoid that the minimization algorithm stops in a local minimum.

Initial guesses		
Parameter	**Initial guess**	**Allowed range**
D (pixels^2/s)	1 - 200	0.01 - 400
k_1 (1/s)	0	0 - 100
k_2 ([c]/s)	0	0 - 100
E_{bleached}	1	0.1 - 3
E_{slice}	1	0.1 - 3
Fitting convergence		
Parameter	**Definition**	**Default value**
$N_{\max}$	Maximum number of function calls	1000
δ	Tolerance of termination	10^{-10}

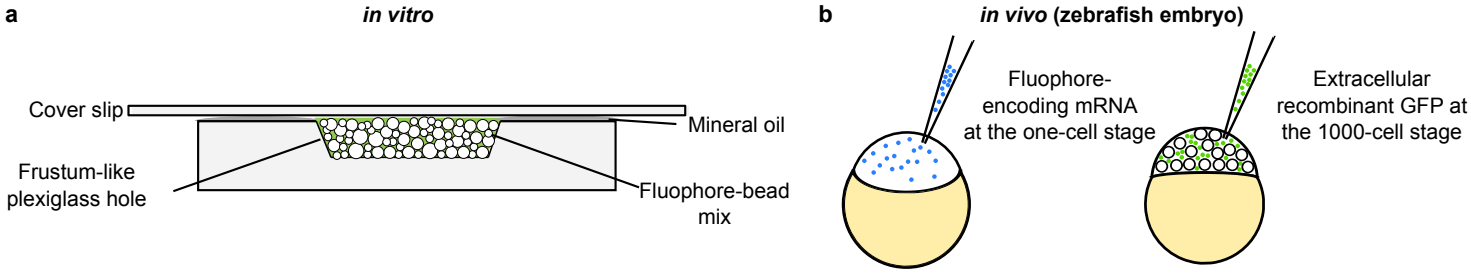

Supplementary Figure 1 | Sample preparation for *in vitro* and *in vivo* FRAP experiments. (a) *In vitro* experiments. Fluorophore solution was pipetted into a frustum-like plexiglass hole. The hole was then sealed with mineral oil and covered with a cover slip. The sample was flipped and placed under an inverted confocal microscope. **(b)** *In vivo* experiments in zebrafish embryos. mRNA encoding a fluorophore was injected into embryos at the one-cell stage, or recombinant GFP was injected into the extracellular space of embryos at the 1000-cell stage.

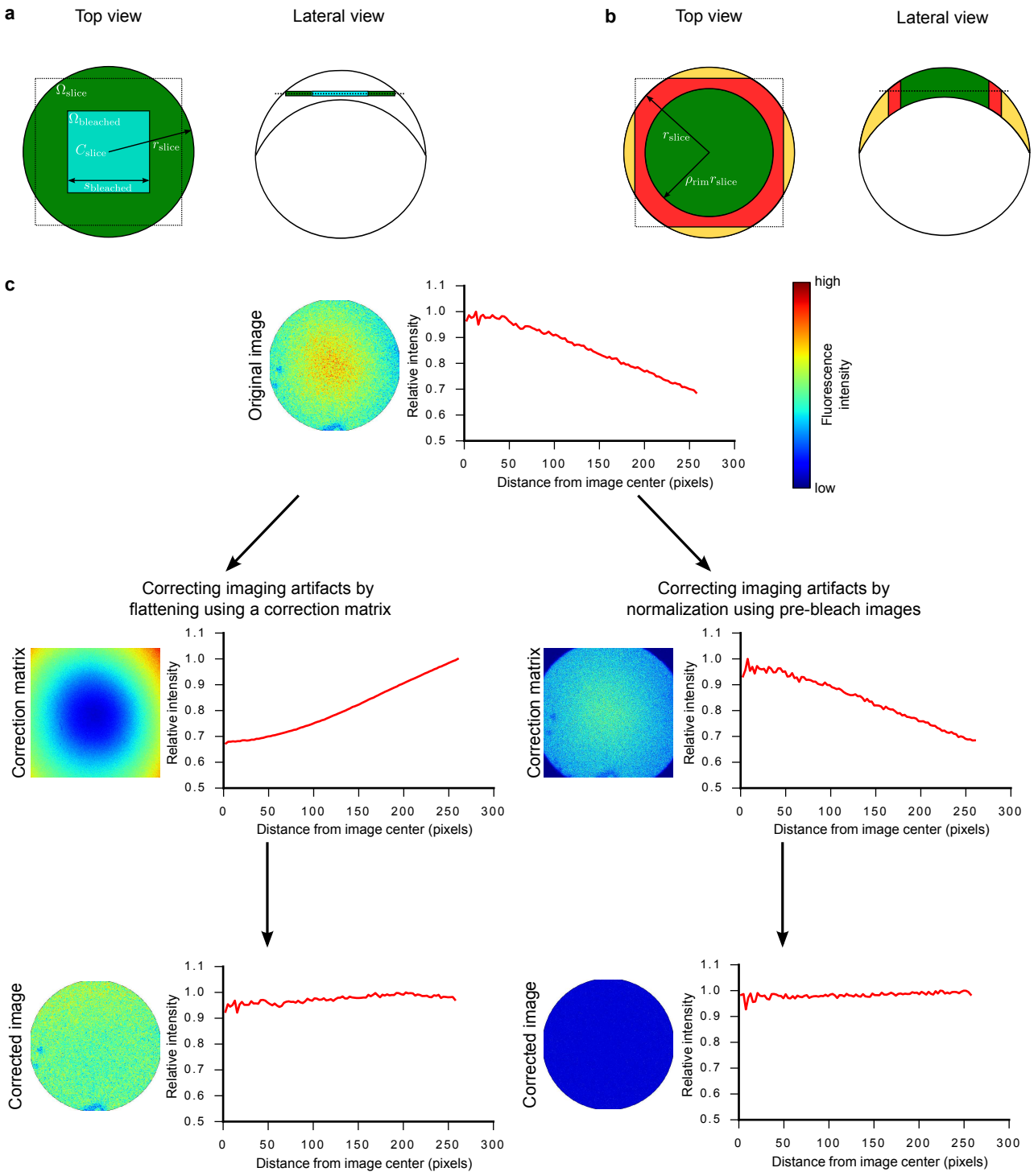

Supplementary Figure 2 | Image analysis in PyFRAP. (a) Basic regions of interest (ROIs) of FRAP analysis: The cyan square indicates the bleached region of the FRAP experiment inside the complete circular geometry within the imaging slice. The dashed lines indicate the location of the acquired image data. **(b)** Rim concentration calculation: Hypothetical data (orange) outside the acquired image (dashed line) is extrapolated through the average concentration in a slim rim of the visible fraction in the imaging slice (red). **(c)** Image manipulation techniques used to correct uneven illumination: Correction was either performed by multiplying the data with a correction matrix (flattening), or by dividing the data through an average pre-bleach image (normalization). The original image shows a pre-bleach measurement of a uniformly distributed fluorophore. Deviations from the theoretical flat intensity profile are due to imaging artifacts.

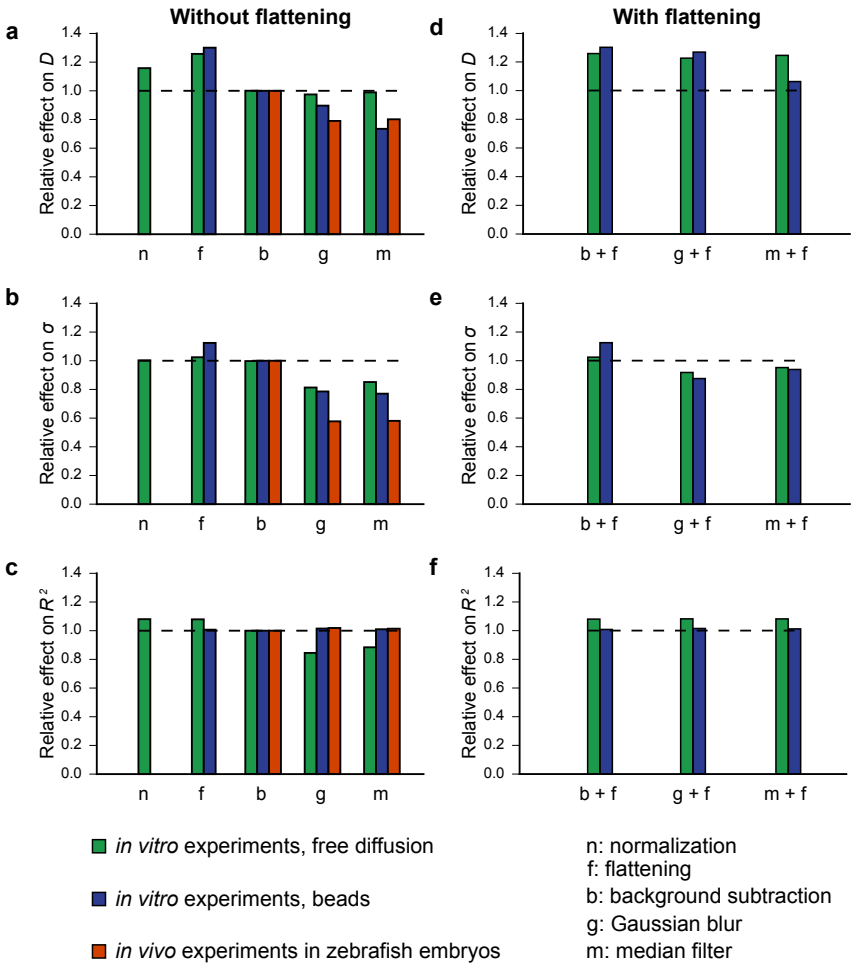

Supplementary Figure 3 | Analysis subset of image correction and smoothing techniques. Data sets were grouped by condition (*in vitro* experiments with free diffusion (green), *in vitro* experiments with beads (blue), and *in vivo* experiments in zebrafish embryos (orange)). Bar plots show the effect of each manipulation (n: normalization, f: flattening, b: background subtraction, g: Gaussian blur, m: median filter) compared to analyses in which no manipulation was applied. Values above or below the dashed line indicate that the manipulation had an effect. **(a,b,c)** Effect on mean diffusion coefficient D, standard deviation σ, and R^2-value if only one of the five image manipulation techniques was applied, respectively. **(e,d,f)** Effect if flattening and one of the three remaining manipulation techniques was applied. *In vivo* experiments with zebrafish embryos were excluded for this analysis (see Materials and Methods and Supplementary Text 1).

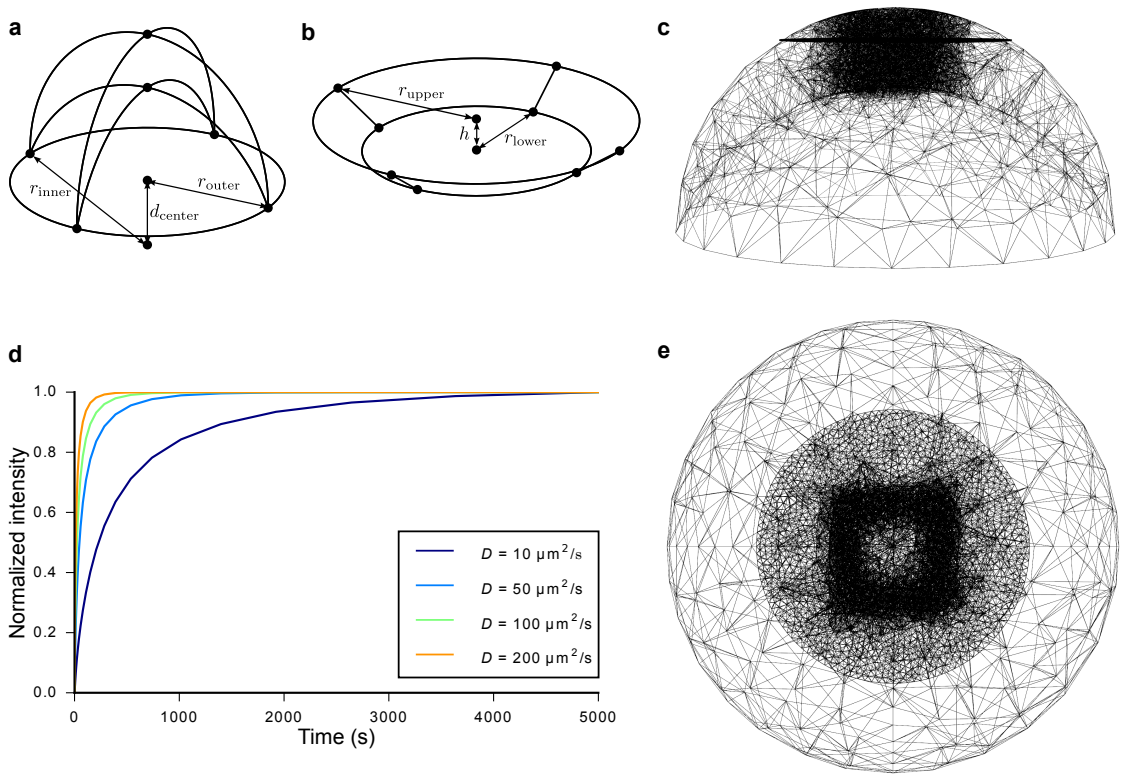

Supplementary Figure 4 | Simulation details for PyFRAP analysis. (a) The zebrafish dome geometry used to analyze *in vivo* experiments is described by the distance between the centers (d_{center}) and the radii (r_{inner}, r_{outer}) of two hemispheres. **(b)** The frustum geometry used to analyze *in vitro* experiments is described by the upper (r_{upper}) and lower (r_{lower}) radius and its height h. **(c)** Lateral and top views of tetrahedral meshes in the zebrafish dome geometry with a boundary layer mesh around the bleached area and a refined mesh in the imaging slice. **(d)** Scaling solution of a simulated FRAP recovery curve for different diffusion coefficients.

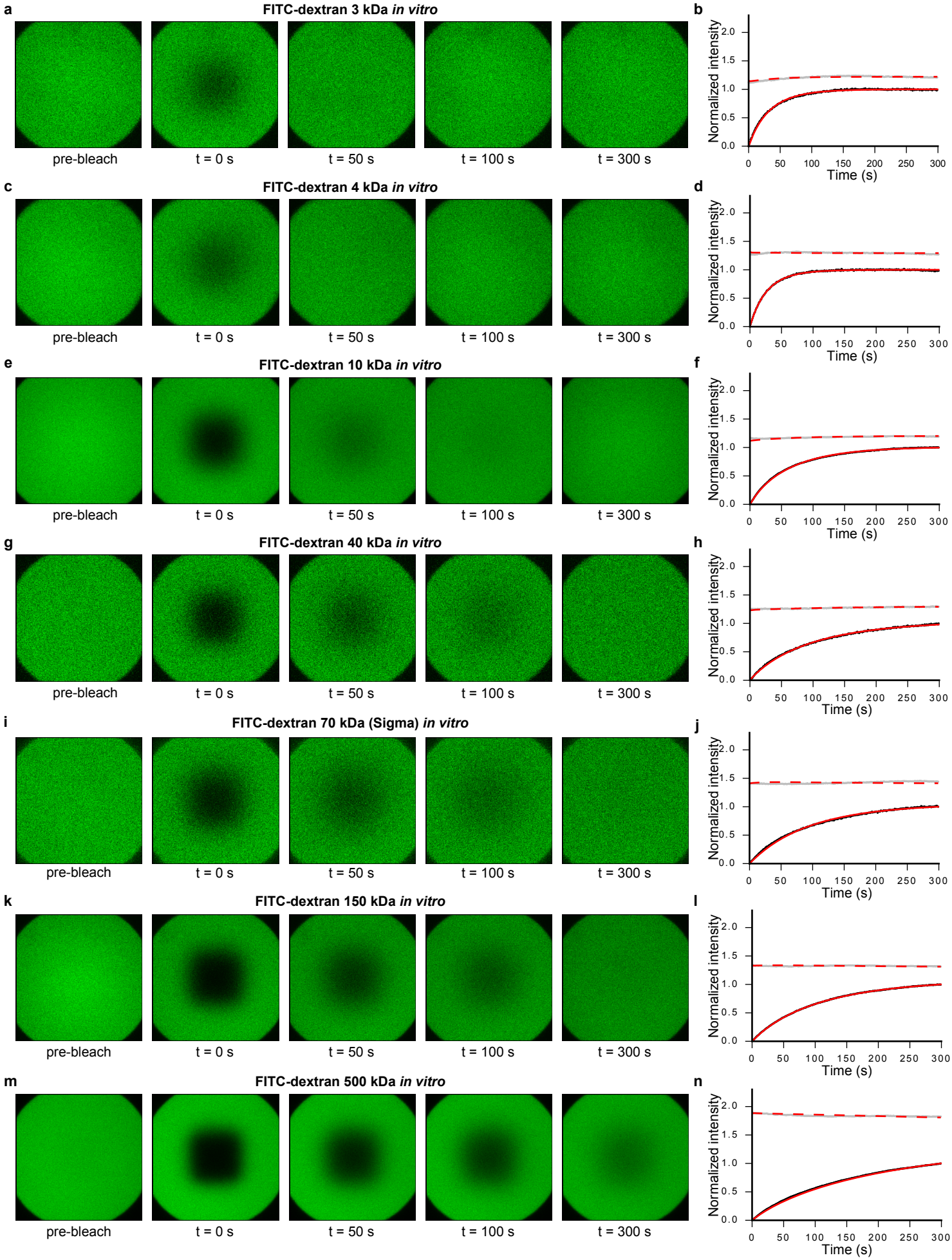

Supplementary Figure 5 | Examples of *in vitro* experiments and the resulting fits to measure free diffusion. (a,c,e,g,i,k,m) *In vitro* FRAP experiments with FITC-dextrans ranging from 3 kDa to 500 kDa. Maximum image intensities are the average pre-conversion intensities to facilitate comparison across data sets. **(b,d,f,h,j,l,n)** Black and gray dots represent data points of bleached and slice ROI, respectively. Red solid and dashed lines show the respective fits. Recovery curves were normalized between 0 (intensity in the bleached ROI at the first post-bleach time point) and 1 (intensity in the bleached ROI at the last post-bleach time point) to facilitate comparison across data sets.

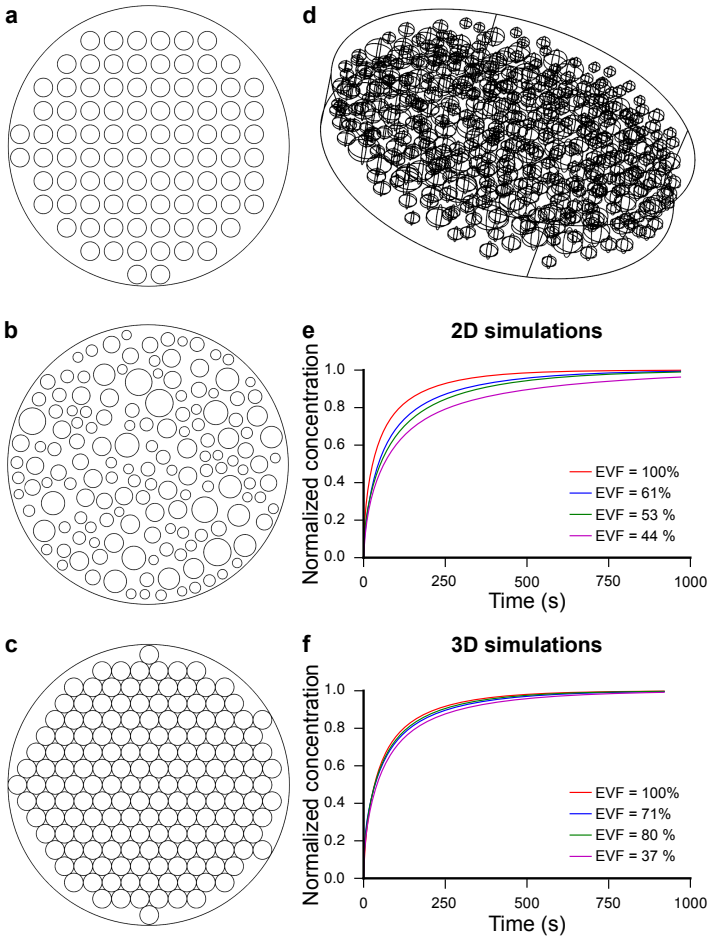

Supplementary Figure 6 | Simulations of tortuous environments in bead experiments. (a,b,c) Regularly (EVF = 59%), randomly (EVF = 56%), and ideally (EVF = 25%) placed beads in a two-dimensional circular domain. **(d)** Randomly (EVF = 78%) placed beads in a three-dimensional cylindrical domain. **(e,f)** Comparison between recovery curves in 2D and 3D bead simulations. Red lines indicate simulations without beads, blue lines indicate simulations with regularly placed beads, green lines indicate simulations with randomly placed beads, and magenta lines indicate simulations with ideally placed beads.

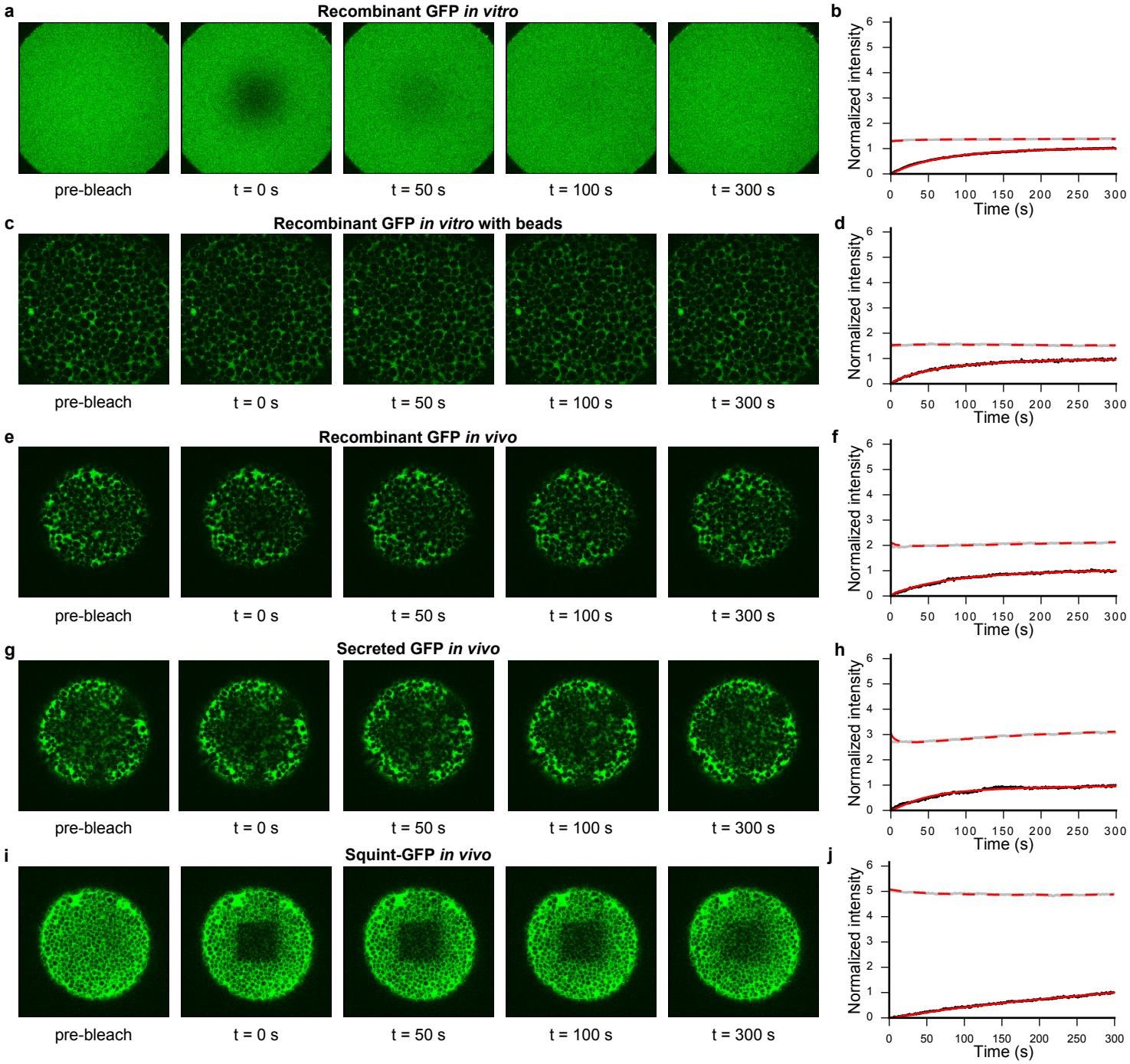

Supplementary Figure 7 | Examples of *in vitro* and *in vivo* experiments and the resulting fits. (a,b) *In vitro* FRAP experiment with recombinant GFP. **(c,d)** *In vitro* FRAP experiment with recombinant GFP mixed with polyacrylamide beads. **(e,f,g,h,i,j)** *In vivo* FRAP experiment in zebrafish embryos with recombinant GFP, secreted GFP, and Squint-GFP, respectively. **(b,d,f,h,j)** Black and gray dots represent data points of bleached and slice ROI, respectively. Red solid and dashed lines show the respective fits. Recovery curves were normalized between 0 (intensity in the bleached ROI at the first post-bleach time point) and 1 (intensity in the bleached ROI at the last post-bleach time point) to facilitate comparison across data sets.

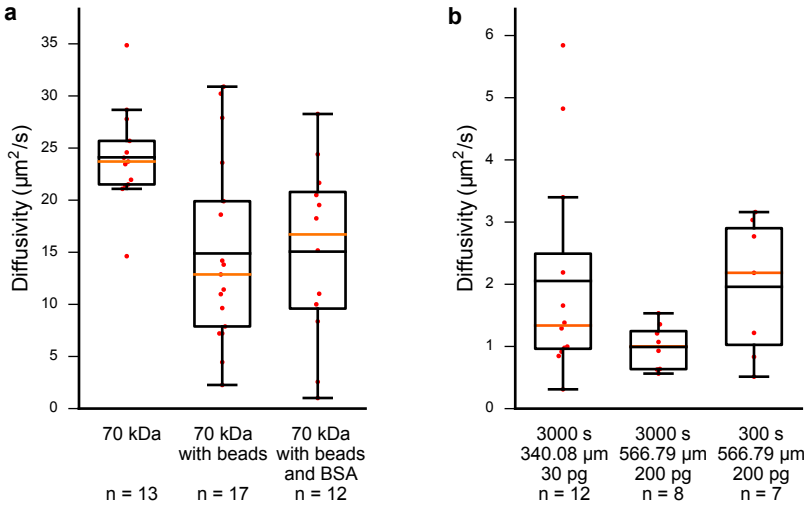

Supplementary Figure 8 | Results of control experiments for *in vitro* and *in vivo* FRAP experiments. (a) Results of control experiments with fluorescent dextran (70 kDa), and beads with or without BSA. BSA does not influence the diffusion of the fluorescent dextran. Box plot shows median (orange line), mean (black line), 25% quantiles (box), and all included data points (red markers). **(b)** Results of control experiments for different amounts (30 - 200 pg) of injected *Squint-GFP* mRNA, varying length of experiments (300 - 3000 s) and magnification (image size: 340.08 - 566.79 µm). Different imaging settings do not affect the measured diffusion coefficient of Squint-GFP. Box plot shows median (orange line), mean (black line), 25% quantiles (box), and all included data points (red markers).

eLIFE elifesciences.org

RESEARCH ARTICLE

Dynamics of BMP signaling and distribution during zebrafish dorsal-ventral patterning

Autumn P Pomreinke†, Gary H Soh†, Katherine W Rogers†, Jennifer K Bergmann, Alexander J Bläßle, Patrick Müller*

Systems Biology of Development Group, Friedrich Miescher Laboratory of the Max Planck Society, Tübingen, Germany

Abstract During vertebrate embryogenesis, dorsal-ventral patterning is controlled by the BMP/Chordin activator/inhibitor system. BMP induces ventral fates, whereas Chordin inhibits BMP signaling on the dorsal side. Several theories can explain how the distributions of BMP and Chordin are regulated to achieve patterning, but the assumptions regarding activator/inhibitor diffusion and stability differ between models. Notably, 'shuttling' models in which the BMP distribution is modulated by a Chordin-mediated increase in BMP diffusivity have gained recent prominence. Here, we directly test five major models by measuring the biophysical properties of fluorescently tagged BMP2b and Chordin in zebrafish embryos. We found that BMP2b and Chordin diffuse and rapidly form extracellular protein gradients, Chordin does not modulate the diffusivity or distribution of BMP2b, and Chordin is not required to establish peak levels of BMP signaling. Our findings challenge current self-regulating reaction-diffusion and shuttling models and provide support for a graded source-sink mechanism underlying zebrafish dorsal-ventral patterning.
DOI: https://doi.org/10.7554/eLife.25861.001

***For correspondence:** pmueller@tuebingen.mpg.de

†These authors contributed equally to this work

Competing interests: The authors declare that no competing interests exist.

Funding: See page 27

Received: 08 February 2017
Accepted: 30 August 2017
Published: 31 August 2017

Reviewing editor: Deborah Yelon, University of California, San Diego, United States

Introduction

The dorsal-ventral axis is one of the earliest coordinate systems established during animal development and divides the embryo into dorsal (back) and ventral (belly) territories. This axis forms under the influence of the BMP/Chordin patterning system. The activator BMP induces the formation of ventral tissues, and BMP signaling is antagonized on the dorsal side by the inhibitor Chordin. There are currently several disparate models that can explain how BMP signaling is restricted to the ventral side (***Ben-Zvi et al., 2008***; ***Barkai and Ben-Zvi, 2009***; ***Francois et al., 2009***; ***Ben-Zvi et al., 2011b***; ***Inomata et al., 2013***; ***Ramel and Hill, 2013***; ***Ben-Zvi et al., 2014***), but the underlying biophysical assumptions have not been fully tested.

In the 'Graded source-sink + mobile BMP model' (Model 1), BMP is produced in a graded, ventrally biased source, and signaling from diffusing BMP is antagonized by binding to its inhibitor Chordin (***Figure 1—figure supplement 1***, ***Table 1***). Chordin (Chd) diffuses from a localized source on the opposing dorsal side and therefore provides a 'sink' that inactivates BMP molecules diffusing through the embryo, helping to shape the signaling distribution into a gradient that peaks ventrally. The distributions of *bmp* and *chd* mRNA in developing embryos are consistent with this idea – initially nearly uniform *bmp* expression refines to a ventrally biased gradient over time (***Ramel and Hill, 2013***; ***Zinski et al., 2017***), and *chd* expression is restricted to the dorsal region (***Miller-Bertoglio et al., 1997***).

Similar to Model 1, BMP signaling activity in the 'Graded source-sink + immobile BMP model' (Model 2, ***Figure 1—figure supplement 1***, ***Table 1***) is also restricted by the inhibitor Chordin diffusing from the dorsal side. However, Model 2 assumes that BMP does not diffuse (***Ramel and Hill,***

eLife digest Animals start life as clumps of cells that ultimately give rise to complex structures and organs. Over a century of research has revealed a small number of proteins that are crucial for complex structures to form from these clumps, including one protein called BMP. Different levels of BMP instruct cells to give rise to different tissues. In zebrafish, BMP is more abundant on one side of the embryo than the other. This gradient in BMP levels causes different tissues to form at distinct positions and helps coordinate embryo development.

Several theories have been proposed to explain how the BMP gradient is established. They all suggest that a second protein – Chordin – plays an important role in influencing how cells sense the BMP gradient by blocking BMP's activity. However, the exact role of Chordin in the formation of the BMP gradient is disputed. To address this, Pomreinke, Soh, Rogers et al. directly tested five theories of how BMP and Chordin molecules spread through embryos.

The experiments used microscopy to track the movements of fluorescent versions of both molecules in zebrafish embryos. The measurements contradict one theory stating that BMP does not move, and another in which Chordin increases the mobility of BMP. Pomreinke, Soh, Rogers et al. also found that embryos that lack Chordin have increased BMP signaling levels only on the side where Chordin is normally made but not on the opposite side where BMP is made, ruling out several of the theories. The findings are most consistent with the idea that the BMP gradient forms mainly as a result of higher production of BMP on one side of the embryo combined with movement of BMP away from where it is made. Chordin produced at the opposite end of the embryo helps to ensure that only the correct cells receive instructions from BMP.

In the future, two approaches could further clarify how the BMP gradient is formed. First, better techniques to directly observe the BMP gradient in normally developing embryos would be useful. Second, new theories that take into account additional players other than BMP and Chordin might help explain some features of development that current theories cannot address. Uncovering the mechanisms that control the formation of BMP gradients will improve our understanding of how clumps of cells can develop into animals.

DOI: https://doi.org/10.7554/eLife.25861.002

2013) and that it binds to Chordin with weaker affinity than in Model 1 (see Materials and methods). Proponents have argued that the similarities between the graded *bmp* mRNA distribution, signaling gradient, and target gene expression indicate negligible BMP diffusion during patterning (***Ramel and Hill, 2013***). Consistent with this, BMP4 was unable to induce long-range signaling in *Xenopus* experiments (***Jones et al., 1996***), although BMP target genes are induced outside of BMP-expressing clones in zebrafish (***Xu et al., 2014***). However, measuring the diffusivity of BMP *in vivo* is the most direct way to determine whether BMP is mobile (***Kicheva et al., 2007***; ***Zinski et al., 2017***).

Although these two relatively simple models are generally supported by biological observations, they do not take into account other regulators known to be crucial for dorsal-ventral patterning, such as the BMP-like ligand ADMP, and Sizzled, an inhibitor of the Chordin protease Tolloid/Xlr. Three models described below include these important dorsal-ventral regulators in addition to BMP and Chordin and have also been shown to explain scale-invariant patterning, a phenomenon in which embryos adjust their tissue proportions to differently sized patterning fields.

The recent 'Long-range accumulation and feedback model' (Model 3, ***Figure 1—figure supplement 1***, ***Table 1***) postulates that BMP and Chordin have equally high mobility, but that dorsal-ventral patterning is controlled by differences in BMP and Chordin protein stability (***Inomata et al., 2013***). In this model, BMP and ADMP induce the secreted, highly diffusible and stable Chordin protease inhibitor Sizzled. This protects Chordin from proteolysis and promotes its expansion towards the ventral side. Over time the resulting inhibition of BMP signaling leads to decreased Sizzled production, destabilizing Chordin and relieving inhibition of BMP. In this way, an appropriate balance between ventral BMP and dorsal Chordin levels can be established even in differently sized embryos.

In the 'Self-regulating reaction-diffusion model' (Model 4, ***Figure 1—figure supplement 1***, ***Table 1***), BMP and Chordin both have low diffusivities and equivalent protein stabilities. Interactions with highly mobile ADMP and Sizzled in two coupled reaction-diffusion networks eventually result in

Table 1. Summary of model assumptions, predictions, and experimental findings.
Model assumptions or predictions that are consistent with the experimental findings (gray) are highlighted in green. NA: no testable model assumptions or predictions.

	Model 1 Graded source-sink (mobile BMP)	Model 2 Graded source-sink (immobile BMP)	Model 3 Long-range accumulation and feedback	Model 4 Self-regulating reaction-diffusion system	Model 5 Shuttling	Experimental findings
Diffusivity of BMP and Chordin	D(BMP) > 0 D(BMP) < D(Chd)	D(BMP) ≈ 0 D(Chd) high	D(BMP) ≈ D(Chd) High	D(BMP) ≈ D(Chd) Low	D(BMP) << D(Chd)	D(BMP) ≤ D(Chd) (≈2 and 6 μm^2/s)
Effect of Chordin on BMP diffusivity	No effect	No effect	No effect	No effect	Chd enhances BMP diffusion	No effect
Half-life of BMP and Chordin	τ(BMP) ≈ τ(Chd)	Unconstrained	τ(BMP) >> τ(Chd)	τ(BMP) ≈ τ(Chd)	τ(BMP) > τ(Chd)*	τ(BMP) ≈ τ(Chd) (130 and 120 min)
pSmad gradient formation kinetics	Progressive rise ventrally, always low dorsally	Progressive rise ventrally, always low dorsally	Initially high dorsally and ventrally	Progressive rise ventrally, always low dorsally	Progressive rise ventrally, always low dorsally	Progressive rise ventrally, always low dorsally
Ventral pSmad peak decreased in the absence of Chordin?	No	No	No	No	Yes	No
Dorso-lateral pSmad expansion in the absence of Chordin?	Yes	Yes	Yes	No	Yes	Yes
Diffusivity of Sizzled relative to BMP/Chordin	NA	NA	D(ADMP) & D(Szl) ≈ D(BMP) & D (Chd)	D(ADMP) & D (Szl) >> D(BMP) & D (Chd)	NA	D(Szl) ≈ D(BMP) & D(Chd) (≈10, 2, and 6 μm^2/s)

*The simplified shuttling model without ADMP presented here is based on the experimentally measured clearance rate constants of BMP and Chordin; the full model for scale-invariant patterning including ADMP (***Ben-Zvi et al., 2008***) assumes a lower stability of Chordin due to Xlr-mediated degradation.
DOI: https://doi.org/10.7554/eLife.25861.003

the restriction of BMP signaling activity on the ventral side, assuming an initial dorsal Chordin or ventral BMP bias (***Francois et al., 2009***). Such a system self-regulates even with noisy initial conditions and could provide robustness during embryogenesis – e.g., the ability of developing organisms to withstand noise in gene expression or fluctuating environmental conditions – that can be difficult to explain with other models.

Finally, the prominent 'Shuttling model' (Model 5, ***Figure 1—figure supplement 1***, ***Table 1***) postulates that Chordin not only acts as an inhibitor of BMP, but also modulates the mobility and distribution of BMP protein (***Ben-Zvi et al., 2008***; ***Barkai and Ben-Zvi, 2009***; ***Ben-Zvi et al., 2011b***; ***Ben-Zvi et al., 2014***). In this model, BMP is poorly diffusive, Chordin is highly diffusive, and BMP mobility increases when bound to Chordin. Cleavage of the BMP/Chordin complex by the uniformly distributed protease Tolloid/Xlr combined with a flux of Chordin from the dorsal side is thought to 'shuttle' BMP towards the ventral side by facilitated diffusion over time. In this way, Chordin is responsible for the accumulation of BMP protein on the ventral side, and actively helps establish the subsequent ventral BMP signaling peak.

These five conflicting models postulate different diffusion (no diffusion, equal diffusion, differential diffusion, facilitated diffusion) and stability properties of BMP and Chordin proteins (***Table 1***, ***Figure 1—figure supplement 1***). However, these biophysical properties have not been fully measured experimentally, in part due to the lack of reagents and techniques to detect active BMP and Chordin in living vertebrate embryos. To test the biophysical tenets of these models, we developed active BMP and Chordin fluorescent fusion proteins, and used a combination of mathematical modeling and quantitative experiments to determine how BMP2b and Chordin gradients form. Additionally, we tested the distinct predictions that the five models make about how BMP signaling changes in the absence of Chordin. We found that (i) BMP2b and Chordin proteins have similar stabilities, (ii) both BMP2b and Chordin diffuse and form gradients in the extracellular space, and (iii) Chordin does not significantly facilitate BMP2b diffusion or play an active role in establishing peak ventral BMP signaling levels. Together, our results are most consistent with dorsal-ventral patterning mediated by Model 1, the 'Graded source-sink + mobile BMP' model.

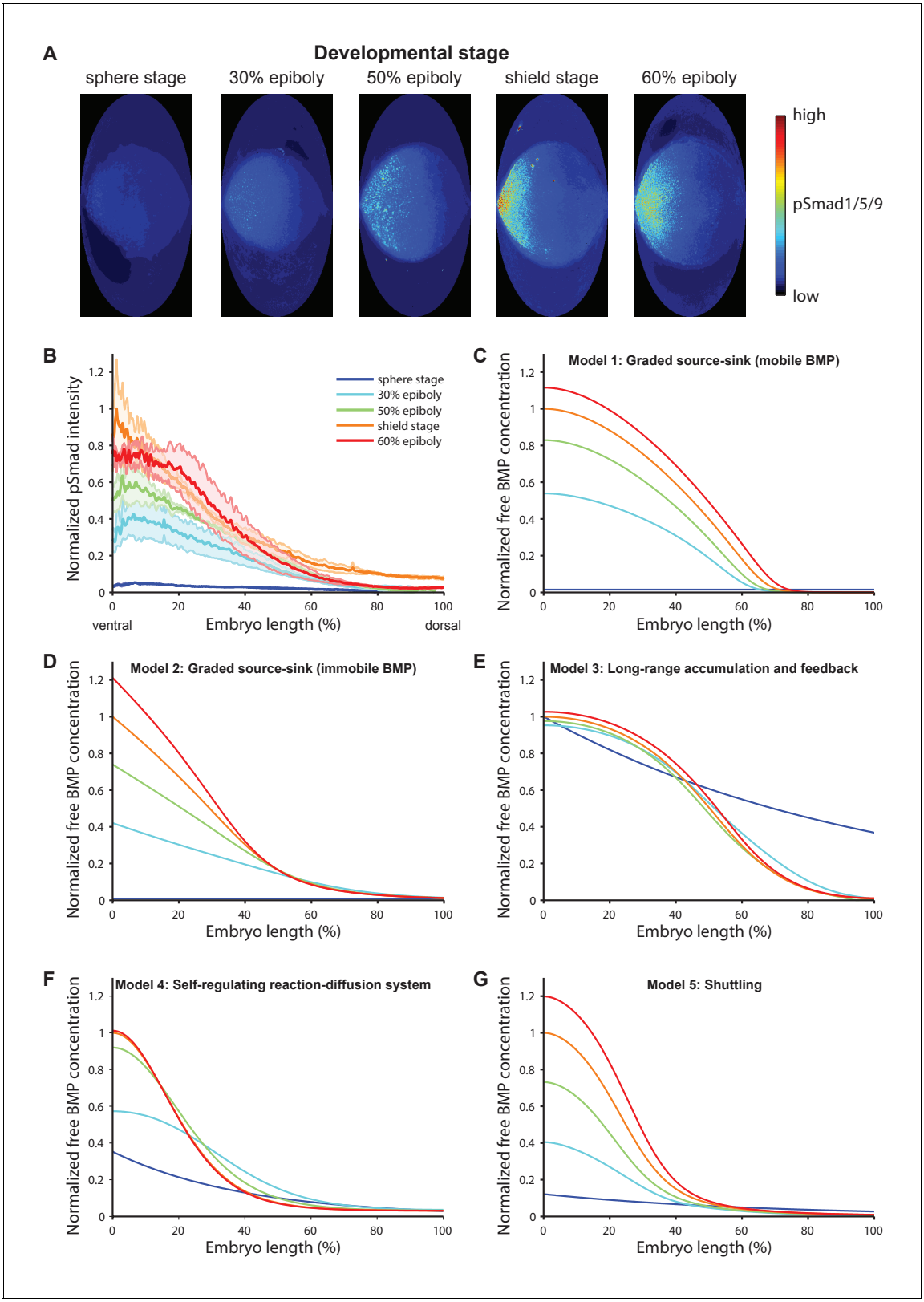

Figure 1. BMP signaling (pSmad1/5/9) gradient formation and simulations of five major dorsal-ventral patterning models over relevant zebrafish developmental stages (3 hr). (**A**) Two-dimensional Hammer-Aitoff projections (2D maps) of pSmad1/5/9-immunostained individual wild type zebrafish embryos at different developmental stages. Embryos were imaged using light sheet microscopy (see Materials and methods for details). (**B**) Quantification of ventral-to-dorsal average pSmad1/5/9 distributions in one-dimensional projections of 2D maps generated for embryos at different

Figure 1 continued on next page

Figure 1 continued

developmental stages (n = 3 for each stage) as in (**A**). Error bars denote standard error. (**C–G**) Gradient formation kinetics simulated for Models 1–5 at relevant zebrafish developmental stages.

DOI: https://doi.org/10.7554/eLife.25861.004

The following figure supplement is available for figure 1:

Figure supplement 1. Mathematical formulation of five major models of BMP/Chordin-mediated dorsal-ventral patterning.

DOI: https://doi.org/10.7554/eLife.25861.005

Results

Chordin does not actively establish peak ventral BMP signaling

BMP signaling induces phosphorylation and nuclear localization of the transcriptional effectors Smad1/5/9 (***Schier and Talbot, 2005***). To quantitatively measure BMP signaling activity during early dorsal-ventral patterning, we imaged pSmad1/5/9-immunostained zebrafish embryos fixed at different developmental stages using *in toto* light sheet microscopy, converted pSmad1/5/9 signaling activities into information-compressed two-dimensional maps (***Schmid et al., 2013***), and quantified pSmad1/5/9 intensities along the ventral-dorsal axis (***Figure 1A***, Materials and methods). Over the course of approximately 3 hr during early zebrafish development, BMP signaling rapidly shifts from a low-level near-uniform distribution to a gradient with peak levels on the ventral side (***Figure 1A+B***, ***Videos 1–5***) (***Tucker et al., 2008***), similar to changes in the distribution of *bmp2b* mRNA over time (***Ramel and Hill, 2013***; ***Zinski et al., 2017***). We simulated pSmad1/5/9 gradient formation kinetics predicted by each of the five models over a similar time period (***Figure 1C–G***). Our measurements are consistent with the gradient kinetics predicted by Models 1, 2, 4, and 5, whereas the dynamics predicted by Model 3 do not resemble the experimentally observed distributions.

All five major models of BMP/Chordin-mediated dorsal-ventral patterning qualitatively explain the formation of a ventral signaling peak, but they assign different roles to the inhibitor Chordin (***Figure 2A–E***, ***Table 1***, and ***Figure 1—figure supplement 1***). Models 1 and 2 assume that a flux of the inhibitor Chordin from the dorsal side restricts the range of BMP signaling activity throughout the embryo. They thus predict that in the absence of Chordin, BMP signaling should be expanded throughout the embryo with a small increase in the peak levels on the ventral side (***Figure 2A+B***). Model 3 adds an additional regulatory layer: Here, the abundance of Chordin is regulated by feedback interactions that modify its stability and affect ventral BMP signaling levels (***Figure 1—figure supplement 1***). Similar to Models 1 and 2, Model 3 also predicts that in the absence of Chordin, BMP signaling should be expanded throughout the embryo (***Figure 2C***).

In Model 4, two reaction-diffusion systems involving BMP/Sizzled and Chordin/ADMP are coupled. In a completely homogenous field of cells with no initial expression biases, this self-organizing system would give rise to both ventral and dorsal BMP peaks (***Francois et al., 2009***). To achieve a single ventral BMP peak, an initial dorsal Chordin or ventral BMP bias is required (see Materials and methods). Under these conditions, the initial advantage in BMP signaling on the ventral side is amplified by autoregulation of BMP production. Since Chordin inhibits the autoregulation of BMP production, the absence of Chordin leads to a more pronounced ventral BMP peak but has no effect in the rest of the embryo (***Figure 2D***). Model 4 thus predicts that in the absence of Chordin, pSmad1/5/9 levels would be increased on the ventral but not the dorsal side.

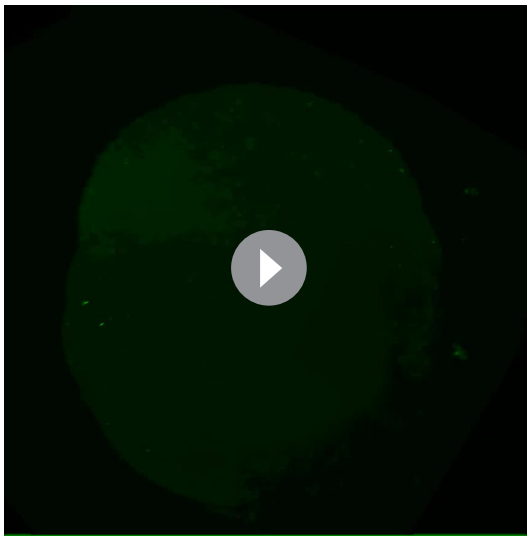

Video 1. 3D reconstruction of pSmad1/5/9 localization in a wild type sphere stage zebrafish embryo imaged by light sheet microscopy.

DOI: https://doi.org/10.7554/eLife.25861.006

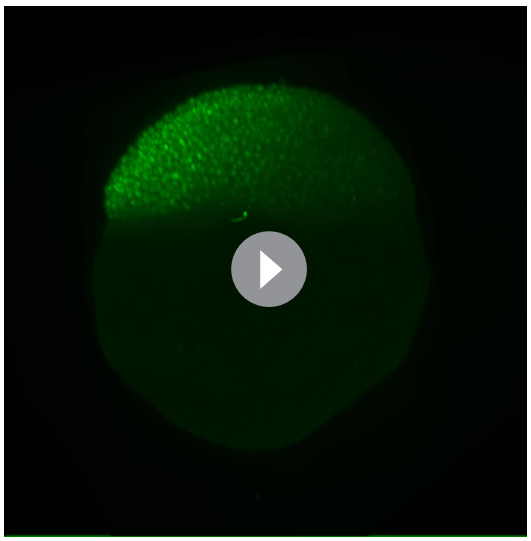

Video 2. 3D reconstruction of pSmad1/5/9 localization in a wild type 30% epiboly stage zebrafish embryo imaged by light sheet microscopy.
DOI: https://doi.org/10.7554/eLife.25861.007

Video 3. 3D reconstruction of pSmad1/5/9 localization in a wild type 50% epiboly stage zebrafish embryo imaged by light sheet microscopy.
DOI: https://doi.org/10.7554/eLife.25861.008

In contrast to Models 1–4, Model 5 assigns a more active role to Chordin in promoting the ventral BMP signaling peak. This model proposes that Chordin activity results in *increased* BMP signaling ventrally: Chordin increases ventral BMP levels by binding to and physically moving BMP protein towards the ventral side. This model therefore predicts that in embryos lacking Chordin, BMP signaling should be lower on the ventral side compared to wild type embryos (***Figure 2E***).

To experimentally test these predictions, we quantitatively measured BMP signaling activity in fixed *chordin*$^{-/-}$ zebrafish embryos (***Video 6***) and their wild type siblings using pSmad1/5/9 immunostaining and *in toto* light sheet microscopy. Strikingly, BMP signaling was increased in dorso-lateral domains in *chordin*$^{-/-}$ mutants compared to wild type embryos, but BMP signaling on the

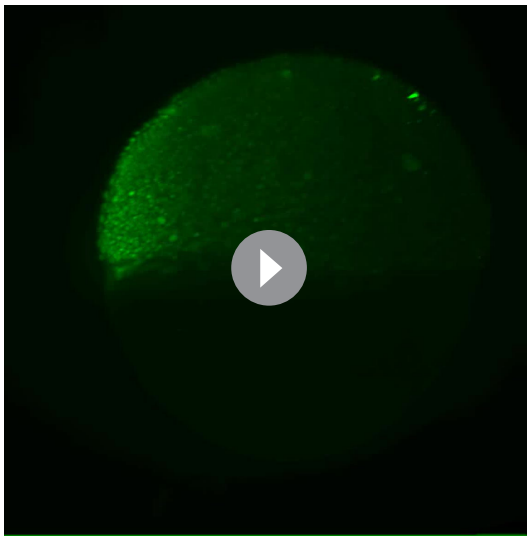

Video 4. 3D reconstruction of pSmad1/5/9 localization in a wild type shield stage zebrafish embryo imaged by light sheet microscopy.
DOI: https://doi.org/10.7554/eLife.25861.009

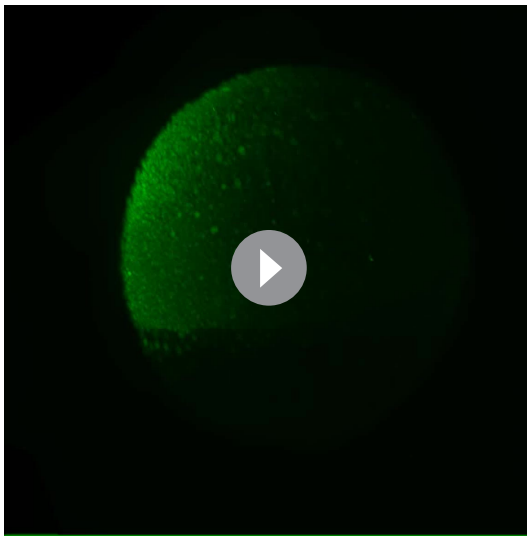

Video 5. 3D reconstruction of pSmad1/5/9 localization in a wild type 60% epiboly stage zebrafish embryo imaged by light sheet microscopy.
DOI: https://doi.org/10.7554/eLife.25861.010

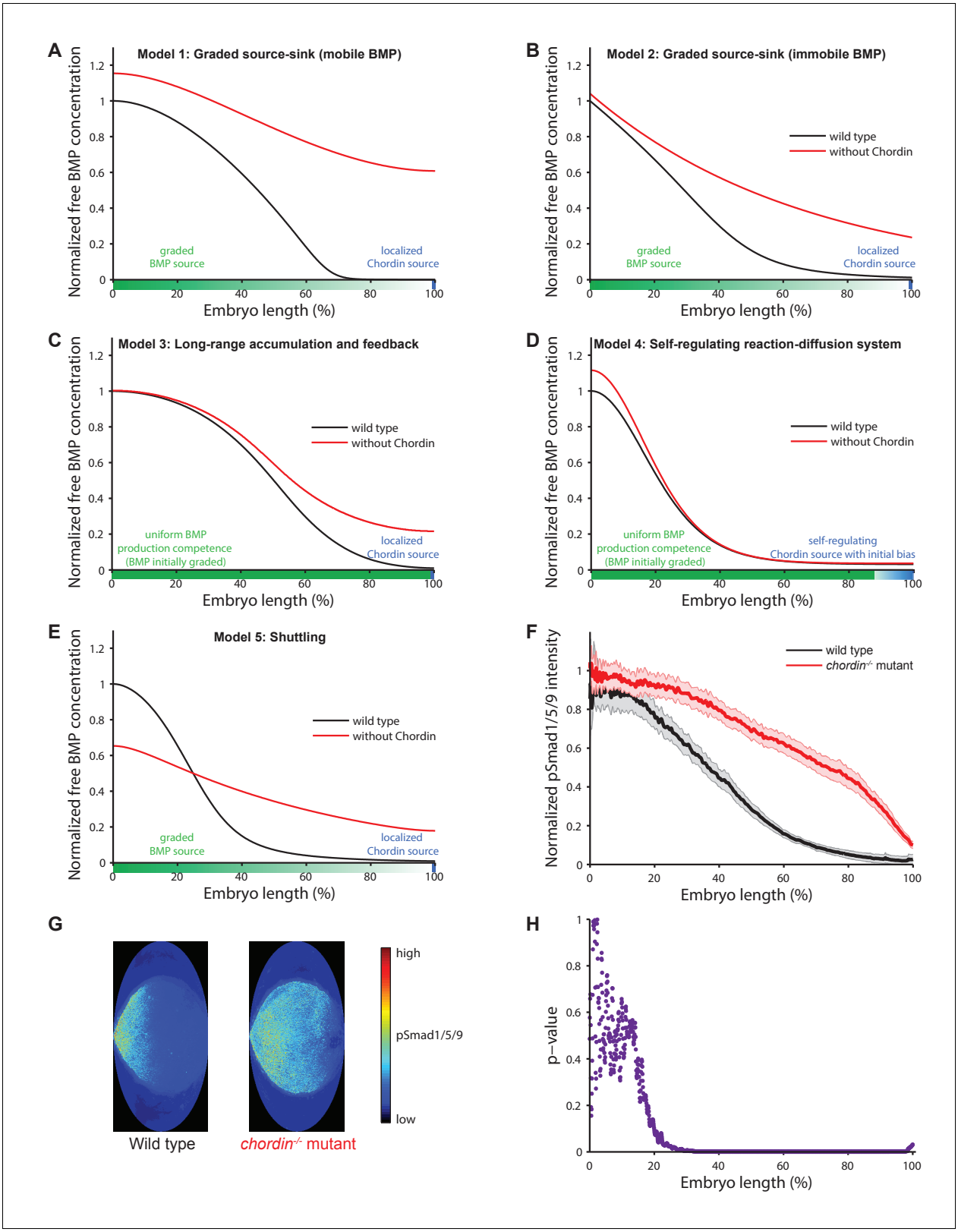

Figure 2. Theoretical predictions for the influence of the inhibitor Chordin on the BMP signaling gradient and experimental test. (**A–E**) Simulations of BMP distributions in five major models of dorsal-ventral patterning in the presence (black) or absence (red) of Chordin. The BMP and Chordin sources are indicated below each graph in green and blue, respectively. Note that the spatial production rates in Models 3 and 4 are modulated over time by feedback. (**F–G**) Quantification of average pSmad1/5/9 distributions in wild type (black) and *chordin*$^{-/-}$ (red) embryos using one-dimensional

Figure 2 continued on next page

Figure 2 continued

projections of 2D maps. Wild type n = 7, *chordin*$^{-/-}$ mutants n = 10. Error bars denote standard error. (**H**) p-values (unpaired two-tailed t-test assuming equal variance) calculated as a function of space between pSmad1/5/9 distributions in wild type and *chordin*$^{-/-}$ embryos shown in (**F**) indicate no significant difference of pSmad1/5/9 on the ventral side but a dramatic expansion into dorsal-lateral domains.

DOI: https://doi.org/10.7554/eLife.25861.011

ventral side was not significantly affected (***Figure 2F–H***), consistent with the predictions from Models 1–3 and observations in *Xenopus* and zebrafish embryos (***Plouhinec et al., 2013***; ***Zinski et al., 2017***), but not with the BMP signaling distributions predicted by Models 4 and 5 (***Table 1***).

BMP and Chordin fluorescent fusion proteins diffuse and rapidly form gradients *in vivo*

In order to understand the underlying basis of BMP/Chordin distribution and directly test the biophysical assumptions of the five dorsal-ventral patterning models, we developed fluorescent fusion proteins. We fused superfolder-GFP (sfGFP [***Pédelacq et al., 2006***]) and the photoconvertible protein Dendra2 (***Gurskaya et al., 2006***) to zebrafish Chordin and BMP2b, the major BMP ligand regulating zebrafish dorsal-ventral patterning (***Kishimoto et al., 1997***; ***Xu et al., 2014***). Basing our design on previously established fusions with small peptide tags (***Cui et al., 1998***; ***Degnin et al., 2004***; ***Sopory et al., 2006***), we inserted fluorescent proteins to label the mature signaling domains, and obtained fusion proteins that are processed similarly and have similar biological activity as untagged versions or constructs fused to small FLAG tags (***Figure 3A–E***, ***Figure 3—figure supplement 1***). Indeed, *BMP2b* mutants (*swr*$^{-/-}$, which are normally severely dorsalized [***Kishimoto et al., 1997***]) can be rescued by injection of mRNA encoding BMP2b-Dendra2 or BMP2b-sfGFP at levels equivalent to untagged BMP2b (***Figure 3C***). In these experiments, the injected mRNA should be uniformly distributed, highlighting the important role of Chordin or other antagonists in shaping the graded BMP signaling distribution.

To measure the kinetics of BMP and Chordin protein gradient formation, we expressed BMP2b-sfGFP and Chordin-sfGFP from local sources in wild type zebrafish embryos (***Müller et al., 2012***) and imaged the distribution profiles over time using light sheet microscopy (***Figure 3F–I***). Importantly, in previous experiments it has been demonstrated that BMP2b clones generated in a similar manner can recapitulate BMP signaling comparable to that observed along the dorsal-ventral axis (***Xu et al., 2014***). Strikingly, both BMP2b-sfGFP and Chordin-sfGFP are secreted and diffuse in the extracellular space (***Figure 3F+G***, ***Videos 7+8***), in contrast to the proposal of Model 2 that only Chordin – but not BMP – diffuses (***Ramel and Hill, 2013***) (***Table 1***) and the absence of long-range BMP4 signaling in *Xenopus* (***Jones et al., 1996***). Both BMP2b-sfGFP and Chordin-sfGFP rapidly establish concentration gradients over the course of one hour (***Figure 3H+I***), consistent with the rapid patterning of the dorsal-ventral axis during zebrafish development.

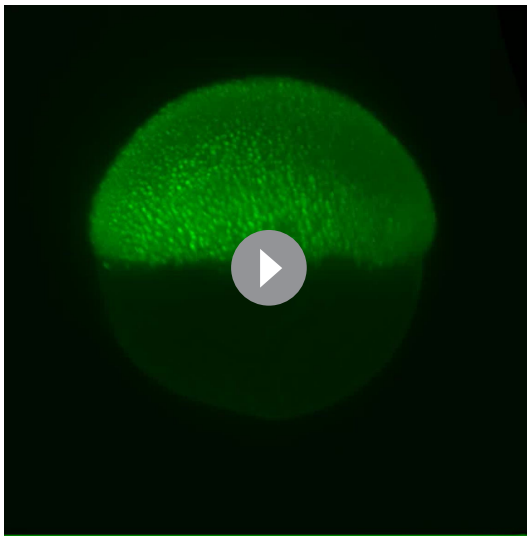

Video 6. 3D reconstruction of pSmad1/5/9 localization in a *chordin*$^{-/-}$ shield stage zebrafish embryo imaged by light sheet microscopy.

DOI: https://doi.org/10.7554/eLife.25861.012

BMP and Chordin fluorescent fusion proteins have similar stabilities *in vivo*

The gradient formed by Chordin-sfGFP has a moderately longer range than the one formed by BMP2b-sfGFP. For example, 60 min post-transplantation the BMP2b-sfGFP signal drops to 50% of the maximal concentration at a distance of 30–40 µm, whereas the gradient formed by Chordin-sfGFP reaches 50% of its maximal concentration at a distance of 50–60 µm from the source boundary at this time point (***Figure 3H+I***). This

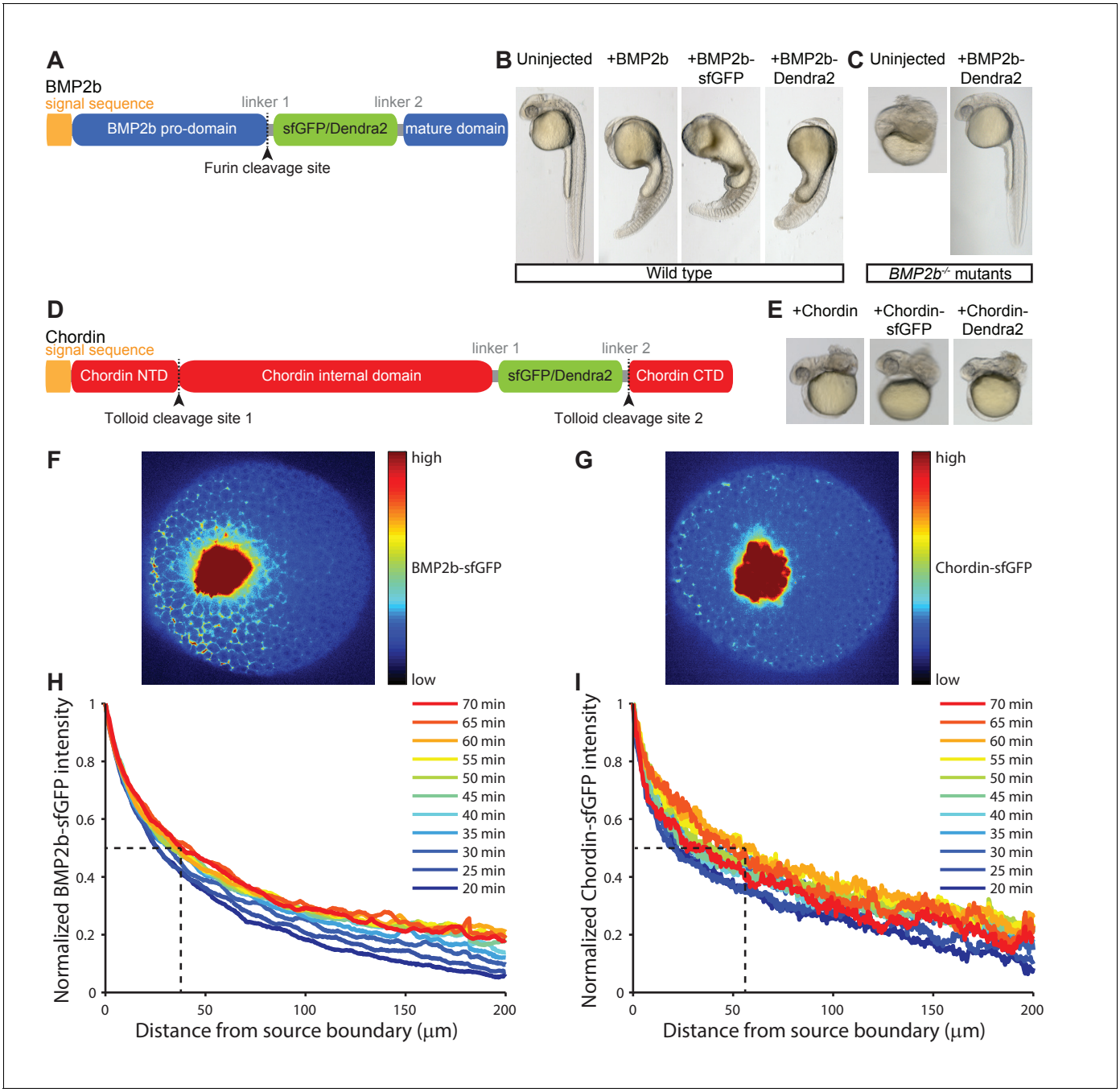

Figure 3. Gradient formation kinetics of fluorescently tagged BMP and Chordin. (**A**) Schematic of BMP2b-sfGFP and -Dendra2 fusion constructs. (**B**) Fluorescent BMP2b fusion constructs can induce ventralization, a BMP-overexpression phenotype (***Kishimoto et al., 1997***). mRNA amounts equimolar to 2 pg of *BMP2b* mRNA were injected at the one-cell stage, and images were taken 30 hr post-fertilization (hpf). (**C**) Rescue of a *BMP2b* mutant (*swr*$^{-/-}$) with BMP2b-Dendra2. 2.74 pg of BMP2b-Dendra2-encoding mRNA were injected at the one-cell stage, and images were taken at 30 hpf. In a separate experiment with 1 pg of BMP2b-sfGFP-encoding mRNA, 20% (9/44) of all injected *swr*$^{-/-}$ mutants were rescued, 16% (7/44) were ventralized, and 64% (28/44) were dorsalized. (**D**) Schematic of Chordin-sfGFP and -Dendra2 fusion constructs. (**E**) Fluorescent Chordin constructs can induce dorsalization, a *Chordin*-overexpression phenotype. mRNA amounts equimolar to 30 pg of *Chordin* mRNA were injected into wild type embryos at the one-cell stage, and images were taken at 30 hpf. F + G) Light sheet microscopy images of BMP- and Chordin-sfGFP gradients forming from a local source in live zebrafish embryos. Approximately 50–75 cells expressing *BMP2b-sfGFP* (**F**) or *Chordin-sfGFP* (**G**) were transplanted into host embryos at sphere stage (see Materials and methods for details). The images show gradient formation in single optical slices approximately 20 min after transplantation. H + I) Quantification of BMP2b-sfGFP (**H**) and Chordin-sfGFP (**I**) gradient formation kinetics from a local source (BMP2b-sfGFP: n = 8; Chordin-sfGFP: n = 5). Dashed lines indicate the distance at which the protein distributions drop to 50% of their maximal concentration 60 min post-transplantation.

Figure 3 continued on next page

Figure 3 continued

DOI: https://doi.org/10.7554/eLife.25861.013

The following figure supplements are available for figure 3:

Figure supplement 1. Detailed characterization of fluorescently tagged BMP2b and Chordin.

DOI: https://doi.org/10.7554/eLife.25861.014

Figure supplement 2. Modeling of BMP and Chordin gradient formation kinetics and comparison to measured gradients.

DOI: https://doi.org/10.7554/eLife.25861.015

suggests that stability or diffusivity might differ between these proteins (***Müller and Schier, 2011***; ***Müller et al., 2013***). Importantly, Models 3 and 5 assume that BMP is more stable than Chordin, whereas the other models assume either similar or unconstrained stabilities (***Table 1***).

To distinguish between these possibilities, we first determined protein stability in living zebrafish embryos using a Fluorescence Decrease After Photoconversion (FDAP) assay (***Müller et al., 2012***; ***Bläßle and Müller, 2015***; ***Rogers et al., 2015***). We expressed BMP2b and Chordin fused to the green-to-red photoconvertible protein Dendra2 uniformly in zebrafish embryos, used brief UV exposure to convert the signal from green to red to generate a pulsed protein pool, and monitored the decrease in extracellular red fluorescence over time (***Figure 4A+B***). For BMP2b-Dendra2, we found a clearance rate constant of $k_1 = (8.9 \pm 0.1) \times 10^{-5}$/s (half-life 130 min, ***Figure 4A***). For Chordin-Dendra2, we measured a similar clearance rate constant of $k_1 = (9.6 \pm 0.3) \times 10^{-5}$/s (half-life 120 min, ***Figure 4B***). The similar clearance rate constants suggest that differential protein stabilities cannot account for the different protein distributions of BMP2b and Chordin. Importantly, these results are inconsistent with the differential protein stabilities predicted by Models 3 and 5 (***Table 1***).

Diffusivity of BMP and Chordin fluorescent fusion proteins *in vivo*

Our finding that BMP2b- and Chordin-Dendra2 fusions have similar stabilities (***Figure 4A+B***) suggests that differences in diffusivity could account for the slight differences in gradient formation kinetics. Indeed, when we fitted a gradient formation model based on local production, uniform diffusion, and clearance constrained with our measured protein half-lives in a realistic three-dimensional zebrafish embryo-like geometry (***Müller et al., 2012***) to the measured protein distributions, we obtained the best agreement between model and data with lower diffusivity of BMP2b (4 μm^2/s) compared to Chordin (6 μm^2/s) (***Figure 3—figure supplement 2A+B***).

Importantly, the five models assume distinct BMP and Chordin diffusion properties (***Table 1***, ***Figure 1—figure supplement 1***), from no BMP diffusion (Model 2) to substantially higher Chordin

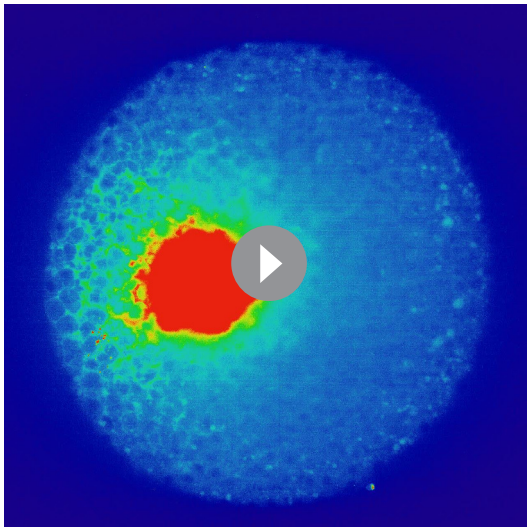

Video 7. Gradient formation in a dome stage wild type embryo with a BMP2b-sfGFP clone.

DOI: https://doi.org/10.7554/eLife.25861.016

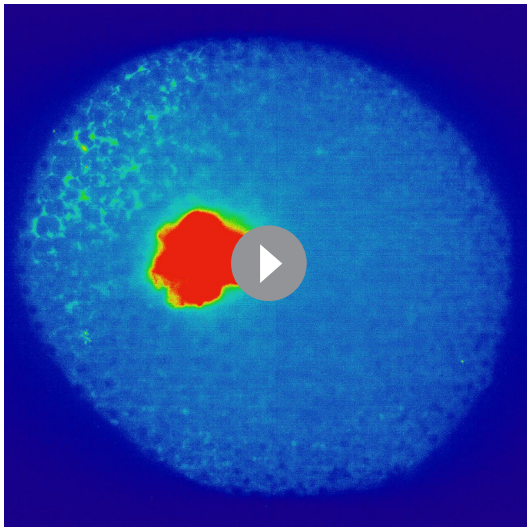

Video 8. Gradient formation in a dome stage wild type embryo with a Chordin-sfGFP clone.

DOI: https://doi.org/10.7554/eLife.25861.017

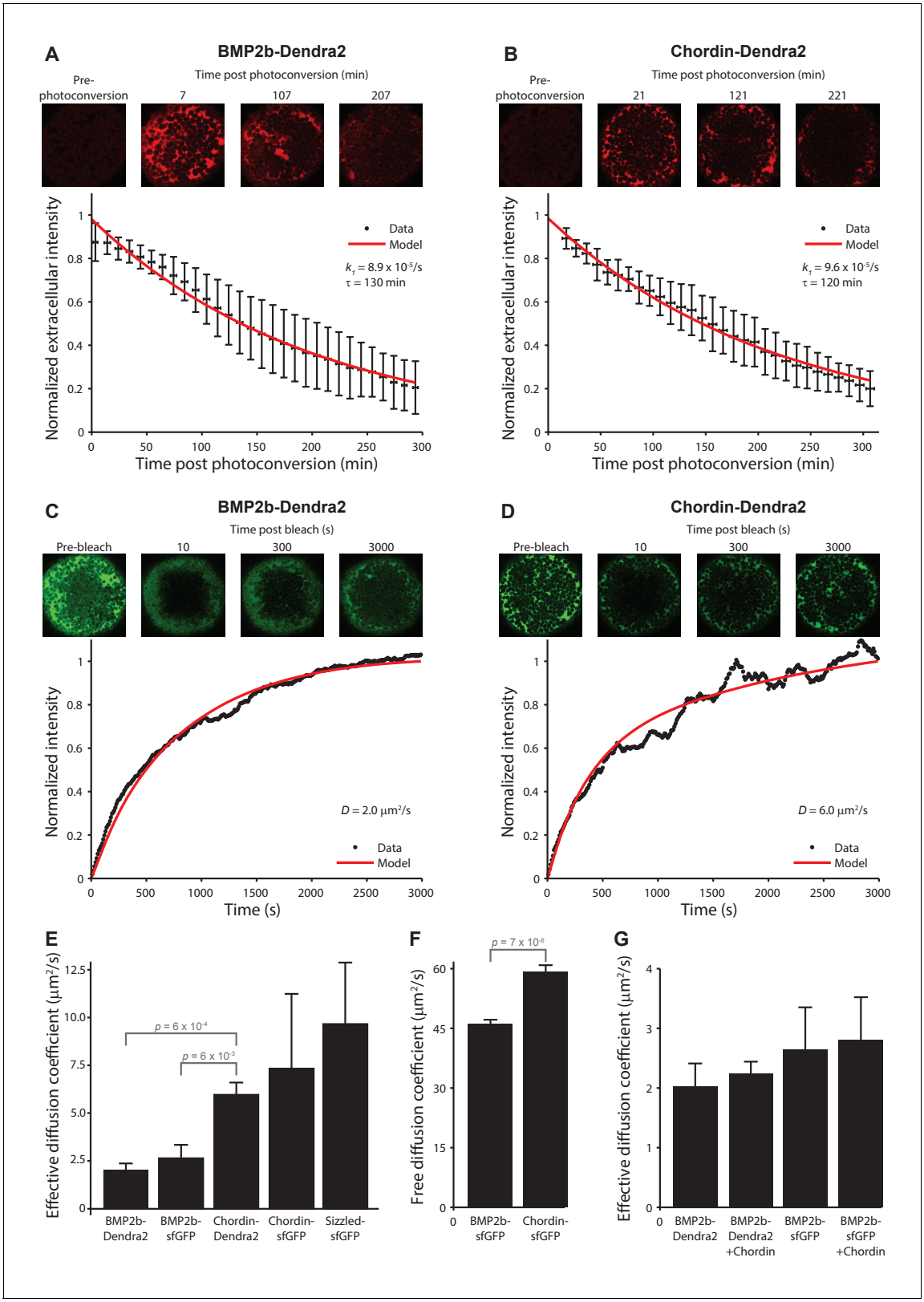

Figure 4. Biophysical measurements of BMP and Chordin protein stability and diffusivity. A + B) FDAP protein stability measurements for BMP2b-Dendra2 (**A**) and Chordin-Dendra2 (**B**). Error bars denote standard deviation. BMP2b-Dendra2: n = 22; Chordin-Dendra2: n = 6. C + D) FRAP effective protein diffusivity measurements for BMP2b-Dendra2 (**C**) and Chordin-Dendra2 (**D**). Data and fits from single experiments are shown. (**E**) Bar chart of the average effective diffusion coefficients from FRAP experiments. Error bars denote standard error. BMP2b-Dendra2: n = 6; BMP2b-sfGFP: n = 8;

Figure 4 continued on next page

Figure 4 continued

Chordin-Dendra2: n = 8; Chordin-sfGFP: n = 6; Sizzled-sfGFP: n = 12. (**F**) Free diffusion coefficients of BMP2b-sfGFP and Chordin-sfGFP measured by Fluorescence Correlation Spectroscopy (FCS) in a diffraction-limited spot within the zebrafish embryonic extracellular space far away from cell membranes (see Materials and methods for details). Error bars denote standard error. BMP2b-sfGFP: n = 17 measurements from 4 embryos; Chordin-sfGFP: n = 19 measurements from 5 embryos. (**G**) Negligible influence of Chordin on BMP2b effective diffusion. Untagged Chordin was co-expressed with BMP2b-Dendra2 (n = 8) or BMP2b-sfGFP (n = 9) in zebrafish embryos subjected to FRAP measurements at blastula stages. The data shown for BMP2b-Dendra2 and BMP2b-sfGFP FRAP experiments without co-expressed *Chordin* is identical to the data shown in (**E**). p-values (unpaired two-tailed t-test assuming equal variance) are shown for statistically significant ($p<0.05$) data sets.

DOI: https://doi.org/10.7554/eLife.25861.018

The following figure supplement is available for figure 4:

Figure supplement 1. Characterization of Sizzled diffusion and its role in gradient formation.

DOI: https://doi.org/10.7554/eLife.25861.019

mobility compared to BMP (Model 5). To directly test these predictions, we determined the effective diffusivities of fluorescently tagged BMP2b and Chordin moving through developing zebrafish embryos. We used a Fluorescence Recovery After Photobleaching (FRAP) assay (***Müller et al., 2012***) that measures the dynamics of re-appearance of fluorescence in a bleached region in embryos uniformly expressing fluorescent fusion proteins (***Figure 4C–E***). We found effective diffusion coefficients of 2–3 $\mu m^2/s$ for BMPs (BMP2b-Dendra2: 2.0 ± 0.4 $\mu m^2/s$; BMP2b-sfGFP: 2.6 ± 0.7 $\mu m^2/s$ (similar to [***Zinski et al., 2017***]) and of 6–7 $\mu m^2/s$ for Chordin (Chordin-Dendra2: 6.0 ± 0.7 $\mu m^2/s$; Chordin-sfGFP: 7.3 ± 3.9 $\mu m^2/s$), indicating that slight differences in diffusivities could underlie the differences in protein distributions. This idea is further supported by the agreement between gradients simulated with the measured diffusivities and clearance rate constants and our experimentally determined protein gradients (***Figure 3—figure supplement 2E–H***). The measured diffusion coefficients are most consistent with Models 1 and 4, which assume either similarly low diffusivities (Model 4) or that BMP has a moderately lower diffusion coefficient than Chordin (Model 1, ***Table 1***). As observed in the BMP2b-sfGFP gradient formation experiment (***Figure 3F–I***), our FRAP data demonstrate that BMP2b-sfGFP is mobile *in vivo*, inconsistent with Model 2.

Strikingly, local diffusion measurements in very small extracellular volumes far away from cell surfaces using Fluorescence Correlation Spectroscopy (FCS) assays showed that BMP2b-sfGFP (free diffusion coefficient: D_f = 46 ± 1 $\mu m^2/s$) and Chordin-sfGFP (free diffusion coefficient: D_f = 59 ± 2 $\mu m^2/$

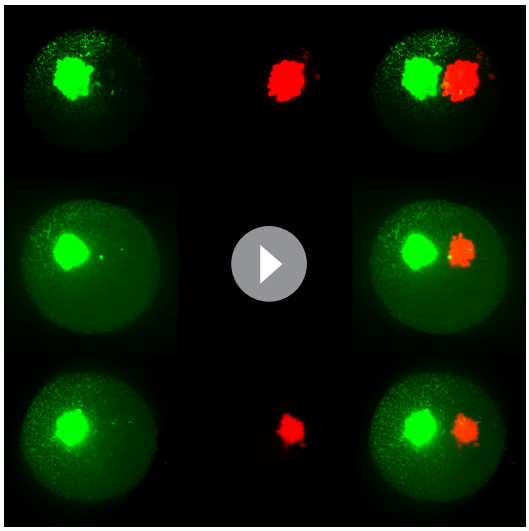

Video 9. Gradient formation in three representative dome stage wild type embryos with BMP2b-sfGFP clones (green) next to clones labeled with Alexa 546-coupled dextran (red).

DOI: https://doi.org/10.7554/eLife.25861.021

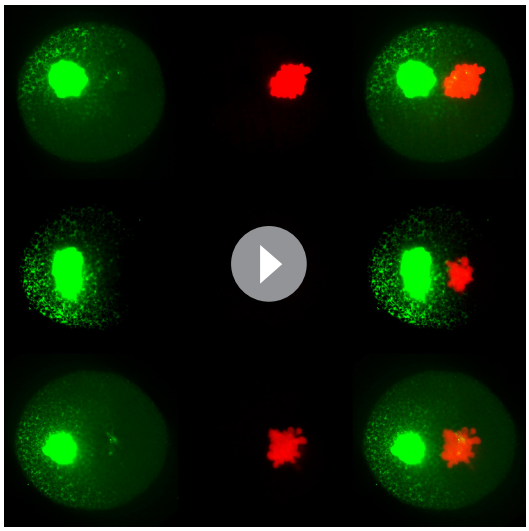

Video 10. Gradient formation in three representative dome stage wild type embryos with BMP2b-sfGFP clones (green) next to *chordin*-expressing clones labeled with Alexa 546-coupled dextran (red).

DOI: https://doi.org/10.7554/eLife.25861.022

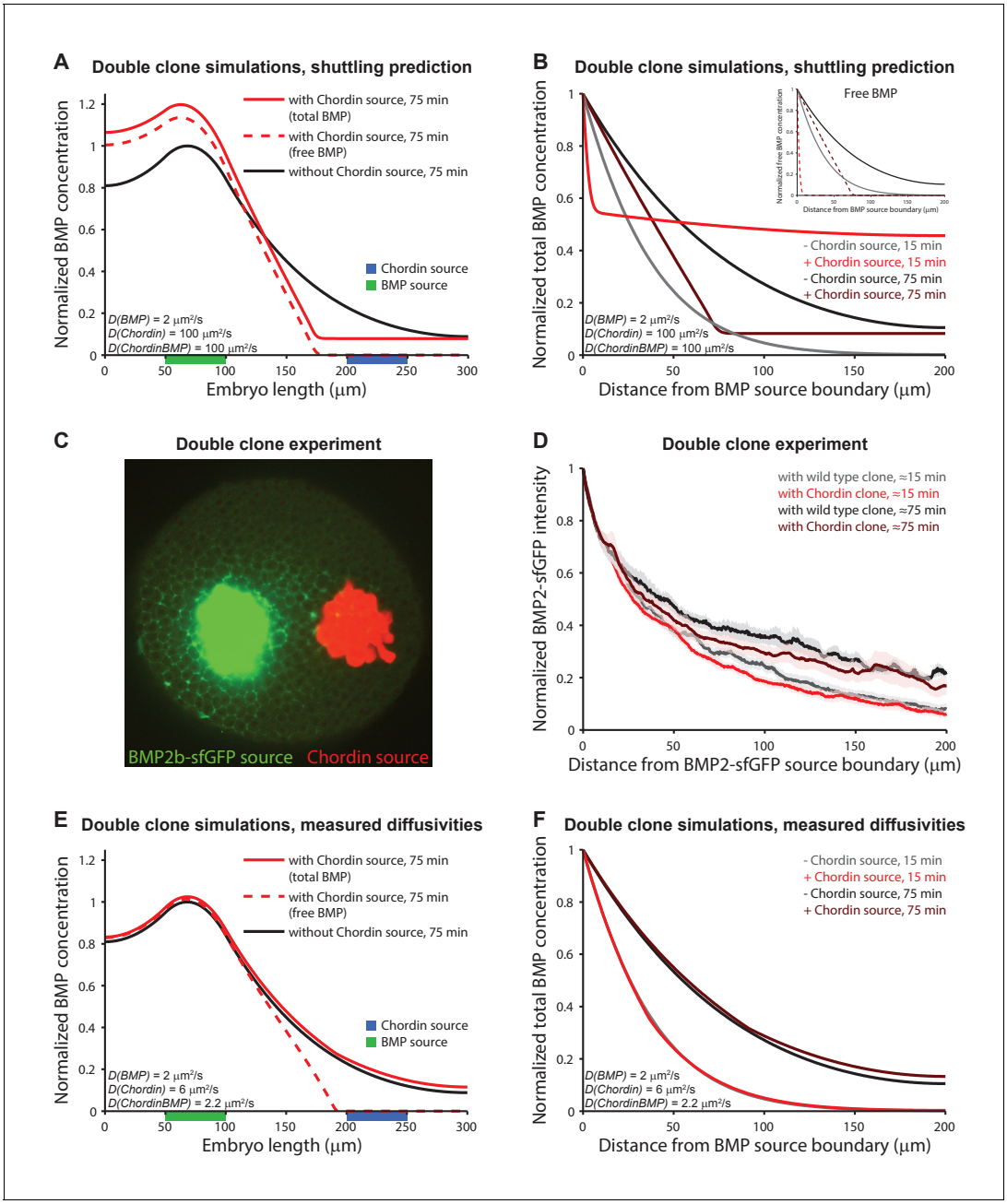

Figure 5. Testing shuttling of BMP2b predicted by Model 5. (**A**) One-dimensional model of two clones expressing BMP (green) or Chordin (blue) with D_{BMP} = 2 μm^2/s, D_{Chd} = 100 μm^2/s, and D_{ChdBMP} = 100 μm^2/s. BMP levels increase over time due to constant production. In the presence of Chordin, the BMP gradient is deflected away from the Chordin source indicative of shuttling (compare black and red lines). Solid lines show total BMP levels (i.e. BMP + ChdBMP in the presence of Chordin), and dashed line shows free BMP levels. (**B**) BMP gradients to the right of the BMP-expressing clone re-normalized to the BMP concentration at the source boundary to demonstrate that the range of BMP is decreased between the two clones in the presence of Chordin. The main panel shows total BMP levels (i.e., BMP + ChdBMP in the presence of Chordin), and the inset shows free BMP levels (dashed lines). (**C**) Experimental test of the predictions in (**A**) and (**B**). Clones of cells expressing BMP2b-sfGFP (green) were generated by transplanting approximately 50–75 cells from a donor embryo into wild type hosts at sphere stage (see Materials and methods for details). Another clone of cells (red) was transplanted next to the BMP2b-sfGFP-expressing clone shortly after. The red clone is marked by the presence of fluorescent Alexa 546-coupled dextran. Cells from red-labeled clones either contained only Alexa 546-coupled dextran (***Video 9***) or Alexa-546-coupled dextran and ectopic *chordin* mRNA (***Video 10***). 15–20 min after transplantation of the clones, embryos were imaged using light sheet microscopy. The image shows gradient formation in a single optical slice approximately 20 min after transplantation. (**D**) Quantification of average BMP2b-sfGFP gradients at ~15 min or ~75 min after transplantation in embryos generated as in (**C**) with (red/brown) or without (black/gray) ectopic Chordin sources. Error bars denote standard error. n = 8 for each condition. (**E**) One-dimensional simulation of two clones expressing BMP (green) or Chordin (blue) with the experimentally measured diffusion coefficients D_{BMP} = 2 μm^2/s, D_{Chd} = 6 μm^2/s, and D_{ChdBMP} = 2.2 μm^2/s. BMP levels increase over time due to constant production.

Figure 5 continued on next page

Figure 5 continued

Solid lines show total BMP levels (i.e. BMP + ChdBMP in the presence of Chordin), and the dashed line shows free BMP levels. Only the distribution of free BMP is affected as a consequence of Chordin binding, and the gradient of total BMP is not deflected away from the Chordin source (compare solid black and red lines). (**F**) Gradients of total BMP levels to the right of the BMP expressing clone simulated with the experimentally measured diffusion coefficients (D_{BMP} = 2 μm^2/s, D_{Chd} = 6 μm^2/s, and D_{ChdBMP} = 2.2 μm^2/s) and renormalized to the concentration at the boundary show that the range of BMP is not decreased between the two clones in the presence of Chordin.

DOI: https://doi.org/10.7554/eLife.25861.020

s) are highly mobile over short spatial and temporal scales (***Figure 4F***), whereas their diffusivities are reduced at the global scale when they move across a field of cells (***Figure 4E***). We hypothesize that the difference between effective diffusivities (measured by FRAP) and local diffusivities (measured by FCS) is due to binding to immobile extracellular molecules, which could serve as diffusion regulators that hinder the mobility of BMP2b and Chordin, similar to what has been proposed for other developmental signals such as Nodal and FGF (***Müller et al., 2012***; ***Müller et al., 2013***).

Sizzled, BMP, and Chordin diffusivities are within the same order of magnitude

Models 3 and 4 assign important roles to the secreted proteins ADMP and Sizzled in regulating BMP signaling and distribution. Model 3 postulates diffusivities of ADMP and Sizzled equivalent to BMP and Chordin, whereas Model 4 requires approximately 25-fold higher diffusivities of ADMP and Sizzled compared to BMP and Chordin (***Table 1***). To measure the diffusivities of ADMP and Sizzled and test these assumptions, we developed fluorescent ADMP and Sizzled fusion proteins (see Materials and methods). Whereas Sizzled fusion proteins had activity comparable to untagged Sizzled (***Figure 4—figure supplement 1A–C***), ADMP fusions with sfGFP or FLAG tags inserted 2, 5, or 11 amino acids after the Furin cleavage site were much less active than untagged ADMP (data not shown), and could therefore not be used for diffusion measurements. Using FRAP, we measured an effective diffusion coefficient of 9.7 ± 3.2 μm^2/s for Sizzled-sfGFP (***Figure 4E***, ***Figure 4—figure supplement 1D***). This measurement is consistent with Model 3, but not Model 4, the latter of which requires much higher Sizzled mobility (***Table 1***).

When parameterized with these measured diffusion coefficients and over a ~100-fold range of ADMP diffusion coefficients, Model 3 can form ventral-dorsal gradients over relevant time scales (***Figure 4—figure supplement 1F–J***), but the kinetics of gradient formation do not reflect the measurements of pSmad1/5/9 distribution profiles in ***Figure 1A+B***. Moreover, the relatively minor difference between BMP/Chordin and Sizzled diffusivity is not compatible with the 25-fold differential required for Model 4 (***Figure 4—figure supplement 1K–P***).

Chordin does not regulate BMP protein diffusivity or distribution

Model 5 (Shuttling) postulates that highly diffusive Chordin enhances the mobility of poorly diffusive BMPs (***Ben-Zvi et al., 2008***). In this model, Chordin is secreted dorsally, binds to relatively immobile BMP, and creates a highly mobile BMP/Chordin complex. This complex then diffuses until Chordin is cleaved by a protease (Xlr), rendering BMP immobile again (***Figure 1—figure supplement 1***). To investigate whether Chordin is not only an inhibitor of BMP, but also enhances BMP diffusivity, we increased Chordin levels and measured the effective diffusivity of fluorescent BMP2b. In embryos overexpressing Chordin, we did not observe a significant change in the effective diffusivity of fluorescently tagged BMP2b compared to embryos that did not overexpress Chordin (BMP2b-Dendra2 + Chordin: 2.2 ± 0.2 μm^2/s; BMP2b-sfGFP + Chordin: 2.8 ± 0.7 μm^2/s; ***Figure 4G***). The ability of Chordin to enhance the diffusivity of BMP, a major tenet of Model 5, is therefore not supported by FRAP data.

Model 5 also predicts that Chordin alters the distribution of BMP protein. Over time, the shuttling of BMP by Chordin causes BMP to accumulate away from the Chordin source, resulting in an opposing peak of BMP. Our observation that Chordin does not affect the diffusivity of BMP challenges this view (***Figure 4G***). However, to directly test whether a Chordin source can alter BMP distribution (***Figure 5A+B***), we juxtaposed clones of BMP2b-sfGFP-producing cells with clones of cells secreting untagged Chordin and imaged the formation of the BMP2b-sfGFP gradient over time using light sheet fluorescence microscopy (***Figure 5C+D***, ***Videos 9–10***). Model 5 predicts a steeper BMP2b-

sfGFP gradient in the presence of an adjacent Chordin-producing clone compared to a wild type clone (***Figure 5A+B***). Although BMP2b-sfGFP gradients tend to be slightly steeper in the presence of a neighboring Chordin-expressing clone compared to a non-Chordin-expressing clone (***Figure 5D***), this minor change is unlikely to account for the formation of a ventral peak in BMP signaling during the short time (hours) required to complete dorsal-ventral patterning (***Figure 1A+B***). We also failed to observe significant redistribution of BMP in simulations of adjacent BMP and Chordin clones using our measured diffusion coefficients and half-lives (***Figure 5E+F***). This suggests that shuttling of BMP2b by Chordin is not relevant for the early aspects of dorsal-ventral patterning in zebrafish embryos.

Discussion

The BMP signaling gradient patterns the dorsal-ventral axis during animal development. Five major models can explain how a ventral peak of BMP signaling forms, but the biophysical assumptions underlying these models differ widely (***Table 1***). After experimentally examining these assumptions, our findings lead to four main conclusions. First, Chordin does not play an active role in generating BMP signaling peaks, but only globally inhibits BMP (***Figure 2***). This is consistent with graded source-sink-type models (e.g. Models 1 and 2) and Model 3, but inconsistent with Models 4 and 5 (***Table 1***). Interestingly, BMP signaling in the absence of Chordin is not raised on the extreme dorsal side, indicating that other extracellular inhibitors such as Follistatin or Noggin (***Umulis et al., 2009***) or inhibitors of *bmp* expression (***Koos and Ho, 1999***; ***Leung et al., 2003***; ***Ramel and Hill, 2013***) that were not included in the tested models might further restrict BMP signaling in these regions. Second, BMP2b and Chordin both diffuse in the extracellular space (***Figure 3F–I***), challenging models involving immobile BMP (Model 2). Third, fluorescently tagged BMP2b and Chordin have similarly high local diffusivities (***Figure 4F***), but on a global scale they move much more slowly through the embryo (***Figure 4E***). These findings rule out Models 2, 3, and 5, but are consistent with Models 1 and 4. Fourth, Chordin does not significantly affect BMP2b diffusion or protein distribution in zebrafish embryos (***Figure 4G***, ***Figure 5***), undermining shuttling models in this developmental context. Instead, our data are most consistent with Model 1, the graded source-sink model of BMP/Chordin-mediated dorsal-ventral patterning during early zebrafish development. Our conclusions are also consistent with a recent complementary study (***Zinski et al., 2017***).

Notably, shuttling models (e.g. Model 5) have gained prominence in many developmental contexts including scale-invariant patterning (***Ben-Zvi et al., 2008***; ***Barkai and Ben-Zvi, 2009***; ***Francois et al., 2009***; ***Plouhinec and De Robertis, 2009***; ***Ben-Zvi and Barkai, 2010***; ***Ben-Zvi et al., 2011a***; ***Haskel-Ittah et al., 2012***), but the fundamental tenet, that is, whether putative shuttles such as Chordin change the diffusivity and distribution of signals such as BMP, has not been directly examined. Alternative models that do not invoke Chordin-dependent facilitated BMP diffusion (Model 4) (***Francois et al., 2009***) or that postulate differential protein stability (Model 3) (***Inomata et al., 2013***) can also explain scale-invariant patterning. Our data do not provide strong evidence for shuttling of BMP2b at time scales relevant for dorsal-ventral patterning during early zebrafish embryogenesis: We failed to observe a significant modulation of BMP2b-sfGFP or BMP2b-Dendra2 diffusivity or distribution by Chordin (***Figure 4G***, ***Figure 5***). It is, however, possible that other BMPs (e.g. BMP4, BMP7, ADMP) are shuttled by interactions with Chordin and its protease Tolloid/Xlr. Indeed, *tolloid* mutants display a mild patterning defect of the ventral tail fin (***Connors et al., 1999***) that might reflect a requirement for the ventral accumulation of a weakly active, dorsally expressed BMP ligand such as ADMP (***Dickmeis et al., 2001***; ***Lele et al., 2001***).

The graded source-sink model (Model 1) that is best supported by our data describes a system in which the graded, ventrally biased distribution of *bmp* mRNA and the dorsally localized *chd* mRNA distribution produce opposing sources of extracellular, diffusing BMP and Chordin protein, which together generate the BMP signaling gradient required for proper dorsal-ventral patterning. Notably, this model fails to take other known dorsal-ventral regulators into account (e.g., ADMP, Sizzled, Follistatin, Noggin). Furthermore, approximately one third of *bmp2b* and *chordin* mutant embryos can be rescued by apparently uniform *bmp* and *chordin* expression, respectively (***Kishimoto et al., 1997***; ***Fisher and Halpern, 1999***) (***Figure 3C***), arguing against a strong requirement for concurrent opposing BMP and Chordin sources as long as one component of the system is biased (i.e. ventrally biased *bmp2b* expression with uniform Chordin, or dorsally biased *chordin* expression with uniform

BMP). Thus, further adjustments to the basic Model 1 will be required to fully describe dorsal-ventral patterning.

Although our results support a role for BMP diffusion in dorsal-ventral patterning, the necessity of signal diffusion for developmental patterning has recently been challenged by several studies (**Brankatschk and Dickson, 2006**; **Roy and Kornberg, 2011**; **Alexandre et al., 2014**; **Dominici et al., 2017**; **Varadarajan et al., 2017**). It will be interesting to determine whether BMP diffusion is indeed required for proper patterning using emerging nanobody-mediated diffusion perturbations (**Harmansa et al., 2015**) or optogenetics-based cell-autonomous modulation of signaling range (**Sako et al., 2016**).

Materials and methods

Immunostainings

To visualize pSmad1/5/9, wild type TE embryos were dechorionated at the one-cell stage using 1 mg/ml of Pronase (Roche, Cat. No. 11 459 643 001). Dechorionated embryos were incubated at 28°C and fixed at different developmental stages in 4% formaldehyde (Roth) in PBS overnight at 4°C on a shaker. Embryos were then stored in 100% methanol at −20°C for at least 2 hr. All subsequent steps were carried out at room temperature. Embryos were re-hydrated with 70%, 50%, and 30% methanol in PBS for 10 min each. The embryos were then washed eight times with PBST (0.1% Tween) for 15 min and blocked twice with blocking solution (10% fetal bovine serum and 1% DMSO in PBST) for 1 hr, and incubated with 1:100 anti-pSmad1/5/9 antibody (Cell Signaling Technology, Cat. No. 9511) for 4 hr. Embryos were washed with blocking solution for 15 min, washed seven times with PBST, blocked with blocking solution for 1 hr, incubated with 1:500 Alexa 488-coupled goat anti-rabbit secondary antibody (Life Technologies, Cat. No. A11008) for 4 hr, and washed similarly to the procedure after primary antibody application. Embryos were then counterstained with DAPI solution (0.2 µg/ml in PBST) for 1 hr and washed with PBST. Immunostainings were performed using an In situ Pro hybridization robot (Abimed/Intavis).

To analyze pSmad1/5/9 distributions in the absence of Chordin, embryos from one pair of *chordin*^{tt250} (**Hammerschmidt et al., 1996**) heterozygous parents were collected, fixed, immunostained with anti-pSmad1/5/9 antibody (Cell Signaling Technology, Cat. No. 13820S) as above, and imaged simultaneously to minimize differences between samples. Embryos were treated as described above, except that progeny from *chordin*$^{+/-}$ incrosses were first permeabilized with ice-cold acetone at −20°C for 7 min before the re-hydration step. After imaging and DNA extraction (**Meeker et al., 2007**), progeny from the *chordin*^{tt250} heterozygote incross were identified as wild type, heterozygous, or homozygous mutant embryos by PCR amplification using the forward primer 5'-TTCG TTTGGAGGACAACTCG-3' and the reverse primer 5'-AACTCAGCAGCAGAAGTCAATTC-3' with an initial denaturation step of 94°C for 3 min; 39 cycles of 94°C for 30 s, 55°C for 40 s, and 72°C for 30 s; and a final extension at 72°C for 5 min with subsequent digestion with MspI (New England Biolabs, Cat. No. R0106) for 2 hr. The genotyping assay for the *chordin*^{tt250} line was designed by the Zebrafish International Resource Center (ZIRC) staff and downloaded from the ZIRC website at http://zebrafish.org.

Generation of fluorescent BMP2b fusions

All constructs were generated by PCR-based methods (**Horton et al., 1990**), contain the consensus Kozak sequence *gccacc* 5' of the start codon, and were inserted into the EcoRI and XhoI sites of the pCS2(+) vector. To generate BMP2b-sfGFP and BMP2b-Dendra2, sequences encoding sfGFP or Dendra2 flanked by LGDPPVAT linkers were inserted two amino acids downstream of the BMP2b Furin cleavage site. Sequences encoding the FLAG tag DYKDDDDK were inserted between the first linker and sfGFP or Dendra2 to generate BMP2b-sfGFP-FLAG and BMP2b-Dendra2-FLAG. To generate BMP2b-FLAG, the FLAG tag was inserted between two LGDPPVAT linkers two amino acids downstream of the BMP2b Furin cleavage site.

Generation of fluorescent Chordin fusions

All constructs were generated by PCR-based methods (**Horton et al., 1990**) and contain the consensus Kozak sequence *gccacc* 5' of the start codon. Chordin was inserted into the ClaI site of pCS2(+).

All other Chordin-containing constructs were inserted into the EcoRI and XbaI sites of the pCS2(+) vector. To generate Chordin-sfGFP and BMP2b-Dendra2, sequences encoding sfGFP or Dendra2 flanked by LGDPPVAT linkers were inserted immediately 5' of the Tolloid cleavage site 2. To generate Chordin-FLAG, sequences encoding the FLAG tag DYKDDDDK were inserted immediately 5' of the Tolloid cleavage site 2 without additional linkers. To generate Chordin-sfGFP-FLAG and Chordin-Dendra2-FLAG, sequences encoding the FLAG tag were inserted between the first linker and sfGFP or Dendra2 of Chordin-sfGFP and Chordin-Dendra2 constructs.

Generation of fluorescent Sizzled fusions

All Sizzled constructs were generated by PCR-based methods (**Horton et al., 1990**), contain the consensus Kozak sequence *gccacc* 5' of the start codon, and were inserted into the EcoRI and XbaI sites of the pCS2(+) vector. To generate Sizzled-sfGFP, sequences encoding sfGFP with an N-terminal LGLG linker were fused to the C-terminus of Sizzled. Sequences encoding the FLAG tag DYKDDDDK were inserted between the LGLG linker and sfGFP to generate Sizzled-sfGFP-FLAG. To generate Sizzled-FLAG, the FLAG tag was fused to the C-terminus of Sizzled separated by an LGLG linker.

mRNA *in vitro* synthesis

mRNA was generated using SP6 mMessage mMachine kits (Thermo Fisher) after vector linearization with NotI-HF (New England Biolabs, Cat. No. R3189). mRNA was purified using LiCl precipitation or Qiagen RNeasy kits following the manufacturers' instructions.

Phenotypic analysis

Scoring of ventralization and dorsalization was executed as previously described (**Mullins et al., 1996**; **Kishimoto et al., 1997**). Embryos were injected at the one- to two-cell stage with equimolar amounts of *BMP2b* (1 pg), *BMP2b-sfGFP* (1.49 pg), and *BMP2b-Dendra2* (1.47 pg) mRNA to assess ventralizing activity. At 1 day post-fertilization, BMP2b-injected embryos were classified as weakly ventralized (V1) to strongly ventralized (V4). V1 embryos have reduced eyes but a prominent head. V2 embryos have no eyes, reduction of the head, and expansion of posterior structures such as somites and tail. V3 embryos completely lack head structures and exhibit a further expanded tail and enlarged blood islands. Finally, V4 embryos lack most structures except for a short, protruding, and expanded tail.

To assess dorsalizing activity of the Chordin constructs, embryos were injected with equimolar amounts of *Chordin* (30 pg), *Chordin-sfGFP* (37 pg), *Chordin-Dendra2* (37 pg), and *Chordin-FLAG* mRNA (30 pg). Embryos were scored at 1 day post-fertilization and classified as weakly dorsalized (C1) to strongly dorsalized (C5) (**Kishimoto et al., 1997**). C1 embryos lack the ventral tail fin. C2 embryos have a further loss of ventral structures, such as the ventral tail vein, and a bent tail. C3 embryos exhibit a tail that is shortened and twisted. C4 embryos have observable head structures and develop eyes with twisting of the posterior structures above the yolk. C5 embryos are fully dorsalized and frequently lyse (**Mullins et al., 1996**; **Kishimoto et al., 1997**).

Rescue of *BMP2b* ($swr^{-/-}$) mutants

Injection of *BMP2b* mRNA can rescue *BMP2b* mutants (**Kishimoto et al., 1997**). To investigate whether tagged BMP2b constructs can rescue $swr^{tc300-/-}$ mutants (**Mullins et al., 1996**), the rescuing amount of *BMP2b* mRNA was first determined (1.8 pg), and equimolar amounts of mRNA encoding fluorescent fusion constructs were subsequently injected into the progeny of heterozygous $swr^{+/-}$ mutant incrosses. Embryos with wild type morphology at 24 hpf were anesthetized and mounted in 2% methylcellulose for imaging with an AxioZoom V16 (ZEISS) microscope at 30–33 hpf. To genotype embryos following DNA extraction (**Meeker et al., 2007**), PCR was performed to amplify a BMP2b fragment with the forward primer 5'-AAAAGCCGAGGAGAAAGCAC-3' and the reverse primer 5'-AGTCCTTCATTGGGGAGATTGTTC-3', and the following thermocycling parameters: An initial denaturation step of 94°C for 3 min; 39 cycles of 94°C for 30 s, 58°C for 40 s, and 72°C for 40 s; and a final extension at 72°C for 5 min. PCR amplicons were subsequently digested with HaeIII (New England Biolabs, Cat. No. R0108) at 37°C for 2 hr. The genotyping assay for the

swr^{tc300} line was designed by the Zebrafish International Resource Center (ZIRC) staff and downloaded from the ZIRC website at http://zebrafish.org.

Preparation of extracellularly enriched fractions for western blotting

Extracellularly enriched and cellular fractions from manually deyolked embryos between sphere and dome stage were obtained as described previously (**Müller et al., 2012**). mRNAs encoding FLAG-tagged constructs were injected at the one- or two-cell stage at equimolar amounts (*BMP2b-FLAG*: 444 pg, *BMP2b-sfGFP-FLAG*: 638 pg, *BMP2b-Dendra2-FLAG*: 630 pg; and *Chordin-FLAG*: 500 pg, *Chordin-sfGFP-FLAG*: 620 pg, *Chordin-Dendra2-FLAG*: 615 pg). For protein samples with BMP2b constructs, fractions from approximately 19 embryos were loaded and resolved by SDS-PAGE using 12% polyacrylamide gels. For protein samples with Chordin constructs, fractions from approximately 17–18 embryos were loaded and resolved in 8% polyacrylamide gels. Proteins were subsequently transferred onto PVDF membranes using a Trans-Blot Turbo Transfer System (Bio-Rad, Cat. No. 170–4272). Membranes were blocked with 5% non-fat milk (Roth, Cat. No. T145.2) in PBST (0.1% Tween) and incubated with anti-FLAG antibody (Sigma, Cat. No. F3165) at a concentration of 1:2000 in non-fat milk in PBST at 4°C overnight. HRP-coupled donkey anti-mouse secondary antibody (Jackson ImmunoResearch, Cat. No. 715-035-150) was used at concentration of 1:25,000 for 3 hr at room temperature. Chemiluminescence was detected using SuperSignal West Dura Extended Duration Substrate (Thermo Fisher, Cat. No. 34075) and imaged with a chemiluminescence imaging system (Fusion Solo, Vilber Lourmat).

Transplantations

To generate clonal sources secreting BMP2b-sfGFP, Chordin-sfGFP, and untagged Chordin (**Figures 3** and **5**), approximately 50–75 cells were transplanted from sphere stage wild type TE donor embryos expressing these constructs into uninjected, sphere stage sibling hosts (similar to [**Müller et al., 2012**]). Transplantations were carried out in 1 x Ringer's buffer. Cells were explanted from donors, extruded briefly into the buffer to wash away cellular debris and extracellular fluorescent protein, and then transplanted into host embryos.

Donor embryos were dechorionated with 1 mg/ml Pronase (Roche, Cat. No. 11 459 643 001) and injected with 1–2 nl injection mix at the one-cell stage. Sibling host embryos were dechorionated together with donors at the one-cell stage, and all embryos were incubated at 28°C until transplantation. Unfertilized or injured embryos were discarded.

For single (**Figure 3**) and double (**Figure 5**) transplantation experiments, BMP2b-sfGFP and Chordin-sfGFP donors were injected with 500 pg mRNA (**Figure 3—figure supplement 1F–H**).

For double transplantation experiments (**Figure 5**), embryos received one transplantation from a donor expressing BMP2b-sfGFP and a second transplantation from a donor injected at the one-cell stage with either 50 pg Alexa 546-coupled dextran (10 kDa, Molecular Probes, Cat. No. D22911) or 1000 pg Chordin mRNA + 50 pg Alexa 546-coupled dextran. Alexa 546-coupled dextran was used to mark the location of the second clone.

2–10 min post-transplantation, embryos were mounted in 1% low-melting NuSieve GTG agarose (Lonza, Cat. No. 50080) dissolved in embryo medium (250 mg/l Instant Ocean salt dissolved in reverse osmosis water). Embryos were immersed in 40°C molten low melting point agarose, pulled into 1.5 mm glass capillary tubes (ZEISS), and positioned with the animal pole perpendicular to the capillary using a metal probe. Agarose tubes were then suspended in embryo medium, and imaged at room temperature using a ZEISS Lightsheet Z.1 microscope (see *Light sheet microscopy* section for further imaging details).

Light sheet microscopy

Fluorescence images in **Figures 1**, **2**, **3** and **5**, and **Figure 3—figure supplement 1** were obtained using a Lightsheet Z.1 microscope (ZEISS). For fixed, immunostained embryos, samples were mounted into a glass capillary sample holder in 1% low-melting NuSieve GTG agarose (Lonza, Cat. No. 50080) in embryo medium with 0.2 µm dark red fluorescent FluoSpheres (Life Technologies, Cat. No. F8807) diluted 1:200,000 from a 2% solids stock. Embryos were imaged at 0°, 45°, 180° and 225° angles (**Schmid et al., 2013**) using identical imaging conditions. For 3D reconstruction, an interactive bead-based registration algorithm was used to determine the threshold that most accurately

selects the beads (**Preibisch et al., 2010**). Reconstructed images were converted to 8-bit format using ImageJ, and Imaris software (Bitplane) was used for 3D data visualization and video generation. The videos were cropped using Avidemux 2.6.

To visualize the entire embryo in a single image, reconstructed images were first converted to 16-bit files using ImageJ, and equirectangular 2D map projections were then generated (**Schmid et al., 2013**). The 2D maps were re-aligned into Hammer-Aitoff projections using Hugin panorama photo stitcher software (http://hugin.sourceforge.net) to orient the peak of pSmad1/5/9 intensity to the ventral pole (left in **Figure 1** panels) and the trough of pSmad1/5/9 intensity to the dorsal pole (right in **Figure 1** panels). For gradient quantifications in **Figure 1A+B** and **Figure 2F–H**, the embryo proper was masked using manual polygon selections in Fiji (**Schindelin et al., 2012**) in order to exclude signal from the yolk syncytial layer and yolk. The 'Plot Profile' function in Fiji was then applied to the entire masked image to determine ventral-to-dorsal gradients. The background signal of immunostained embryos was determined by finding the lowest value in the profiles of sphere stage embryos (**Figure 1A+B**) and the lowest value in the profiles of *chordin*$^{-/-}$ embryos (**Figure 2F+G**), respectively. These background values were subtracted from the data sets, and the profiles were normalized to the highest value in each data series. The mean and standard error of the normalized data sets was then calculated piece-wise for every point along the ventral-to-dorsal profile.

For transplantation experiments in **Figures 3** and **5**, imaging began 5 to 20 min post-transplantation and continued for approximately 1 hr (see *Transplantation* section for further details). The following imaging conditions were used:

- W Plan-Apochromat 20 x objective, 0.5 x zoom
- dual side light sheets
- 488 nm laser (100 mW) at 6% power (for sfGFP-containing constructs)
- 561 nm laser (20 mW) at 5% power (for double transplantations only; to detect Alexa 546 signal)
- separate exposure to 488/561 nm lasers (in double transplantation experiments only) to avoid cross-talk
- exposure time: 250 ms
- average light sheet thickness: 6.4 µm
- 3 µm intervals between z-slices; 60 slices per embryo (≈180 µm total)
- 5 min intervals between imaging

Gradients were quantified using maximum intensity projections of 15 z-slices similar to the approach in (**Müller et al., 2012**). A rectangular region of interest abutting the clone with a fixed height of 86.34 µm (corresponding to 189 pixels) and varying widths depending on embryo length was drawn in Fiji (**Schindelin et al., 2012**), and the average intensity in 0.457 µm strips was calculated from the maximum intensity projections. Background intensity resulting from autofluorescence was measured similarly in uninjected embryos (for single transplantation experiments, n = 4) or in uninjected embryos transplanted with a clone of cells containing Alexa 546-coupled dextran (for double transplantation experiments, n = 2). A single value for background subtraction was determined by calculating the average of the intensity profile values. After subtracting the background value from the experimental intensity profiles, the data was normalized to the value closest to the clonal source boundary. This approach allows for the comparison of the relative gradient range, which is independent of constant production rates. We assume constant production rates over the relatively short time scales of observation (≈80 min).

Embryos with low signal-to-noise ratios were excluded from analysis.

Fluorescence decrease after photoconversion (FDAP) experiments

FDAP experiments were carried out as described in (**Müller et al., 2012**; **Rogers et al., 2015**). Embryos were injected at the one-cell stage with either 60 pg *BMP2b-Dendra2* mRNA + 0.5 ng Alexa 488-dextran (3 kDa, Molecular Probes) or 150 pg *Chordin-Dendra2* mRNA + 0.5 ng Alexa 488-dextran. To assess background fluorescence, embryos were injected with 0.5 ng Alexa 488-dextran only. Embryos were mounted in 1% low melting point agarose in glass-bottom Petri dishes (MatTek Corporation) covered with embryo medium to hydrate the agarose during imaging.

FDAP experiments were performed using an LSM 780 (ZEISS) confocal microscope. Pre-conversion and post-conversion images were acquired using an LD C-Apochromat 40x/1.1 NA water

immersion objective. A single pre-photoconversion image was first acquired for each sample followed by photoconversion and multiposition time-lapse imaging with 10 min intervals for approximately 300 min. For photoconversion, embryos were illuminated with a Sola SE II LED lamp at 100% power for 30 s through a C-Apochromat 10x/0.45 NA objective and an AHF F36-500 UV filter cube. For both pre- and post-conversion images, Alexa 488 was excited using a 488 nm Argon laser, and a DPSS 561 nm laser was used to excite photoconverted Dendra2. The emission signal between 494–576 nm (Alexa 488) and 578–696 nm (photoconverted Dendra2) was collected using a 32 channel GaAsP QUASAR detector array. Embryos that produced only low levels of photoconverted Dendra2 signal or whose position shifted significantly over time as well as embryos with non-uniform signal distribution or embryos that died were excluded from analysis. Sample numbers: n = 22 for BMP2b-Dendra2 (with n = 17 background embryos); n = 6 for Chordin-Dendra2 (with n = 1 background embryo).

All experiments were analyzed using PyFDAP (**Bläßle and Müller, 2015**; **Rogers et al., 2015**), version 1.1.2. PyFDAP extracts the extracellular and intracellular photoconverted Dendra2 signal by masking the Alexa 488 signal, and fits the resulting average intensities with a linear decay model. The ordinary differential equation describing linear protein decay is given by

$$\frac{dc}{dt} = -k_1 c$$

where c is the concentration of the protein and k_1 is its clearance rate constant. We assume that Dendra2 signal is directly proportional to the protein concentration. The analytical solution of this equation is given by

$$c(t) = c_0 e^{-k_1 t} + y_0$$

where $c_0 + y_0$ is the protein's concentration at $t = 0$, and y_0 is the protein's concentration at $t = \infty$. The half-life τ of the protein can then be calculated as

$$\tau = \ln(2)/k$$

PyFDAP estimates a lower bound for y_0 by computing the maximum relative effect of photobleaching $F_{i,r}$. For each background data set, the strongest influence of photobleaching was computed by taking the minimum over all differences of background intensity $B_{j,r}$ and background noise N_i, and the difference between pre-conversion background intensity $B_{\mathrm{pre},i,r}$ and noise level. Here, r denotes the region under consideration, i.e. extracellular, intracellular, or the entire imaging slice; i indicates the ith data set, and j counts the background data sets. The average over all b background data sets was then taken to arrive at the mean effect of photobleaching. The factor

$$F_{i,r} = \frac{1}{b}\sum_{j=1}^{b} \min_t \left(\frac{B_{j,r}(t) - N_i}{B_{\mathrm{pre}_{j,r}} - N_i} \right)$$

was used to scale the pre-conversion intensity of the FDAP data set according to

$$y_{0_{i,r}} \geq F_{i,r}\left(I_{\mathrm{pre}_{i,r}} - N_i\right) + N_i$$

This lower bound was then used to constrain a Nelder-Mead simplex algorithm when minimizing

$$SSD = \sum_n (\bar{I}(t_n) - c(t_n))^2$$

Fluorescence recovery after photobleaching (FRAP) experiments

FRAP experiments and data analysis were carried out as previously described (**Müller et al., 2012**; **Müller et al., 2013**) using an LSM 780 NLO confocal microscope (ZEISS) and an LD LCI Plan-Apochromat 25x water immersion objective. Embryos were injected at the one-cell stage with 30 pg of mRNA encoding BMP2b-sfGFP, 60 pg of mRNA encoding BMP2b-Dendra2, 60 pg of mRNA encoding Chordin-sfGFP, 120 pg of mRNA encoding Chordin-Dendra2, or 30 pg of mRNA encoding Sizzled-sfGFP. To analyze the effect of Chordin on BMP2b diffusion, embryos were injected at the one-cell stage with 30 pg of mRNA encoding BMP2b-sfGFP plus 60 or 200 pg of mRNA encoding

Chordin, or 60 pg of mRNA encoding BMP2b-Dendra2 plus 200 pg of mRNA encoding Chordin. Embryos were mounted in 1% low-melting point agarose in glass-bottom Petri dishes (MatTek Corporation) covered with embryo medium to hydrate the agarose during imaging. Embryos with low or non-uniform fluorescence and embryos that died or whose position shifted significantly over time were excluded from analysis.

For FRAP data analysis, the fits of a model with uniform production, diffusion, and clearance were constrained with the clearance rate constants of BMP2b-Dendra2 and Chordin-Dendra2 fusions measured by FDAP in the present study (BMP2b-Dendra2: $k_1 = 8.9 \times 10^{-5}$/s; Chordin-Dendra2: $k_1 = 9.6 \times 10^{-5}$/s). Sizzled-sfGFP fits were constrained with the clearance constant measured for BMP2b-Dendra2 assuming similar protein stability. As shown previously, the estimation of diffusion coefficients does not sensitively depend on the values of clearance rate constants if the time scales of observation (here: 50 min) and protein stability (here: approximately 120 min) are similar (***Müller et al., 2012***).

Fluorescence correlation spectroscopy (FCS) experiments

The FCS experiments were done using an LD C-Apochromat 40x/1.1 NA water immersion objective on an LSM 780 NLO confocal microscope (ZEISS). Embryos were injected at the one-cell stage with 30 pg of mRNA encoding BMP2b-sfGFP or 60 pg of mRNA encoding Chordin-sfGFP. Embryos were mounted in 1% low-melting point agarose in glass-bottom Petri dishes (MatTek Corporation) and covered with embryo medium to hydrate the agarose during imaging. The fluorophores (sfGFP, Alexa 488) were excited using an Argon 488 nm laser, and the emission light between 494 and 542 nm was collected using a 32-channel GaAsP QUASAR detector array. Before each FCS experiment, the pinhole was aligned and set to 1 Airy unit, and the instrument was calibrated using a solution of 40 nM Alexa 488 dye (Thermo Fisher) in water. For each FCS sample, fluorescence fluctuations were measured for 10 s with 10 repeats, and any irregularities in the 100 s count trace resulting from cellular movements were excluded from analysis.

Auto-correlation curves for Alexa 488 were freely fitted to determine the structural parameter as well as the diffusion time, the triplet state fraction, and the triplet state relaxation time of Alexa 488 for every experiment. The auto-correlation curves for BMP2b-sfGFP and Chordin-sfGFP were fitted with a fixed structural parameter, fixed triplet state fraction, and fixed triplet relaxation time determined from the Alexa 488 calibration measurements. The curves were fitted using ZEISS ZEN Pro software with a one-component 'free diffusion with triplet state correction' model. The first 10^{-6} seconds lag time for the correlation curve was excluded in the fitting (***Yu et al., 2009***; ***Müller et al., 2013***). The diffusion coefficient was then calculated by comparing the diffusion time of BMP2b-sfGFP and Chordin-sfGFP with Alexa 488 (reference diffusion coefficient: 435 μm^2/s [***Petrásek and Schwille, 2008***]).

Since the values of the triplet state fraction and the triplet state relaxation time of sfGFP are unknown and not necessarily identical to those of Alexa 488, we also freely fitted the autocorrelation curves for BMP2b-sfGFP and Chordin-sfGFP with the experimentally measured structural parameter as the only constraint, and determined free diffusion coefficients of $D = 35 \pm 2$ μm^2/s for BMP2b-sfGFP (n = 17 measurements from 4 embryos) and $D = 50 \pm 3$ μm^2/s for Chordin-sfGFP (n = 19 measurements from 5 embryos), within a deviation of approximately 20–30% compared to the diffusion coefficients determined by constraining the fits with a fixed structural parameter, fixed triplet state fraction, and fixed triplet relaxation time ($D = 46 \pm 1$ μm^2/s for BMP2b-sfGFP, and $D = 59 \pm 2$ μm^2/s for Chordin-sfGFP; values reported in ***Figure 4***). The similar diffusion coefficients determined by differently constrained fits indicate that the diffusion time measured in our experiments does not sensitively depend on the values of the triplet state fraction and triplet state relaxation time.

Mathematical modeling of BMP2b-sfGFP and Chordin-sfGFP gradient formation

The geometry of the zebrafish blastoderm was approximated by the complement of two spheres with a columnar subdomain placed off-center to represent the signal source region with the same parameters as described in ***Müller et al. (2012)***. Gradient formation was simulated with the source-diffusion-sink model

$$\frac{\partial c}{\partial t} = D\nabla^2 c - k_1 c + \delta_s k_2$$

with

$$\delta_s = \begin{cases} 1 & \text{in the source} \\ 0 & \text{otherwise} \end{cases}$$

For ***Figure 3—figure supplement 2***, the experimental data were fitted with solutions from a 50 × 50 parameter grid spanning all possible combinations of 50 diffusion coefficients (logarithmically spaced from 0.1 $\mu m^2/s$ to 50 $\mu m^2/s$) and 50 clearance rate constants (logarithmically spaced from 1 × 10^{-5}/s to 5 × 10^{-4}).

Simulations of previous models

The finite element method was used for all numerical simulations. All geometries are one-dimensional representations of embryos. The solution at each time step in the discretized geometries was determined using a sparse LU factorization algorithm (UMFPACK), and the time stepping was computed using a backward Euler step method (Comsol Multiphysics). Simulations in ***Figure 1C–E,G*** (Models 1, 2, 3, and 5) were executed for a total of 10080 s (i.e., for approximately 3 hr from sphere to shield stage during zebrafish embryogenesis [***Kimmel et al., 1995***]) and read out every 2520 s (i.e., approximately every 42 min at relevant zebrafish stages). The simulation in ***Figure 1F*** (Model 4) was executed for a total of 20 time steps near steady state and read out at every fifth time step.

The following model descriptions comprise the complete wild type systems. For simulations of *chordin* mutants, the Chordin flux was set to 0 (Models 1, 2, 3, and 5), or the Chordin-dependent terms were removed from the equations and the initial concentration of Chordin was set to 0 (Model 4). To focus on the role of Chordin in regulating BMP signaling and distribution, we did not include other negative regulators of BMP such as Noggin and Follistatin (***Umulis et al., 2009***). For the interpretation of the simulations, we assume that the distribution of free BMPs is correlated with BMP signaling and the distribution of pSmad1/5/9.

To facilitate comparison of the models, the distribution profiles of free BMP are shown as a function of relative embryo length, and the solutions were normalized to the ventral-most free BMP concentration at shield stage (i.e., at t = 7560 s for Models 1, 2, 3, and 5, and at t = 15 for Model 4) in wild type simulations.

Model 1: Graded source-sink (mobile BMP)

In the graded source-sink model, the BMP source $\rho_{BMP}(x)$ was modeled after the known distribution of *bmp2b* mRNA between sphere stage and 30% epiboly (***Ramel and Hill, 2013***). The model does not include autoregulation of BMP production since positive feedback only appears to be important for later stages of development (***Ramel and Hill, 2013***; ***Zinski et al., 2017***). Chordin binds BMP irreversibly and acts as a sink. The model was simulated using the following equations:

$$\frac{\partial[\mathrm{BMP}]}{\partial t} = D_{\mathrm{BMP}}\nabla^2[\mathrm{BMP}] - \kappa[\mathrm{Chd}][\mathrm{BMP}] - \lambda_{\mathrm{BMP}}[\mathrm{BMP}] + \rho_{\mathrm{BMP}}(x)$$

$$\frac{\partial[\mathrm{Chd}]}{\partial t} = D_{\mathrm{Chd}}\nabla^2[\mathrm{Chd}] - \kappa[\mathrm{Chd}][\mathrm{BMP}] - \lambda_{\mathrm{Chd}}[\mathrm{Chd}]$$

$$\frac{\partial[\mathrm{ChdBMP}]}{\partial t} = D_{\mathrm{ChdBMP}}\nabla^2[\mathrm{ChdBMP}] + \kappa[\mathrm{Chd}][\mathrm{BMP}] - \lambda_{\mathrm{Chd}}[\mathrm{ChdBMP}]$$

Embryo geometry and boundary conditions

Embryo length: 300 × 10^{-6} m (300 µm, the typical length of the zebrafish blastoderm)
Constant Chordin flux from the dorsal boundary: 5 × 10^{-14} mol/(m^2•s)
No-flux boundary condition for all other species on both ventral and dorsal boundaries

Parameter values

D_{BMP} = 2 $\mu m^2/s$ (measured in the present study)
D_{Chd} = 7 $\mu m^2/s$ (measured in the present study)
D_{ChdBMP} = 7 $\mu m^2/s$

λ_{BMP} = 8.9 × 10^{-5}/s (measured in the present study)
λ_{Chd} = 9.6 × 10^{-5}/s (measured in the present study)
κ = 400 × 10^{3} m^3/(mol•s)
$\rho_{BMP}(x)$ = 0.57 × 10^{-9} × e^{-5000x} mol/m^3 (accounting for the inhomogeneous ventrally peaking distribution of *bmp2b* mRNA in zebrafish embryos)

Initial conditions

BMP initial concentration: 2.85 × 10^{-8} mol/m^3 everywhere (one-twentieth of the concentration used for *Xenopus* frogs in [***Inomata et al., 2013***])
Chordin initial concentration: 0 mol/m^3 everywhere
Chordin-BMP complex initial concentration: 0 mol/m^3 everywhere

Model 2: Graded source-sink (immobile BMP)

As for Model 1, the graded source-sink model (immobile BMP) was modeled without autoregulation of BMP production since positive feedback only appears to be important for later stages of development (***Ramel and Hill, 2013***; ***Zinski et al., 2017***). Here κ, which reflects the binding between Chordin and BMP, is smaller than in Model 1 to obtain a realistic-free BMP distribution; using the same value for κ as in Model 1 creates an unrealistically steep free BMP gradient. The model was simulated using the following equations:

$$\frac{\partial[\mathrm{BMP}]}{\partial t} = -\kappa[\mathrm{Chd}][\mathrm{BMP}] - \lambda_{\mathrm{BMP}}[\mathrm{BMP}] + \rho_{\mathrm{BMP}}(x)$$

$$\frac{\partial[\mathrm{Chd}]}{\partial t} = D_{\mathrm{Chd}}\nabla^2[\mathrm{Chd}] - \kappa[\mathrm{Chd}][\mathrm{BMP}] - \lambda_{\mathrm{Chd}}[\mathrm{Chd}]$$

$$\frac{\partial[\mathrm{ChdBMP}]}{\partial t} = D_{\mathrm{ChdBMP}}\nabla^2[\mathrm{ChdBMP}] + \kappa[\mathrm{Chd}][\mathrm{BMP}] - \lambda_{\mathrm{Chd}}[\mathrm{ChdBMP}]$$

Embryo geometry and boundary conditions

Embryo length: 300 × 10^{-6} m (300 µm, the typical length of a zebrafish blastoderm)
Constant Chordin flux from the dorsal boundary: 5 × 10^{-14} mol/(m^2•s)
No-flux boundary condition for all other species on both ventral and dorsal boundaries

Parameter values

D_{Chd} = 7 μm^2/s (measured in the present study)
D_{ChdBMP} = 7 μm^2/s
λ_{BMP} = 8.9 × 10^{-5}/s (measured in the present study)
λ_{Chd} = 9.6 × 10^{-5}/s (measured in the present study)
κ = 4 × 10^{3} m^3/(mol•s)
$\rho_{BMP}(x)$ = 0.57 × 10^{-9} × e^{-5000x} mol/m^3 (accounting for the inhomogenous ventrally peaking distribution of *bmp2b* mRNA in zebrafish embryos)

Initial conditions

BMP initial concentration: 2.85 × 10^{-8} mol/m^3 everywhere (one-twentieth of the concentration used for *Xenopus* frogs in [***Inomata et al., 2013***]).
Chordin initial concentration: 0 mol/m^3 everywhere
Chordin-BMP complex initial concentration: 0 mol/m^3 everywhere

Model 3: Long-range accumulation and feedback

The model was developed for frog embryogenesis. For the simulations in the present study the equations, geometry, initial conditions, and parameters used were exactly as described in (***Inomata et al., 2013***):

$$\frac{\partial[\mathrm{BMP}]}{\partial t} = D\nabla^2[\mathrm{BMP}] + \frac{v_{\mathrm{BMP}}([\mathrm{ADMP}]+[\mathrm{BMP}])^{10}}{k_{\mathrm{BMP}}^{10}+([\mathrm{ADMP}]+[\mathrm{BMP}])^{10}} - \lambda_{\mathrm{BMP}}[\mathrm{BMP}]$$

$$+\frac{\lambda_{\mathrm{Chd}}[\mathrm{ChdBMP}]}{1+\frac{[\mathrm{Szl}]}{ki}+\frac{[\mathrm{Chd}]+[\mathrm{ChdBMP}]+[\mathrm{ChdADMP}]}{km}} - k[\mathrm{Chd}][\mathrm{BMP}]$$

$$\frac{\partial[\mathrm{Chd}]}{\partial t} = D\nabla^2[\mathrm{Chd}] + \frac{v_{\mathrm{Chd}}k_{\mathrm{Chd}}^{10}}{k_{\mathrm{Chd}}^{10}+([\mathrm{ADMP}]+[\mathrm{BMP}])^{10}} - \frac{\lambda_{\mathrm{Chd}}[\mathrm{Chd}]}{1+\frac{[\mathrm{Szl}]}{ki}+\frac{[\mathrm{Chd}]+[\mathrm{ChdBMP}]+[\mathrm{ChdADMP}]}{km}}$$

$$-k[\mathrm{Chd}][\mathrm{BMP}] - k[\mathrm{Chd}][\mathrm{ADMP}]$$

$$\frac{\partial[\mathrm{ADMP}]}{\partial t} = D\nabla^2[\mathrm{ADMP}] + \frac{v_{\mathrm{ADMP}}k_{\mathrm{ADMP}}^{10}}{k_{\mathrm{ADMP}}^{10}+([\mathrm{ADMP}]+[\mathrm{BMP}])^{10}} - \lambda_{\mathrm{BMP}}[\mathrm{ADMP}]$$

$$+\frac{\lambda_{\mathrm{Chd}}[\mathrm{ChdADMP}]}{1+\frac{[\mathrm{Szl}]}{ki}+\frac{[\mathrm{Chd}]+[\mathrm{ChdBMP}]+[\mathrm{ChdADMP}]}{km}} - k[\mathrm{Chd}][\mathrm{ADMP}]$$

$$\frac{\partial[\mathrm{Szl}]}{\partial t} = D\nabla^2[\mathrm{Szl}] + \frac{v_{\mathrm{Szl}}([\mathrm{ADMP}]+[\mathrm{BMP}])^{20}}{k_{\mathrm{Szl}}^{20}+([\mathrm{ADMP}]+[\mathrm{BMP}])^{20}} - \lambda_{\mathrm{Szl}}[\mathrm{Szl}]$$

$$\frac{\partial[\mathrm{ChdBMP}]}{\partial t} = D\nabla^2[\mathrm{ChdBMP}] - \frac{\lambda_{\mathrm{Chd}}[\mathrm{ChdBMP}]}{1+\frac{[\mathrm{Szl}]}{ki}+\frac{[\mathrm{Chd}]+[\mathrm{ChdBMP}]+[\mathrm{ChdADMP}]}{km}} + k[\mathrm{Chd}][\mathrm{BMP}]$$

$$\frac{\partial[\mathrm{ChdADMP}]}{\partial t} = D\nabla^2[\mathrm{ChdADMP}] - \frac{\lambda_{\mathrm{Chd}}[\mathrm{ChdADMP}]}{1+\frac{[\mathrm{Szl}]}{ki}+\frac{[\mathrm{Chd}]+[\mathrm{ChdBMP}]+[\mathrm{ChdADMP}]}{km}} + k[\mathrm{Chd}][\mathrm{ADMP}]$$

Embryo geometry and boundary conditions

Embryo length: 1000 × 10^{-6} m (1000 µm, the typical length of a frog embryo)
Constant Chordin flux from the dorsal boundary: 4.8 × 10^{-12} mol/(m^2•s)
No-flux boundary condition for all other species on both ventral and dorsal boundaries

Parameter values

km = 25 × 10^{-6} mol/m^3
ki = 25 × 10^{-6} mol/m^3
v_{Chd} = 5 × 10^{-10} mol/(m^3•s)
k_{Chd} = 7 × 10^{-8} mol/m^3
v_{BMP} = 1.4 × 10^{-10} mol/(m^3•s)
k_{BMP} = 3.5 × 10^{-7} mol/m^3
v_{Szl} = 100 × 10^{-6} mol/(m^3•s)
k_{Szl} = 1 × 10^{-6} mol/m^3
v_{ADMP} = 3.2 × 10^{-9} mol/(m^3•s)
k_{ADMP} = 3 × 10^{-8} mol/m^3
λ_{Chd} = 1 × 10^{-3}/s
λ_{BMP} = 2 × 10^{-4}/s
λ_{Szl} = 3.8 × 10^{-5}/s
D = 15 µm^2/s
k = 280 m^3/(mol•s)

Initial conditions

BMP initial concentration: 0.57 × 10^{-6} × e^{-1000x} mol/m^3 throughout the embryo (the amplitude of this distribution is the same as in [***Inomata et al., 2013***], but the initial BMP profile was modeled as a gradient instead of uniform)
Chordin initial concentration: 0 mol/m^3 everywhere

ADMP initial concentration: 0 mol/m^3 everywhere
Sizzled initial concentration: 0 mol/m^3 everywhere
Chordin-BMP complex initial concentration: 0 mol/m^3 everywhere
Chordin-AMP complex initial concentration: 0 mol/m^3 everywhere

For the simulations in ***Figure 4—figure supplement 1E–J***, all parameters were identical to the parameter values listed above except for *D*(BMP) = 3 µm^2/s, *D*(Chd) = 6 µm^2/s, *D*(ChdADMP) = 10 µm^2/s, and *D*(ChdBMP) = 10 µm^2/s. *D*(Sizzled) was set to 150 µm^2/s in ***Figure 4—figure supplement 1E***, and to 10 µm^2/s in ***Figure 4—figure supplement 1F–J***. *D*(ADMP) was varied from 0.1 µm^2/s to 150 µm^2/s as indicated in ***Figure 4—figure supplement 1E–J***.

Model 4: Self-regulating reaction-diffusion system

The non-dimensional model, geometry, initial conditions, and parameters used for the simulations were similar to the ones described in [***Francois et al., 2009***]:

$$\frac{\partial[\mathrm{BMP}]}{\partial t} = D_{\mathrm{BMP}}\nabla^2[\mathrm{BMP}] + \frac{[\mathrm{BMP}]^2}{(1+[\mathrm{Chd}])[\mathrm{Szl}]} - \mu_{\mathrm{BMP}}[\mathrm{BMP}] + \rho_{\mathrm{BMP}}$$

$$\frac{\partial[\mathrm{Chd}]}{\partial t} = D_{\mathrm{Chd}}\nabla^2[\mathrm{Chd}] + \frac{[\mathrm{Chd}]^2}{[\mathrm{ADMP}]} - \mu_{\mathrm{Chd}}[\mathrm{Chd}] + \rho_{\mathrm{Chd}}$$

$$\frac{\partial[\mathrm{ADMP}]}{\partial t} = D_{\mathrm{ADMP}}\nabla^2[\mathrm{ADMP}] + [\mathrm{Chd}]^2 - \mu_{\mathrm{ADMP}}[\mathrm{ADMP}]$$

$$\frac{\partial[\mathrm{Szl}]}{\partial t} = D_{\mathrm{Szl}}\nabla^2[\mathrm{Szl}] + [\mathrm{BMP}]^2 - \mu_{\mathrm{Szl}}[\mathrm{Szl}]$$

Embryo geometry and boundary conditions

Embryo length: 25
No-flux boundary conditions on the ventral and dorsal boundaries

Parameter values

$D_{Chd} = D_{BMP} = 6$
$\mu_{Chd} = \mu_{BMP} = 1.2$
$\rho_{Chd} = \rho_{BMP} = 0.1$
$\mu_{ADMP} = \mu_{Szl} = 1.5$
$D_{ADMP} = D_{Szl} = 150$

Initial conditions

BMP initial concentration: $\rho_{BMP} = e^{-0.1x}$
Chordin initial concentration of 1 from position 0 to 24 and Chordin initial concentration of 10 from 24 to 25 (i.e., the dorsal organizer) in the simulated embryo
ADMP initial concentration: 1 everywhere
Sizzled initial concentration: 1 everywhere

For the simulations in ***Figure 4—figure supplement 1K–P***, all parameters were identical to the parameter values listed above except for *D*(BMP) = 3 and *D*(Chd) = 6. *D*(Sizzled) was set to 150 in ***Figure 4—figure supplement 1K***, and to 10 in ***Figure 4—figure supplement 1L–P***. *D*(ADMP) was varied from 0.1 to 150 as indicated in ***Figure 4—figure supplement 1K–P***.

Model 5: Shuttling

For Model 5, a minimal transport model that excludes the effects of downstream patterning circuits was used to illustrate the biophysical aspects of shuttling (***Ben-Zvi et al., 2008***):

$$\frac{\partial[\mathrm{BMP}]}{\partial t} = D_{\mathrm{BMP}}\nabla^2[\mathrm{BMP}] - \kappa[\mathrm{Chd}][\mathrm{BMP}] + \lambda[\mathrm{Xlr}][\mathrm{ChdBMP}] - \lambda_{\mathrm{BMP}}[\mathrm{BMP}] + \rho_{\mathrm{BMP}}(x)$$

$$\frac{\partial[\mathrm{Chd}]}{\partial t} = D_{\mathrm{Chd}}\nabla^2[\mathrm{Chd}] - \kappa[\mathrm{Chd}][\mathrm{BMP}] - \lambda_{\mathrm{Chd}}[\mathrm{Chd}]$$

$$\frac{\partial[\mathrm{ChdBMP}]}{\partial t} = D_{\mathrm{ChdBMP}}\nabla^2[\mathrm{ChdBMP}] + \kappa[\mathrm{Chd}][\mathrm{BMP}] - \lambda[\mathrm{Xlr}][\mathrm{ChdBMP}] - \lambda_{\mathrm{Chd}}[\mathrm{ChdBMP}]$$

Embryo geometry and boundary conditions

Embryo length: 300×10^{-6} m (300 µm)
Constant Chordin flux from the dorsal boundary: 3×10^{-14} mol/(m^2•s)
No-flux boundary condition for all other species on both ventral and dorsal boundaries

Parameter values

D_{BMP} = 0.1 µm^2/s
D_{Chd} = 10 µm^2/s
D_{ChdBMP} = 10 µm^2/s
$\lambda_{BMP} = 8.9 \times 10^{-5}$/s (measured in the present study)
$\lambda_{Chd} = 9.6 \times 10^{-5}$/s (measured in the present study)
$\kappa = 100 \times 10^3$ m^3/(mol•s)
$\lambda = \kappa$
[Xlr] = 2×10^{-8} mol/m^3
$\rho_{BMP}(x) = 0.57 \times 10^{-10} \times e^{-5000x}$ mol/m^3 (accounting for the inhomogeneous ventrally peaking distribution of *bmp2b* mRNA in zebrafish embryos)

Initial conditions

BMP initial concentration: $0.57 \times 10^{-7} \times e^{-5000x}$ mol/m^3 throughout the embryo
Chordin initial concentration: 0 mol/m^3 everywhere
Chordin-BMP complex initial concentration: 0 mol/m^3 everywhere

Shuttling simulations of adjacent BMP and Chordin clones shown in *Figure 5*

The one-dimensional simulations in ***Figure 5*** were executed similarly to the ones described above and solved at 15 and 75 min for comparison to the zebrafish embryo double transplantation experiments. The solutions in ***Figure 5A*** and ***Figure 5E*** were normalized to the highest free BMP concentration in the simulation without the Chordin source, and the solutions in ***Figure 5B*** and ***Figure 5F*** were normalized to the free BMP concentration at the BMP source boundary (at 100 µm) for each condition to facilitate comparison between the gradient ranges.

The double transplantation experiments were modeled using the following equations:

$$\frac{\partial[\mathrm{BMP}]}{\partial t} = D_{\mathrm{BMP}}\nabla^2[\mathrm{BMP}] - \lambda_{\mathrm{BMP}}[\mathrm{BMP}] - \kappa[\mathrm{Chd}][\mathrm{BMP}] + \lambda[\mathrm{Xlr}][\mathrm{ChdBMP}] + \delta_{\mathrm{BMP}}\eta_{\mathrm{BMP}}$$

$$\frac{\partial[\mathrm{Chd}]}{\partial t} = D_{\mathrm{Chd}}\nabla^2[\mathrm{Chd}] - \kappa[\mathrm{Chd}][\mathrm{BMP}] + \delta_{\mathrm{Chd}}\eta_{\mathrm{Chd}}$$

$$\frac{\partial[\mathrm{ChdBMP}]}{\partial t} = D_{\mathrm{ChdBMP}}\nabla^2[\mathrm{ChdBMP}] + \kappa[\mathrm{Chd}][\mathrm{BMP}] - \lambda[\mathrm{Xlr}][\mathrm{ChdBMP}]$$

with

$$\delta_{\mathrm{BMP}} = \begin{cases} 1 \text{ in the BMP source} \\ 0 \text{ otherwise} \end{cases}$$

and

$$\delta_{\mathrm{Chd}} = \begin{cases} 1 \text{ in the Chordin source} \\ 0 \text{ otherwise} \end{cases}$$

Embryo geometry and boundary conditions

Embryo length: 300×10^{-6} m (300 µm)
BMP source: between 50 and 100 µm from the left boundary
Chordin source: between 200 and 250 µm from the left boundary
No-flux boundary conditions on the left and right boundaries

Parameter values for simulations of shuttling predictions (***Figure 5A+B***)

D_{BMP} = 2 µm^2/s (measured in the present study)
λ_{BMP} = 0.0001/s (similar to measurements in the present study)
η_{BMP} = 5×10^{-5} mol/(m^3•s)
η_{Chd} = 5×10^{-5} mol/(m^3•s)
D_{Chd} = 100 µm^2/s
$D_{ChdBMP} = D_{Chd}$
$\kappa = 10 \times 10^3$ m^3/(mol•s)
$\lambda = \kappa$
[Xlr] = 2×10^{-7} mol/m^3

Parameter values for simulations with experimentally measured diffusivities (***Figure 5E+F***)

D_{BMP} = 2 µm^2/s (measured in the present study)
λ_{BMP} = 0.0001/s (similar to measurements in the present study)
η_{BMP} = 5×10^{-5} mol/(m^3•s)
η_{Chd} = 5×10^{-5} mol/(m^3•s)
D_{Chd} = 6 µm^2/s (measured in the present study)
D_{ChdBMP} = 2.2 µm^2/s (measured in the present study)
$\kappa = 10 \times 10^3$ m^3/(mol s)
$\lambda = \kappa$
[Xlr] = 2×10^{-7} mol/m^3

Initial conditions

BMP initial concentration: 0 mol/m^3 everywhere
Chordin initial concentration: 0 mol/m^3 everywhere
Chordin-BMP complex initial concentration: 0 mol/m^3 everywhere

Acknowledgements

We are grateful to Hans Meinhardt for valuable discussions of BMP/Chordin-mediated dorsal-ventral patterning mechanisms. We thank Edgar Herrera and Luciano Marcon for support with immunostainings, light sheet microscopy, data reconstruction, and helpful discussions. We acknowledge Matteo Pilz and Sarah Keim for technical assistance. This work was supported by the Max Planck Society and a Human Frontier Science Program (HFSP) Career Development Award to PM.

Additional information

Funding

Funder	Grant reference number	Author
Max-Planck-Gesellschaft		Patrick Müller
Human Frontier Science Program	Career Development Award (CDA00031/2013-C)	Patrick Müller

The funders had no role in study design, data collection and interpretation, or the decision to submit the work for publication.

Author contributions

Autumn P Pomreinke, Gary H Soh, Data curation, Formal analysis, Investigation, Visualization, Methodology, Writing—review and editing; Katherine W Rogers, Conceptualization, Resources, Data curation, Formal analysis, Investigation, Visualization, Methodology, Writing—review and editing; Jennifer K Bergmann, Resources, Data curation, Formal analysis, Investigation, Visualization; Alexander J Bläßle, Data curation, Software, Formal analysis, Investigation, Visualization, Methodology, Writing—review and editing; Patrick Müller, Conceptualization, Resources, Data curation, Software, Formal analysis, Supervision, Funding acquisition, Validation, Investigation, Visualization, Methodology, Writing—original draft, Project administration, Writing—review and editing

Author ORCIDs

Katherine W Rogers, http://orcid.org/0000-0001-5700-2662
Patrick Müller, http://orcid.org/0000-0002-0702-6209

Decision letter and Author response

Decision letter https://doi.org/10.7554/eLife.25861.024
Author response https://doi.org/10.7554/eLife.25861.025

Additional files

Supplementary files

- Transparent reporting form

DOI: https://doi.org/10.7554/eLife.25861.023

References

Alexandre C, Baena-Lopez A, Vincent JP. 2014. Patterning and growth control by membrane-tethered Wingless. *Nature* **505**:180–185. DOI: https://doi.org/10.1038/nature12879, PMID: 24390349

Barkai N, Ben-Zvi D. 2009. 'Big frog, small frog'–maintaining proportions in embryonic development: delivered on 2 July 2008 at the 33rd FEBS Congress in Athens, Greece. *The FEBS Journal* **276**:1196–1207. DOI: https://doi.org/10.1111/j.1742-4658.2008.06854.x, PMID: 19175672

Ben-Zvi D, Shilo BZ, Fainsod A, Barkai N. 2008. Scaling of the BMP activation gradient in Xenopus embryos. *Nature* **453**:1205–1211. DOI: https://doi.org/10.1038/nature07059, PMID: 18580943

Ben-Zvi D, Barkai N. 2010. Scaling of morphogen gradients by an expansion-repression integral feedback control. *PNAS* **107**:6924–6929. DOI: https://doi.org/10.1073/pnas.0912734107, PMID: 20356830

Ben-Zvi D, Pyrowolakis G, Barkai N, Shilo BZ. 2011a. Expansion-repression mechanism for scaling the Dpp activation gradient in Drosophila wing imaginal discs. *Current Biology* **21**:1391–1396. DOI: https://doi.org/10.1016/j.cub.2011.07.015, PMID: 21835621

Ben-Zvi D, Shilo BZ, Barkai N. 2011b. Scaling of morphogen gradients. *Current Opinion in Genetics & Development* **21**:704–710. DOI: https://doi.org/10.1016/j.gde.2011.07.011, PMID: 21873045

Ben-Zvi D, Fainsod A, Shilo BZ, Barkai N. 2014. Scaling of dorsal-ventral patterning in the Xenopus laevis embryo. *BioEssays* **36**:151–156. DOI: https://doi.org/10.1002/bies.201300136, PMID: 24323952

Bläßle A, Müller P. 2015. PyFDAP: automated analysis of fluorescence decay after photoconversion (FDAP) experiments. *Bioinformatics* **31**:972–974. DOI: https://doi.org/10.1093/bioinformatics/btu735, PMID: 25380959

Brankatschk M, Dickson BJ. 2006. Netrins guide Drosophila commissural axons at short range. *Nature Neuroscience* **9**:188–194. DOI: https://doi.org/10.1038/nn1625, PMID: 16429137

Connors SA, Trout J, Ekker M, Mullins MC. 1999. The role of tolloid/mini fin in dorsoventral pattern formation of the zebrafish embryo. *Development* **126**:3119–3130. PMID: 10375503

Cui Y, Jean F, Thomas G, Christian JL. 1998. BMP-4 is proteolytically activated by furin and/or PC6 during vertebrate embryonic development. *The EMBO Journal* **17**:4735–4743. DOI: https://doi.org/10.1093/emboj/17.16.4735, PMID: 9707432

Degnin C, Jean F, Thomas G, Christian JL. 2004. Cleavages within the prodomain direct intracellular trafficking and degradation of mature bone morphogenetic protein-4. *Molecular Biology of the Cell* **15**:5012–5020. DOI: https://doi.org/10.1091/mbc.E04-08-0673, PMID: 15356272

Dickmeis T, Rastegar S, Aanstad P, Clark M, Fischer N, Korzh V, Strähle U. 2001. Expression of the anti-dorsalizing morphogenetic protein gene in the zebrafish embryo. *Development Genes and Evolution* **211**:568–572. DOI: https://doi.org/10.1007/s00427-001-0190-3, PMID: 11862464

Dominici C, Moreno-Bravo JA, Puiggros SR, Rappeneau Q, Rama N, Vieugue P, Bernet A, Mehlen P, Chédotal A. 2017. Floor-plate-derived netrin-1 is dispensable for commissural axon guidance. *Nature* **545**:350–354. DOI: https://doi.org/10.1038/nature22331, PMID: 28445456

Fisher S, Halpern ME. 1999. Patterning the zebrafish axial skeleton requires early chordin function. *Nature Genetics* **23**:442–446. DOI: https://doi.org/10.1038/70557, PMID: 10581032

Francois P, Vonica A, Brivanlou AH, Siggia ED. 2009. Scaling of BMP gradients in Xenopus embryos. *Nature* **461**: E1. DOI: https://doi.org/10.1038/nature08305, PMID: 19736667

Gurskaya NG, Verkhusha VV, Shcheglov AS, Staroverov DB, Chepurnykh TV, Fradkov AF, Lukyanov S, Lukyanov KA. 2006. Engineering of a monomeric green-to-red photoactivatable fluorescent protein induced by blue light. *Nature Biotechnology* **24**:461–465. DOI: https://doi.org/10.1038/nbt1191, PMID: 16550175

Hammerschmidt M, Pelegri F, Mullins MC, Kane DA, van Eeden FJ, Granato M, Brand M, Furutani-Seiki M, Haffter P, Heisenberg CP, Jiang YJ, Kelsh RN, Odenthal J, Warga RM, Nüsslein-Volhard C. 1996. dino and mercedes, two genes regulating dorsal development in the zebrafish embryo. *Development* **123**:95–102. PMID: 9007232

Harmansa S, Hamaratoglu F, Affolter M, Caussinus E. 2015. Dpp spreading is required for medial but not for lateral wing disc growth. *Nature* **527**:317–322. DOI: https://doi.org/10.1038/nature15712, PMID: 26550827

Haskel-Ittah M, Ben-Zvi D, Branski-Arieli M, Schejter ED, Shilo BZ, Barkai N. 2012. Self-organized shuttling: generating sharp dorsoventral polarity in the early Drosophila embryo. *Cell* **150**:1016–1028. DOI: https://doi.org/10.1016/j.cell.2012.06.044, PMID: 22939625

Horton RM, Cai ZL, Ho SN, Pease LR. 1990. Gene splicing by overlap extension: tailor-made genes using the polymerase chain reaction. *BioTechniques* **8**:528–535. DOI: https://doi.org/10.2144/000114017, PMID: 2357375

Inomata H, Shibata T, Haraguchi T, Sasai Y. 2013. Scaling of dorsal-ventral patterning by embryo size-dependent degradation of Spemann's organizer signals. *Cell* **153**:1296–1311. DOI: https://doi.org/10.1016/j.cell.2013.05.004, PMID: 23746842

Jones CM, Armes N, Smith JC. 1996. Signalling by TGF-beta family members: short-range effects of Xnr-2 and BMP-4 contrast with the long-range effects of activin. *Current Biology* **6**:1468–1475. DOI: https://doi.org/10.1016/S0960-9822(96)00751-8, PMID: 8939607

Kicheva A, Pantazis P, Bollenbach T, Kalaidzidis Y, Bittig T, Jülicher F, González-Gaitán M. 2007. Kinetics of morphogen gradient formation. *Science* **315**:521–525. DOI: https://doi.org/10.1126/science.1135774, PMID: 17255514

Kimmel CB, Ballard WW, Kimmel SR, Ullmann B, Schilling TF. 1995. Stages of embryonic development of the zebrafish. *Developmental Dynamics* **203**:253–310. DOI: https://doi.org/10.1002/aja.1002030302, PMID: 8589427

Kishimoto Y, Lee KH, Zon L, Hammerschmidt M, Schulte-Merker S. 1997. The molecular nature of zebrafish swirl: BMP2 function is essential during early dorsoventral patterning. *Development* **124**:4457–4466. PMID: 9409664

Koos DS, Ho RK. 1999. The nieuwkoid/dharma homeobox gene is essential for bmp2b repression in the zebrafish pregastrula. *Developmental Biology* **215**:190–207. DOI: https://doi.org/10.1006/dbio.1999.9479, PMID: 10545230

Lele Z, Nowak M, Hammerschmidt M. 2001. Zebrafish admp is required to restrict the size of the organizer and to promote posterior and ventral development. *Developmental Dynamics* **222**:681–687. DOI: https://doi.org/10.1002/dvdy.1222, PMID: 11748836

Leung T, Bischof J, Söll I, Niessing D, Zhang D, Ma J, Jäckle H, Driever W. 2003. bozozok directly represses bmp2b transcription and mediates the earliest dorsoventral asymmetry of bmp2b expression in zebrafish. *Development* **130**:3639–3649. DOI: https://doi.org/10.1242/dev.00558, PMID: 12835381

Meeker ND, Hutchinson SA, Ho L, Trede NS. 2007. Method for isolation of PCR-ready genomic DNA from zebrafish tissues. *BioTechniques* **43**:610–614. DOI: https://doi.org/10.2144/000112619, PMID: 18072590

Miller-Bertoglio VE, Fisher S, Sánchez A, Mullins MC, Halpern ME. 1997. Differential regulation of chordin expression domains in mutant zebrafish. *Developmental Biology* **192**:537–550. DOI: https://doi.org/10.1006/dbio.1997.8788, PMID: 9441687

Mullins MC, Hammerschmidt M, Kane DA, Odenthal J, Brand M, van Eeden FJ, Furutani-Seiki M, Granato M, Haffter P, Heisenberg CP, Jiang YJ, Kelsh RN, Nüsslein-Volhard C. 1996. Genes establishing dorsoventral pattern formation in the zebrafish embryo: the ventral specifying genes. *Development* **123**:81–93. PMID: 9007231

Müller P, Schier AF. 2011. Extracellular movement of signaling molecules. *Developmental Cell* **21**:145–158. DOI: https://doi.org/10.1016/j.devcel.2011.06.001, PMID: 21763615

Müller P, Rogers KW, Jordan BM, Lee JS, Robson D, Ramanathan S, Schier AF. 2012. Differential diffusivity of Nodal and Lefty underlies a reaction-diffusion patterning system. *Science* **336**:721–724. DOI: https://doi.org/10.1126/science.1221920, PMID: 22499809

Müller P, Rogers KW, Yu SR, Brand M, Schier AF. 2013. Morphogen transport. *Development* **140**:1621–1638. DOI: https://doi.org/10.1242/dev.083519, PMID: 23533171

Petrásek Z, Schwille P. 2008. Precise measurement of diffusion coefficients using scanning fluorescence correlation spectroscopy. *Biophysical Journal* **94**:1437–1448. DOI: https://doi.org/10.1529/biophysj.107.108811, PMID: 17933881

Plouhinec JL, De Robertis EM. 2009. Systems biology of the self-regulating morphogenetic gradient of the Xenopus gastrula. *Cold Spring Harbor Perspectives in Biology* **1**:a001701. DOI: https://doi.org/10.1101/cshperspect.a001701, PMID: 20066084

Plouhinec JL, Zakin L, Moriyama Y, De Robertis EM. 2013. Chordin forms a self-organizing morphogen gradient in the extracellular space between ectoderm and mesoderm in the Xenopus embryo. *PNAS* **110**:20372–20379. DOI: https://doi.org/10.1073/pnas.1319745110, PMID: 24284174

Preibisch S, Saalfeld S, Schindelin J, Tomancak P. 2010. Software for bead-based registration of selective plane illumination microscopy data. *Nature Methods* **7**:418–419. DOI: https://doi.org/10.1038/nmeth0610-418, PMID: 20508634

Pédelacq JD, Cabantous S, Tran T, Terwilliger TC, Waldo GS. 2006. Engineering and characterization of a superfolder green fluorescent protein. *Nature Biotechnology* **24**:79–88. DOI: https://doi.org/10.1038/nbt1172, PMID: 16369541

Ramel MC, Hill CS. 2013. The ventral to dorsal BMP activity gradient in the early zebrafish embryo is determined by graded expression of BMP ligands. *Developmental Biology* **378**:170–182. DOI: https://doi.org/10.1016/j.ydbio.2013.03.003, PMID: 23499658

Rogers KW, Blässle A, Schier AF, Müller P. 2015. Measuring protein stability in living zebrafish embryos using fluorescence decay after photoconversion (FDAP). *Journal of Visualized Experiments*:52266. DOI: https://doi.org/10.3791/52266, PMID: 25650549

Roy S, Kornberg TB. 2011. Direct delivery mechanisms of morphogen dispersion. *Science Signaling* **4**:pt8. DOI: https://doi.org/10.1126/scisignal.2002434, PMID: 22114143

Sako K, Pradhan SJ, Barone V, Inglés-Prieto Á, Müller P, Ruprecht V, Čapek D, Galande S, Janovjak H, Heisenberg CP. 2016. Optogenetic control of nodal signaling reveals a temporal pattern of nodal signaling regulating cell fate specification during gastrulation. *Cell Reports* **16**:866–877. DOI: https://doi.org/10.1016/j.celrep.2016.06.036, PMID: 27396324

Schier AF, Talbot WS. 2005. Molecular genetics of axis formation in zebrafish. *Annual Review of Genetics* **39**:561–613. DOI: https://doi.org/10.1146/annurev.genet.37.110801.143752, PMID: 16285872

Schindelin J, Arganda-Carreras I, Frise E, Kaynig V, Longair M, Pietzsch T, Preibisch S, Rueden C, Saalfeld S, Schmid B, Tinevez JY, White DJ, Hartenstein V, Eliceiri K, Tomancak P, Cardona A. 2012. Fiji: an open-source platform for biological-image analysis. *Nature Methods* **9**:676–682. DOI: https://doi.org/10.1038/nmeth.2019, PMID: 22743772

Schmid B, Shah G, Scherf N, Weber M, Thierbach K, Campos CP, Roeder I, Aanstad P, Huisken J. 2013. High-speed panoramic light-sheet microscopy reveals global endodermal cell dynamics. *Nature Communications* **4**:2207. DOI: https://doi.org/10.1038/ncomms3207, PMID: 23884240

Sopory S, Nelsen SM, Degnin C, Wong C, Christian JL. 2006. Regulation of bone morphogenetic protein-4 activity by sequence elements within the prodomain. *Journal of Biological Chemistry* **281**:34021–34031. DOI: https://doi.org/10.1074/jbc.M605330200, PMID: 16966322

Tucker JA, Mintzer KA, Mullins MC. 2008. The BMP signaling gradient patterns dorsoventral tissues in a temporally progressive manner along the anteroposterior axis. *Developmental Cell* **14**:108–119. DOI: https://doi.org/10.1016/j.devcel.2007.11.004, PMID: 18194657

Umulis D, O'Connor MB, Blair SS. 2009. The extracellular regulation of bone morphogenetic protein signaling. *Development* **136**:3715–3728. DOI: https://doi.org/10.1242/dev.031534, PMID: 19855014

Varadarajan SG, Kong JH, Phan KD, Kao TJ, Panaitof SC, Cardin J, Eltzschig H, Kania A, Novitch BG, Butler SJ. 2017. Netrin1 Produced by Neural Progenitors, Not Floor Plate Cells, Is Required for Axon Guidance in the Spinal Cord. *Neuron* **94**:790–799. DOI: https://doi.org/10.1016/j.neuron.2017.03.007, PMID: 28434801

Xu PF, Houssin N, Ferri-Lagneau KF, Thisse B, Thisse C. 2014. Construction of a vertebrate embryo from two opposing morphogen gradients. *Science* **344**:87–89. DOI: https://doi.org/10.1126/science.1248252, PMID: 24700857

Yu SR, Burkhardt M, Nowak M, Ries J, Petrásek Z, Scholpp S, Schwille P, Brand M. 2009. Fgf8 morphogen gradient forms by a source-sink mechanism with freely diffusing molecules. *Nature* **461**:533–536. DOI: https://doi.org/10.1038/nature08391, PMID: 19741606

Zinski J, Bu Y, Wang X, Dou W, Umulis D, Mullins M. 2017. Systems biology derived source-sink mechanism of BMP gradient formation. *eLife* **6**:e22199. DOI: https://doi.org/10.7554/eLife.22199, PMID: 28826472

Scale-invariant patterning by size-dependent inhibition of Nodal signalling

María Almuedo-Castillo[1], Alexander Bläßle[1], David Mörsdorf[1], Luciano Marcon[1], Katherine W. Rogers[1,2], Alexander F. Schier[2], and Patrick Müller[1,*]

[1]Friedrich Miescher Laboratory of the Max Planck Society, Tübingen, Germany

[2]Department of Molecular and Cellular Biology, Harvard University, Cambridge, USA

[*]Correspondence to: patrick.mueller@tuebingen.mpg.de (P.M.)

Individuals can vary significantly in size, but the proportions of their body plans are often maintained. We generated smaller zebrafish by removing 30% of their cells at blastula stages and found that these embryos developed into normally patterned individuals. Strikingly, the proportions of all germ layers adjusted to the new embryo size within two hours after cell removal. Since Nodal/Lefty signalling controls germ layer patterning, we performed a computational screen for scale-invariant models of this activator/inhibitor system. This analysis predicted that the concentration of the highly diffusive inhibitor Lefty increases in smaller embryos, leading to a decreased Nodal activity range and contracted germ layer dimensions. *In vivo* studies confirmed that Lefty levels increased in smaller embryos, and embryos with reduced Lefty concentration or with diffusion-hindered Lefty failed to scale their tissue proportions. These results reveal that size-dependent inhibition of Nodal signalling allows scale-invariant patterning.

Despite often significant variability in size, embryos faithfully generate the correct tissue proportions[1, 2]. During development, tissue patterning is achieved by gradients of signalling proteins that induce distinct differentiation programs in discrete spatial domains[3, 4]. To adjust tissue patterning and organ proportions to their body size, embryos need to appropriately scale the underlying signalling gradients[5]. Scaling mechanisms for individual tissue-specific signalling systems at different stages of development have been proposed, but how these mechanisms are integrated and coordinated during development to generate the correct proportions of all tissues is currently unclear[5-15]. Here, we analyzed how signalling gradients adjust tissue proportions in differently sized zebrafish embryos and identified a novel size-dependent mechanism that mediates scale-invariant germ layer patterning to provide the correct amount of progenitor cells for all future tissues.

We found that removal of 30% of cells by extirpation from the animal pole before gastrulation (Fig. 1a) generates zebrafish embryos that become normally patterned adults. Extirpated embryos developed into smaller individuals with the same number of proportionally thinner somites as untreated embryos (Fig. 1a). Consistently, the size of various organs including hatching gland (a mesodermal derivative, *hgg1*-positive) and eye (an ectodermal derivative, *vsx2*-positive) was reduced in individuals developing from extirpated embryos (Fig. 1b). Strikingly, scaling of tissue proportions to embryo size already occurred during gastrulation stages within 2 hours following extirpation. Using *in situ* hybridization, we quantified the extent of ectoderm (*sox3*-positive, Fig. 1c) and mesendoderm (*fascin*-positive, Fig. 1d) and found that germ layer proportions adjusted progressively after extirpation: At 1 hour post extirpation (hpe), extirpated embryos had excess mesendoderm and insufficient ectodermal progenitors since cells were removed from the animal pole containing presumptive ectoderm (Fig. 1c,d). Interestingly, 1 hour later (2 hpe) ectoderm and mesendoderm proportions had adjusted in extirpated embryos (Fig. 1c,d). Even though cells were removed from the animal pole, the number of endodermal precursor cells (*sox17*- and *sox32*-positive) at the opposite side within the marginal zone of extirpated embryos was also proportionally reduced by gastrulation stages (Supplementary Fig. 1a).

Cell density and proliferation rates did not change in extirpated embryos (Supplementary Fig. 1b-d), indicating that neither changes in cell density nor compensatory proliferation underlie germ layer scaling. Moreover, the spatial expression kinetics of *goosecoid* – a highly sensitive indicator of developmental progression – were similar in untreated and extirpated embryos at different developmental time points (Supplementary Fig. 1e); thus, scaling can also not be explained by altered developmental speed in differently sized embryos.

Since the Nodal/Lefty activator/inhibitor system patterns the germ layers during early development, we hypothesized that Nodal signalling adjusts in smaller embryos to allow

proportionate patterning. The activator Nodal is secreted from the marginal zone of the embryo and induces endoderm and mesoderm, whereas the highly diffusive Nodal inhibitor Lefty, which is also expressed at the margin and induced by Nodal signaling, limits the mesendodermal domain[16, 17]. To test whether Nodal signalling adjusts in smaller embryos, we measured the extent of Nodal activity (phosphorylation of the Nodal signal transducer Smad2/3, pSmad2/3) and found that it scaled by 2 hpe (Fig. 1e). Using *in toto* light-sheet imaging, we confirmed that both the Nodal signalling target *fascin*[17-19] as well as Nodal signalling itself scaled throughout the embryonic marginal zone (Fig. 1f).

To identify the mechanism by which Nodal signalling might sense embryo size and adjust tissue proportions, we performed a computational screen including all known interactions in the Nodal/Lefty system while keeping model complexity to a minimum (Fig. 2a,b, Supplementary Note). We constrained the screen with the measured biophysical properties, including Nodal/Lefty diffusivities and half-lives[17]. We screened more than 400,000 parameter combinations representing the production of Lefty, the inhibition strength, and the Nodal-mediated feedback on Nodal and Lefty production. By assessing the overlap between Nodal signalling in simulations of normally sized and shortened embryos, we found that systems capable of scaling require precise levels of highly diffusive Lefty, whose concentration increases in extirpated embryos to adjust the Nodal signalling gradient (Fig. 2c-e). In such systems, the boundary located more proximal to the marginal zone in shortened compared to normally sized embryos affects the long-range Lefty but not the short-range Nodal gradient (Fig. 2c). Since we shortened embryos prior to the onset of Lefty protein secretion without removing *Lefty*-expressing cells from the marginal zone (Supplementary Fig. 1f-k), the same amount of Lefty should be produced in early extirpated and untreated embryos. Therefore, the concentration of Lefty should increase in smaller embryos, contracting the Nodal activity range to re-establish the correct tissue dimensions relative to the new size of the embryo.

In our simulations of the Nodal/Lefty system, scale-invariant patterning only became apparent around 2 hpe, as observed experimentally (Fig. 1c,d). The simulations further closely matched the time window of germ layer specification: Nodal signalling levels and mesendoderm specification expand as development proceeds, Nodal signalling levels peak around 2 hpe (6 hours post fertilization), and Nodal signalling rapidly decreases afterwards (Supplementary Movie 1). Together, the experimental observations and computational simulations suggest that germ layer scaling at 2 hpe results from adjustments in mesendoderm expansion dynamics over time rather than from shrinking an initially too broadly specified mesendodermal domain.

Our model predicted that scaling crucially depends on the levels of Lefty (Fig. 2d, Fig. 3a,b). To test this prediction, we assessed mesendoderm proportions in embryos with varying numbers of functional *lefty* alleles (*lefty1* and *lefty2*)[20]. As expected, both untreated and extirpated double-homozygous *lefty1*$^{-/-}$;*lefty2*$^{-/-}$ mutants showed dramatically expanded mesendoderm[20] (Fig. 3c-f, Supplementary Fig. 2a-d). In contrast, untreated and shortened double-heterozygous *lefty1*$^{+/-}$;*lefty2*$^{+/-}$ embryos exhibited nearly normal mesendoderm proportions, indicating that one functional allele of each *lefty* is sufficient for proper spatial Nodal signalling and scaling, possibly due to dosage adjustments that result in similar amounts of protein (Fig. 3c-f, Supplementary Fig. 2a-d). Normally sized and extirpated single-homozygous *lefty2*$^{-/-}$ mutants had excess mesendoderm. In striking contrast, single-homozygous *lefty1*$^{-/-}$ embryos displayed expanded mesendoderm only after extirpation (Fig. 3c-f, Supplementary Fig. 2a-d). Interestingly, Lefty1 is less inhibitory than its paralog Lefty2 (Supplementary Fig. 2e,f); thus, while highly active Lefty2 is sufficient for germ layer patterning in normally sized embryos, the correct levels of poorly active Lefty1 are only required for scale-invariant patterning in significantly smaller embryos. These experimental findings support the simulations of our size-dependent inhibition model (Fig. 2d, Fig. 3a,b),

showing that a small reduction in Lefty production, which does not significantly affect mesendoderm formation, abrogates scaling.

The second prediction of our model is that scaling depends on the high diffusivity of Lefty, which must reach the end of the patterning field to act as a size sensor (Fig. 2e, Fig. 4a,b). To test this prediction, we decreased Lefty diffusivity and determined the consequences on scaling. To obtain a patterning system in which the diffusion of Lefty1 can be experimentally manipulated, we first generated embryos in which the only source of Lefty was Lefty1-GFP. We rescued *lefty1*$^{-/-}$;*lefty2*$^{-/-}$ double mutants by injecting highly precise and physiologically relevant amounts (see Online Methods for details) of *lefty1-GFP* mRNA into the yolk syncytial layer (YSL) to mimic the secretion of endogenous Lefty from the marginal zone (Fig. 4c). Consistent with the high diffusivity of Lefty[17], Lefty1-GFP reached the end of the patterning field within 60 min after YSL injection (Fig. 4d,e, Supplementary Movie 2). A large proportion of *lefty1*$^{-/-}$;*lefty2*$^{-/-}$ mutant embryos was rescued to adulthood with this method in normally sized (~70% fully or partially rescued) and extirpated (~60% fully or partially rescued) embryos (Fig. 4f-h, Supplementary Fig. 3a-d). Thus, Lefty1-GFP provided from the marginal zone is sufficient not only to pattern germ layers but also to allow scaling. Next, to hinder Lefty1-GFP diffusion we used a "morphotrap" – an mCherry-labeled membrane-bound GFP-binding nanobody[21]. Co-injection of mRNA encoding the morphotrap and *lefty1-GFP* mRNA into one-cell stage embryos changed the localization of Lefty1-GFP from uniform extracellular to strongly membrane-associated (Supplementary Fig. 3f). Crucially, the diffusion coefficient of Lefty1-GFP in embryos expressing the morphotrap was significantly lower (D = 7.7 ± 3.2 μm^2/s for Lefty1-GFP, and 0.2 ± 0.2 μm^2/s for Lefty1-GFP + morphotrap; Supplementary Fig. 3i,j), whereas the activity of Lefty was only modestly affected by morphotrap binding (Supplementary Fig. 3g,h). We then injected mRNA encoding the morphotrap into *lefty1*$^{-/-}$;*lefty2*$^{-/-}$ mutant embryos at the one-cell stage and generated local sources of Lefty1-GFP at the marginal zone (Fig. 4d,e). The expression of the

morphotrap dramatically changed the range of Lefty1-GFP from a nearly uniform distribution to a short-range gradient that did not reach the end of the embryo (Fig. 4d,e, Supplementary Movie 2, Supplementary Movie 3). This change in Lefty distribution correlated with a steep drop in the rescue of extirpated embryos (Fig. 4f,g), and rescue efficiency was inversely correlated with mesendoderm amount (Fig. 4g,h, Supplementary Fig. 3d,e). Simulations of the size-dependent inhibition model with hindered Lefty diffusion recapitulated the experimentally observed change in Lefty distribution (Fig. 4a,b,d,e). The decreased Lefty range precludes scaling of Nodal signalling since Lefty cannot reach the distal end of the patterning field to act as a size sensor. In normally sized experimental or simulated embryos, hindered Lefty diffusion did not significantly affect germ layer patterning (Fig. 4b,f-h). In simulated embryos, this finding can be explained by Nodal-mediated positive feedback, where sufficiently high Nodal levels at the marginal zone maintain signalling in spite of increased Lefty-mediated inhibition (Fig. 4b). Together, these observations show that hindering Lefty diffusion prevents scaling in extirpated embryos, supporting the prediction of the size-dependent inhibition model.

The third prediction of our model is that inhibitor levels increase to reduce Nodal signalling in extirpated embryos (Fig. 2c). To test this prediction, we quantified GFP intensity after injection of physiologically relevant amounts of *lefty1-GFP* mRNA in the YSL and found that extirpated embryos exhibited higher GFP intensity than normally sized embryos (Fig. 5a). To assess whether this increase in inhibitor concentration is required for germ layer scaling, we analyzed mesendoderm patterning in untreated and extirpated *lefty1*$^{-/-}$;*lefty2*$^{-/-}$ mutants upon exposure to the small-molecule Nodal inhibitor SB-505124[20]. In contrast to the YSL-injection rescue approach, a reduction in embryo size should not affect the concentration of the tonic Nodal inhibitor in this experimental setup (Supplementary Fig. 4a-d). A large fraction of untreated *lefty1*$^{-/-}$;*lefty2*$^{-/-}$ mutants (~90%, Fig. 5b) was rescued by 4.8 µM of Nodal inhibitor exposure. In contrast, exposure of extirpated *lefty1*$^{-/-}$;*lefty2*$^{-/-}$ mutants to the same

inhibitor concentration resulted in abnormal mesendoderm proportions, and only ~30% displayed some phenotypic rescue (Fig. 5b, Supplementary Fig. 4e,f). These results show that tonic size-independent inhibition levels effective in normally sized embryos do not allow scaling, since inhibitor concentration cannot increase in shortened embryos.

Our model implies that increasing tonic Nodal inhibitor levels should restore the appropriate Nodal signalling range in extirpated embryos. Consistent with this prediction, increasing the exposure of the small-molecule Nodal inhibitor from 4.8 µM to 6-7 µM significantly improved the rescue of extirpated *lefty1*$^{-/-}$;*lefty2*$^{-/-}$ mutants from 26% to 64% (Fig. 5c, Supplementary Fig. 4g), demonstrating that increased inhibitor levels are required for scaling in extirpated embryos.

Together, four lines of evidence suggest that scale-invariant germ layer patterning is achieved by size-dependent inhibition of Nodal signalling. First, reduction of Lefty levels (Fig. 3) precludes scaling. Second, decreasing Lefty diffusivity interferes with scale-invariant patterning (Fig. 4). Third, the concentration of the Nodal inhibitor Lefty increases in extirpated embryos (Fig. 5a). Fourth, augmented drug-mediated dampening of Nodal signalling rescues scaling of germ layer proportions in extirpated embryos (Fig. 5c, Supplementary Fig. 4g). In agreement with our mathematical model (Fig. 2, Supplementary Fig. 5), these results support the idea that the concentration and high diffusivity of Lefty are essential to adjust germ layer proportions. While tissue proportions might be further refined by interactions with other signalling pathways such as BMP[18] and FGF[22], the scaled distribution of the Nodal signal transducer pSmad2/3 – which is independent of BMP and FGF – and the scaled tissue proportions in *lefty* mutants rescued by feedback-uncoupled Lefty – in which Lefty production is not under any transcriptional regulation – demonstrate the central role of Lefty in germ layer scaling. Importantly, Nodal/Lefty-mediated scale-invariant patterning is not based on previously postulated feedback-dependent activator/inhibitor

systems[23] but purely on size-dependent Nodal inhibition mediated by Lefty, providing a foundation for the proportionate allocation of all future tissues.

The scaling mechanism that we found crucially depends on the coupling of inhibitor concentration to embryo size, which is conferred by the high diffusivity of Lefty. Strikingly, a similar mechanism based on the coupling of cell volume to the concentration of a cell cycle inhibitor has recently been found to control cell size in yeast[24]. It is therefore possible that this simple mechanism might be widespread across various levels of biological organization to coordinate growth with cellular functions and patterning.

Acknowledgements

We thank Gary H. Soh for developing the extirpation device and the 2D map visualization workflow, Markus Affolter for providing the morphotrap construct, and Jelena Raspopovic and Nathan Lord for helpful comments. This work was supported by EMBO long-term fellowships to M.A.C. and L.M., and funding from the Max Planck Society, an ERC Starting Grant, and a Human Frontier Science Program Career Development Award to P.M.

Author Contributions

D.M. performed the experiments in Supplementary Fig. 3g-j and contributed to experiments in Fig. 4f,h; M.A.C. performed all other experiments; M.A.C., A.B., D.M., and P.M. analyzed the data; A.B. performed the mathematical analysis and simulations with assistance from L.M. and P.M.; K.W.R. and A.F.S. contributed the data in Supplementary Fig. 2e,f and provided the *lefty* mutants before publication; M.A.C, A.F.S., and P.M. conceived the study; A.F.S. and P.M. conceptualized the scaling model; P.M. developed the extirpation assay and supervised the project; M.A.C. and P.M. wrote the manuscript with input from all authors.

References

1. Morgan, T.H. Half embryos and whole embryos from one of the first two blastomeres. *Anatomischer Anzeiger* **10**, 623-685 (1895).
2. Cooke, J. Control of somite number during morphogenesis of a vertebrate, *Xenopus laevis*. *Nature* **254**, 196-199 (1975).
3. Wartlick, O., Kicheva, A. & González-Gaitán, M. Morphogen gradient formation. *Cold Spring Harbor Perspectives in Biology* **1**, a001255-a001255 (2009).
4. Rogers, K.W. & Schier, A.F. Morphogen gradients: From generation to interpretation. *Annual Review of Cell and Developmental Biology* **27**, 377-407 (2011).
5. Umulis, D.M. & Othmer, H.G. Mechanisms of scaling in pattern formation. *Development* **140**, 4830-4843 (2013).
6. Gregor, T., Bialek, W., de Ruyter van Steveninck, R.R., Tank, D.W. & Wieschaus, E.F. Diffusion and scaling during early embryonic pattern formation. *Proc Natl Acad Sci U S A* **102**, 18403-18407 (2005).
7. Gregor, T., McGregor, A.P. & Wieschaus, E.F. Shape and function of the Bicoid morphogen gradient in dipteran species with different sized embryos. *Developmental Biology* **316**, 350-358 (2008).
8. Ben-Zvi, D., Shilo, B.-Z., Fainsod, A. & Barkai, N. Scaling of the BMP activation gradient in *Xenopus* embryos. *Nature* **453**, 1205-1211 (2008).
9. Ben-Zvi, D., Pyrowolakis, G., Barkai, N. & Shilo, B.Z. Expansion-repression mechanism for scaling the Dpp activation gradient in *Drosophila* wing imaginal discs. *Current Biology* **21**, 1391-1396 (2011).
10. Hamaratoglu, F., de Lachapelle, A.M., Pyrowolakis, G., Bergmann, S. & Affolter, M. Dpp signaling activity requires Pentagone to scale with tissue size in the growing *Drosophila* wing imaginal disc. *PLoS Biology* **9**, e1001182 (2011).
11. Wartlick, O. *et al.* Dynamics of Dpp signaling and proliferation control. *Science* **331**, 1154-1159 (2011).
12. Cheung, D., Miles, C., Kreitman, M. & Ma, J. Scaling of the Bicoid morphogen gradient by a volume-dependent production rate. *Development* **138**, 2741-2749 (2011).
13. Wartlick, O., Jülicher, F. & González-Gaitán, M. Growth control by a moving morphogen gradient during *Drosophila* eye development. *Development* **141**, 1884-1893 (2014).
14. Kicheva, A. *et al.* Coordination of progenitor specification and growth in mouse and chick spinal cord. *Science* **345**, 1254927-1254927 (2014).
15. Uygur, A. *et al.* Scaling pattern to variations in size during development of the vertebrate neural tube. *Developmental Cell* **37**, 127-135 (2016).
16. Schier, A.F. Nodal morphogens. *Cold Spring Harbor Perspectives in Biology* **1**, a003459-a003459 (2009).
17. Müller, P. *et al.* Differential diffusivity of Nodal and Lefty underlies a reaction-diffusion patterning system. *Science* **336**, 721-724 (2012).
18. Bennett, J.T. *et al.* Nodal signaling activates differentiation genes during zebrafish gastrulation. *Developmental Biology* **304**, 525-540 (2007).
19. Liu, Z. *et al.* Fscn1 is required for the trafficking of TGF-beta family type I receptors during endoderm formation. *Nature Communications* **7**, 12603 (2016).

20. Rogers, K.W. *et al.* Nodal patterning without Lefty inhibitory feedback is functional but fragile. *in review* (2017).
21. Harmansa, S., Hamaratoglu, F., Affolter, M. & Caussinus, E. Dpp spreading is required for medial but not for lateral wing disc growth. *Nature* **527**, 317-322 (2015).
22. van Boxtel, A.L. *et al.* A temporal window for signal activation dictates the dimensions of a Nodal signaling domain. *Developmental Cell* **35**, 175-185 (2015).
23. Gierer, A. & Meinhardt, H. A theory of biological pattern formation. *Kybernetik* **12**, 30-39 (1972).
24. Schmoller, K.M., Turner, J.J., Koivomagi, M. & Skotheim, J.M. Dilution of the cell cycle inhibitor Whi5 controls budding-yeast cell size. *Nature* **526**, 268-272 (2015).
25. Thisse, B.T.C., Schilling, T.F. & Postlethwait, J.H. Structure of the zebrafish snail1 gene and its expression in wild-type, spadetail and no tail mutant embryos. *Development* **119**, 1203-1215(1993).
26. Schindelin, J. *et al.* Fiji: an open-source platform for biological-image analysis. *Nature Methods* **9**, 676-682 (2012).
27. Feng, X., Adiarte, E.G. & Devoto, S.H. Hedgehog acts directly on the zebrafish dermomyotome to promote myogenic differentiation. *Developmental Biology* **300**, 736-746 (2006).
28. Schmid, B. *et al.* High-speed panoramic light-sheet microscopy reveals global endodermal cell dynamics. *Nature Communications* **4**, 2207 (2013).
29. Saerens, D. *et al.* Identification of a universal VHH framework to graft non-canonical antigen binding loops of camel single-domain antibodies. *Journal of Molecular Biology* **352**, 597-607 (2005).
30. Wang, Y., Wang, X., Wohland, T. & Sampath, K. Extracellular interactions and ligand degradation shape the Nodal morphogen gradient. *eLife* **5**, pii: e13879 (2016).
31. Xu, C. *et al.* Nanog-like regulates endoderm formation through the Mxtx2-Nodal pathway. *Developmental Cell* **22**, 625-638 (2012).
32. Marcon, L., Diego, X., Sharpe, J. & Müller, P. High-throughput mathematical analysis identifies Turing networks for patterning with equally diffusing signals. *eLife* **5**, pii: e14022 (2016).
33. Inomata, H., Shibata, T., Haraguchi, T. & Sasai, Y. Scaling of dorsal-ventral patterning by embryo size-dependent degradation of Spemann's organizer signals. *Cell* **153**, 1296-1311 (2013).
34. Kicheva, A. *et al.* Kinetics of morphogen gradient formation. *Science* **315**, 521-525 (2007).
35. Rasolonjanahary, M., Vasiev, B. Scaling of morphogenetic patterns in reaction-diffusion systems. *Journal of Theoretical Biology* **404**, 109-119 (2016).
36. Ben-Zvi, D. & Barkai, N. Scaling of morphogen gradients by an expansion-repression integral feedback control. *Proc Natl Acad Sci U S A* **107**, 6924-6929 (2010).

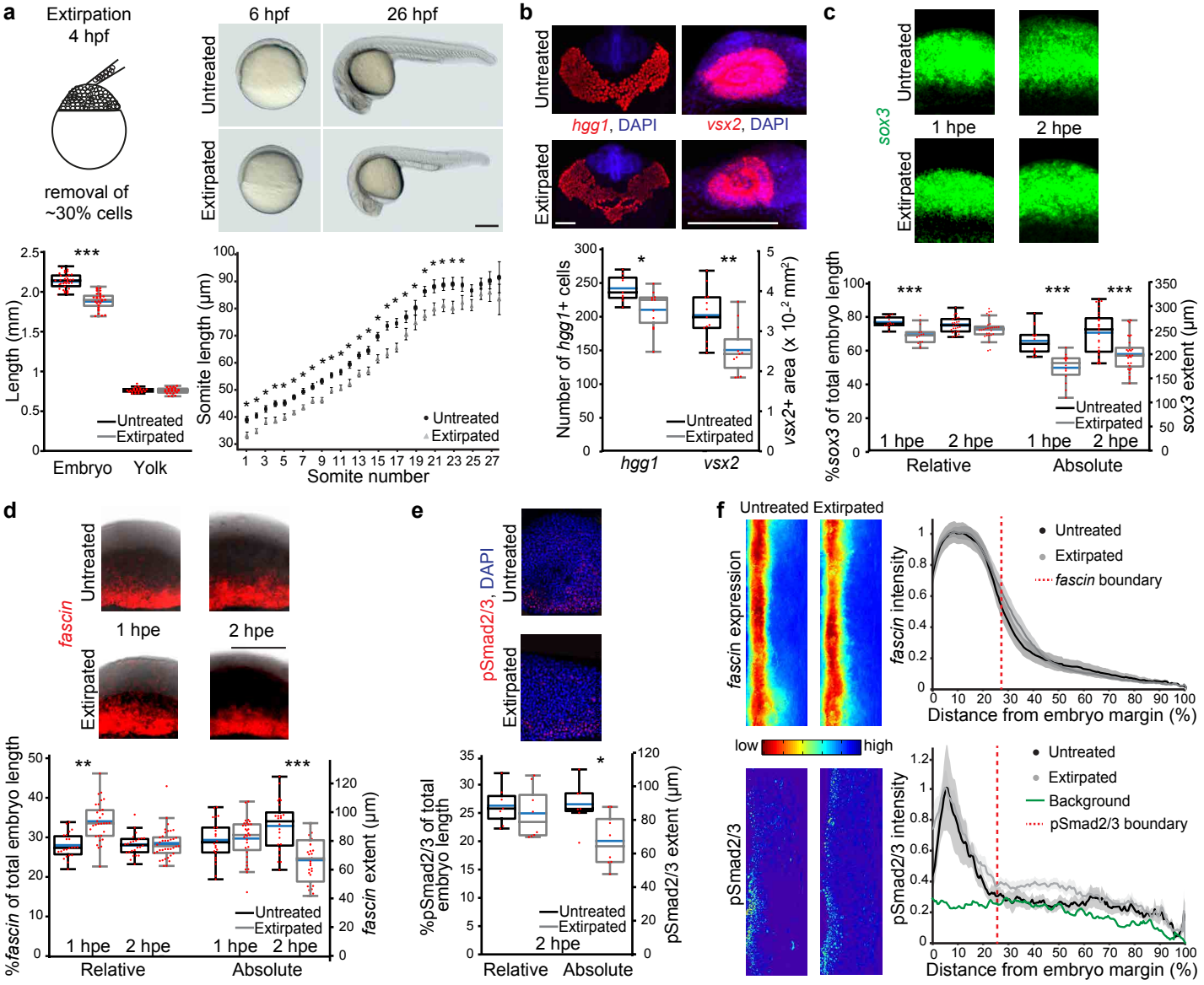

Figure 1 | Scaling in smaller embryos after extirpation. (a) Schematic of embryo extirpation; lateral views. The total length of extirpated embryos (grey bars; black: untreated) at 1 day post fertilization is smaller (***p<0.00001), whereas yolk size remains unchanged (n[untreated]=40, n[extirpated]=37; p>0.05). The length of the 24 posterior-most somites is proportionately smaller in extirpated embryos (n[untreated]=15, n[extirpated]=13; *p<0.05). Error bars: SEM (in "Somite length" graph). **(b)** Maximum intensity projections of confocal FISH stacks and quantification of *hgg1*- (n[untreated]=9, n[extirpated]=11; **p<0.01) and *vsx2*-positive cells (n[untreated]=13, n[extirpated]=11; **p<0.01). **(c,d)** Maximum intensity projections of lateral confocal FISH stacks, and quantification of the relative and absolute length of *sox3* (ectoderm) and *fascin* (mesendoderm) domains. Ectoderm proportions are smaller at 1 h post extirpation (hpe) (n[untreated]=14, n[extirpated]=14; ***p<0.001) but scale by 2 hpe (n[untreated]=28, n[extirpated]=28; p>0.05). Similarly, mesendoderm proportions are too large at 1 hpe (n[untreated]=22, n[extirpated]=32; **p<0.01) but scale by 2 hpe (n[untreated]=28, n[extirpated]=37; p>0.05). **(e)** Average intensity projections of lateral confocal pSmad2/3 immunostaining stacks and quantification of the absolute and relative length of pSmad2/3. Nodal signalling scales at 2 hpe (n[untreated]=7, n[extirpated]=8; p>0.05). **(f)** 2D maps of 3D-reconstruced embryos imaged by light-sheet microscopy, and quantification of normalized *fascin* and pSmad2/3 domains along the vegetal-animal axis show scaling (*fascin*: n[untreated]=9, n[extirpated]=9; pSmad2/3: n[untreated]=5, n[extirpated]=6). Box plots (a-e) show median (blue line), mean (untreated: black, extirpated: grey lines), 25% quantiles (box) and all included data points (red markers). Scale bars: 200 µm.

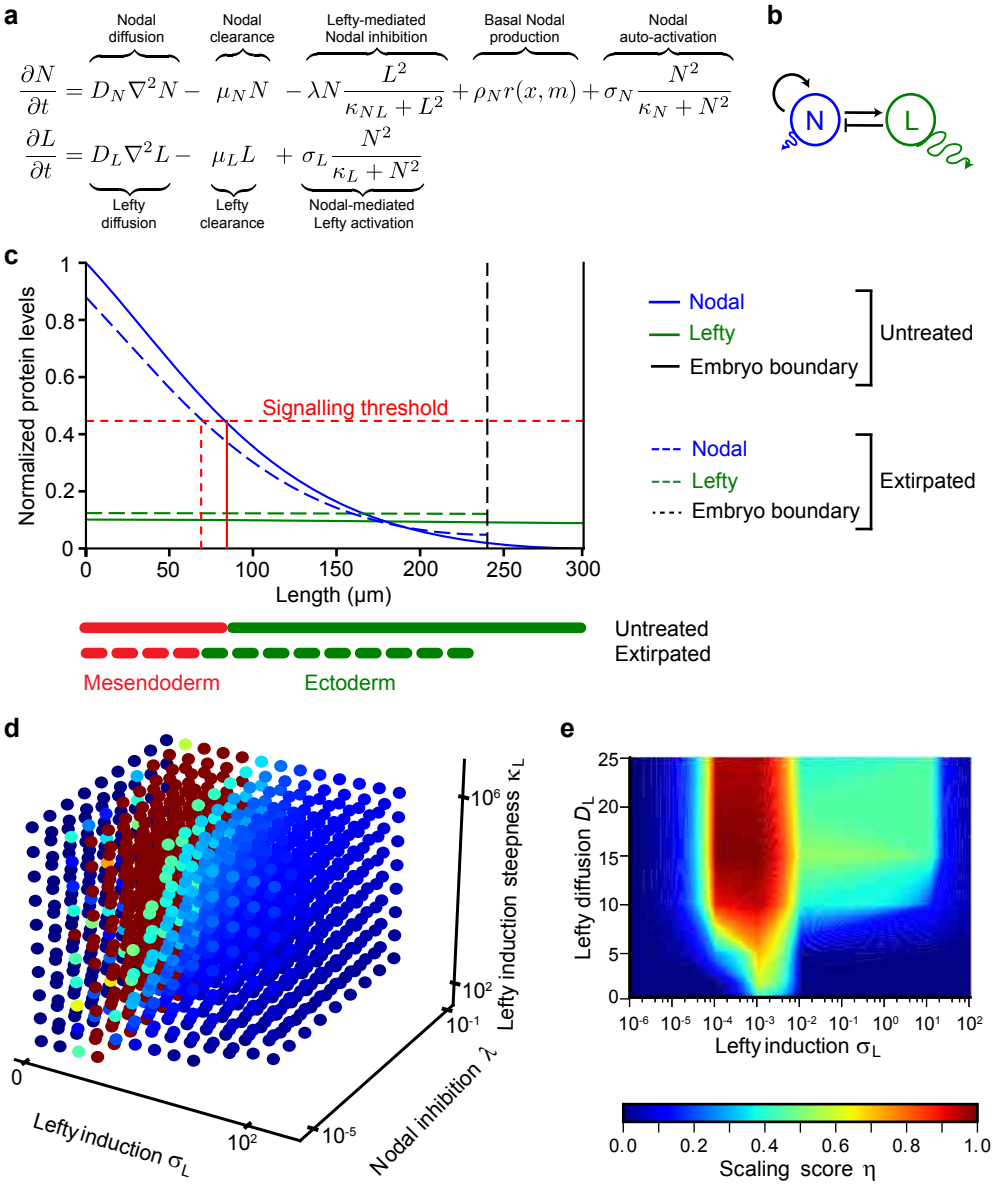

Figure 2 | Computational screen for parameters conferring scale-invariance. **(a,b)** Equations and network describing the known interactions in the Nodal/Lefty activator/inhibitor system. **(c)** Example of a scale-invariant system identified by the screen, showing an increase in Lefty and dampening of Nodal signalling after extirpation. Simulations were fitted to the experimentally measured total length and mesendoderm extent (Nodal signalling output). **(d)** Parameter screen showing the influence of Lefty levels (σ_L), Nodal inhibition strength (λ), and Lefty induction steepness (κ_L) on scaling; maximum projection through the six-dimensional parameter space with the following discrete values: for σ_L 0, 10^{-4}, 10^{-3}, 10^{-2}, 11.12, 22.23, 33.34, 44.45, 55.56, 66.67, 77.78, 88.89, and 10^2; for λ 10^{-5}, 1.12 x 10^{-2}, 2.23 x 10^{-2}, 3.34 x 10^{-2}, 4.45 x 10^{-2}, 5.56 x 10^{-2}, 6.67 x 10^{-2}, 7.78 x 10^{-2}, 8.89 x 10^{-2}, and 10^{-1}; for κ_L 10^2, 1.12 x 10^5, 2.23 x 10^5, 3.34 x 10^5, 4.45 x 10^5, 5.56 x 10^5, 6.67 x 10^5, 7.78 x 10^5, 8.89 x 10^5, and 10^6. Parameter configurations resulting in biologically unrealistic gradients were excluded. **(e)** Parameter screen showing the influence of Lefty diffusivity on scaling; maximum projection through the six-dimensional parameter space. The model predicts that scaling should fail if Lefty induction or diffusion are too low (i.e. D_L less than ~7 $\mu m^2/s$).

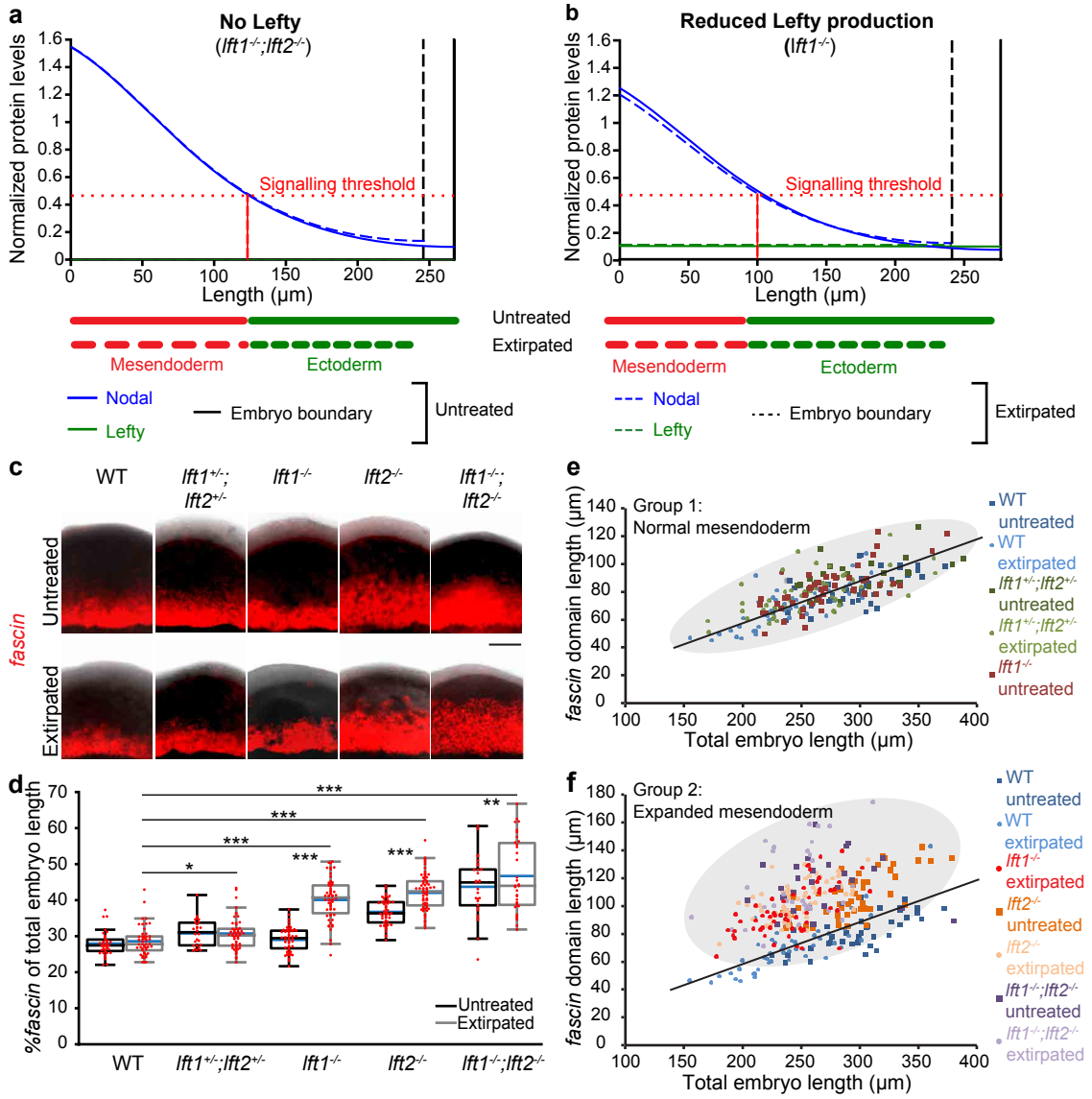

Figure 3 | Germ layer scaling depends on Lefty levels. (a,b) Simulations of the size-dependent inhibition model when Lefty production is abolished **(a)** or reduced **(b)**. Simulations of the "No Lefty" scenario (a) demonstrate that in the complete absence of Lefty, mesendoderm is extended and does not scale. Simulations of the "Reduced Lefty production" scenario (b) predict that reduction in Lefty induction should prevent scaling in shortened embryos without a significant change in mesendoderm specification in normally sized embryos. These two simulated scenarios resemble the experimental observations in *lft1-/-*;*lft2*$^{-/-}$ ("No Lefty") and *lft1*$^{-/-}$ ("Reduced Lefty production") mutants. **(c)** Maximum intensity projections of lateral confocal stacks of *fascin* FISH in untreated and extirpated embryos with different numbers of functional *lefty* alleles. **(d)** Quantification of mesendoderm (*fascin*-positive) proportions. WT (wild type) untreated embryos slightly differ from *lft1*$^{+/-}$;*lft2*$^{+/-}$ untreated and extirpated embryos (*p<0.05) and strongly differ from *lft1*$^{-/-}$ extirpated, *lft2*$^{-/-}$ untreated, *lft2*$^{-/-}$ extirpated, *lft1*$^{-/-}$;*lft2*$^{-/-}$ untreated, and *lft1*$^{-/-}$;*lft2*$^{-/-}$ extirpated embryos (***p<0.0001). Box plot shows median (blue line), mean (untreated: black; extirpated: grey lines), 25% quantiles (box) and all included data points (red markers). **(e,f)** Quantification of *fascin* extent relative to embryo length. The encircled domains cluster two groups. Group 1 shows a similar ratio of mesendoderm to embryo length as observed in wild type individuals and includes *lft1*$^{+/-}$;*lft2*$^{+/-}$ untreated and extirpated, and *lft1*$^{-/-}$ untreated embryos (e). Group 2 exhibits larger mesendodermal domains relative to total embryo length and includes *lft1*$^{-/-}$ extirpated, *lft2*$^{-/-}$ untreated and extirpated, and *lft1*$^{-/-}$;*lft2*$^{-/-}$ untreated and extirpated embryos (f). Group 1 shows a linear increase of mesendoderm with embryo size, whereas Group 2 clusters in a wider circular domain showing absence of scaling. WT: n[untreated]=38, n[extirpated]=49; *lft1*$^{+/-}$;*lft2*$^{+/-}$: n[untreated]=26, n[extirpated]=55; *lft1*$^{-/-}$: n[untreated]=50, n[extirpated]=58; *lft2*$^{-/-}$: n[untreated]=50, n[extirpated]=63; *lft1*$^{-/-}$;*lft2*$^{-/-}$: n[untreated]=29; n[extirpated]=34). Scale bar: 70 µm.

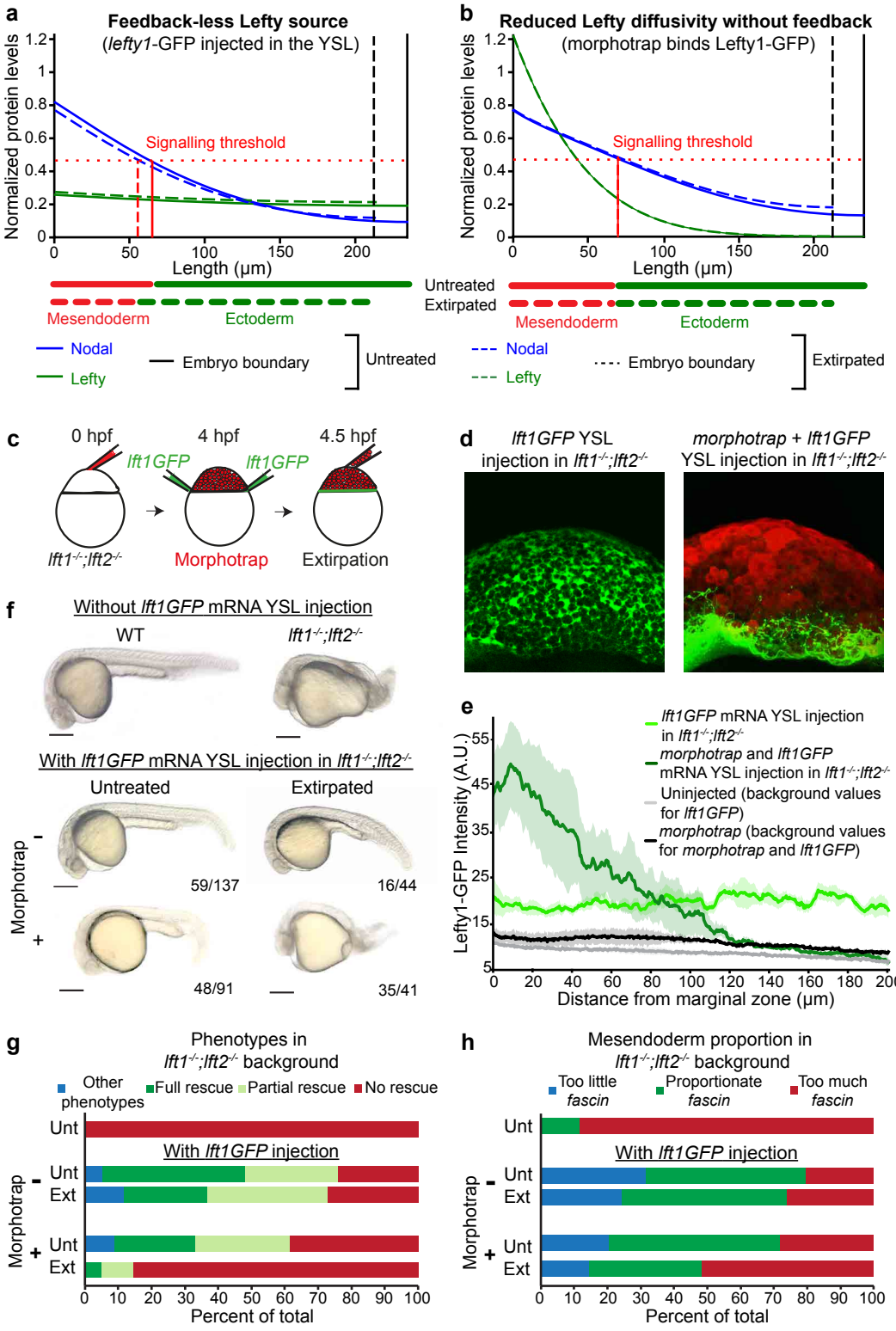

Figure 4 | High Lefty diffusivity is required for scaling. (a,b) Simulations of the model without feedback-inhibition and hindered Lefty diffusion predict that a reduction in Lefty diffusivity - preventing Lefty from reaching the animal pole - should preclude scaling. **(c)** Schematic of morphotrap-mediated Lefty1-GFP diffusion hindrance in extirpated embryos. **(d)** Maximum intensity projections of confocal stacks of *lft1*$^{-/-}$;*lft2*$^{-/-}$ embryos injected with or without *morphotrap* (at the one-cell-stage) and *lefty1-GFP* mRNA in the YSL (at sphere stage). Lateral views. **(e)** Quantification of the spatial distribution of Lefty1-GFP secreted from the YSL. The morphotrap prevents spreading of Lefty1-GFP towards the animal pole of the embryo. n=6 for the group injected with *lefty1-GFP* mRNA only, and n=3 for the group injected with *morphotrap* and *lefty1-GFP* mRNA. The experimentally determined distributions of Lefty1-GFP with morphotrap-mediated diffusion hindrance strongly resemble the simulation of the "Reduced Lefty diffusivity" scenario (b). Error bars represent SEM. **(f)** Lateral views of representative 26 hpf *lft1*$^{-/-}$;*lft2*$^{-/-}$ embryos with different treatments. **(g)** Phenotype distributions in *lft1*$^{-/-}$;*lft2*$^{-/-}$ embryos after different treatments (n[*lft1*$^{-/-}$;*lft2*$^{-/-}$]=39; *lft1*$^{-/-}$;*lft2*$^{-/-}$+*lft1GFP*: n[untreated]=137, n[extirpated]=44; *lft1*$^{-/-}$;*lft2*$^{-/-}$+*morphotrap*+*lft1GFP*: n[untreated]=91, n[extirpated]=44). Embryos with partial rescue display imperfect tails and reduced cephalic structures (i.e. very mild Lefty-mutant phenotypes). **(h)** Fraction of treated *lft1*$^{-/-}$;*lft2*$^{-/-}$ embryos with low (<22%), normal (22-33%) and high (>34%) mesendoderm proportions (n[*lft1*$^{-/-}$;*lft2*$^{-/-}$]=35; *lft1*$^{-/-}$;*lft2*$^{-/-}$+*lft1GFP*: n[untreated]=55, n[extirpated]=56; *lft1*$^{-/-}$;*lft2*$^{-/-}$+*morphotrap*+*lft1GFP*: n[untreated]=27, n[extirpated]=29). The fraction of rescued and non-rescued *lft1*$^{-/-}$;*lft2*$^{-/-}$ embryos correlates with the fraction of normal and high mesendoderm proportions in (g) and (h). Unt: Untreated; Ext: Extirpated. Scale bars: 200 μm.

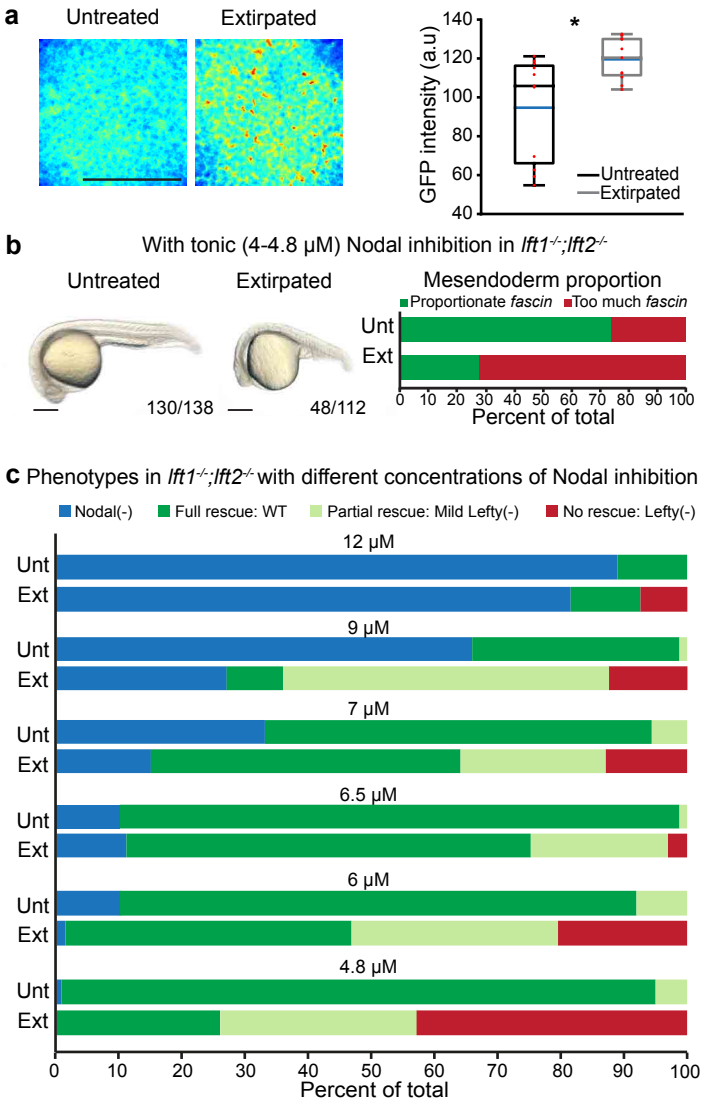

Figure 5 | Lefty concentration increases in extirpated embryos to allow scaling. (a) Animal pole views of maximum intensity confocal stack projections of WT untreated and extirpated embryos injected with *lefty1-GFP* mRNA in the YSL, and quantification of GFP intensity; *p<0.05; n[untreated]=11, n[extirpated]=11. Box plot shows median (blue line), mean (untreated: black; extirpated: grey lines), 25% quantiles (box) and all included data points (red markers). **(b)** Phenotype and mesendoderm quantification (n[untreated]=27, n[extirpated]=18) in *lft1*$^{-/-}$;*lft2*$^{-/-}$ embryos exposed to 4-4.8 µM of the Nodal inhibitor SB-505124. **(c)** Phenotype quantification in *lft1*$^{-/-}$;*lft2*$^{-/-}$ embryos exposed to different concentrations of the Nodal inhibitor SB-505124. Untreated: 4.8 µM n=138, 6 µM n=160, 6.5 µM n=80, 7 µM n=106, 9 µM n=85, 12 µM n=36; extirpated: 4.8 µM n=112, 6 µM n=146, 6.5 µM n=64, 7 µM n=108, 9 µM n=56, 12 µM n=27. Exposure to higher concentrations of the Nodal inhibitor SB-505124 increases *lft1*$^{-/-}$;*lft2*$^{-/-}$ mutant rescue after extirpation. The fraction of rescued and non-rescued *lft1*$^{-/-}$;*lft2*$^{-/-}$ embryos correlates with the fraction of normal and high mesendoderm proportions in (b) and (c). Unt: Untreated; Ext: Extirpated. Scale bars: 200 µm.

Online Methods

Generating smaller embryos by extirpation

Extirpation assays were performed using a glass capillary holder mounted on a Hamilton syringe and fixed in a micromanipulator (Narishige). Extirpations were performed in 4 hour post-fertilization (hpf) pronase-dechorionated sphere stage embryos in Ringer's solution (116 mM NaCl, 2.8 mM KCl, 1 mM $CaCl_2$, 5 mM HEPES). To allow wound healing after extirpation, embryos were left undisturbed for 30 min at 28°C. The wound typically healed within 15 min after extirpation, and the extirpated embryos were then transferred to normal embryo medium. To assess the survival of extirpated embryos without considering other mechanical disruptions of the extirpation assay (such as wound healing failure or mechanical constraints due to changes in the embryo/yolk ratio), embryos that did not survive extirpation or that did not proceed to gastrulation were discarded.

For quantification of cell numbers, extirpated cells from pools of 10 embryos were transferred to individual PCR tubes containing 0.05% Trypsin solution (Gibco), and incubated for 15 min at 37°C. Dissociated cells were then quantified using a Neubauer chamber on an Olympus CKX41 microscope. Ten to 20 pools of extirpated cells from 10 embryos were quantified per extirpation experiment. The average number of extirpated cells per embryo was 820 ± 130 cells, which corresponds to $\sim$30% of the cells of an embryo at sphere stage ($\sim$3000 cells).

Whole-mount *in situ* hybridization

fascin, hgg1, vsx2, sox3, sox17, and *sox32* RNA probes for *in situ* hybridization assays were synthesized using SP6 or T7 polymerase (Roche) and DIG- (Roche) or DNP- (Perkin Elmer) modified ribonucleotides. RNA probes were purified by ethanol precipitation with 7.5 M lithium chloride. For chromogenic *in situs*, embryos were fixed overnight at 4°C in 4% formaldehyde and then processed using an In situ Pro hybridization robot (Abimed/Intavis) and as previously described[25] with the following modifications: no proteinase K treatment before 90% epiboly stage; no pre-absorption of the anti-DIG antibody; 5% dextran sulfate (Sigma) added to the hybridization solution; riboprobes were denatured at 80°C for 15 min and chilled on ice prior to hybridization using a final concentration of 1-2 ng/µl.

For fluorescent *in situs* (FISH), the following modifications were used: the blocking solution contained 2% Blocking Reagent (Roche) in 1x MABTw; incubation with anti-DIG (Roche) or anti-DNP-POD (Perkin-Elmer) antibodies at a dilution of 1:150 in blocking solution was carried out overnight with shaking at 4°C; after antibody incubation, embryos were washed six times for 20 to 30 min at room temperature with PBS containing 0.1% Tween (PBST), and the signal was developed with 100 µl of TSA Cy3 or Cy5 at a dilution of 1:75 in amplification buffer (Perkin Elmer) for 1 h at room temperature without shaking.

For imaging, embryos were embedded in 1% low-melting point agarose, transferred to glass bottom culture dishes (MatTek corporation), and oriented manually. Only embryos mounted with the animal-vegetal axis completely parallel to the cover glass were used for analysis. For chromogenic *in situ* samples, images were captured using an Axio Zoom.V16 (ZEISS). For fluorescent *in situ* samples, confocal laser scanning microscopy was performed using an LSM 780 NLO microscope (ZEISS). Images were processed using Fiji[26]. The number of *hgg1, sox17,* and *sox32+* cells was quantified using the "multi-point selection" tool[26]. *fascin* and *sox3* expression domains in the central-most embryo regions were quantified using the "measure" tool in Fiji. *fascin* was quantified from the margin of the embryo to the end of the domain with high expression values. *sox3* was quantified from the animal pole to the end of the domain with high expression values. The size of embryos (from the margin to the animal pole) was measured similarly using bright-field images.

Immunostaining

For immunostainings, anti-phospho-Histone H3 (1:500, Cell Signaling Technologies) and anti-pSmad2/3 (1:5,000, Cell Signaling Technologies) antibodies were used. Immunostaining for phospho-Histone H3 was carried out as described previously[27]. For pSmad2/3, specimens were incubated in cold acetone

at -20°C for 20 min before blocking[22]. To ensure staining specificity, samples were exposed to low concentrations of anti-pSmad2/3 antibody (1:5,000), and the signal was amplified using HRP-conjugated anti-rabbit antibodies and TSA Cy3 or Cy5 at a dilution of 1:75 in amplification buffer (Perkin Elmer) for 45 min at room temperature without shaking. Embryos were mounted for imaging as described above for FISH, but with the dorsal-ventral axis parallel to the cover glass in the case of phospho-Histone H3 staining. Confocal laser scanning microscopy was performed using an LSM 780 NLO (ZEISS) confocal microscope, and images were processed using Fiji.

The number of phospho-Histone H3-positive cells was quantified over a depth of 140 μm using the "find maxima" plug-in in Fiji, with a fixed noise tolerance of 10,000 and manual correction.

pSmad2/3 distributions were quantified from the margin of the embryo to the end of pSmad2/3 nuclear staining using the "measure" tool in Fiji. Non-nuclear staining was excluded. The size of embryos from the margin to the animal pole was measured similarly using DAPI-stained images.

Light-sheet imaging and analysis

For 3D imaging, a Lightsheet Z.1 microscope (ZEISS) was used. Embryos were embedded in 1% low-melting point agarose and mounted in glass capillaries. For merging of the different views, far-red or green fluorescent beads (Thermo Fischer Scientific) were added to the agarose at a 1:200,000 dilution. After 3D reconstruction, 2D maps were generated as described previously[28].

To quantify the signal distribution in the resulting 2D maps, images were opened in Fiji and rotated by 90°. The region corresponding to the whole embryo was selected, and the average intensity of *fascin* or pSmad2/3 from every point of the embryonic vegetal-animal axis was obtained using the "plot profile" plug-in in Fiji. Distances in pixels were transformed into percentages of total embryo length with the vegetal-most side defined as 0% and the animal-most side as 100%. Intensity was then normalized by subtracting background values (i.e. the lowest intensity value closest to the animal pole of the embryo) and setting the highest intensity value to 1. For the quantification of pSmad2/3 distributions, background values were obtained by imaging *lefty* mRNA-injected embryos after pSmad2/3 immunostaining and normalized using the highest intensity value from the uninjected experimental data sets. 2D maps of DAPI were used as controls to rule out spatial inhomogeneities along the embryonic vegetal-animal axis (not shown). The graphs in Fig. 1f represent average maps obtained from several embryos.

Cell density quantifications

Cell density measurements were performed in untreated and extirpated H2A::GFP transgenic embryos. Embryos were mounted at 1 hpe and 2 hpe as described above for phospho-Histone H3 immunostaining. The number of cells was quantified as described above for pH3+ cells but over a depth of 80 μm. Given the high density of cells, segmentation errors of the Fiji plug-in were carefully corrected manually.

Mathematical modelling and statistical analysis

Details of the computational screen and the parameters used for modelling of the size-dependent inhibition system are described in the Supplementary Note.

Two tests were performed to assess whether experimental data was normally distributed: Kolmogorov-Smirnov ($\alpha = 0.05$) and Shapiro-Wilk tests ($\alpha = 0.05$). To check whether experimental groups were significantly different, two-sided Student's t-tests ($\alpha = 0.05$) were performed if the groups followed a normal distribution according to at least one of the tests. Mann-Whitney U tests ($\alpha = 0.05$) were performed if the groups did not follow a normal distribution.

Injection of *lefty1-GFP* mRNA into the YSL

mRNA encoding Lefty1-GFP[17] was generated by plasmid linearization with NotI-HF (NEB), purification with a Qiagen PCR clean-up kit, and *in vitro* transcription using SP6 mMessage mMachine kits (Ambion). To mimic endogenous Lefty secretion, a physiologically relevant amount of 100 pg of *lefty1-GFP* mRNA was precisely injected into 4 hpf (sphere stage) pronase-dechorionated embryos at two

equidistant points (1 nl of 50 ng/µl *lefty1-GFP* mRNA per point) within the embryonic yolk syncytial layer (YSL). To identify physiologically relevant amounts, 40, 60, 80, 100, 160, and 200 pg of *lefty1-GFP* mRNA were tested in a careful titration series, and 100 pg of *lefty1-GFP* mRNA were found to most efficiently rescue *lefty1*$^{-/-}$;*lefty2*$^{-/-}$ mutants.

Extirpations were performed 20-30 min after YSL injections. Embryos were divided into three groups: one group was fixed at shield stage and processed for FISH, the second was incubated in embryo medium at 28°C in 24-well plates covered with 2% agarose (1 embryo per well) for phenotypic analysis at 24 hpf, and the third group was processed for imaging 45-60 min after YSL injections. Mounting for imaging was done as described above for FISH samples. Movies were recorded with identical imaging conditions. Embryos were imaged for a total of ∼100 min, and Fiji was used to generate movies. For measurements of Lefty1-GFP intensity, injections of *lefty1-GFP* mRNA in the YSL and extirpations were performed as described above, but imaging was carried out 1.5-2 h after injection. Samples were captured with identical imaging conditions. 20 stacks were used for z-projections over a depth of 53 µm, and the intensity of equivalent areas of the images was quantified using the "measure" plug-in in Fiji.

Hindering Lefty1-GFP diffusion

The morphotrap construct[21] comprises a strong GFP binder ($K_D \sim 0.3$ nM)[29]. The morphotrap construct was digested with XhoI and XbaI to insert the morphotrap into a *pCS2+* expression plasmid. mRNA was generated as described above for *lefty1-GFP*. 1 nl containing 100 - 150 pg mRNA encoding the morphotrap was injected into one-cell stage embryos for experiments shown in the top panel of Supplementary Fig. 3f. Transplantation of cells expressing the morphotrap (bottom panel of Supplementary Fig. 3f) was performed as described above for extirpation experiments. Briefly, 50 - 100 cells were transplanted from a sphere stage donor previously injected with 200 pg morphotrap-encoding mRNA into sphere stage host embryos previously injected with 50 pg *lefty1-GFP* mRNA.

Testing the effect of morphotrap binding on Lefty1-GFP activity

Wild type (TE) embryos were injected at the one-cell stage with 1 nl injection mix containing 5 or 30 pg *lefty1-GFP* mRNA and 0.05% phenol red. To test the effect of the morphotrap on Lefty1-GFP activity, 150 pg of *morphotrap* mRNA was included in the injection mix. Lefty overexpression phenotypes were evaluated at 24 hpf. Three groups of Nodal loss-of-function phenotypes were defined according to their strength (Supplementary Fig. 3g): mild (S1), intermediate (S2), and severe (S3). For imaging, embryos were mounted in 2% methylcellulose in embryo medium. Bright-field images were acquired with an Axio Zoom.V16 (ZEISS).

Lefty1-GFP gradient measurements

The physiologically relevant amount of 100 pg mRNA encoding Lefty1-GFP was injected into the YSL of *lefty1*$^{-/-}$;*lefty2*$^{-/-}$ embryos. One group of embryos was additionally injected with 150 pg of *morphotrap* mRNA at the one-cell stage. 90 min after YSL injections, embryos were mounted and imaged using a Zeiss LSM 780 NLO (ZEISS) confocal laser scanning microscope. Embryos were imaged between 90-140 min after YSL injections. To measure gradients of secreted Lefty1-GFP from the YSL, maximum intensity projections were generated from 28 stacks over a depth of 194 µm, and the "plot profile" plug-in in Fiji[26] was used to obtain the intensity of Lefty1-GFP from every point of the vegetal-animal axis in a central region of the embryo. Background values were obtained by imaging *lefty1*$^{-/-}$;*lefty2*$^{-/-}$ uninjected embryos (for the group injected with *lefty1-GFP* mRNA) or *lefty1*$^{-/-}$;*lefty2*$^{-/-}$ injected with morphotrap (for the group injected with *morphotrap* + *lefty1-GFP* mRNA).

Fluorescence Recovery After Photobleaching (FRAP)

Wild type (TE) embryos were injected at the one-cell stage with 1 nl injection mix containing 50 pg *lefty1-GFP* mRNA and 0.05% phenol red. In experiments where the effect of the morphotrap on Lefty1-GFP diffusivity was measured, 200 pg of mRNA encoding the morphotrap were included in the injection

mix. Pronase-dechorionated embryos were selected for homogenous expression of the morphotrap using an Axio Zoom.V16 (ZEISS). Embryos were mounted around oblong to sphere stage in 1% low-melting agarose using 35 mm Glass Bottom Microwell Dishes (MatTek). FRAP was performed and analyzed as described previously[17] using an LSM 780 NLO (ZEISS) confocal microscope at an imaging depth of 30-40 µm.

lefty1$^{-/-}$;*lefty2*$^{-/-}$ mutant rescue with the small-molecule Nodal inhibitor SB-505124

Rescue experiments were performed as recently described[20]. Extirpations were performed in 4 hpf pronase-dechorionated embryos at sphere stage as described above. 30-40 min after extirpation, embryos were transferred to 24-well plates covered with 2% agarose (1 embryo per well) and treated with 4.8 µM SB-505124 in embryo medium starting 40 min after extirpation (30% epiboly stage). Embryos were then separated into two groups: one group was fixed 2-2.5 h after extirpation (shield stage) and processed for FISH, and the second group was further incubated with the inhibitor at 28°C until 24 hpf (20 h after extirpation) for phenotypic analysis. For the experiments with increasing Nodal inhibitor exposure, different concentrations from 6 to 12 µM SB-505124 in embryo medium were tested.

Code availability

The source code for custom scripts used for data analysis in this study are available from the corresponding author.

Data availability

The data that support the findings of this study are available from the corresponding author.

Supplementary Note. Screening for models of scale-invariant patterning

We found that embryos rapidly adjusted their tissue proportions after they were shortened by removal of 30% of their cells. This assay allowed us to shorten embryos at a defined developmental stage and directly analyze both short- and long-term developmental consequences. Previous studies only analyzed the long-term developmental consequences of size manipulations, making it difficult to directly link size-sensing mechanisms to later changes in morphology. We did not find evidence for changes in proliferation rates nor cell density in response to experimental shortening (Supplementary Fig. 1), thus ruling out the possibility that cells change their size in smaller embryos. Instead smaller embryos must adjust the dimensions of their tissues to the smaller embryo size for proportionate patterning (Fig. 1).

We hypothesized that the Nodal/Lefty germ layer patterning system might sense embryo size and proportionally adjust tissue dimensions. We therefore performed a systematic computational screen and identified a novel scale-invariant patterning model based on size-dependent changes in the concentration of the highly diffusive long-range Nodal inhibitor Lefty. The screen comprised more than 400,000 parameter configurations constrained with all of our previous biophysical *in vivo* measurements[17] as well as the quantitative spatiotemporal aspects of germ layer patterning that we found in this study. This approach represents one of the most exhaustive multi-objective data fitting pursuits based on quantitative biological data, and yielded insights into the behaviour of the scale-invariant Nodal/Lefty patterning system over a wide range of parameter configurations (Fig. 2). Importantly, our model can directly recapitulate the kinetics of scale-invariant patterning over relevant time scales during zebrafish embryogenesis (Supplementary Movie 1), whereas efforts based on steady-state assumptions often model patterning over unrealistic time scales.

We experimentally confirmed four major predictions of this size-dependent inhibition model with direct experimental manipulations and quantification of protein levels and diffusivity. We measurably altered inhibitor concentration (Fig. 3, Supplementary Fig. 2) and diffusivity (Fig. 4, Supplementary Fig. 3) and determined that these factors are crucial for the scaling mechanism to function.

Our model explains how early signalling adjustments in response to shortening of the patterning field assure the correct proportions of all future tissues. Previously postulated scaling mechanisms rely on a tight feedback-mediated coupling between signalling molecules and modulators that change the signals diffusion or clearance to adjust patterning to tissue size. In contrast, we identified a novel scale-invariant patterning mechanism – size-dependent inhibition – that is independent of a feedback-mediated coupling between the signal Nodal and its modulator Lefty. Instead, the long-range distribution of Lefty acts as a size sensor to scale the spatial extent of Nodal signalling, and it is sufficient to couple the changes in Lefty concentration to embryo size in order to confer scaling.

Modelling spatio-temporal Nodal/Lefty dynamics in wild type embryos

To identify scale-invariant patterning models for the Nodal/Lefty activator/inhibitor system, we performed a computational screen including the known positive and negative interactions of the signalling network[16, 17, 30]. We constrained the screen with measured biophysical properties including the diffusivities and protein stabilities of Nodal and Lefty[17], and systematically varied the unknown parameters to identify systems that recapitulate the scaling observed during germ layer patterning. To keep model complexity minimal, we did not account for spatial biases influencing the Nodal/Lefty system[31] and did not explicitly model receptor interactions[32].

The Nodal/Lefty system can be described by the following equations:

$$\begin{aligned} \frac{\partial N}{\partial t} &= D_N \nabla^2 N - \mu_N N - \lambda N \frac{L^2}{\kappa_{NL} + L^2} + \rho_N r(x,m) + \sigma_N \frac{N^2}{\kappa_N + N^2} \quad && x \in [0,l] \\ \frac{\partial L}{\partial t} &= D_L \nabla^2 L - \mu_L L + \sigma_L \frac{N^2}{\kappa_L + N^2} && x \in [0,l] \end{aligned} \tag{1}$$

$N(x,t)$ and $L(x,t)$ denote Nodal and Lefty protein levels at time t and position $x \in [0,l]$ across the animal-vegetal axis. Nodal and Lefty diffuse at rates D_N and D_L and are removed with the clearance rate constants μ_N and μ_L[17].

Nodal is initially induced at the marginal zone independently of Nodal feedback[16] (Supplementary Fig. 1), which was modelled with the constant Nodal production term $\rho_N r(x,m)$, where ρ_N is the production rate constant, and $r(x,m)$ is a rectangular pulse function given by

$$r(x,m) = \begin{cases} 1 & \text{if } x < m, \\ 0 & \text{else} \end{cases}$$

with m corresponding to the length of Nodal's production domain.

Moreover, Nodal feeds back on its own transcription[16] and thus undergoes auto-activation with the rate constant σ_N. Since Nodal feedback is limited by the finite amount of cellular material, we account for the saturation of Nodal auto-activation using a Hill-type function with the steepness parameter κ_N.

Nodal also induces its inhibitor Lefty. Similar to the term for Nodal auto-activation described above, Nodal-mediated Lefty induction is limited by the finite amount of cellular material, which we account for using a Hill-type function with steepness κ_L and a maximum induction rate σ_L.

Our experiments with *lefty1*$^{-/-}$ mutants indicate that Nodal inhibition might work cooperatively, and the inhibition of Nodal might be non-linear. We therefore chose a Hill-type function with steepness κ_{NL} and maximum inhibition rate λ to describe Lefty-mediated Nodal inhibition.

Since molecules cannot leave the embryo (modelled for a length of $[0,l]$) due to a tight enveloping layer, we used the following Neumann boundary conditions:

$$\left.\frac{\partial N}{\partial x}\right|_{x=0} = 0, \left.\frac{\partial L}{\partial x}\right|_{x=0} = 0, \left.\frac{\partial N}{\partial x}\right|_{x=l} = 0, \left.\frac{\partial L}{\partial x}\right|_{x=l} = 0 \tag{2}$$

In the following, we will refer to the system given by equations (1) and (2) as the *size-dependent inhibition* model.

Modelling spatio-temporal Nodal/Lefty dynamics without feedback

A subset of our perturbation experiments was conducted in double-homozygous *lefty1*$^{-/-}$;*lefty2*$^{-/-}$ mutants rescued by generation of highly precise and physiologically relevant (see Online Methods for details) Lefty1-GFP sources in the yolk syncytial layer (YSL). In these experiments, Lefty is no longer controlled by Nodal, but constantly produced in a similar region as Nodal specified by $r(x,m)$ with rate ρ_L, resulting in the following equations:

$$\begin{aligned} \frac{\partial N}{\partial t} &= D_N \nabla^2 N - \mu_N N - \lambda N \frac{L^2}{\kappa_{NL} + L^2} + \rho_N r(x,m) + \sigma_N \frac{N^2}{\kappa_N + N^2} && x \in [0,l] \\ \frac{\partial L}{\partial t} &= D_L \nabla^2 L - \mu_L L + \rho_L r(x,m) && x \in [0,l] \end{aligned} \tag{3}$$

This system is subject to the same boundary conditions as the size-dependent inhibition model. In the following, we will refer to the system given by equations (3) and (2) as the *size-dependent inhibition without feedback* model.

Screening for scaling solutions

We performed a computational screen to identify parameter combinations that can recapitulate the timing and spatial extent of Nodal signalling that we measured during germ layer patterning in differently sized zebrafish embryos.

A signalling threshold as a readout of Nodal signalling can be described as

$$\tau_i := N(t, x = F_i) \tag{4}$$

where $i \in \mathrm{U}, \mathrm{E}$ represent results from experiments in untreated and extirpated experiments, respectively, and F_i is the extent of the mesendodermal domain determined using *fascin* FISH measurements.

To assess how well a given parameter combination scales in differently sized embryos, a "scaling score" can be described as

$$\eta := \begin{cases} 1 & \text{if } R_{\mathrm{U}} \subseteq R_{\mathrm{E}} \vee R_{\mathrm{E}} \subseteq R_{\mathrm{U}} \\ \dfrac{|R_{\mathrm{U}} \cap R_{\mathrm{E}}|}{|R_{\mathrm{U}} \cup R_{\mathrm{E}}| - |R_{\mathrm{U}} \cap R_{\mathrm{E}}|} & \text{else} \end{cases} \tag{5}$$

Here R_i, $i \in \mathrm{U}, \mathrm{E}$ represents the interval between the threshold $\tau_{i,-}$ required to produce a Nodal signalling-dependent domain of size $F_{i,-} = \bar{F}_i - 2\sigma_i$ and the threshold that generates a Nodal readout of size $F_{i,+} = \bar{F}_i + 2\sigma_i$, where $\bar{F}_i$ is the mean size of the Nodal readout domain and σ_i the respective standard error. In other words, the scaling score η describes the overlap of the two threshold intervals produced by two times the standard error of the *fascin* domain measurements for the untreated (U) and extirpated (E) experiments. In the case that one interval completely overlaps with the other, η yields a score of 1. Thus, η provides a measure of scaling within the experimental measurement error.

To investigate whether the size-dependent inhibition model described by equations (1) and (2) scales according to our data of the spatial extent of *fascin* domains, we performed an extensive screen over a parameter space Θ for all unknown model parameters. The screened parameter space Θ was defined within a similar range as previously used values for inhibition strength[8, 33] and production rates[34]. We explored the space Θ of unknown parameters by varying each parameter over multiple orders of magnitude in three separate screens. Due to high computational costs, we kept either σ_L or κ_N fixed while varying all other parameters in the screens. A list of all known or fixed parameters can be found in Supplementary Table 1, and details about the screens are listed in Supplementary Table 2. For each set of unknown parameters $\theta \in \Theta$, one simulation was run until time T, where T represents the time of Nodal signalling readout. For the size-dependent inhibition model, θ was defined as

$$\theta = \{\sigma_L, \sigma_N, \lambda, \kappa_L, \kappa_N, \kappa_{NL}\} \tag{6}$$

The scaling score η was then determined for each simulation to assess whether the tested parameter configuration leads to scaling. To provide a good degree of scaling, we required scenarios to have $\eta(\theta) \geq 0.9$, i.e. at least a 90% overlap of the untreated and extirpated measurement error. All simulations used the experimentally measured total embryo lengths l_i and mesendoderm domain sizes F_i (Supplementary Table 3). Scenarios with the required degree of scaling are denoted as $\Theta_{\mathrm{scaling}} \subset \Theta$.

Parameter	Description	Value	Reference
D_N	Effective Nodal diffusivity	$1.85\ \mu\mathrm{m}^2/\mathrm{s}$	17
D_L	Effective Lefty diffusivity	$15.0\ \mu\mathrm{m}^2/\mathrm{s}$	17
μ_N	Nodal clearance rate constant	$1.11 \cdot 10^{-4}/\mathrm{s}$	17
μ_L	Lefty clearance rate constant	$0.61 \cdot 10^{-4}/\mathrm{s}$	17
ρ_N	Nodal production rate constant	10 nmol/(µm· s)	n.a.
m	Size of marginal zone	0.298 µm	n.a.
Δx	Size of mesh	0.99 µm	n.a.
T	End time of simulation	7200 s	n.a.
Δt	Size of time step	7.2 s	n.a.

Supplementary Table 1. Default values used for simulations of the Nodal/Lefty system if not specified differently in Supplementary Table 2. Nodal and Lefty diffusion coefficients and clearance rate constants represent the mean values of the two zebrafish Nodals Cyclops and Squint and the two Leftys Lefty1 and Lefty2 measured previously[17].

Filtering of screen results

To exclude parameter configurations that produce unrealistic Nodal gradients and Lefty levels, we implemented three filters for the screening results.

There is currently no information about endogenous Nodal or Lefty protein levels or their production rates, but we assume that the ratio between Nodal and Lefty levels does not exceed two orders of

magnitude. With this filter, parameter configurations were excluded for which

$$\frac{\max(N(x,T))}{\max(L(x,T))} \notin (\frac{1}{100}, 100)$$

The second filter excludes unrealistically flat Nodal gradients. We only selected Nodal gradients that show a proper difference between the level at the margin $N(0,T)$ and the animal pole $N(l,T)$ by considering parameter configurations for which the Nodal gradient at readout time T decreases to 10 percent of the levels at the marginal zone, i.e.

$$\frac{N(l,T)}{N(0,T)} \leq 0.1$$

Similarly, all parameter configurations that result in signalling thresholds

$$\tau > 0.5 \max(N(x,T))$$

were excluded. With a signalling threshold below 50% of the maximum Nodal level throughout the embryo at readout time T, we only consider systems that can produce sufficiently steep gradients and signalling thresholds.

Parameter	Description	Range	Steps
	Initial screen		
σ_L	Maximum Lefty production rate	0.01 – 100 nmol/(µm· s)	10
σ_N	Maximum Nodal auto-activation rate	$1 \cdot 10^{-3}$ – 1 nmol/(µm· s)	10
λ	Maximum Nodal inhibition rate	$1 \cdot 10^{-5}$ – $1 \cdot 10^{-1}$/s	10
κ_N	Steepness of Nodal auto-activation Hill function	$0.3334 \cdot 10^6$ nmol^2/µm^2	*
κ_L	Steepness of Lefty induction Hill function	100 – $1 \cdot 10^6$ nmol^2/µm^2	10
κ_{NL}	Steepness of Nodal inhibition Hill function	100 – $1 \cdot 10^6$ nmol^2/µm^2	10
	Second screen		
σ_L	Maximum Lefty production rate	0.01 nmol/(µm· s)	*
σ_N	Maximum Nodal auto-activation rate	$1 \cdot 10^{-3}$ – 1 nmol/(µm· s)	10
λ	Maximum Nodal inhibition rate	$1 \cdot 10^{-5}$ – $1 \cdot 10^{-1}$/s	10
κ_N	Steepness of Nodal auto-activation Hill function	100 – $1 \cdot 10^6$ nmol^2/µm^2	10
κ_L	Steepness of Lefty induction Hill function	100 – $1 \cdot 10^6$ nmol^2/µm^2	10
κ_{NL}	Steepness of Nodal inhibition Hill function	100 – $1 \cdot 10^6$ nmol^2/µm^2	10
	Third screen		
σ_L	Maximum Lefty production rate	0.0001 – 0.001 nmol/(µm· s)	2
σ_N	Maximum Nodal auto-activation rate	$1 \cdot 10^{-3}$ – 1 nmol/(µm· s)	10
λ	Maximum Nodal inhibition rate	$1 \cdot 10^{-5}$ – $1 \cdot 10^{-1}$/s	10
κ_N	Steepness of Nodal auto-activation Hill function	100 – $1 \cdot 10^6$ nmol^2/µm^2	10
κ_L	Steepness of Lefty induction Hill function	100 – $1 \cdot 10^6$ nmol^2/µm^2	10
κ_{NL}	Steepness of Nodal inhibition Hill function	100 – $1 \cdot 10^6$ nmol^2/µm^2	10

Supplementary Table 2. Parameter screens for scaling solutions of the size-dependent inhibition model. Parameters marked with an asterisk were held constant during the indicated screen.

		Untreated			Extirpated		
Model	Perturbation	l_U(µm)	F_U(µm)	σ_U(µm)	l_E(µm)	F_E(µm)	σ_E(µm)
SDI	None	298.0	83.7	2.0	241.0	69.5	2.5
SDI	No Lefty	267.9	115.3	3.4	246.3	114.3	4.5
SDI	Reduced Lefty production	277.1	80.7	2.0	242.4	97.5	2.5
SDIWF	+Lefty-GFP	251.6	69.0	3.6	227.5	60.6	3.4
SDIWF	+morphotrap +Lefty-GFP	234.6	70.9	3.4	214.9	73.2	4.6

Supplementary Table 3. Domain sizes used for simulations of embryo length l_i and mesendodermal region F_i, and the measured standard error of mesendodermal extent σ_i used for the computation of the scaling score η. SDI: size-dependent inhibition model (equations (1) and (2)); SDIWF: size-dependent inhibition model without feedback (equations (3) and (2)).

An intermediate level of Lefty-mediated Nodal inhibition is required for scaling

The central finding from our screen was that the shrunken mesendodermal domain results from an increase in Lefty concentration throughout the embryo. To show the relationship between Lefty induction and Nodal inhibition, we reduced the 6-dimensional parameter space Θ using a maximum projection of scaling scores by

$$\eta_{\max}(\theta, I) = \max_{i \notin I} H(k_i \in \theta)$$

where H are all scaling scores over the complete parameter space Θ, and $I = i_1, i_2, ...$ are the indices of the parameters of interest.

Maximum projections of scaling scores are displayed in Fig. 2d,e and in Supplementary Fig. 5f,g. From these plots it is clear that Lefty has an important role in scaling. Only large values for the maximum inhibition rate λ provide good scaling (Supplementary Fig. 5f). However, as the maximum Lefty induction rate σ_L increases, large values of λ become less favorable, indicating that the abundance of Lefty and its inhibition strength on Nodal need to be properly balanced (Supplementary Fig. 5f).

Similar conclusions can be drawn about the relationship between σ_L and the steepness parameter of Lefty induction κ_L. For intermediate values of σ_L, both a quick or a slow rise in Lefty levels allow scaling, whereas scaling is precluded with low values of σ_L (Supplementary Fig. 5g). However, with larger maximum Lefty induction rates σ_L, Lefty induction needs to be slowed down by higher values of the steepness parameter κ_L (Supplementary Fig. 5g), making sure that Lefty is produced at the right rate to provide scaling at the proper time.

In double-homozygous *lefty1*$^{-/-}$;*lefty2*$^{-/-}$ mutants mesendoderm does not scale, resulting in expanded *fascin* domains of similar size in untreated ($F_U = 115$ µm) and extirpated ($F_E = 114$ µm) embryos. To test whether the size-dependent inhibition model can reproduce these experimental observations, we simulated all parameter configurations $\theta \in \Theta_{\text{scaling}}$ of the full model (equations (1) and (2)) with $\sigma_L = 0$, mimicking the absence of Lefty. If the simulations reproduced the measured *fascin* domains (Supplementary Table 3) within 20 µm, we recorded the original parameter configuration θ of the full model in $\Theta_{\text{NoLft}} \subset \Theta_{\text{scaling}}$. A non-scaling Nodal profile can be seen in Supplementary Fig. 5b; since the dashed and solid lines do not overlap at the intercept with the signalling threshold, this parameter configuration does not scale.

Proper Lefty levels are therefore crucial for size-dependent inhibition and scaling. To further illustrate that even small changes in Lefty levels can influence scaling, we lowered σ_L by 20%, 30%, and 50% for all parameter configurations in Θ_{NoLft}, which abrogate scaling (Supplementary Fig. 5c, Fig. 3a,b). All tested parameter configurations for lowered σ_L resulted in an expansion of the *fascin* domain to varying degrees and decreased the system's ability to scale. We recorded all parameter configurations $\theta \in \Theta_{\text{noLft}}$ for which at least one of the three Lefty induction permutations provided an expansion of *fascin* domain less than 30 µm in Θ_{lowP} and its corresponding permutation parameter set.

Mesendoderm scaling fails if Lefty diffusion is reduced

We propose that Lefty senses embryo size due to its high diffusivity allowing it to reach the animal pole within the time scale of germ layer formation. To test this hypothesis, multiple scenarios with Lefty diffusion coefficients ranging from $D_L = 0.35$ µm^2/s to $D_L = 20.0$ µm^2/s were analyzed. Simulations with $D_L \geq 7$ µm^2/s showed good scaling behavior, while lower rates of diffusion abrogated scaling (Fig. 2e, Fig. 4b, Supplementary Fig. 5h).

We further tested whether the model can reproduce the rescue experiments with Lefty1-GFP. Since these experiments were executed in *lefty1*$^{-/-}$;*lefty2*$^{-/-}$ mutants, Nodal cannot induce Lefty. In the "size-dependent inhibition without feedback" model, we therefore removed Nodal-mediated Lefty induction and simulated equations (3) and (2) with the parameter configuration

$$\tilde{\theta} = \{\sigma_L, \sigma_N, \lambda, \kappa_N, \kappa_{NL}\}$$

We first tested whether the feedback-less model can reproduce the *fascin* domains in mutants rescued by exogenous *lefty-GFP* mRNA injection. Simulations were performed using values for auto-activation σ_N

Model	Perturbation	σ_L nmol/(µm· s)	σ_N nmol/(µm· s)	λ $1/s$	κ_L $\mathrm{nmol}^2/\mu\mathrm{m}^2$	κ_N $\mathrm{nmol}^2/\mu\mathrm{m}^2$	κ_{NL} $\mathrm{nmol}^2/\mu\mathrm{m}^2$	Suppl. Fig.
SDI	None	$1 \cdot 10^{-2}$	1	0.07778	100	445000	445000	5a
SDI	No Lefty	0	1	0	0	445000	0	5b
SDI	Reduced Lefty production	$6.5 \cdot 10^{-7}$	1	0.07778	100	445000	445000	5c
SDI WF	+Lefty-GFP	7.5	1	0.02650	0	445000	445000	5d
SDI WF	+morphotrap +Lefty-GFP	7.5	1	0.00321	0	445000	445000	5e

Supplementary Table 4. Optimal parameter configurations that satisfy all experimental observations. SDI: size-dependent inhibition model (equations (1) and (2)); SDIWF: size-dependent inhibition model without feedback (equations (3) and (2)).

and steepness parameters κ_N and κ_{NL} taken from scaling parameter configurations $\theta \in \Theta_{\mathrm{lowP}}$ of the full model with feedback. We screened the remaining two unknown parameters σ_L and λ, which represent exogenous production of Lefty-GFP and its inhibition strength, respectively. The scaling configuration $\tilde{\theta}$ was selected that reproduced the measured *fascin* domains of $F_U = 68$ µm and $F_E = 60$ µm with the threshold $\tau(\theta)$ of the corresponding simulation of the full model with feedback.

We then simulated the feedback-less model for each scaling parameter configuration $\tilde{\theta}$ with the reduced Lefty1-GFP diffusion coefficients measured in the presence of the morphotrap ($D_L = 0.35$ $\mu\mathrm{m}^2/\mathrm{s}$). Since the morphotrap modestly lowers Lefty activity (Supplementary Fig. 3g,h), λ was allowed to be smaller than the one in $\tilde{\theta}$. Finally, we selected parameter configurations $\tilde{\theta} \in \tilde{\Theta}_{\mathrm{lowD}}(\theta)$ that fit the *fascin* domains measured in embryos with Lefty-GFP + morphotrap ($F_U = 69$ µm and $F_E = 71$ µm) within a 20 µm range.

Nodal gradients for the feedback-less model with and without morphotrap are shown in Supplementary Fig. 5d,e. While the feedback-less model with normal Lefty diffusion scales, reducing Lefty diffusion to $D_L = 0.35$ $\mu\mathrm{m}^2/\mathrm{s}$ precludes scaling.

Extensions of the size-dependent inhibition model

Separate modelling of Nodal protein distributions and Nodal signalling

To keep model complexity minimal, we executed our screens with a system that describes both signalling and protein levels in the single variable N. This was based on the assumption that signal transduction acts at faster time scales than other kinetics in the model, such as protein clearance and inhibition.

In a more realistic description of the biological system, the merged $N(x,t)$ can be uncoupled into separate variables $S(x,t)$ – representing pSmad2/3 levels over space and time – and $N(x,t)$ – representing Nodal protein levels over space and time – as follows:

$$\begin{aligned}
\frac{\partial N}{\partial t} &= D_N \nabla^2 N - \mu_N N - \lambda N \frac{L^2}{\kappa_{NL} + L^2} + \rho_N r(x,m) + \sigma_N \frac{S^2}{\kappa_N + S^2} && x \in [0,l] \\
\frac{\partial L}{\partial t} &= D_L \nabla^2 L - \mu_L L + \sigma_L \frac{S^2}{\kappa_L + S^2} && x \in [0,l] \\
\frac{\partial S}{\partial t} &= \sigma_S \frac{N^2}{\kappa_S + N^2} - \mu_S S && x \in [0,l]
\end{aligned} \tag{7}$$

Here, σ_S represents the maximum rate of signal transduction that is described by a Hill-type function with steepness parameter κ_S. Moreover, Nodal signalling $S(x,t)$ decays linearly with the rate constant μ_S. Similar to our original model, we applied no-flux Neumann boundary conditions to all reactants:

$$\left.\frac{\partial N}{\partial x}\right|_{x=0} = 0, \left.\frac{\partial L}{\partial x}\right|_{x=0} = 0, \left.\frac{\partial S}{\partial x}\right|_{S=0} = 0, \left.\frac{\partial N}{\partial x}\right|_{x=l} = 0, \left.\frac{\partial L}{\partial x}\right|_{x=l} = 0, \left.\frac{\partial S}{\partial x}\right|_{x=l} = 0 \tag{8}$$

In contrast to the models used for screening (equations (1) and (3)), Nodal auto-activation and Lefty induction are no longer directly dependent on the levels of $N(x,t)$, but are now under the control of $S(x,t)$.

The extended model (equations (7) and (8)) also scales. We simulated this model with similar parameters as the two-component model (Supplementary Table 5) and chose a clearance rate constant $\mu_S = 5.333 \cdot 10^{-2}$/s and a maximum transduction rate constant $\sigma_S = 1.6680 \cdot 10^4$ nmol/(µm· s) together with a steepness parameter of $\kappa_S = 7.9119914 \cdot 10^7$ $\mathrm{nmol}^2/\mu\mathrm{m}^2$ for $S(x,t)$, which results in much faster turnover kinetics compared to the rest of the system. The signal decays roughly 500 times faster than both Nodal and Lefty proteins and reaches a high maximum transduction rate σ_S at relatively low Nodal protein levels. Simulations of this extended model also resulted in a flat Lefty profile (Supplementary Fig. 5i,j, Supplementary Movie 4). Nodal signalling levels read out at the threshold indicated by the dashed red line in Supplementary Fig. 5i,j result in gradients with a similar extent as the experimentally measured pSmad2/3 gradients (Fig. 1f) at roughly 25% of total embryo length.

σ_L nmol/(µm· s)	σ_N nmol/(µm· s)	λ $1/s$	κ_L $\mathrm{nmol}^2/\mu\mathrm{m}^2$	κ_N $\mathrm{nmol}^2/\mu\mathrm{m}^2$	κ_{NL} $\mathrm{nmol}^2/\mu\mathrm{m}^2$	ρ_N nmol/(µm· s)	σ_S nmol/(µm· s)	μ_S $1/s$	κ_S $\mathrm{nmol}^2/\mu\mathrm{m}^2$
0.045445	1.8356	0.0656	77.505	424316	354120	5.599	16680	0.05333	79119914

Supplementary Table 5. Parameter configurations that result in scaling of the extended size-dependent inhibition model (equations (7) and (8)).

Modelling of bound and free Nodal

Our models rely on the assumption that free, unbound Nodal protein activates signal transduction and correlates with Nodal signalling. In the following, we extended the model to also take into account inactive Nodal bound to Lefty ($C(x,t)$):

$$\begin{aligned}
\frac{\partial N}{\partial t} &= D_N \nabla^2 N - \mu_N N - \lambda N \frac{L^2}{\kappa_{NL} + L^2} + \rho_N r(x,m) + \sigma_N \frac{N^2}{\kappa_N + N^2} && x \in [0,l] \\
\frac{\partial L}{\partial t} &= D_L \nabla^2 L - \mu_L L + \sigma_L \frac{N^2}{\kappa_L + N^2} && x \in [0,l] \\
\frac{\partial C}{\partial t} &= D_C \nabla^2 C - \mu_C C + \lambda N \frac{L^2}{\kappa_{NL} + L^2} && x \in [0,l]
\end{aligned} \tag{9}$$

The total Nodal concentration can be calculated as

$$N_{\mathrm{total}}(x,t) = N(x,t) + C(x,t) \tag{10}$$

We assume that Nodal bound to Lefty $C(x,t)$ diffuses with a diffusion coefficient D_C and is removed with a clearance rate constant μ_C. No-flux Neumann boundary conditions for the system are given by

$$\left.\frac{\partial N}{\partial x}\right|_{x=0} = 0, \left.\frac{\partial L}{\partial x}\right|_{x=0} = 0, \left.\frac{\partial C}{\partial x}\right|_{x=0} = 0, \left.\frac{\partial N}{\partial x}\right|_{x=l} = 0, \left.\frac{\partial L}{\partial x}\right|_{x=l} = 0, \left.\frac{\partial C}{\partial x}\right|_{x=l} = 0 \tag{11}$$

For bound Nodal $C(x,t)$ we chose the mean of Lefty and Nodal diffusion and clearance ($D_C = 8.5$ $\mu\mathrm{m}^2/\mathrm{s}$ and $\mu_C = 0.86 \cdot 10^{-4}$/s). Simulations of the model (equations (9) and (11)) with the parameters defined for the two-component model (Supplementary Table 4) are shown in Supplementary Fig. 5k,l. Despite a difference in absolute values, the shape of the total Nodal profile $N_{\mathrm{total}}(x,t)$ is similar to free Nodal $N(x,t)$.

Comparison of the size-dependent inhibition mechanism to other scaling models

Previously described scaling mechanisms rely on modulators, whose concentrations change depending on tissue size to adjust signalling activity range by modulating the signal's diffusion or clearance[5, 35]. The Nodal/Lefty activator/inhibitor system is an excellent candidate for a modulator-based scaling mechanism: i) Lefty (modulator) inhibits Nodal activity by binding and preventing it from activating its receptors, ii) Nodal activity range is unaffected by the size reduction in extirpated embryos since the Nodal

distribution is restricted to the marginal zone due to its low diffusivity[17], iii) Lefty diffuses significantly faster than Nodal and exhibits a nearly uniform distribution[17] (Fig. 2c, Fig. 4d, Supplementary Fig. 3i, Supplementary Movie 2), and iv) the production of Lefty is independent of the changes in size since Lefty-producing cells are located at the margin, which remains unaffected after extirpation (Supplementary Fig. 1f-k).

An example of modulator-based scaling mechanisms is the recently proposed "expansion-repression" model, in which scaling of signalling gradients is achieved by an expander that increases the signal's range and that is itself repressed by the signal[36]. Superficially, our model can be interpreted as a mirror image of the "expansion-repression" model – i.e. a "contraction-activation" system – since the "inhibitor" or "contractor" Lefty restricts the signal's (Nodal) range and is activated by the signal. However, we show that Nodal-mediated Lefty activation is dispensable for scaling (Fig. 4, Fig. 5, Supplementary Fig. 3, Supplementary Fig. 4). Therefore, in contrast to previously postulated scaling networks, our simple model is a new scaling system that does not depend on the feedback between signal and modulator. Since in our system the modulator Lefty inhibits the signal, it is sufficient to couple the changes in the concentration of Lefty to size in order to confer proportionate patterning. Importantly, this also implies that scale-invariant patterning driven by the Nodal/Lefty pathway is not based on previously postulated feedback-based activator/inhibitor systems[23] but purely on size-dependent Nodal inhibition mediated by Lefty.

Movie Legends for Supplementary Movies 1-4

Supplementary Movie 1

Temporal dynamics of the scaling model. Nodal signalling levels (blue, solid line: normally sized embryo, dashed line: extirpated embryo) peak at the time of Nodal readout (red). Nodal signalling levels decrease rapidly afterwards, matching the time window of germ layer specification. Grey bars indicate the extent of the mesendodermal domain, and green lines show Lefty levels (solid line: normally sized embryo, dashed line: extirpated embryo).

Supplementary Movie 2

Lefty1-GFP diffusion from the marginal zone in *lefty1*$^{-/-}$;*lefty2*$^{-/-}$ embryos. Time-lapse imaging over 70 min after yolk syncytial layer (YSL) injections reveals high mobility of Lefty1-GFP emerging from the YSL. Lefty1-GFP levels increase in the YSL and over time localize to the extracellular space. Lefty1-GFP moves over a long distance to the animal pole within $\sim$40 min. Maximum intensity projection of a $60\,\mu\mathrm{m}$ z-stack. The animal pole is at the top, and Lefty1-GFP signal is shown in green.

Supplementary Movie 3

Lefty1-GFP diffusion from the marginal zone in *lefty1*$^{-/-}$;*lefty2*$^{-/-}$ embryos expressing the GFP binding morphotrap. Time-lapse imaging over 70 min after YSL injections reveals hindered movement of Lefty1-GFP from the YSL in the presence of morphotrap. The morphotrap drastically changes the distribution of Lefty1-GFP from diffuse extracellular to membrane-bound. Maximum intensity projection of a $60\,\mu\mathrm{m}$ z-stack. The animal pole is at the top, and an overlay of the Lefty1-GFP signal (green) with the morphotrap signal (red) is shown.

Supplementary Movie 4

Temporal dynamics of the extended scaling model. Nodal signalling, i.e. pSmad2/3 levels (magenta, solid line: normally sized embryo, dashed line: extirpated embryo), peaks at the time of Nodal readout (red). Nodal signalling levels decrease rapidly afterwards, matching the time window of germ layer specification. Dashed-dotted lines indicate the extent of the pSmad2/3 domain, blue lines show Nodal, and green lines show Lefty levels (solid line: normally sized embryo, dashed line: extirpated embryo).

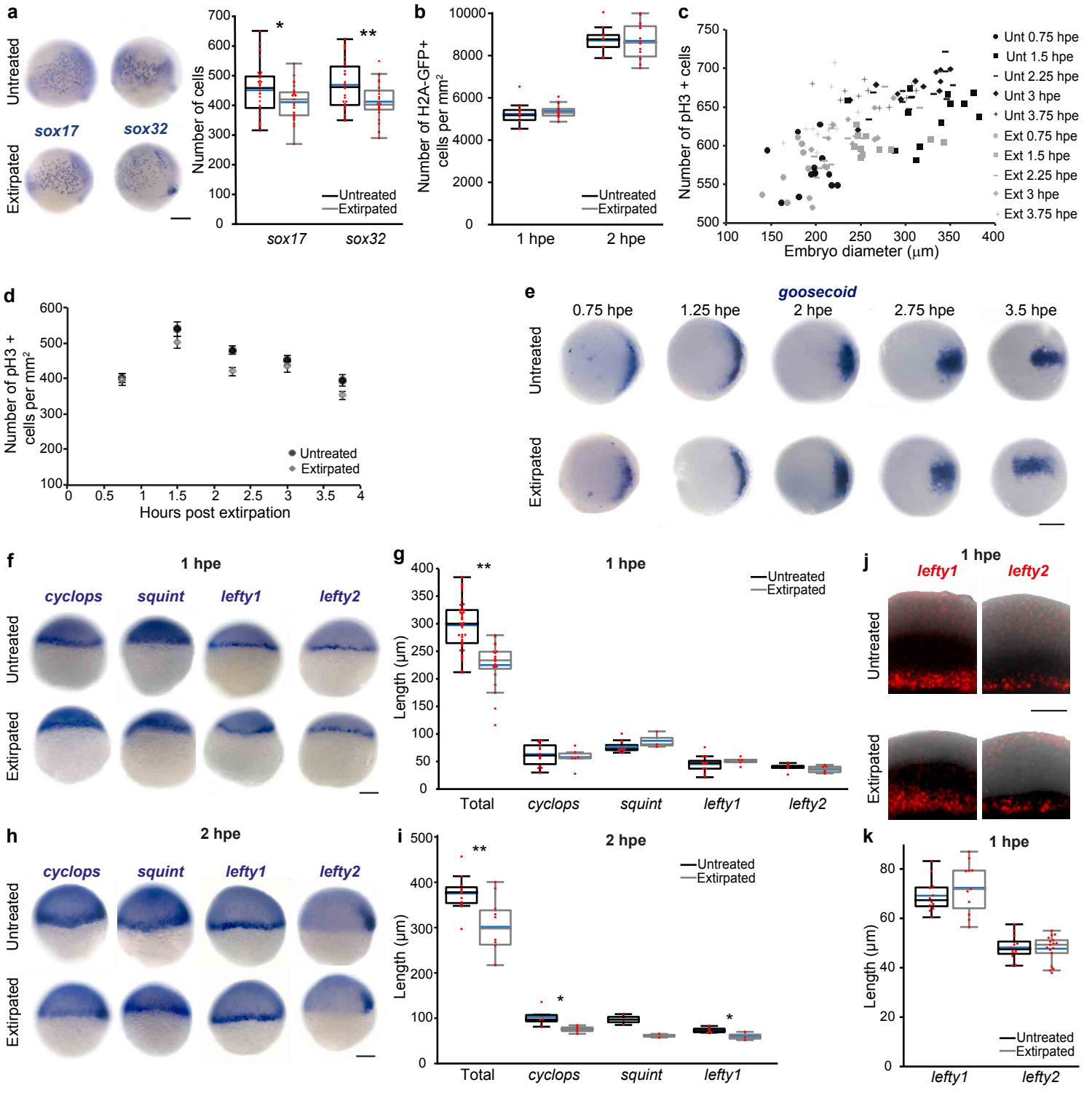

Supplementary Figure 1 | Germ layer proportions scale in extirpated embryos without changes in cell proliferation, cell density, or developmental speed. (a) Lateral views and quantification of the number of endodermal cells positive for *sox17* (untreated, n=30; extirpated, n=27; *p<0.05) and *sox32* (untreated, n=26; extirpated, n=28; **p<0.01). **(b)** Cell density measured in untreated and extirpated H2A::GFP embryos at different time points after extirpation. n>=9 for all groups. **(c,d)** Number of proliferating cells (phospho-Histone H3 (pH3) positive) relative to embryo diameter (c), and density of proliferating cells (d) in untreated and extirpated embryos at different time points after extirpation. n≥11 for all groups. Individual data points are shown in (c); mean and SEM of the same data are shown in (d). **(e)** Animal pole view images of *goosecoid* expression. Changes in the *goosecoid* expression domain during development proceed with the same speed in untreated and extirpated embryos. **(f,h)** Lateral images of embryos analyzed for the expression of *cyclops* and *squint* Nodals, and *lefty1* and *lefty2* Leftys in untreated and extirpated embryos at 1 hour (f) and 2 hours (h) post extirpation. **(g,i)** Quantification of total embryo length and length of gene expression domains at 1 hour (g) and 2 hours (i) post extirpation. *Nodal* and *Lefty* expression domains are unchanged in differently sized embryos at 1 hpe but scale by 2 hpe. **(j)** Maximum intensity projections of lateral confocal stacks of *lefty1* and *lefty2* FISH in untreated and extirpated embryos at 1 hpe. n>=10 for all groups. **(k)** Quantification of *lefty* expression domains. hpe: hours post extirpation. Box plots (a,b,g,i,k) show median (blue line), mean (untreated: black; extirpated: grey lines), 25% quantiles (box) and all included data points (red markers). Unt: Untreated; Ext: Extirpated. Scale bars: 200 µm (a,e) and 100 µm (f,h,j).

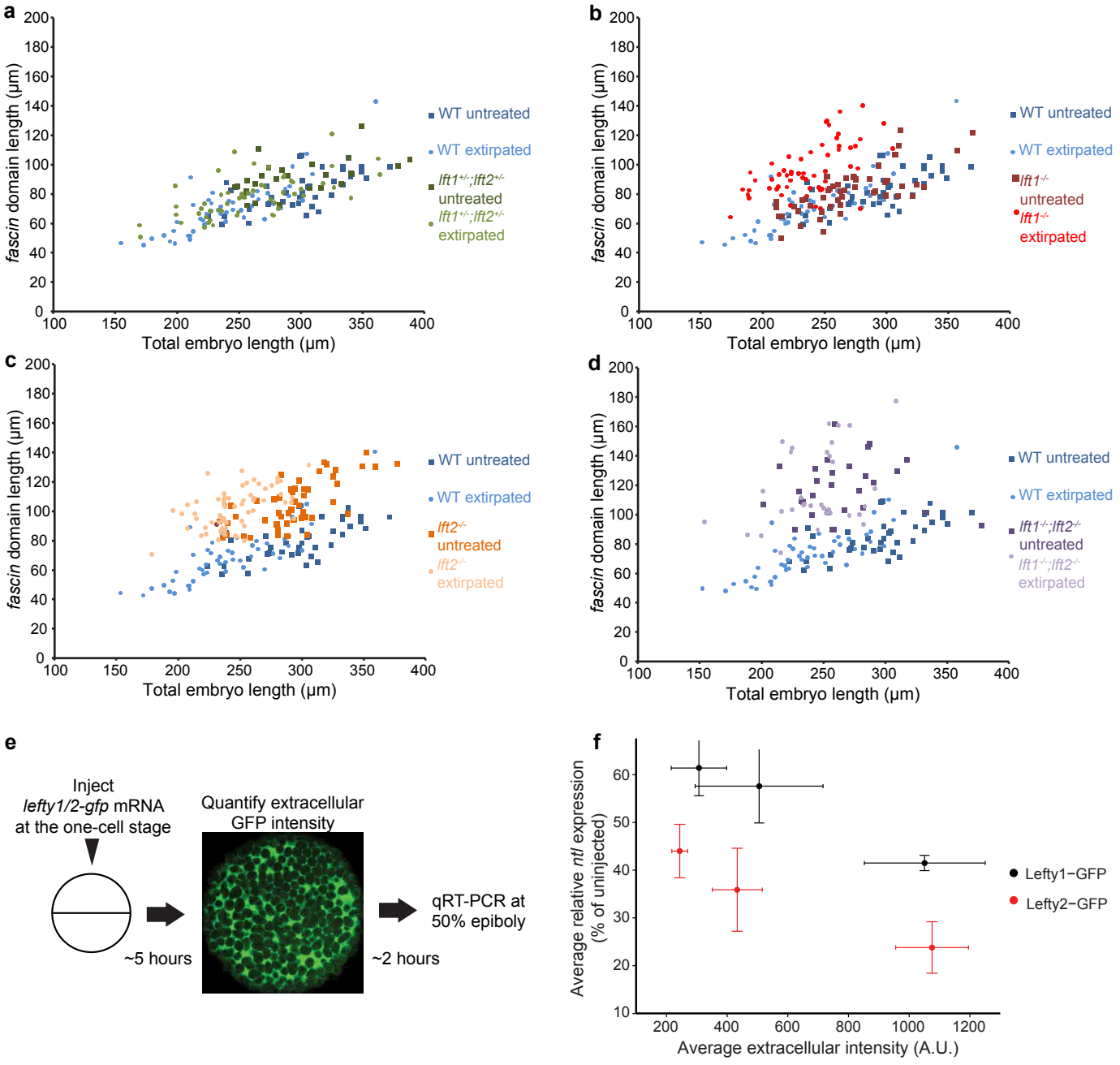

Supplementary Figure 2 | Lack of Lefty1 precludes germ layer scaling. (a-d) Quantification of *fascin* extent relative to embryo length. The different *lefty* mutant groups are shown along with data from wild type embryos. *lft1*$^{+/-}$;*lft2*$^{+/-}$ untreated and extirpated, and *lft1*$^{-/-}$ untreated embryos show a linear increase of mesendoderm with embryo size, similar to the linear increase observed in wild type individuals. In contrast, *lft1*$^{-/-}$ extirpated, *lft2*$^{-/-}$ untreated and extirpated, and *lft1*$^{-/-}$;*lft2*$^{-/-}$ untreated and extirpated embryos cluster in a wider circular domain showing absence of scaling. WT: n[untreated]=38, n[extirpated]=49; *lft1*$^{+/-}$;*lft2*$^{+/-}$: n[untreated]=26, n[extirpated]=55; *lft1*$^{-/-}$: n[untreated]=50, n[extirpated]=58; *lft2*$^{-/-}$: n[untreated]=50, n[extirpated]=61; *lft1*$^{-/-}$;*lft2*$^{-/-}$: n[untreated]=29; n[extirpated]=34). **(e)** Schematic of experiments to assess the activity of Lefty1 and Lefty2. Embryos were injected at the one-cell stage with different amounts of *lefty1*- or *lefty2-gfp* mRNA. Extracellular GFP intensity was quantified at 5 hpf, and sibling embryos were collected at 50% epiboly. qRT-PCR using primers for the Nodal target gene *no tail* (*ntl*) was used to assess inhibitory activity. **(f)** Average *ntl* expression is plotted against average extracellular intensity. At similar intensities, Lefty2-GFP consistently repressed *ntl* expression more effectively than Lefty1-GFP. Error bars: SEM.

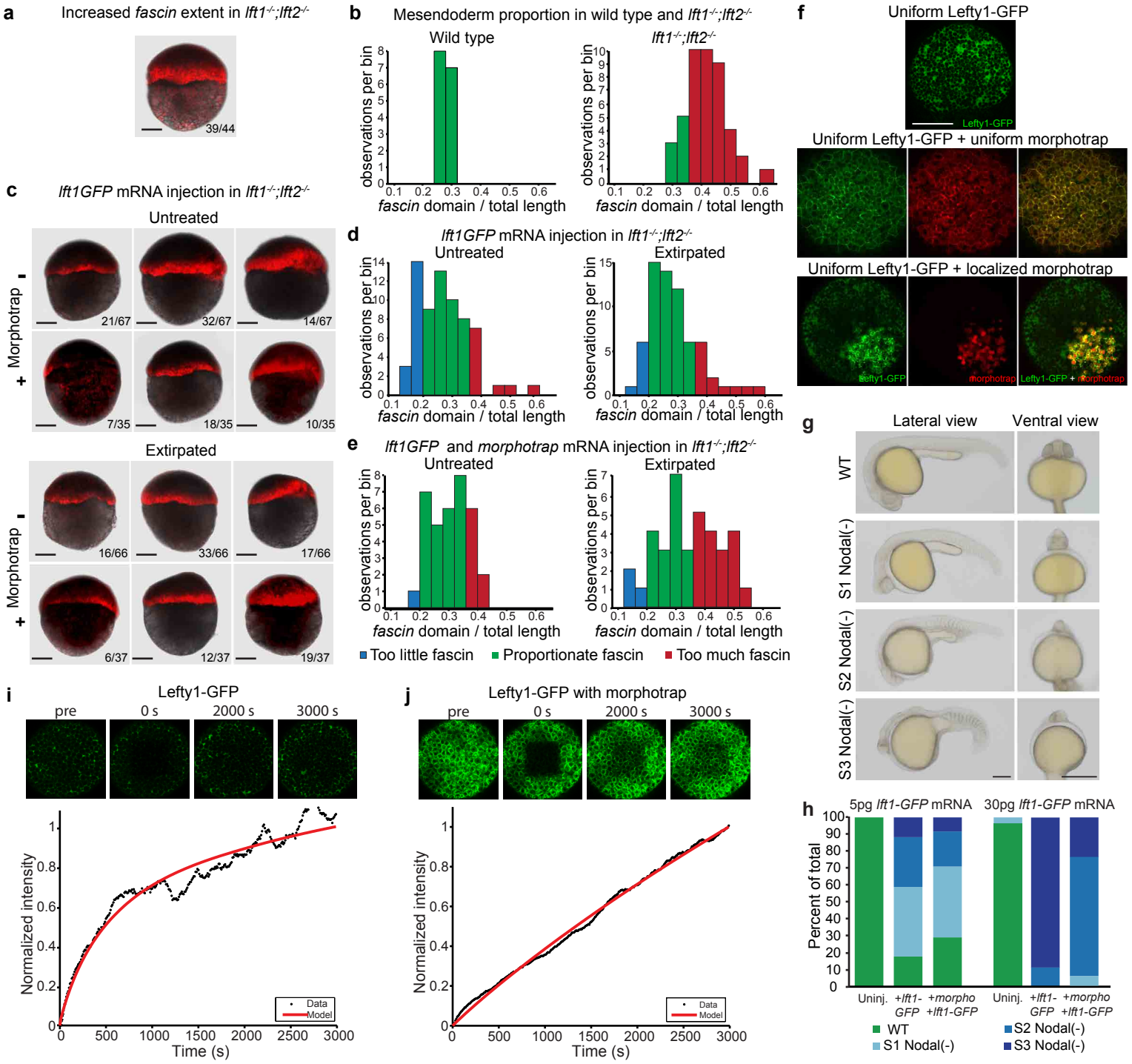

Supplementary Figure 3 | Experimentally hindering Lefty1-GFP diffusion in zebrafish embryos. (a,c) Maximum intensity projections of lateral confocal stacks of *fascin* expression in *lft1*$^{-/-}$;*lft2*$^{-/-}$ embryos subjected to different treatments. Representative embryos for each treatment are shown. **(b,d,e)** Mesendoderm proportions in differently sized embryos. Note that the fraction of embryos with normal mesendoderm extent is equivalent to the fraction of rescued *lft1*$^{-/-}$;*lft2*$^{-/-}$ embryos shown in Fig. 4. **(f)** Maximum intensity projections of confocal stacks of 30-50% epiboly stage embryos. Animal pole views. The upper image shows an embryo injected with *lefty1-GFP* mRNA at the one-cell stage. The middle panel shows an embryo co-injected with *morphotrap*-encoding mRNA and *lefty1-GFP* mRNA at the one-cell stage. The lower panel shows an embryo injected with *lefty1-GFP* mRNA at the one-cell stage and transplanted with a *morphotrap*-expressing clone at sphere stage. The morphotrap changes the distribution of Lefty1-GFP from uniform extracellular to strongly membrane-associated. **(g,h)** Morphotrap binding modestly affects Lefty activity**.** Lateral and ventral views of 24 hpf wild type embryos injected with *morphotrap* or different concentrations of *lefty1-GFP* mRNA. Representative embryos for each phenotypic category are shown (g). Distribution of phenotypes after different treatments (h). Three groups of Nodal loss-of-function phenotypes were defined according to their strength: mild (S1), intermediate (S2), and severe (S3). For 5 pg of *lft1-GFP* mRNA: uninjected n=32, +*lft1-GFP* n=34, +*morphotrap*+*lft1-GFP* n=24. For 30 pg of *lft1-GFP* mRNA: uninjected n=30, +*lft1-GFP* n=26, +*morphotrap*+*lft1-GFP* n=34). **(i,j)** FRAP experiments demonstrate that Lefty1-GFP diffusion is hindered by the morphotrap. Representative FRAP data for Lefty1-GFP (i), and Lefty1-GFP with morphotrap (j). Microscopy images are shown before photobleaching (pre), immediately after (0 s), as well as 2000 s and 3000 s after photobleaching. Diffusion coefficients and production rates were fitted to the recovery curves using previously published values for Lefty1-GFP protein stability. The mean diffusion coefficients were 7.7 ± 3.2 μm^2/s for Lefty1-GFP (n=6) and 0.2 ± 0.2 μm^2/s for Lefty1-GFP with morphotrap (n=4). Note that a diffusion coefficient of 0.1 μm^2/s is the minimal value allowed in the model used for fitting and on the order of the speed of cell movements during early zebrafish development. Scale bars: 200 μm.

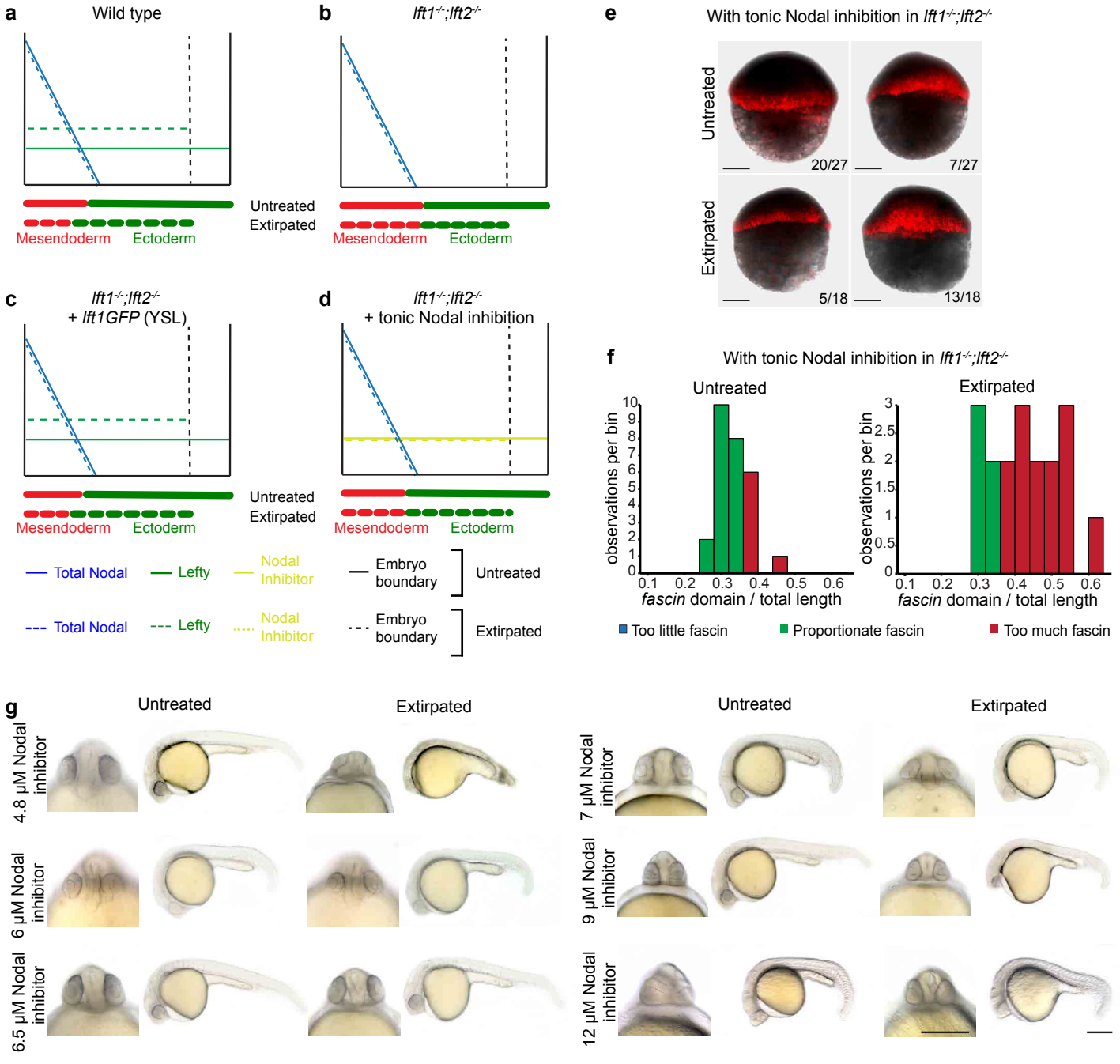

Supplementary Figure 4 | An increase in Lefty concentration is required for scale-invariant patterning. (a-d) Simplified qualitative models of Nodal (i.e. total Nodal, in contrast to the free Nodal shown in the simulations throughout the paper) and Lefty gradients in different scenarios to explain experimental observations. In contrast to our rescue approach using ectopic Lefty gradients, most of the extirpated *lft1*$^{-/-}$;*lft2*$^{-/-}$ mutants exposed to the Nodal inhibitor SB-505124 are unable to restore normal mesendoderm proportions. In contrast to ectopic Lefty proteins (c), the Nodal inhibitor is provided tonically, and its concentration does not increase after a reduction in embryo size (d). **(e)** Maximum intensity projections of confocal stacks of *fascin* expression in *lft1*$^{-/-}$;*lft2*$^{-/-}$ embryos exposed to the Nodal inhibitor SB-505124. Lateral views. Representative embryos for each treatment are shown. **(f)** Mesendoderm proportions in embryos treated with the Nodal inhibitor SB-505124. **(g)** Lateral views of 26 hpf *lft1*$^{-/-}$;*lft2*$^{-/-}$ embryos exposed to different concentrations of the Nodal inhibitor SB-505124. Representative embryos for each treatment are shown. Scale bars: 200 µm.

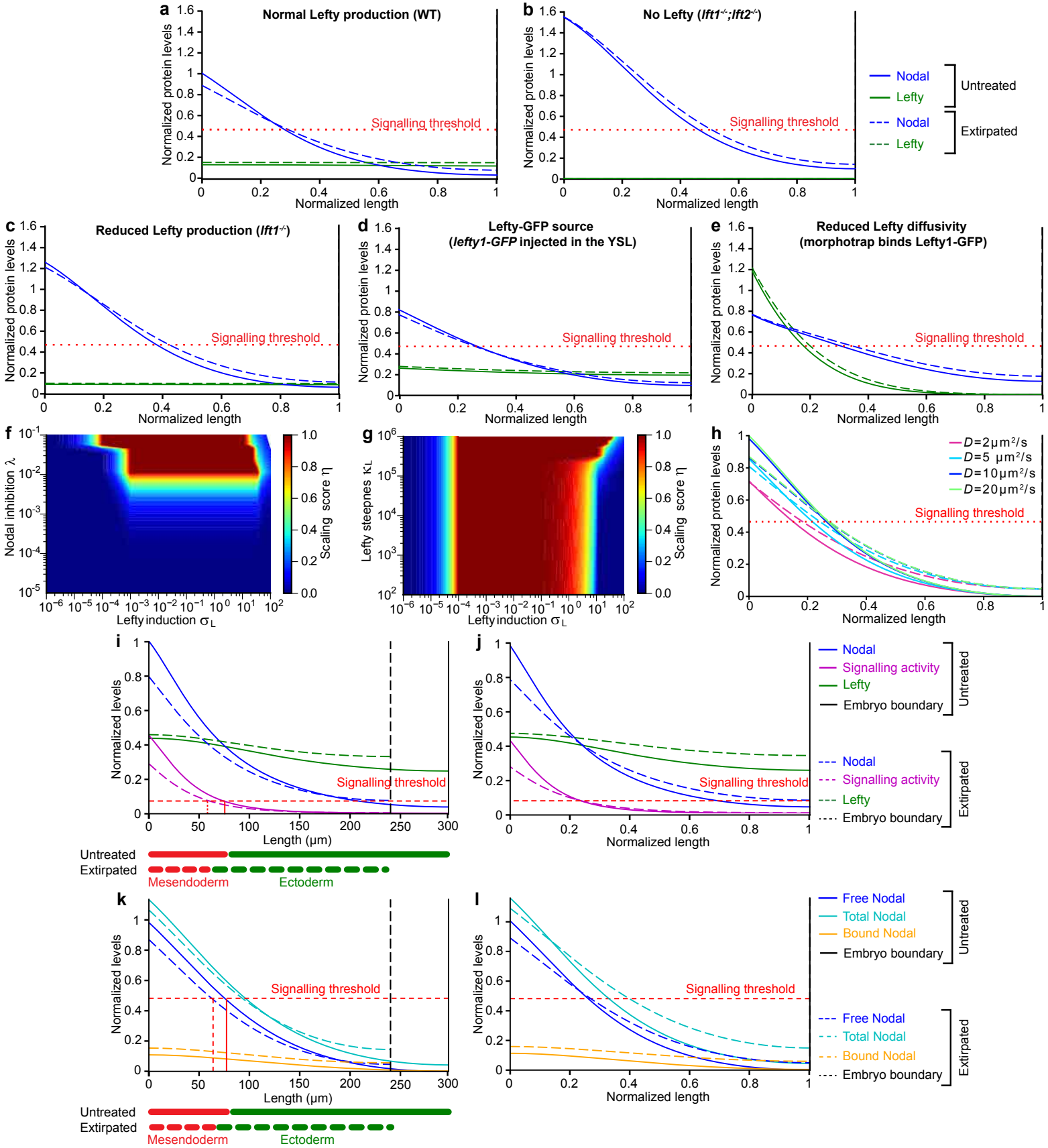

Supplementary Figure 5 | Summary and extensions of the size-dependent inhibition model for scale-invariant patterning. **(a-e)** Normalized Nodal and Lefty protein profiles scaled to embryo size for simulations of the size-dependent inhibition model with normal Lefty production (a), no Lefty production (b), reduced Lefty production (c), and feedback-less Lefty inhibition in the absence (d) or presence of morphotrap (e). In contrast to the graphs shown in Fig. 2, Fig. 3, and Fig. 4, these graphs show normalized length for both untreated and extirpated embryos. Here, models scale when the dashed and solid lines overlap at the intercept with the signaling threshold. Normal Lefty induction in the model corresponds to 10^{-6}, and the reduced Lefty induction was set to 6.5 x 10^{-7} corresponding to a 30% decrease in induction. Normal Lefty diffusivity was set to D_L = 15 μm²/s, and Lefty diffusivity in the presence of morphotrap was set to D_L = 0.35 μm²/s. All simulation parameter values are listed in Supplementary Table 3 (Supplementary Note). **(f,g)** Relationship between the maximum rate of Lefty induction and the strength of Lefty-mediated Nodal inhibition (f) or between the maximum rate of Lefty induction and Lefty induction steepness (g). The plots show maximum projections through the six-dimensional parameter space of the size-dependent inhibition model. **(h)** Simulation of the full model with different values for Lefty diffusivities. A minimal diffusion coefficient of approximately 7-10 μm²/s is required for scale-invariant patterning. **(i-l)** Extensions of the size-dependent inhibition model. (i,j) Simulations with separate variables for signalling and protein levels showing results for absolute (i) and normalized (j) embryo length. (k,l) Simulations of the size-dependent inhibition system explicitly modelling total, free, and Lefty-bound (inhibited) Nodal protein, showing results for absolute (k) and normalized (l) embryo length.